2016

Ultrafast and Nonlinear Spectroscopy of Colloidal Nanomaterials

Tony Eugene Karam
Louisiana State University and Agricultural and Mechanical College, tkaram2@lsu.edu

ULTRAFAST AND NONLINEAR SPECTRSOCOPY OF COLLOIDAL NANOMATERIALS

A Dissertation

Submitted to the Graduate Faculty of the
Louisiana State University and
Agricultural and Mechanical College
in partial fulfillment of the
requirements for the degree of
Doctor of Philosophy

in

The Department of Chemistry

by
Tony Eugene Karam
B.S., Saint Joseph University, 2008
M.S., American University of Beirut, 2011
May 2016

ACKNOWLEDGMENTS

I am very grateful to Professor Louis Haber for providing me with the opportunity to join his group and to work on all these exciting research projects. I am very thankful for his constant encouragements, guidance, and support. All of this work would have not been possible without his mentorship and motivation. I am also very grateful to Professor Isiah Warner for his constant support and encouragements. I am also thankful for the opportunity to be part of the collaborative work with his research group. Additionally, I would like to thank my Committee members Professor Les Butler and Professor David Young for their time and guidance. I am also very grateful to Professor Kenneth Lopata for his support and valuable advices.

I am deeply indebted to Dr. Noureen Siraj for providing me with the nanoGUMBOS samples. I greatly appreciate all the great work she put towards this project and all of the valuable discussions we had. I am grateful to Dr. Raphael Cueto for his immense help with the characterization of the nanoparticle samples. Moreover, I am very thankful for the help given by Dr. Xin Li and Professor Gerald Schneider on the X-ray and neutron experiments. I would also like to thank Dr. Christopher Stanley at Oak Ridge National Laboratory for his exceptional help with the SANS experiment and Dr. Sungsik Lee at Argonne National Laboratory for giving me the opportunity to perform the SAXS and ASAXS experiments. I am also grateful to Dr. Dongmei Cao, Dr. Xiaochu Wu, and Ying Xiao for their help with electron microscopy and Dr. Thomas Blanchard for his help with ICP-OES. Furthermore, I am grateful to Dr. Zhenyu Zhang for his help and support with the laser system. Finally, I would like to thank the members of the Haber group: Raju Kumal, Emily Harwell, Rami Khoury, Holden Smith, Joel Taylor, and Jeewan Ranasinghe. It has been a real pleasure working with all of you.

TABLE OF CONTENTS

LIST OF FIGURES

LIST OF SCHEMES

LIST OF ABBREVIATIONS

Abbreviation	Name
SERS	surface-enhanced Raman scattering
SHG	second harmonic generation
SFG	sum frequency generation
TiO_2	titanium dioxide
MSA	mercaptosuccinic acid
UV	ultraviolet
NIR	near-infrared
TEM	transmission electron microscopy
HRTEM	high-resolution transmission electron microscopy
CCD	charge-coupled device
MG	malachite green
BG	brilliant green
MetG	methyl green
SAXS	small-angle X-ray scattering
DLS	dynamic light scattering
$AgNO_3$	silver nitrate
NaOH	sodium hydroxide
Ti	titanium
SAED	small-angle electron diffraction
cs	core-shell
css	core-shell-shell

CTAB	cetyltrimethylammonium bromide
EDS	energy dispersive X-ray spectroscopy
ICP-OES	inductively coupled plasma optical emission spectroscopy
OPA	optical parametric amplifier
NaCl	sodium chloride
Rhd 110	rhodamine 110
CO	carbon monoxide
CO_2	carbon dioxide
TTIP	titanium (IV) tetraisopropoxide ($Ti[OCH(CH_3)_2]_4$)
$HAuCl_4$	gold chloride
$NaBH_4$	sodium borohydride
Au	gold
DSSCs	dye-sensitized solar cells
$Ru(bipy)_3Cl_2$	Tris(bipyridine)ruthenium(II) chloride
BETI	bis(pentafluoroethylsulfonyl)imide
GUMBOS	group of uniform materials based on organic salts
IMET	intermolecular energy transfer
$Ru(bipy)_3Cl_2.6H_2O$	tris (2,2'-bipyridyl)dichlororuthenium (II) hexahydrate
Li	lithium
MLCT	metal to ligand charge transfer
MC	metal centered
TCPP	meso-tetra(4-carboxyphenyl)porphyrin

Zn	zinc
[P66614][Cl]	trihexyl(tetradecyl)phosphonium chloride

ABSTRACT

In the first part of this dissertation, the adsorption isotherms, resonance coupling, and fluorescence of molecular dyes on the surface of plasmonic nanoparticles are investigates. SHG is also used to investigate the growth of a silver shell on the surface of gold nanoparticles in real time. Additionally, gold-silver-gold core-shell-shell nanoparticles possess extinction peak wavelengths that can be controlled over the visible and near-infrared regions and enhanced photothermal effect. Transient absorption measurements determine that the phonon-phonon scattering lifetime is considerably faster in the core-shell-shell nanoparticles than in the gold nanospheres and gold nanorods, which contributes to the higher photothermal efficiencies. Transient absorption is also used to investigate the ultrafast excited-state relaxation dynamics of the different dyes adsorbed on the core-shell-shell surface and the size-dependent dynamics o interfacial charge transfer between the gold nanoclusters and the TiO_2 bandgap in TiO_2-Au nanocomposites.

In the second part of this dissertation, the ultrafast spectroscopy of size-selected ($[Ru(bipy)_3][BETI]_2$) nanoGUMBPS are reported. The nanoGUMBOS show spectral shifts and size-dependent relaxation dynamics. Long-lived acoustic phonon oscillations with size-dependent frequencies are also observed, where the phonon frequency increases as the nanoparticle size increases, suggesting a very low coupling between electronic and phonon degrees of freedom and a strong hydrophobic interaction with the aqueous solvent. Furthermore, Transient absorption measurements of porphyrin-based nanoGUMBOS reveal that efficient electron transfer and energy transfer is observed between the porphyrin groups leading to shorter excited-state lifetimes. Additionally, the excited-state dynamics of brilliant green – BETI and carbazole – BETI nanoGUMBOS are investigated using pump-probe transient absorption. Brilliant green – BETI nanoGUMBOS exhibit enhanced NIR fluorescence compared to the parent dye in water. The overall excited-state dynamics of brilliant green molecular dye in water are longer than those in the colloidal nanoGUMBOS. The torsional degrees of freedom of the phenyl ring in brilliant green are hindered in the nanoGUMBOS. Additionally, the SHG signal of [BG][BETI] nanoGUMBOS is remarkably enhanced due to the increase of the second order susceptibility tensor $\chi^{(2)}$ of the nanoGUMBOS. Transient

absorption measurement of carbazole – BETI nanoGUMBOS reveal the presence of optical gain and stimulated emission during the excited-state relaxation dynamics.

CHAPTER 1 – INTRODUCTION

1.1 Surface Enhanced Plasmon Resonance

Gold nanoparticles are of great interest for potential applications in molecular sensing, catalysis, and biologically relevant technologies due to their chemical, electronic, and optical properties.[1–9] The localized surface plasmon resonances from coherent oscillations of the free electrons[10–12] depend on the gold nanoparticle size, shape, and surrounding medium and can lead to significant optical field enhancements for processes such as surface-enhanced Raman scattering (SERS)[13,14] and surface-enhanced fluorescence.[15,16] Nonlinear optical signals such as second harmonic generation (SHG) and sum frequency generation (SFG) are also significantly enhanced due to the nanoparticle plasmon resonance.[17–24] Figure 1.1 shows a schematic representation of the oscillation of the surface plasmon electrons under incident electromagnetic radiation.

More information on the excited-state dynamics of plasmonic nanoparticles is essential for the development and optimization of emerging technological applications. The excited-state relaxation dynamics of gold nanoparticles can be characterized by different spectral regions that correspond to different relaxation processes.[24-27] A higher-energy, excited-state absorption spectral region near 480 nm is attributed to the interband excitation of electrons from the gold *d* band to the *sp* band above the Fermi level, with excited-state dynamics specified by the electronic interband transition lifetime. A lower-energy depletion spectrum near 550 nm corresponds to the plasmon resonance region with relaxation dynamics described by electron-phonon and phonon-phonon scattering lifetimes. At even lower spectral energies, excited-state absorption centered near 600 nm is attributed to nonequilibrium “hot” electron distributions, with lifetimes that are also governed by the plasmon dynamics.[28] In general, the excited-state dynamics from the interband transition and electron-phonon scattering are independent of the size and shape of the gold nanoparticles for sizes ranging from approximately 2 nm to 60 nm.

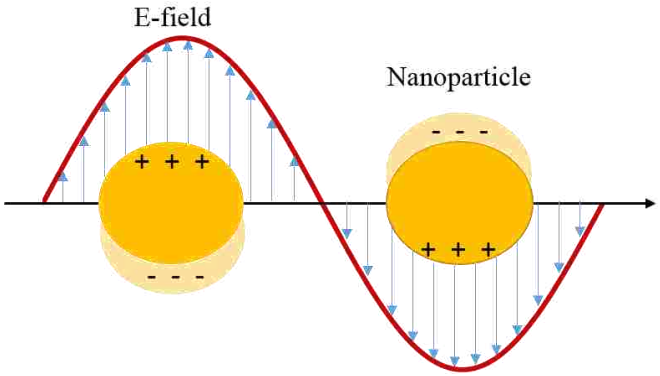

Figure 1.1. Illustration of the electrons oscillations at the surface plasmon resonance.

1.2 Optical Coherence

Coherence provide a wave with the ability to produce interference effects such as interference of light, to the motion of atoms. Understanding coherence and more specifically optical coherence is essential for the study of time-resolved ultrafast processes. The interference between two waves can be constructive or destructive depending on the phase difference between them. Coherence can be viewed as spatial and temporal correlations between the waves involved.[29] The average correlation function of temporal coherence (Ω), such as intensity, at times t and t' is given by

$$\langle \Omega(t)\Omega(t') \rangle \sim \exp\left(-\frac{t}{\tau_c}\right) \qquad (1.1)$$

where τ_c is the coherence time. On the other hand, the coherence length of a light wave is expressed as the distance traveled in time τ_c at the speed of light c.[29]

$$l_c = c\tau_c \qquad (1.2)$$

The uncertainty of coherent light pulses arising from the Fourier analysis is given by

$$\left(\frac{\Delta\lambda}{\lambda^2}\right) l_c \sim 1 \qquad (1.3)$$

Considering a laser interacting with a simple two-level molecule, a coherent combination of ground (*s*-like) and excited (*p*-like) wave functions can be created.[29, 30] The laser-induced coherent state can become incoherent due to interactions of the optically excited atoms or molecules among themselves or the surroundings, which cause the temporal randomization of phase coherence known as dephasing. In

a semi-classical treatment, the superposition of the ground state $\psi_a(r)$ and the excited state $\psi_b(r)$ due to a laser field E can be considered as a simple wave propagating in the direction z given by

$$E(z,t) = \varepsilon \cos(\omega t - kz) = \frac{1}{2}\varepsilon[\exp(i[\omega t - kz]) + \exp(-i[\omega t - kz])] \qquad (1.4)$$

where ε is the amplitude and ω is the frequency of the radiation. The wave function of the molecule excited by laser pulses is given by

$$\psi(r,t) = a(t)\exp(-i\omega_a t)\,\psi_a(r) + b(t)\exp(-i\omega_b t)\,\psi_b(r) \qquad (1.5)$$

The time-dependent molecular polarization is given by

$$\begin{aligned} P_m(t) &= \langle\psi(r,t)|\hat{\mu}|\psi(r,t)\rangle \\ &= ab^*\mu_{ba}\exp(-i[\omega_a - \omega_b]t) + a^*b\mu_{ab}\exp(-i[\omega_b - \omega_a]t) \end{aligned} \qquad (1.6)$$

where $\hat{\mu}$ is the dipole-moment operator and μ_{ab} and μ_{ba} are the transition moment matrix elements. By assuming $\mu_{ab} = \mu_{ba} = \mu$ and $\omega_b = \omega_a = \omega_0$, equation 6 becomes

$$P_m(t) = \mu[ab^*\exp(i\omega_0 t) + a^*b\exp(i\omega_0 t) \qquad (1.7)$$

where ω_0 is the transition frequency. Thus, the time-dependent laser-induced polarization $P(t)$ is zero if there is no coherent superposition of the ground state and the excited state. Ultrafast and nonlinear spectroscopy uses laser pulses to induce coherent processes in non-coherent systems such as molecules and colloidal suspensions.

1.3 Nonlinear Spectroscopy

1.3.1 Overview of Nonlinear Spectroscopy

Light-matter interactions can be described by linear and nonlinear optical processes. Nonlinear optical processes can be described by the nonlinear contribution to the polarization intensity caused by an intense incident laser beam. When light interacts with a sample, such as molecules or materials, the electric field of the light $\widetilde{\mathrm{E}}(\mathrm{t})$ causes a polarization of the sample $\widetilde{\mathrm{P}}(\mathrm{t})$ given by a generalized equation,[31]

$$\begin{aligned} \widetilde{\mathrm{P}}(\mathrm{t}) &= \chi^{(1)}\widetilde{\mathrm{E}}(\mathrm{t}) + \chi^{(2)}\widetilde{\mathrm{E}}^2(\mathrm{t}) + \chi^{(3)}\widetilde{\mathrm{E}}^3(\mathrm{t}) + \ \ldots \\ &= \widetilde{\mathrm{P}}^{(1)}(\mathrm{t}) + \widetilde{\mathrm{P}}^{(2)}(\mathrm{t}) + \widetilde{\mathrm{P}}^{(3)}(\mathrm{t}) + \ \ldots \end{aligned} \qquad (1.8)$$

where, $\chi^{(1)}$ is the linear or first-order susceptibility, and $\chi^{(2)}$ and $\chi^{(3)}$ are the second-order and third-order susceptibilities, respectively. The terms $\tilde{P}^{(1)}(t)$, $\tilde{P}^{(2)}(t)$, and $\tilde{P}^{(3)}(t)$ are the first-order, second-order, and third-order polarizations, respectively. In principle, this power series continues to additional higher-order terms that are usually negligibly small. Under low light intensities, this process is normally completely dominated by the first-order or linear spectroscopic interaction so that the polarization of the sample is linearly proportional to the incident optical electric field and the overall number of photons absorbed or scattered is linearly proportional to the incent optical intensity, where the intensity is proportional to the optical electric field squared. A first-order polarization of the sample can either scatter at the incident optical frequency, or absorb a single photon energy, leading to an excited state of the sample that relaxes back to the ground state by either radiative or nonradiative processes. However, under higher intensity light, or in samples with larger higher-order susceptibilities, the second-, third-, or higher-order optical interactions are not negligible and may even provide a substantial optical signal. Hence, a second-order polarization of the sample can either scatter at twice the incident optical frequency, in a process known as second harmonic generation, [32, 33] or the sample can absorb the energy corresponding to two incident photons, leading to a higher excited state of the sample, that will relax back to the ground state, through different radiative and nonradiative processes. Second-order and higher-order optical processes are nonlinear processes and comprise the field of nonlinear spectroscopy. Sum frequency generation is second order nonlinear technique where two incident photons of frequency $\omega_1$and ω_2 add coherently to scatter a photon of frequency $\omega_1 + \omega_2$. If both incident photons have a frequency of ω, the scattered photon is at a frequency of 2ω, giving rise to second harmonic generation. A scheme of the sum-frequency generation is shown in Figure 1.2.

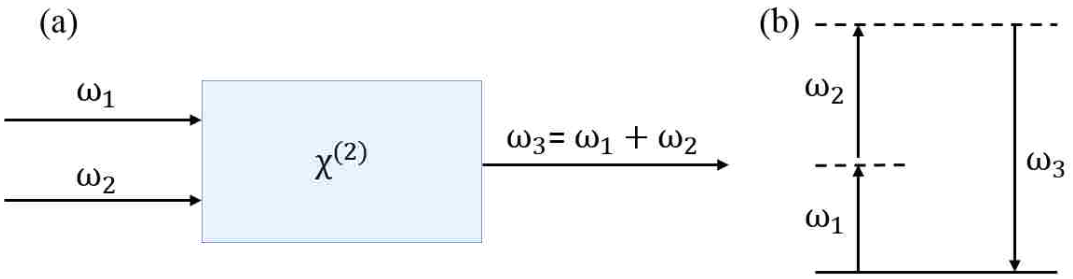

Figure 1.2. (a) Scheme of sum-frequency generation at a crystalline surface. (b) Energy-level description of sum frequency-generation.

1.3.2 Second Harmonic Generation

Second harmonic generation is a nonlinear optical process in which two photons at the same frequency ω add coherently to generate a third photon at double the frequency 2ω. The nonlinear polarization created due to the electric field of an intense laser beam is given by[31]

$$\tilde{P}^{(2)}(t) = 2\epsilon_0 EE^* + \left(\epsilon_0 \chi^{(2)} E^2 e^{-i2\omega t} + c.c.\right) \qquad (1.9)$$

where ϵ_0 is the permittivity of free space. The first term of the equation consists of a frequency contribution at 2ω, which leads to the generation of radiation at the second-harmonic frequency. Second harmonic generation is typically forbidden in bulk media with a center of inversion, which makes it a surface-specific technique ideal for the study of colloidal nanoparticle surfaces. [34] Hence, SHG can be used to study the adsorption of various molecules and chemical reactions at the surface of centrosymmetric nanoparticles.

Recent SHG research has studied TiO_2 microparticles,[35] liposomes,[36] carbon black,[37] and noble metal nanoparticles of gold, silver, and gold−silver alloys.[38,39,40,41] By measuring the SHG signal from a colloidal nanoparticle sample as a function of a bulk molecular adsorbate and by fitting the results to a modified Langmuir isotherm model, the free energy of adsorption and the adsorbate site density can be determined.[42]

1.4 Ultrafast Spectroscopy

Spectroscopy is the study of the interaction between light and matter, which provides valuable information on the quantum energy levels of the sample. However, in ultrafast spectroscopy, temporally short laser pulses are used to directly probe the dynamics of a system directly as a function of time. Femtosecond laser pulses are usually used for this purpose because the duration of the laser pulses must be shorter than the time scale of the dynamics of interest.[43] Ultrafast spectroscopy probes the dynamics of a sample using a probe pulse following an excitation of the sample using a pump pulse that is resonant with the transition as a function of the pump-probe time delay. The wave function of the system transitioning from an initial state χ_0 to resonant excited states is given by

$$\psi = \sum_{n=0} a_n \varphi_n \qquad (1.11)$$

where a_n are the amplitudes of the eigenstates of the system φ_n. In the limit of ultrashort pulses ($\tau \to 0$), a_n can be expressed as

$$a_n = C\langle \varphi_n | \chi_0 \rangle \qquad (1.12)$$

where C is a constant that dependent on various factors such as field amplitude of the pulse and the electronic transition dipole moment. $\langle \varphi_n | \chi_0 \rangle$ is the overlap integral between the initial and final states known as the Franck-Condon factor. The time-dependent wave function is given by

$$\psi(t) = \sum_{n=0} a_n \exp(-{}^{iE_n t}/_{\hbar}) \varphi_n \qquad (1.13)$$

where E_n are the excited-state energies. The short excitation pulses create a wave packet, which is a coherent superposition of excited states that diphase over time with respect to one another.

1.5 Plasmon-Exciton Resonance Coupling

The resonant coupling of plasmonic nanoparticles with organic adsorbates can give rise to strong coupling that can be measured by extinction spectroscopy.[44, 45] New exciton-plasmon polariton peaks and Fano-type profiles can be observed due to the resonant coupling of molecules to the plasmon band. These quantum mechanical states described by a coupled-oscillator Hamiltonian are separated by a Rabi

splitting energy $\hbar\omega_c$.[46] The higher and lower energies produced can be calculated according to the coupled-oscillator model and are given by[47]

$$E^{\pm} = \frac{E_p + E_{ex}}{2} \pm [(\frac{\hbar\Omega_R}{2})^2 + \frac{1}{4}(E_p - E_{ex})^2]^{\frac{1}{2}} \qquad (1.10)$$

where E_p and E_{ex} are the energies of the plasmon and the exciton modes, respectively. $\hbar\Omega_R$ is known as Rabbi splitting. Resonance coupling has been observed between organic dye molecules and various plasmonic nanomaterials such as silver nanoparticles on a substrate,[48] noble metal nanovoids,[49] gold nanorods in colloidal suspension, [45] and colloidal gold nanoparticles.[44]

1.6 Scope of the Dissertation

This dissertation describes the use of ultrafast and nonlinear spectroscopy to investigate the interaction of light with two different types of nanomaterials: plasmonics and nanoGUMBOS. SHG is used to study the adsorption properties of dye molecules on the surface of colloidal plasmonic nanoparticles. It is also used to monitor the growth of nanoshells in real-time. Additionally, the nonlinear optical enhancement of gold-silver core-shell nanoparticles and brilliant green-based nanoGUMBOS are reported. Resonanace coupling between dye molecules and plasmonic nanoparticles is studied in colloidal suspensions. Furthermore, the synthesis and photothermal effect of novel plasmonic gold-silver-gold core-shell-shell nanoparticles are investigated. Transient absorption is used to study processes such as energy transfer, lattice vibrations, heat transport, optical gain, and stimulated emission in various colloidal plasmonics and nanoGUMBOS samples. These nonlinear and ultrafast spectroscopic techniques are demonstrated to provide a great wealth of information on the colloidal nanoparticles and nanomaterials that are studied, including the surface chemistry, molecular adsorption, optical and plasmonic interactions, and excited-state relaxation dynamics.

1.7 References

(1) El-Sayed, I.; Huang, X.; El-Sayed, M. Surface Plasmon Resonance Scattering and Absorption of Anti-EGFR Antibody Conjugated Gold Nanoparticles in Cancer Diagnostics: Applications in Oral Cancer. *Nano Lett.* **2005**, *5*, 829−834.

(2) El-Sayed, I.; Huang, X.; El-Sayed, M. Selective Laser Photothermal Therapy of Epithelial Carcinoma Using Anti-EGFR Antibody Conjugated Gold Nanoparticles. *Cancer Lett.* **2006**, *239*, 129−135.

(3) Kamat, P. V. Photophysical, Photochemical and Photocatalytic Aspects of Metal Nanoparticles. *J. Phys. Chem. B* **2002**, *106*, 7729−7744.

(4) Narayanan, R.; El-Sayed, M. A. Catalysis with Transition Metal Nanoparticles in Colloidal Solution: Nanoparticle Shape Dependence and Stability. *J. Phys. Chem. B* **2005**, *109*, 12663−12676.

(5) Haes, A. J.; Van Duyne, R. P. A Nanoscale Optical Biosensor: Sensitivity and Selectivity of an Approach Based on the Localized Surface Plasmon Resonance Spectroscopy of Triangular Silver Nanoparticles. *J. Am. Chem. Soc.* **2002**, *124*, 10596−10604.

(6) Sperling, R. A.; Gil, P. R.; Zhang, F.; Zanella, M.; Parak, W. J. Biological Applications of Gold Nanoparticles. *Chem. Soc. Rev.* **2008**, *37*, 1896−1908.

(7) Freddi, S.; D'Alfonso, L.; Collini, M.; Caccia, M.; Sironi, L.; Tallarida, G.; Caprioli, S.; Chirico, G. Excited-State Lifetime Assay for Protein Detection on Gold Colloids− Fluorophore Complexes. *J. Phys. Chem. C* **2009**, *113*, 2722−2730.

(8) Prigodich, A. E.; Lee, O.-S.; Daniel, W. L.; Seferos, D. S.; Schatz, G. C.; Mirkin, C. A. Tailoring DNA Structure to Increase Target Hybridization Kinetics on Surfaces. *J. Am. Chem. Soc.* **2010**, *132*, 10638−10641.

(9) Kamat, P. V. Meeting the Clean Energy Demand: Nanostructure Architectures for Solar Energy Conversion. *J. Phys. Chem. C* **2007**, *111*, 2834−2860.

(10) Link, S.; El-Sayed, M. Shape and Size Dependence of Radiative, Non-radiative and Photothermal Properties of Gold Nanocrystals. *Int. Rev. Phys. Chem.* **2000**, *19*, 409−453.

(11) Daniel, M.-C.; Astruc, D. Gold Nanoparticles: Assembly, Supramolecular Chemistry, Quantum-Size-Related Properties, and Applications toward Biology, Catalysis, and Nanotechnology. *Chem. Rev.* **2004**, *104*, 293−346.

(12) Chandra, M.; Dowgiallo, A. M.; Knappenberger, K. L. Controlled Plasmon Resonance Properties of Hollow Gold Nanosphere Aggregates. *J. Am. Chem. Soc.* **2010**, *132*, 15782−15789.

(13) Stiles, P. L.; Dieringer, J. A.; Shah, N. C.; Van Duyne, R. P. Surface-Enhanced Raman Spectroscopy. *Annu. Rev. Anal. Chem.* **2008**, *1*, 601−626.

(14) Brus, L. Noble Metal Nanocrystals: Plasmon Electron Transfer Photochemistry and Single Molecule Raman Spectroscopy. *Acc. Chem. Res.* **2008**, *41*, 1742−1749.

(15) Tam, F.; Goodrich, G. P.; Johnson, B. R.; Halas, N. J. Plasmonic Enhancement of Molecular Fluorescence. *Nano Lett.* **2007**, *7*, 496−501.

(16) Lakowics, J. R.; Geddes, C. D.; Gryczynski, I.; Malicka, J.; Gryczynski, Z.; Aslan, K.; Lukomska, J.; Matveeva, E.; Zhang, J.; Badugu, R.; et al. Advances in Surface-Enhance Fluorescence. *J. Fluoresc.* **2004**, *14*, 425−441.

(17) Baldelli, S.; Eppler, A. S.; Anderson, E.; Shen, Y.-R.; Somorjai, G. A. Surface Enhanced Sum Frequency Generation of Carbon Monoxide Adsorbed on Platinum Nanoparticle Arrays. *J. Chem. Phys.* **2000**, *113*, 5432−5438.

(18) Bordnyuk, A. N.; Weeraman, C.; Yatawara, A.; Jayathilake, H. D.; Stiopkin, I.; Liu, Y.; Benderskii, A. V. Vibrational Sum Frequency Generation Spectroscopy of Dodecanethiol on Metal Nanoparticles. *J. Phys. Chem. C* **2007**, *111*, 8925−8933.

(19) Vance, F. W.; Lemon, B. J.; Hupp, J. T. Enormous Hyper-Rayleigh Scattering from Nanocrystalline Gold Particle Suspensions. *J. Phys. Chem. B* **1998**, *102*, 10091−10093.

(20) Butet, J.; Bachelier, G.; Russier-Antoine, I.; Jonin, C.; Benichou, E.; Brevet, P.-F. Interference between Selected Dipoles and Octupoles in the Optical Second-Harmonic Generation from Spherical Gold Nanoparticles. *Phys. Rev. Lett.* **2010**, *105*, 077401.

(21) Hao, E. C.; Schatz, G. C.; Johnson, R. C.; Hupp, J. T. Hyper-Rayleigh Scattering from Silver Nanoparticles. *J. Chem. Phys.* **2002**, *117*, 5963−5966.

(22) Duboisset, J.; Russier-Antoine, I.; Benichou, E.; Bachelier, G.; Jonin, C.; Brevet, P. F. Single Metallic Nanoparticle Sensitivity with Hyper-Rayleigh Scattering. *J. Phys. Chem. C* **2009**, *113*, 13477−13481.

(23) Chandra, M.; Knappenberger, K. L. Nanoparticle Surface Electromagnetic Fields Studied by Single-Particle Nonlinear Optical Spectroscopy. *Phys. Chem. Chem. Phys.* **2013**, *15*, 4177−4182.

(24) Dadap, J. I.; Shan, J.; Eisenthal, K. B.; Heinz, T. F. Second-Harmonic Rayleigh Scattering from a Sphere of Centrosymmetric Material. *Phys. Rev. Lett.* **1999**, *83*, 4045−4048.

(25) Ahmadi, T. S.; Logunov, S. L.; El-Sayed, M. A. Picosecond Dynamics of Colloidal Gold Nanoparticles. *J. Phys. Chem.* **1996**, *100*, 8053–8056.

(26) Logunov, S. L.; Ahmadi, T. S.; El-Sayed, M. A.; Khoury, J. T.; Whetten, R. L. Electron Dynamics of Passivated Gold Nanocrystals Probed by Subpicosecond Transient Absorption Spectroscopy. *J. Phys. Chem. B.* **1997**, *101*, 3713–3719.

(27) Hodak, J. H.; Martini, I.; Hartland, G. V. Spectroscopy and Dynamics of Nanometer-Sized Noble Metal Particles. *J. Phys. Chem. B* **1998**, *102*, 6958–6967.

(28) Link, S.; Burda, C.; Mohamed, M. B.; Nikoobakht, B.; El-Sayed, M. A. Femtosecond Transient-Absorption Dynamics of Colloidal Gold Nanorods: Shape Independence of the Electron-Phonon Relaxation Time. *Phys. Rev. B* **2000**, *61*, 6086.

(29) Zewail, A. H.; Thomas, J. M. 4D Electron Microscopy. Imaging in Space and Time; Imperial College Press, **2010**.

(30) Sargent III, M.; Scully, M. O. Lamb Jr., W. E. Laser Physics; Addison-Wesley, Reading, **1974**.

(31) Boyd, R. Nonlinear Optics; Academic Press: New York, **2010**.

(32) Haber, L. H.; Kwok, S. J. J.; Semeraro1, M.; Eisenthal, K. B. Probing the Colloidal Gold Nanoparticle/Aqueous Interface with Second Harmonic Generation. *Chem. Phys. Lett.* **2011**, *507*, 11–14.

(33) Karam, T. E.; Haber, L.H. Molecular Adsorption and Resonance Coupling at the Colloidal Gold Nanoparticle Interface. *J. Phys. Chem. C* **2014**, *118*, 642−649.

(34) Eisenthal, K. Second Harmonic Spectroscopy of Aqueous Nano- and Microparticle Interfaces. *Chem. Rev.* **2006**, *106*, 1462−1477.

(35) Liu, Y.; Dadap, J.; Zimdars, D.; Eisenthal, K. B. Study of Interfacial Charge-Transfer Complex on TiO2 Particles in Aqueous Suspension by Second-Harmonic Generation. *J. Phys. Chem. B* **1999**, *103*, 2480−2486.

(36) Liu, J.; Subir, M.; Nguyen, K.; Eisenthal, K. B. Second Harmonic Studies of Ions Crossing Liposome Membranes in Real Time. *J. Phys. Chem. B* **2008**, *112*, 15263−15266.

(37) Wang, H.-F.; Troxler, T.; Yeh, A.-G.; Dai, H.-L. Adsorption at a Carbon Black Microparticle Surface in Aqueous Colloids Probed by Optical Second-Harmonic Generation. *J. Phys. Chem. C* **2007**, *111*, 8708−8715.

(38) Vance, F. W.; Lemon, B. J.; Hupp, J. T. Enormous Hyper-Rayleigh Scattering from Nanocrystalline Gold Particle Suspensions. *J. Phys. Chem. B* **1998**, *102*, 10091−10093.

(39) Hao, E. C.; Schatz, G. C.; Johnson, R. C.; Hupp, J. T. Hyper-Rayleigh Scattering from Silver Nanoparticles. *J. Chem. Phys.* **2002**, *117*, 5963−5966.

(40) Russier-Antoine, I.; Benichou, E.; Bachelier, G.; Jonin, C.; Brever, P. F. Multipolar Contributions of the Second Harmonic Generation from Silver and Gold Nanoparticles. *J. Phys. Chem. C* **2007**, *111*, 9044−9048.

(41) Jin, R.; Jureller, J.; Kim, H.; Scherer, N. Correlating Second Harmonic Optical Responses of Single Ag Nanoparticles with Morphology. *J. Am. Chem. Soc.* **2005**, *127*, 12482−12483.

(42) Wang, H.; Yan, E.; Liu, Y.; Eisenthal, K. B. Energetics and Population of Molecules at Microscopic Liquid and Solid Surfaces. *J. Phys. Chem. B* **1998**, *102*, 4446−4450.

(43) Dantus, M.; Gross, P. Ultrafast spectroscopy. *Encyclopedia of Applied Physics* **1998**, *22*, 431-456.

(44) Karam, T. E.; Haber, L.H. Molecular Adsorption and Resonance Coupling at the Colloidal Gold Nanoparticle Interface. *J. Phys. Chem. C* **2014**, *118*, 642−649.

(45) Ni, W.; Chen, H.; Su, J.; Sun, Z.; Wang, J.; Wu, H. Effects of Dyes, Gold Nanocrystals, pH, and Metal Ions on Plasmonic and Molecular Resonance Coupling. *J. Am. Chem. Soc.* **2010**, *132*, 4806−4814.

(46) Hutchison, J. A.; Liscio, A.; Schwartz, T.; Canaguier-Durand, A.; Genet, C.; Palermo, V.; Samori, P.; Ebbesen, T. Tuning the WorkFunction via Strong Coupling. *Adv. Mater.* **2013**, *25*, 2481−2485.

(47) Pérez-González, O.; Aizpurua, J.; Zabala, N. Optical Transport and Sensing in Plexcitonic Nanocavities. *Opt. Express* **2013**, *21*, 15847–15858.

(48) Cade, N. I.; Ritman-Meer, T.; Richards, D. Strong Coupling of Localized Plasmons and Molecular Excitons in Nanostructured Silver Films. *Phys. Rev. B* **2009**, *79*, 241404(R).

(49) Sugawara, Y.; Kelf, T. A.; Baumber, J. J.; Abdelsalam, M. E.; Bartlett, P. N. Strong Coupling between Localized Plasmons and Organic Excitons in Metal Nanovoids. *Phys. Rev. Lett.* **2006**, *97*, 266808.

CHAPTER 2 – MOLECULAR ADSORPTION AND RESONANACE COUPLING AT THE GOLD NANOPARTICLE INTERFACE*

2.1 Introduction

The interest in gold nanoparticles[1–9] arises from the localized surface plasmon resonances[10-12], which makes them advantageous for potential applications in molecular sensing, catalysis, and biologically relevant technologies due to their chemical, electronic, and optical properties. In particular, significant optical field enhancement is observed at the surface of plasmonic nanoparticles. [13-24] However, more information on the surface properties of colloidal metal nanoparticles and their interactions with different molecules is essential for the development and optimization of these emerging technological applications.[1–5]

Second harmonic generation spectroscopy can be used for the investigation of the surface properties and interfacial chemistry of colloidal gold nanoparticles.[25,26] SHG is a powerful technique for the study of various colloidal samples such as TiO_2 microparticles,[27] liposomes,[28] carbon black,[29] and noble metal nanoparticles of gold, silver, gold−silver alloys.[19,21,30,31], and organic molecules adsorbed on the surface of plasmonic nanoparticles.[32] Related SHG characterizations of colloidal nanoparticles using $\chi^{(3)}$ measurements can be used to obtain the surface charge densities[33] and acid−base equilibrium constants[34] at the nanoparticle surface. Additionaly, strong between plasmonic nanoparticles and organic adsorbates can give rise to molecular and plasmonic resonance coupling, which can be measured by extinction spectroscopy.[35-38] Fano-type resonances have also been observed in plasmonic nanostructures and metamaterials[39–41] and have been investigated computationally[42,43] from the interference of localized molecular excited states with a plasmonic continuum leading to the characteristic asymmetric line shape.[44] In general, more work is needed to correlate molecular and plasmonic resonance coupling with

precise, surface-specific adsorption measurements that accurately account for the adsorption properties ofdifferent molecular dyes to a plasmonic nanoparticle sample.

In this chapter, SHG is used to monitor the adsorption isotherms of malachite green, brilliant green, and methyl green to the surface of 80 nm colloidal gold nanoparticles capped with mercaptosuccinic acid (MSA) in aqueous suspension. The free energies of adsorption and the number of adsorbate sites per nanoparticle are determined for each molecule by fitting the experimental results to the modified Langmuir model. The molecular adsorption properties are shown to be highly dependent on the adsorbate molecular structure as well as the environment of the nanoparticle surface. In addition, complementary measurements from visible extinction spectroscopy show the formation of new exciton−plasmon polariton peaks and Fano-type profiles from resonance coupling which overlap with plasmon and molecular spectral depletions and are highly sensitive to the molecular interactions with the plasmonic gold nanoparticles.

2.2. Experimental Section

2.2.1. Nanoparticle Synthesis and Characterization

The colloidal gold nanoparticle sample is prepared by seeded growth using hydroquinone reduction, followed by thiolation and dialysis.[45–47] All chemicals are purchased from Sigma-Aldrich and used without further purification in ultrapure water. For the synthesis of gold nanoparticle seeds, 900 μL of 34 mM sodium citrate is added to 30 mL of 290 μM gold chloride in water under boiling and vigorous stirring conditions. The colloidal solution undergoes a color change from pale yellow to bright red after 10 min and is removed from heat and cooled to room temperature. For the seeded growth of the 80 nm gold nanoparticles, 100 μL of 29 mM gold chloride and 50 μL of the prepared gold colloidal seeds are added to 9.7 mL of water, followed by the addition of 25 μL of 34 mM sodium citrate and 100 μL of 0.03 M hydroquinone under vigorous stirring at room temperature. The solution is left stirring at room temperature for 60 min. The synthesis is repeated until a total of 150 mL of the 80 nm colloidal gold nanoparticle solution is produced. The nanoparticle solution is dialyzed against a solution of 22 mM

mercaptosuccinic acid in water for 3 days and then against nanopure pure water for an additional 3 days in order to first attach the MSA capping agent and then to remove excess salts and reactants.

Transmission electron microscopy (TEM), extinction spectroscopy, and dynamic light scattering are used to characterize the gold nanoparticle sample. Figure 2.1 shows a representative TEM image of the gold nanoparticle sample. After surveying over 500 particles, the nanoparticles diameter is determined to be 80 ± 6 nm. Figure 2.2 shows the extinction spectrum of the nanoparticle solution. The 80 nm gold nanoparticles have significant scattering and absorption contributions to the overall extinction spectra. The localized surface plasmon resonance peak is observed at a center wavelength of 550 nm.

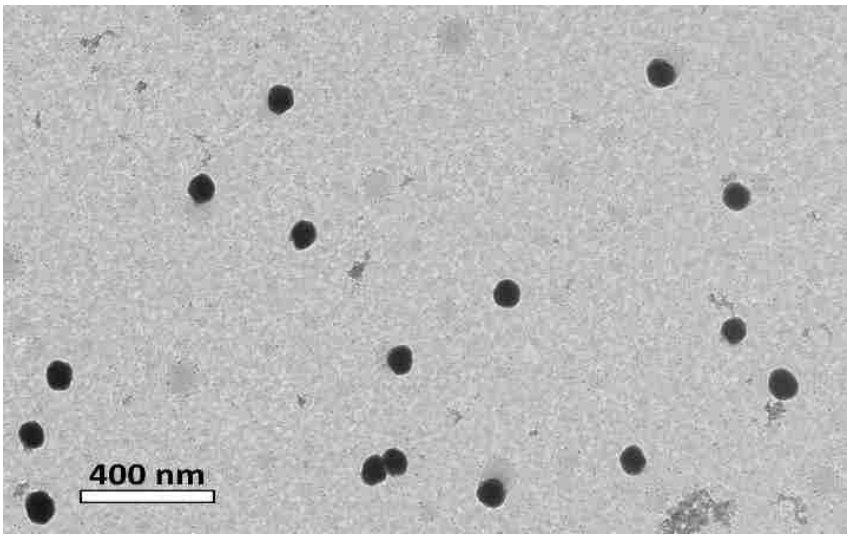

Figure 2.1. Transmission electron microscopy image of gold nanoparticles on a carbon-coated copper grid. After analysis of 500 particles, the nanoparticle diameter is determined to be 80.0 ± 6.1 nm.

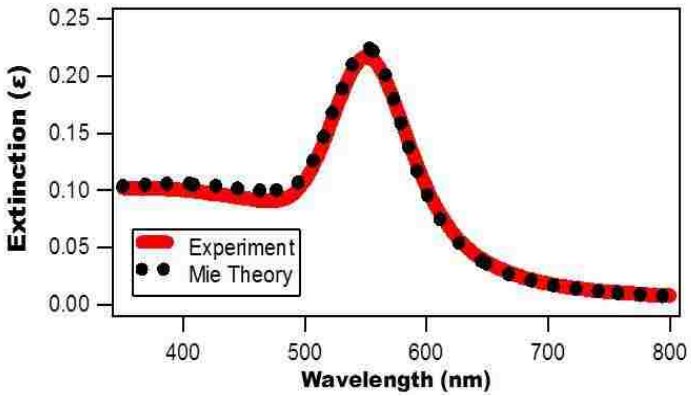

Figure 2.2. Extinction spectrum of 80 nm colloidal gold nanoparticles diluted in water (red line) overlapped with the best fit using Mie Theory (dotted black line) at a concentration of 6.8×10^8 nanoparticles/mL.

2.2.2 Second Harmonic Generation

The second harmonic generation setup is composed of an ultrafast laser system, an optical setup, and a high-sensitivity CCD spectroscopy detector, similar to previously reported experimental setups.[48,49] A titanium:sapphire oscillator laser produces 75 fs pulses centered at 800 nm with a repetition rate of 80 MHz and an average power of 2.7 W. The laser beam is focused to a 1 cm quartz cuvette containing the colloidal sample at a diluted concentration of 3.7×10^8 nanoparticles/mL in water using a 20 mm focal length lens. An optical filter is placed in front of the cuvette to remove any residual SHG light prior to the sample. Another filter is placed after the sample to remove the fundamental light while transmitting the SHG signal, which is collected in the forward direction and refocused to a monochromator connected to a high-sensitivity spectroscopy charge coupled device detector. The different dye solutions are added using a computer-controlled burette during automated stirring. Several spectral scans are acquired for each addition of the dye solution, and the isotherms are acquired several times for statistical analysis.

2.3 Results and Discussion

The spectra containing the SHG signals for each concentration of the added molecular dyes are analyzed to obtain the corresponding adsorption isotherms. For example, Figure 2.3, a-c display representative spectra obtained at different malachite green, brilliant green, and methyl green concentrations, respectively. The lower wavelength peak is assigned to second harmonic generation while the rise at higher wavelengths is attributed to two-photon fluorescence.[50,51] The spectra are fit using Gaussian functions plus second-order polynomials to represent the SHG and fluorescence signal, respectively, in the measured wavelength range. The corresponding fits all accurately describe the measured spectra, as shown in Figure 2.3 using solid gray lines, with SHG peaks centered at 400.5 ± 0.1 nm and full width at half-maxima of 2.5 ± 0.1 nm. The peak centers and widths stay constant to within experimental uncertainty for all added dye concentrations. The spectra corresponding to the nanoparticle solution in water without the addition of molecular dyes exhibit SHG signal due mostly to the colloidal nanoparticles. The SHG intensities then increase as the added dye concentrations are increased, reaching maxima as the adsorbates at the gold nanoparticle interface reach their saturation values.

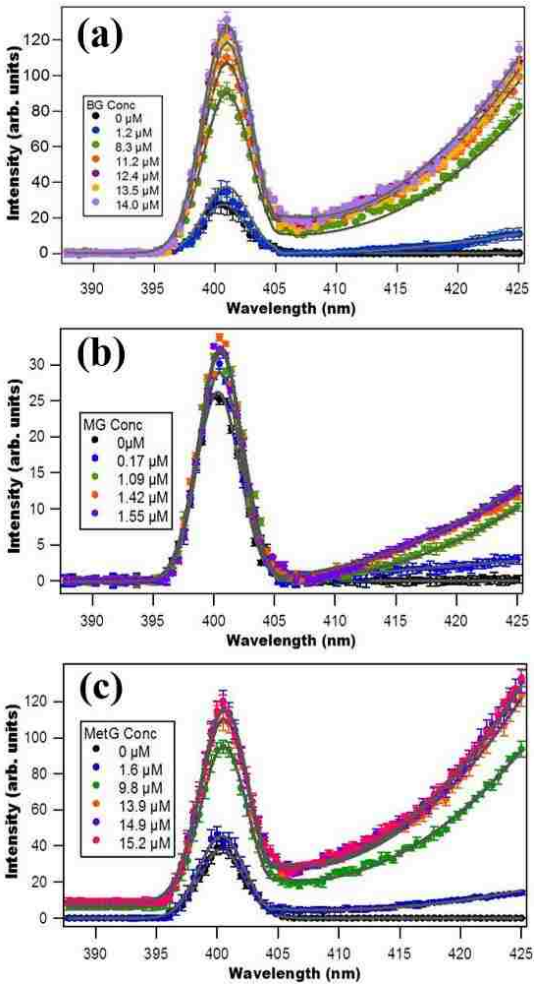

Figure 2.3. Spectra of gold nanoparticles solutions at various (a) malachite green, (b) brilliant green, and (c) methyl green concentrations. The SHG peak is detected near 400 nm.

The adsorption isotherms obtained from the SHG results from additions of malachite green, brilliant green, and methyl green to the colloidal gold nanoparticle sample are shown in Figure 2.4, a-c respectively. The experimental data are corrected to account for the contribution from hyper-Rayleigh scattering from the free dye molecules in solution. The hyper-Rayleigh scattering signal as a function of concentration for the three dye solutions is shown in the Appendix 1. More details about this correction method are provided in the Appendix 1. The corrected experimental data are then compared to the modified Langmuir models,[32,48] which includes the depletion of adsorbates from the bulk. The modified Langmuir model is given by

$$\frac{N}{N_{max}} = \frac{\left(C + N_{max} + \frac{55.5}{K}\right) - \sqrt{(C + N_{max} + \frac{55.5}{K})^2 - 4CN_{max}}}{2N_{max}} \quad (2.1)$$

where N is the adsorbate population on the nanoparticle surface, N_{max} is the maximum number of adsorbate sites on the nanoparticle surface multiplied by the concentration of nanoparticles in the solution, C is the adsorbate bulk concentration added, and K is the adsorption equilibrium constant.[32] Each adsorption isotherm is analyzed to find the best fit parameters for K and N_{max}. The free energy of adsorption is obtained using the equation, $\Delta G° = -RT\ ln\ K$. The maximum number of adsorbate sites on each nanoparticle is determined from N_{max} and the known nanoparticle concentration.

The best fits to the measured adsorption isotherms using the modified Langmuir model are shown as red dashed lines in Figure 2.4. The free energies of adsorption obtained from the best fit parameters for malachite green, brilliant green, and methyl green adsorbing to the colloidal gold nanoparticles are −12.5 ± 0.1, −10.0 ± 0.3, and −11.1 ± 0.1 kcal/mol, respectively. Additionally, the corresponding number of adsorption sites per particle for the three different molecules determined from the best fits are (9.18 ± 0.2) × 10^3, (3.01 ± 0.2) × 10^4, and (1.78 ± 0.04) × 10^4 sites per particle, respectively. This corresponds to adsorption site areas of 219 ± 11 A^2 for malachite green, 67 ± 9 A^2 for brilliant green, and 113 ± 5 A^2 for methyl green, respectively. These results can be understood based on several factors, including adsorbate interactions with the nanoparticle surface as well as adsorbate−adsorbate repulsions. The positively charged molecular dyes all have strong electrostatic attractions to the negatively charged surface. However, the high surface densities of the adsorbates contribute to adsorbate−adsorbate repulsion, which decreases the free energy of adsorption magnitude. Of the three molecules, malachite green has the largest overall free energy of adsorption magnitude while also having the lowest adsorbate site density. Brilliant green has the lowest free energy of adsorption magnitude while consequently having the highest adsorbate site density. Methyl green is doubly charged, leading a stronger electrostatic attraction to the surface as well as greater adsorbate−adsorbate repulsion, and these interactions are counterbalancing. The different molecular structures, especially around the charged nitrogen centers, contribute to different

electrostatic potentials at the resulting adsorption site, including the interactions between with the negatively charged carboxylates as well as image-charge attractions with the metal surface.

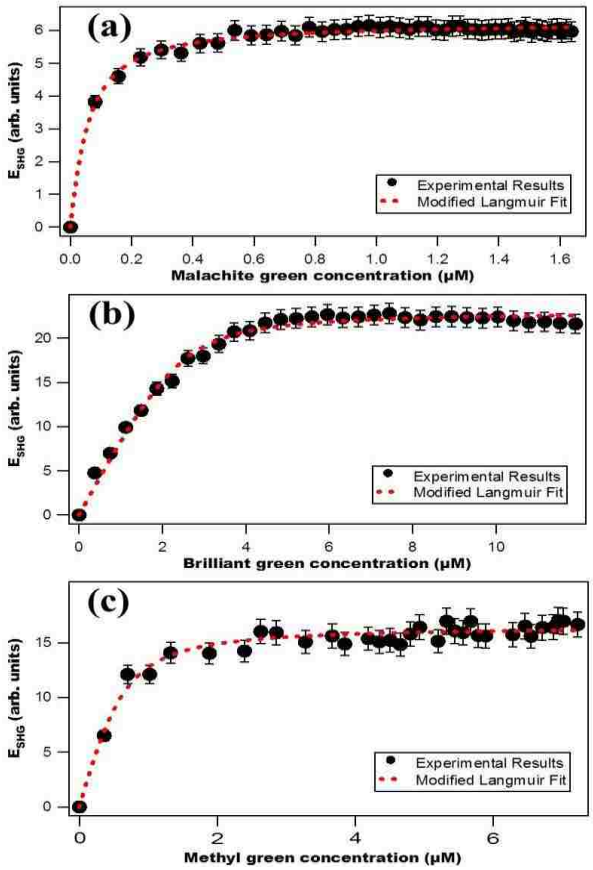

Figure 2.4. Adsorption isotherm results (black dots) obtained from second harmonic generation measurements as a function of (a) malachite green, (b) brilliant green, (c) and methyl green concentrations. The experimental data are compared with the best fits from the modified Langmuir model (dotted red lines).

The molecular adsorbate tilt angle with respect to the nanoparticle surface is expected to play a key important role in these surface-specific interactions.[52] The SHG signal has been shown previously to depend on the geometrical orientation of the molecules on the nanoparticle surface.[53,54] Here, the signal amplitude of the adsorption isotherm at the plateau will depend on the tilt angle of the molecular adsorbate. From our measured SHG results, the best fits of the amplitudes from the adsorption isotherms using the modified Langmuir model is 7.5 ± 0.1, 18.4 ± 0.4, and 23.1 ± 0.3 in directly comparable arbitrary units for malachite green, methyl green, and brilliant green using the same nanoparticle sample concentrations described above. These values follow the same trend as N_{max} where malachite green has

the smallest SHG amplitude and brilliant green has the largest SHG amplitude at the plateau. These SHG signal amplitudes compare to an initial SHG amplitude of 39.8 ± 0.8 for the nanoparticles before adding the dye molecules. The values of the SHG amplitudes and the N_{max} values are closely related to the tilt angle, since a smaller tilt angle allows more molecules to be closely packed on the nanoparticle surface. Results for the SHG adsorption isotherms of malachite green, brilliant green, and methyl green to colloidal polystyrene sulfate microparticles are also measured using this setup and are discussed in the Appendix 1, showing excellent agreement with existing literature values.[32]

Comparing these results to previous SHG adsorption isotherm measurements provides a more complete assessment of molecular adsorption to different colloidal nanoparticle samples. The free energies of adsorption of malachite green to 16 nm gold nanoparticles coated in citrate and 1.05 μm polystyrene sulfate microparticles in water have been previously measured to be −15.4 ± 0.4 and −11.1 ± 0.1 kcal/mol, respectively, with corresponding adsorbate site areas of 71 ± 14 and 192 ± 24 A^2 , respectively. Our results indicate that malachite green binds less strongly and with lower site densities to 80 nm gold nanoparticles capped in MSA than to 16 nm gold nanoparticles coated in citrate. It is important to note that MSA forms a tightly bound layer due to the gold−sulfur bond while citrate is only loosely bound to the gold surface. In the gold−citrate surface, malachite green may penetrate the citrate layer and access the gold surface directly to experience a stronger image-charge attraction. For the gold−MSA surface, the tightly bound MSA will increase the separation distance between the adsorbate and the metal surface, leading to a shielding and weakening of the image-charge attraction.[55] However, malachite green has a slightly higher free energy of adsorption and a similar site density on the gold nanoparticles capped in MSA compared with polystyrene sulfate microparticles. By changing the capping agent, the adsorption of molecules to the surface of gold nanoparticles can be significantly altered. The effect of the capping agent on the adsorption properties can be further investigated by performing the same SHG study while changing the capping agent for gold nanoparticle samples of the same size. This has important implications for molecular sensing applications where modifications in the chemical environment of the metal nanoparticle surface can dramatically change the adsorption properties.

In addition to the adsorption properties of molecules to the surface of gold nanoparticles, spectral resonance coupling[35] between the molecules and the plasmonic nanoparticles is observed. Figure 2.5 shows the extinction spectra of gold nanoparticles in water after the addition of different concentrations of brilliant green and after subtracting the dye spectra at the corresponding concentrations. The corresponding extinction spectra of the gold nanoparticles with malachite green and methyl green are provided in the Appendix 1. A splitting of the plasmonic peak is seen near the molecular excited states. The magnitudes of the newly formed peaks increase as the added dye concentrations are increased while the plasmon spectra are depleted, accompanied by wavelength shifts. It is also important to note that the characteristic long wavelength peaks from gold nanoparticle aggregation are not seen in any of these spectra, confirming that gold nanoparticle aggregation is not occurring as the molecular dyes are added.[56] The molecule concentrations are chosen to span the relevant concentrations of the adsorption isotherms determined from the SHG measurements above for each triphenylmethane dye.

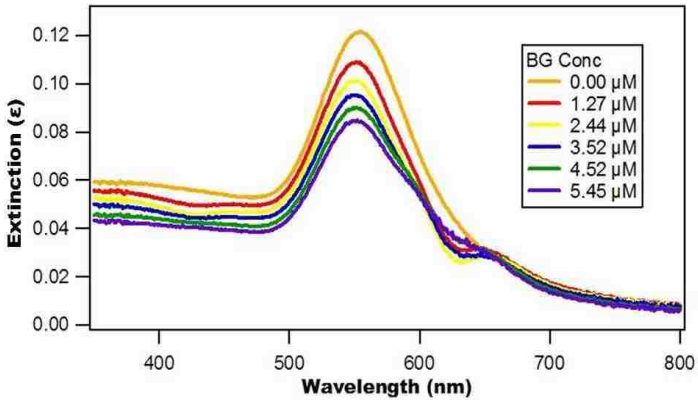

Figure 2.5. Extinction spectra of gold nanoparticles capped with MSA in water at increasing brilliant green concentrations after subtracting the spectra of the dye alone in water at the corresponding concentrations. The 80 nm colloidal gold nanoparticles are initially diluted to 3.7×10^8 nanoparticles/mL in water.

From a more careful analysis, the various components of the resonance coupling are determined from the gold nanoparticles interacting with malachite green, brilliant green, and methyl green. Figure 2.6, a–c are obtained after subtracting the extinction spectra of the gold nanoparticles and the dyes alone in water from the ones generated from the mixtures of both at the corresponding concentrations. This figure show the change in the extinction spectra as a result of the molecule–plasmon interactions,

including the polariton and Fano-type spectra as well as the plasmon and molecule depletions. Each of these difference spectra are first fit to depletion spectra of the plasmon and molecule to reveal additional peaks that are not from either the plasmon or the molecule, where a positive intensity peak at longer wavelengths and a negative intensity peak at shorter wavelengths are assigned as the $|P-\rangle$ and $|P+\rangle$ polaritons, respectively, overlapped with a Fano-type profile. Figure 2.7, a–c show these extra peaks formed for the three dyes compared to the spectra generated from the best fits of the plasmon and molecule depletions. Additional data are reported in the Appendix 1, including the fitting results for the different spectral components. Interestingly, the center wavelengths and full width at half-maxima of the polariton peaks stay relatively constant for each molecule as the concentrations are increased.

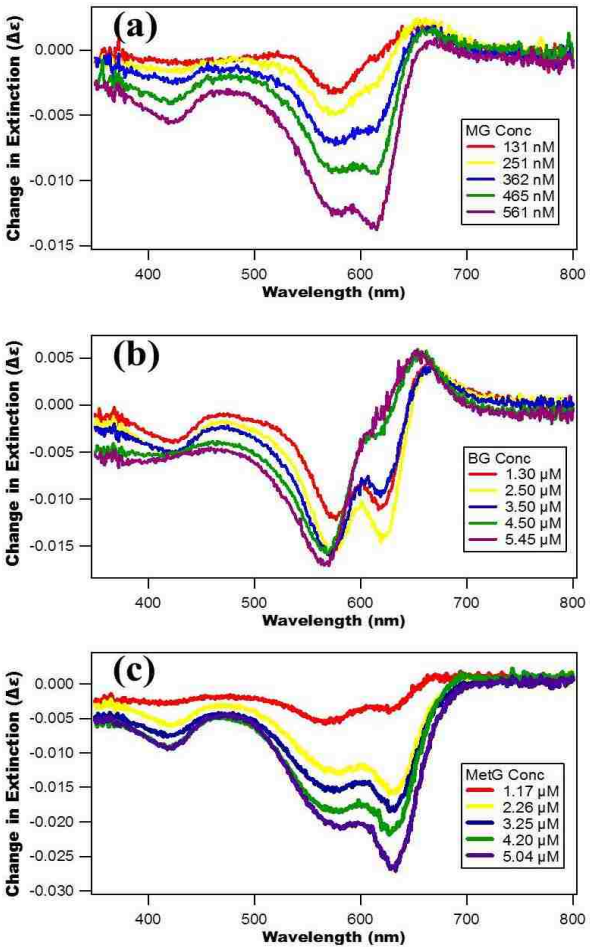

Figure 2.6. Difference spectra obtained from subtracting gold nanoparticle and dye molecule extinction spectra alone in water from the spectra measured from mixtures of both at corresponding concentrations for (a) malachite green, (b) brilliant green, and (c) methyl green.

This indicates that the plasmon−molecule interaction is dominant compared to other possibilities such as dye aggregation,[57] although further experimental and theoretical investigations are needed for a more careful understanding of this effect. The center wavelengths of the $|P+\rangle$ polaritons for malachite green, brilliant green, and methyl green are 579 ± 0.4, 567 ± 0.2, and 575 ± 0.7 nm, respectively, while

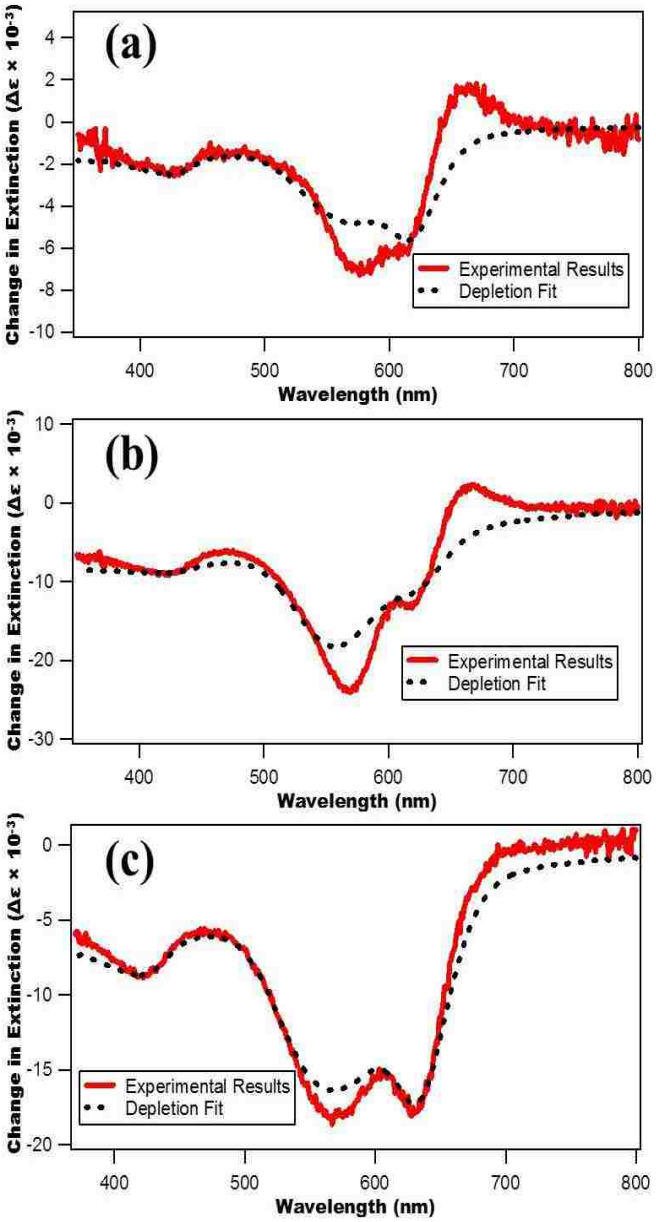

Figure 2.7. Spectral analysis of representative difference spectra from the dye molecules (a) 362 nM malachite green, (b) 3.50 μM brilliant green, and (c) 2.26 μM methyl green interacting with the colloidal gold nanoparticles in water. The residuals show a combination of polariton peaks and Fano-type resonances.

the center wavelengths of the |P−⟩ polaritons are 655 ± 0.6, 664 ± 0.4, and 670 ± 1.5 nm, respectively. The energy difference between the two polariton peaks is assigned to be the Rabi splitting energy,[36] which is determined to be 263, 320, and 306 meV for malachite green, brilliant green, and methyl green, respectively. These Rabi splitting energies are a measurement of the spectral coupling strengths between molecular excited states and the plasmon resonance and are expected to depend critically on the adsorption tilt angle as well as the quantum mechanical overlaps.

The depletion and polariton intensities are shown in Figure 2.8 as a function of the dye concentrations. The plasmon depletion intensities exhibit a similar trend for the three different dyes, with increasing depletion as the molecular concentrations are increased. The molecular depletions have different trends with increasing concentrations as part of this signal is due to the molecule being removed from the solution upon adsorption, while another part of this signal is due to the possible plasmonic optical-field enhancements after adsorption. The plasmon depletions, the molecular depletions, and the polariton intensities of the different dye molecules have similar trends when compared to their adsorption properties. Brilliant green has the largest N_{max} value and the largest plasmon depletion. Malachite green has the smallest N_{max} value and the smallest plasmon depletion. However, malachite green has the largest molecular depletion, indicating that it has the lowest level of plasmonic enhancement, possibly due to a large adsorption tilt angle, with the adsorbate lying relatively flat on the surface. Brilliant green has the lowest molecular depletion, the largest Rabi splitting, and the largest polariton intensities, indicating that it has largest relative coupling strength with the plasmonic nanoparticle. Methyl green has intermediate values of molecular depletion, Rabi splitting, and polariton intensities, and it also has an intermediate N_{max} value among the three dyes. In addition, the polariton intensities remain somewhat constant as the concentrations are increased, which may occur due to quantum interferences as well as plasmonic interactions with dyes in the bulk solution. Even though malachite green, brilliant green, and methyl green have similar chemical structures and absorption spectra, they exhibit different adsorption properties at the gold nanoparticle surface as well as different spectroscopic interactions from plasmonic−molecular resonance coupling.

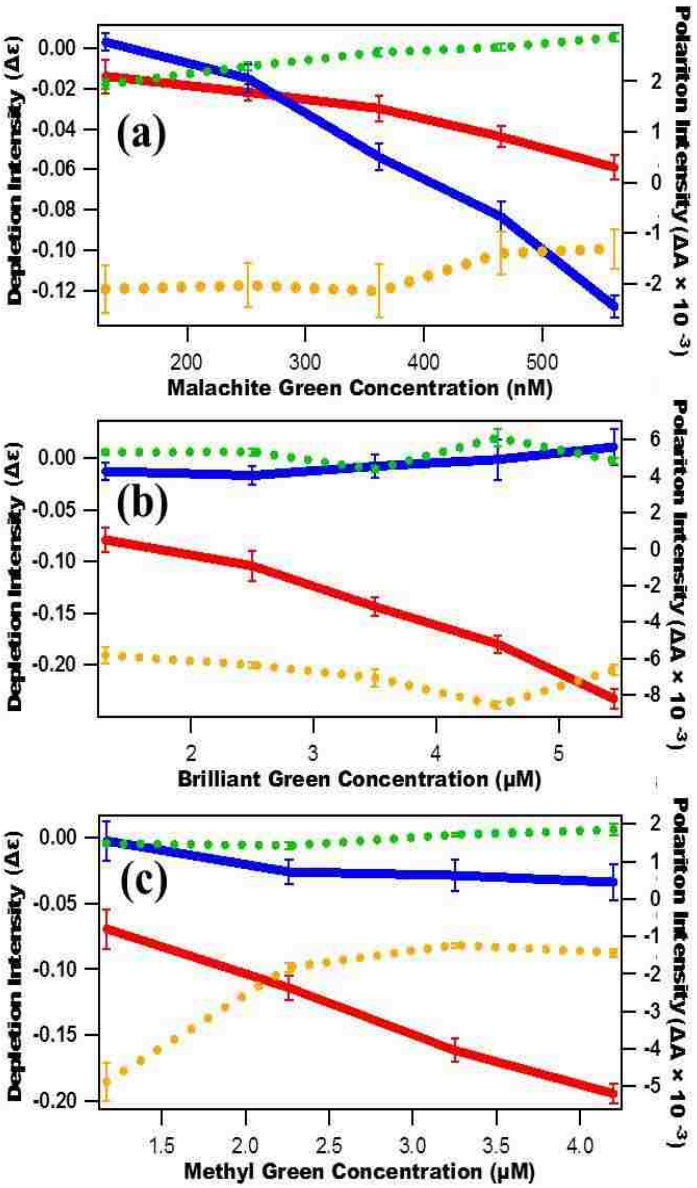

Figure 2.8. Depletion intensities of the plasmon (solid red line) and the molecule (solid blue line) as well as the polariton |P-⟩ (dashed green line) and |P+⟩ (dashed orange line) intensities at different (a) malachite green, (b) brilliant green, and (c) methyl green concentrations.

2.4. Conclusion

Second harmonic generation is used to study the adsorption properties of three triphenylmethane dyes to the surface of 80 nm gold nanoparticles capped in mercaptosuccinic acid in aqueous colloidal suspension. The SHG results are analyzed using a modified Langmuir model to determine the free energies of adsorption and the adsorbate site densities at the nanoparticle surface. Malachite green is observed to bind more strongly to the surface of the gold nanoparticles than brilliant green and methyl

green but has a lower adsorbate site density. These differences are discussed in terms of the image-charge effect, adsorbate−adsorbate repulsion, and the adsorption tilt angle on the gold nanoparticle surface. Additional comparisons with previous literature results show that malachite green binds less strongly to gold nanoparticles capped with mercaptosuccinic acid than to gold nanoparticles coated with citrate, confirming expectations of weakening image-charge effects due to a tightly bound layer that increases the separation distance between the adsorbates and the metallic surface. Complementary results show plasmonic and molecular resonance coupling as hybrid polaritons and Fano-type profiles are observed using extinction spectroscopy at different molecular concentrations along the adsorption isotherm. Analysis of the spectral changes displays interesting trends involving plasmon and molecular depletions as well as Rabi splitting energies and polariton intensities that correlate with the SHG adsorption isotherm measurements.

2.5 References

(1) El-Sayed, I.; Huang, X.; El-Sayed, M. Surface Plasmon Resonance Scattering and Absorption of Anti-EGFR Antibody Conjugated Gold Nanoparticles in Cancer Diagnostics: Applications in Oral Cancer. *Nano Lett.* **2005**, *5*, 829−834.

(2) El-Sayed, I.; Huang, X.; El-Sayed, M. Selective Laser Photothermal Therapy of Epithelial Carcinoma Using Anti-EGFR Antibody Conjugated Gold Nanoparticles. *Cancer Lett.* **2006**, *239*, 129−135.

(3) Kamat, P. V. Photophysical, Photochemical and Photocatalytic Aspects of Metal Nanoparticles. *J. Phys. Chem. B* **2002**, *106*, 7729− 7744.

(4) Narayanan, R.; El-Sayed, M. A. Catalysis with Transition Metal Nanoparticles in Colloidal Solution: Nanoparticle Shape Dependence and Stability. *J. Phys. Chem. B* **2005**, *109*, 12663−12676.

(5) Haes, A. J.; Van Duyne, R. P. A Nanoscale Optical Biosensor: Sensitivity and Selectivity of an Approach Based on the Localized Surface Plasmon Resonance Spectroscopy of Triangular Silver Nanoparticles. *J. Am. Chem. Soc.* **2002**, *124*, 10596−10604.

(6) Sperling, R. A.; Gil, P. R.; Zhang, F.; Zanella, M.; Parak, W. J. Biological Applications of Gold Nanoparticles. *Chem. Soc. Rev.* **2008**, *37*, 1896−1908.

(7) Freddi, S.; D'Alfonso, L.; Collini, M.; Caccia, M.; Sironi, L.; Tallarida, G.; Caprioli, S.; Chirico, G. Excited-State Lifetime Assay for Protein Detection on Gold Colloids− Fluorophore Complexes. *J. Phys. Chem. C* **2009**, *113*, 2722−2730.

(8) Prigodich, A. E.; Lee, O.-S.; Daniel, W. L.; Seferos, D. S.; Schatz, G. C.; Mirkin, C. A. Tailoring DNA Structure to Increase Target Hybridization Kinetics on Surfaces. *J. Am. Chem. Soc.* **2010**, *132*, 10638−10641.

(9) Kamat, P. V. Meeting the Clean Energy Demand: Nanostructure Architectures for Solar Energy Conversion. *J. Phys. Chem. C* **2007**, *111*, 2834−2860.

(10) Link, S.; El-Sayed, M. Shape and Size Dependence of Radiative, Non-radiative and Photothermal Properties of Gold Nanocrystals. *Int. Rev. Phys. Chem.* **2000**, *19*, 409−453.

(11) Daniel, M.-C.; Astruc, D. Gold Nanoparticles: Assembly, Supramolecular Chemistry, Quantum-Size-Related Properties, and Applications toward Biology, Catalysis, and Nanotechnology. *Chem. Rev.* **2004**, *104*, 293−346.

(12) Chandra, M.; Dowgiallo, A. M.; Knappenberger, K. L. Controlled Plasmon Resonance Properties of Hollow Gold Nanosphere Aggregates. *J. Am. Chem. Soc.* **2010**, *132*, 15782−15789.

(13) Stiles, P. L.; Dieringer, J. A.; Shah, N. C.; Van Duyne, R. P. Surface-Enhanced Raman Spectroscopy. *Annu. Rev. Anal. Chem.* **2008**, *1*, 601−626.

(14) Brus, L. Noble Metal Nanocrystals: Plasmon Electron Transfer Photochemistry and Single Molecule Raman Spectroscopy. *Acc. Chem. Res.* **2008**, *41*, 1742−1749.

(15) Tam, F.; Goodrich, G. P.; Johnson, B. R.; Halas, N. J. Plasmonic Enhancement of Molecular Fluorescence. *Nano Lett.* **2007**, *7*, 496− 501.

(16) Lakowics, J. R.; Geddes, C. D.; Gryczynski, I.; Malicka, J.; Gryczynski, Z.; Aslan, K.; Lukomska, J.; Matveeva, E.; Zhang, J.; Badugu, R.; et al. Advances in Surface-Enhance Fluorescence. *J. Fluoresc.* **2004**, *14*, 425−441.

(17) Baldelli, S.; Eppler, A. S.; Anderson, E.; Shen, Y.-R.; Somorjai, G. A. Surface Enhanced Sum Frequency Generation of Carbon Monoxide Adsorbed on Platinum Nanoparticle Arrays. *J. Chem. Phys.* **2000**, *113*, 5432−5438.

(18) Bordnyuk, A. N.; Weeraman, C.; Yatawara, A.; Jayathilake, H. D.; Stiopkin, I.; Liu, Y.; Benderskii, A. V. Vibrational Sum Frequency Generation Spectroscopy of Dodecanethiol on Metal Nanoparticles. *J. Phys. Chem. C* **2007**, *111*, 8925−8933.

(19) Vance, F. W.; Lemon, B. J.; Hupp, J. T. Enormous HyperRayleigh Scattering from Nanocrystalline Gold Particle Suspensions. *J. Phys. Chem. B* **1998**, *102*, 10091−10093.

(20) Butet, J.; Bachelier, G.; Russier-Antoine, I.; Jonin, C.; Benichou, E.; Brevet, P.-F. Interference between Selected Dipoles and Octupoles in the Optical Second-Harmonic Generation from Spherical Gold Nanoparticles. *Phys. Rev. Lett.* **2010**, *105*, 077401.

(21) Hao, E. C.; Schatz, G. C.; Johnson, R. C.; Hupp, J. T. HyperRayleigh scattering from silver nanoparticles. *J. Chem. Phys.* **2002**, *117*, 5963−5966.

(22) Duboisset, J.; Russier-Antoine, I.; Benichou, E.; Bachelier, G.; Jonin, C.; Brevet, P. F. Single Metallic Nanoparticle Sensitivity with Hyper Rayleigh Scattering. *J. Phys. Chem. C* **2009**, *113*, 13477−13481.

(23) Chandra, M.; Knappenberger, K. L. Nanoparticle surface electromagnetic fields studied by single-particle nonlinear optical spectroscopy. *Phys. Chem. Chem. Phys.* **2013**, *15*, 4177−4182.

(24) Dadap, J. I.; Shan, J.; Eisenthal, K. B.; Heinz, T. F. SecondHarmonic Rayleigh Scattering from a Sphere of Centrosymmetric Material. *Phys. Rev. Lett.* **1999**, *83*, 4045−4048.

(25) Eisenthal, K. Second Harmonic Spectroscopy of Aqueous Nanoand Microparticle Interfaces. *Chem. Rev.* **2006**, *106*, 1462−1477.

(26) Boyd, R. Nonlinear Optics; Academic Press: New York, 2010.

(27) Liu, Y.; Dadap, J.; Zimdars, D.; Eisenthal, K. B. Study of Interfacial Charge-Transfer Complex on TiO2 Particles in Aqueous Suspension by Second-Harmonic Generation. *J. Phys. Chem. B* **1999**, *103*, 2480−2486.

(28) Liu, J.; Subir, M.; Nguyen, K.; Eisenthal, K. B. Second Harmonic Studies of Ions Crossing Liposome Membranes in Real Time. *J. Phys. Chem. B* **2008**, *112*, 15263−15266.

(29) Wang, H.-F.; Troxler, T.; Yeh, A.-G.; Dai, H.-L. Adsorption at a Carbon Black Microparticle Surface in Aqueous Colloids Probed by Optical Second-Harmonic Generation. *J. Phys. Chem. C* **2007**, *111*, 8708−8715.

(30) Russier-Antoine, I.; Benichou, E.; Bachelier, G.; Jonin, C.; Brever, P. F. Multipolar Contributions of the Second Harmonic Generation from Silver and Gold Nanoparticles. *J. Phys. Chem. C* **2007**, *111*, 9044−9048.

(31) Jin, R.; Jureller, J.; Kim, H.; Scherer, N. Correlating Second Harmonic Optical Responses of Single Ag Nanoparticles with Morphology. *J. Am. Chem. Soc.* **2005**, *127*, 12482−12483.

(32) Wang, H.; Yan, E.; Liu, Y.; Eisenthal, K. B. Energetics and Population of Molecules at Microscopic Liquid and Solid Surfaces. *J. Phys. Chem. B* **1998**, *102*, 4446−4450.

(33) Yan, E. C. Y.; Liu, Y.; Eisenthal, K. B. New Method for Determination of Surface Potential of Microscopic Particles by Second Harmonic Generation. *J. Phys. Chem. B* **1998**, *102*, 6331−6336.

(34) Subir, M.; Liu, J.; Eisenthal, K. B. Protonation at the Aqueous Interface of Polymer Nanoparticles with Second Harmonic Generation. *J. Phys. Chem. C* **2008**, *112*, 15809−15812.

(35) Ni, W.; Chen, H.; Su, J.; Sun, Z.; Wang, J.; Wu, H. Effects of Dyes, Gold Nanocrystals, pH, and Metal Ions on Plasmonic and Molecular Resonance Coupling. *J. Am. Chem. Soc.* **2010**, *132*, 4806− 4814.

(36) Hutchison, J. A.; Liscio, A.; Schwartz, T.; Canaguier-Durand, A.; Genet, C.; Palermo, V.; Samori, P.; Ebbesen, T. Tuning the WorkFunction via Strong Coupling. *Adv. Mater.* **2013**, *25*, 2481−2485.

(37) Cade, N. I.; Ritman-Meer, T.; Richards, D. Strong Coupling of Localized Plasmons and Molecular Excitons in Nanostructured Silver Films. *Phys. Rev. B* **2009**, *79*, 241404(R).

(38) Sugawara, Y.; Kelf, T. A.; Baumber, J. J.; Abdelsalam, M. E.; Bartlett, P. N. Strong Coupling between Localized Plasmons and Organic Excitons in Metal Nanovoids. *Phys. Rev. Lett.* **2006**, *97*, 266808.

(39) Hao, F.; Nordlander, P.; Sonnefraud, Y.; Van Dorpe, P.; Maier, S. A. Tunability of Subradiant Dipolar and Fano-Type Plasmon Resonances in Metallic Ring/Disk Cavities: Implications for Nanoscale Optical Sensing. *ACS Nano* **2009**, *3*, 643−652.

(40) Francescato, Y.; Giannini, V.; Maier, S. A. Plasmonic Systems Unveiled by Fano Resonances. *ACS Nano* **2012**, *6*, 1830−1838.

(41) Luk'yanchuk, B.; Zheludev, N.; Maier, S. A.; Halas, N. J.; Norlander, P.; Giessen, H.; Tow Chong, C. The Fano Resonance in Plasmonic Nanostructures and Metamaterials. *Nat. Mater.* **2010**, *9*, 707−715.

(42) Lopata, K.; Neuhauser, D. Molecular nanopolaritonics: Cross manipulation of near-field plasmons and molecules. I. Theory and application to junction control. *J. Chem. Phys.* **2007**, *127*, 154715.

(43) Lopata, K.; Neuhauser, D. Multiscale Maxwell−Schrö dinger modeling: A split field finite-difference time-domain approach to molecular nanopolaritonics. *J. Chem. Phys.* **2009**, *130*, 104707.

(44) Fano, U. Effect of Configuration Interaction on Intensities and Phase Shifts. *Phys. Rev.* **1961**, *124*, 1866−1878.

(45) Brown, K. R.; Walter, D. G.; Natan, M. J. Seeding of Colloidal Au Nanoparticle Solutions. 2. Improved Control of Particle Size and Shape. *Chem. Mater.* **2000**, *12*, 306−313.

(46) Perrault, S.; Chan, W. Synthesis and Surface Modification of Highly Monodispersed, Spherical Gold Nanoparticles of 50−200 nm. *J. Am. Chem. Soc.* **2009**, *131*, 17042−17043.

(47) Jana, N. R.; Gearheart, L.; Murphy, C. J. Evidence for SeedMediated Nucleation in the Chemical Reduction of Gold Salts to Gold Nanoparticles. *Chem. Mater.* **2001**, *13*, 2313−2322.

(48) Haber, L. H.; Kwok, S.; Semeraro, M.; Eisenthal, K. B. Probing the Colloidal Gold Nanoparticle/Aqueous Interface with Second Harmonic Generation. *Chem. Phys. Lett.* **2011**, *507*, 11−14.

(49) Haber, L. H.; Eisenthal, K. B. Molecular Excited-State Relaxation Dynamics at the Colloidal Microparticle Interface Monitored with Pump−Probe Second Harmonic Generation. *J. Phys. Chem. B* **2013**, *117*, 4249−4253.

(50) Bhasikuttan, A. C.; Sapre, A. V.; Okada, T. Ultrafast Relaxation Dynamics from the S2 State of Malachite Green Studied with Femtosecond Upconversion Spectroscopy. *J. Phys. Chem. A* **2003**, *107*, 3030−3035.

(51) Denk, W.; Strickler, J. H.; Webb, W. W. Two-Photon Laser Scanning Fluorescence Microscopy. *Science* **1990**, *248*, 73−76.

(52) De Beer, A. G. F.; Roke, S. Sum Frequency Generation Scattering from the Interface of an Isotropic Particle: Geometrical and Chiral Effects. *Phys. Rev. B* **2007**, *75*, 245438.

(53) Gonella, G.; Dai, H. L. Determination of Adsorption Geometry on Spherical Particles from Nonlinear Mie Theory Analysis of Surface Second Harmonic Generation. *Phys. Rev. B* **2011**, *84*, 121402(R).

(54) Lakowics, J. R. Radiative Decay Engineering 5: Metal-Enhanced Fluorescence and Plasmon Emission. *Anal. Biochem.* **2005**, *337*, 171− 194.

(55) Brü esch, P.; Christen, T. The Electric Double Layer at a Metal Electrode in Pure Water. *J. Appl. Phys.* **2004**, *95*, 2846−2856.

(56) Vance, F. W.; Lemon, a B. I.; Hupp, J. T. Enormous HyperRayleigh Scattering from Nanocrystalline Gold Particle Suspensions. *J. Phys. Chem. B* **1998**, *102*, 10091−10093.

(57) Spano, F. C. The Spectral Signatures of Frenkel Polarons in Hand J-Aggregates. *Acc. Chem. Res.* **2010**, *43*, 429−439.

CHAPTER 3 – REAL-TIME MONITORING OF THE GROWTH OF SILVER NANOSHELLS WITH ENHANCED NONLINEAR OPTICAL RESPONSE

3.1 Introduction

Gold and silver nanoparticles have been widely investigated due to their remarkable localized surface plasmon resonances arising from coherent oscillations of free electrons.[1-10] The plasmon resonance depends on the nanoparticle size, shape, composition and surrounding medium, which can be advantageous for various processes such as surface-enhanced Raman scattering (SERS)[11, 12] and surface-enhanced fluorescence.[13, 14] Additionally, plasmonic nanoparticles can lead to the enhancement of nonlinear optical processes such second harmonic generation (SHG) and sum-frequency generation,[15–22] which is very beneficial for applications in nonlinear nano-optics and sensing.[23–25]

Several synthetic strategies have been employed to design new plasmonic nanoparticles based on a core-shell configuration for optimized optical properties. Various nanoparticle shapes have been reported such as gold nanorods,[26, 27] gold nanodumbbells,[28] and dimers of gold and silver nanospheres.[29–31] Recently, the synthesis and optical properties of plasmonic nanoparticles with a core-shell structure such as gold-silica core-shell nanoparticles,[32, 33] gold-silver core-shell nanoparticles,[34, 35] and gold-silver-gold core-shell-shell nanoparticles[36] were reported.

SHG is a powerful spectroscopic technique for the study of nanoparticle surfaces in colloidal suspension.[37] SHG is a surface-specific nonlinear spectroscopic technique that is typically forbidden in bulk media that possess a center of inversion, leading to a negligible second-order susceptibility $\chi^{(2)}$ values in these centrosymmetric bulk media. However, the symmetry is broken at interfaces such as nanoparticle surfaces, resulting in nonzero second-order susceptibility $\chi^{(2)}$ values, making SHG a sensitive probe for surface studies.[38] SHG can also be used for the characterization of colloidal nanoparticles using the $\chi^{(3)}$ technique to obtain the surface charge densities[39, 40] and the acid-base equilibrium constants.[41] SHG has been used for the in-situ investigation of the growth of gold nanoshells at the surface of SiO_2 nanoparticles.[42] For these in-situ studies, the time-dependent SHG signal provides

valuable information on the surface morphology and optical properties of nanomaterial surfaces in real time during the shell growth.

In this chapter, in-situ SHG is used to probe the real-time growth of silver nanoshells on the surface of gold nanospheres in colloidal suspension. The SHG signal is observed to reach a plateau at longer times, which is indicative of the formation of a stable, full silver shell. Small angle X-ray scattering (SAXS), and high-resolution transmission electron microscopy are used to characterize the gold-silver core-shell samples. Additionally, it is observed that the SHG signal of gold-silver core-shell nanoparticles is enhanced by a factor of more than 20 and 60 times compared to gold and silver nanoparticles of similar sizes and same concentrations, respectively.

3.2 Experimental Section

3.2.1 Nanoparticle Synthesis

The colloidal gold nanoparticles are prepared by a seeded growth method.[43–45] All chemicals are purchased from Sigma Aldrich and used without further purification in ultrapure water. The gold seeds are prepared by reducing 30 mL of 290 μM gold chloride in water by adding 900 μL of 34 mM sodium citrate under boiling and vigorous stirring conditions. The colloidal solution undergoes color change from pale yellow to bright red after 10 min, resulting in the formation of 12.5 ± 1.0 nm gold seeds. Larger spherical gold nanoparticles are prepared by adding 100 μL of 29 mM gold chloride and 75 μL of the prepared gold colloidal seeds to 9.7 mL of water, followed by the addition of 25 μL of 34 mM sodium citrate and 100 μL of 0.03 M hydroquinone, with subsequent vigorous stirring at room temperature for 60 min.

Silver nanoparticles are prepared by adding $AgNO_3$, sodium citrate, and potassium iodide to an aqueous solution of ascorbic acid under boiling conditions.[46] Briefly, 100 μL of 100 mM ascorbic acid is added to 47.5 ml of boiling water, followed by consecutive additions of 250 μL of 60 mM silver nitrate, 1.0 mL of 30 mM sodium citrate, and 30 μL of 100 μM potassium iodide, with continued boiling and vigorous stirring for 60 min.

Gold-silver core-shell nanoparticles are prepared by reducing $AgNO_3$ with a mild reducing agent under basic conditions.[34] Briefly, 0.5 mL of the prepared gold nanospheres are added to 1.0 mL of water, followed by the addition of 3 μL of 100 mM of ascorbic acid, 1.5 μL of 100 mM of $AgNO_3$, and 4 μL of 100 mM NaOH under vigorous stirring at room temperature. Silver ions have a high affinity to the gold nanoparticle surface, resulting in a full, uniform silver shell coverage to all colloidal gold nanoparticles.

3.2.2 Characterization

High-resolution transmission electron microscopy (HRTEM), extinction spectroscopy and small angle x-ray scattering (SAXS) are used to characterize the samples under study. Figure 3.1 (a) shows the extinction spectrum of the gold-silver core-shell nanoparticles. The experimental results are overlapped with the best fit using Mie Theory for 65-11 nm gold-silver core-shell nanoparticles at a concentration of 1.5×10^9 nanoparticles/mL.

3.2.3 In-Situ Second Harmonic Generation

The second harmonic generation optical setup is described in chapter 2 and consists of a femtosecond Ti:sapphire laser, an optical setup, and a monochromator coupled to a CCD detector. Multiple spectra and background are acquired using a computer-controlled beam block with automated file saving in order to accurately obtain the SHG spectrum of the colloidal nanoparticle sample as a function of time during the growth of the silver shell.

3.3 Results and Discussion

Figure 3.1(b) shows the HRTEM image of gold-silver core-shell nanoparticles with a 65 ± 4 nm gold core and 11 ± 1 nm silver shell. Additional TEM images are provided in Appendix 2. Figure 3.1(c) shows the small angle electron diffraction (SAED) image of 65-11 nm gold-silver core-shell nanoparticles where the crystal packing corresponding to gold unit cells in the core and silver unit cells in the shell are observed. The SAXS spectra of the gold core and the gold-silver core-shell colloidal nanoparticle samples acquired at the Advanced Photon Source (APS) at Argonne National Laboratory are shown in Figure 3.2, a-b, respectively. The data are fit using a polydisperse log-normal model obtained from the NIST website with a core diameter of 64 nm and a shell width of 11 nm.

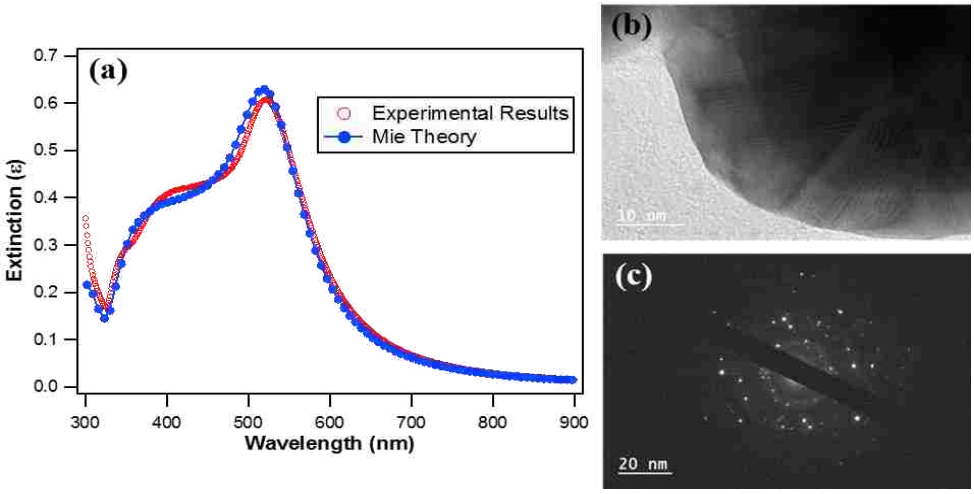

Figure 3.1 (a) Extinction spectra of 65-11 nm gold-silver core-shell nanoparticles. The experimental results are overlapped with the best fit using Mie Theory at a concentration of 1.5×10^9 nanoparticles/mL. (b) HRTEM image of gold-silver core-shell nanoparticles. (c) SAED of gold-silver core-shell nanoparticles.

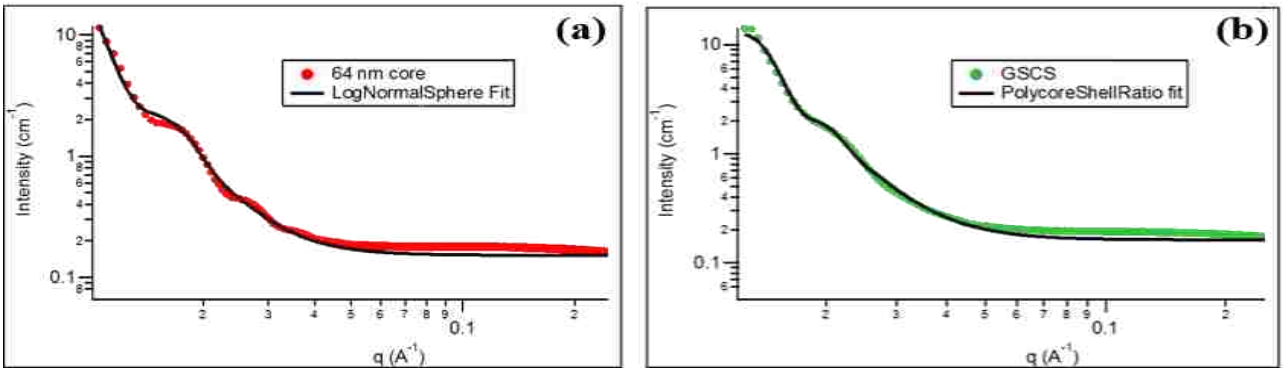

Figure 3.2 SAXS spectra of (a) the gold core sample and (b) gold-silver core-shell nanoparticle sample in water. The experimental data are fit using a polydisperse log-normal model.

The growth of a silver shell on the surface of the colloidal gold nanoparticles is investigated in real time using SHG for detailed monitoring of the silver shell growth and analysis of the SHG enhancement. Figure 3.3 shows the evolution of the SHG signal during the in-situ growth of the silver shell at the colloidal gold surface (red circles). The corresponding SHG spectra are shown in Appendix 2. The signal increases substantially during the first 90 seconds, then continues to increase slowly and steadily until a plateau is reached after approximately 17 minutes. The stable and constant SHG signal after the plateau indicates the completion of the silver shell formation on the gold nanoparticle, resulting in a stable sample of gold-silver core-shell nanoparticles in colloidal suspension. The silver shells are uniform in thickness, as confirmed by HR-TEM measurements. These results demonstrate that the seeded

growth of the gold-silver core-shell can be successfully monitored in real-time using SHG. Additionally, this work provides a powerful technique for the in-situ investigation of the growth of various nanoshells and nanomaterials in colloidal suspension, where valuable information on the surface structure, morphology, and topology can be obtained. The results are compared to a control experiment, where the SHG signal is measured in time for the reduction of $AgNO_3$ with the addition of ascorbic acid and sodium hydroxide at the same concentrations as the core-shell experiment, but without the addition of gold nanoparticles. These control measurements are also shown in Figure 3.3 (blue circles). For the control, the SHG signal is characterized by a small and fast increase for the first 60 seconds, followed by a plateau at 90 seconds. The maximum intensity of the SHG signal of the of the colloidal gold-silver core-shell nanoparticle sample at the plateau is approximately 17 times larger than the SHG signal increase observed in the control experiment.

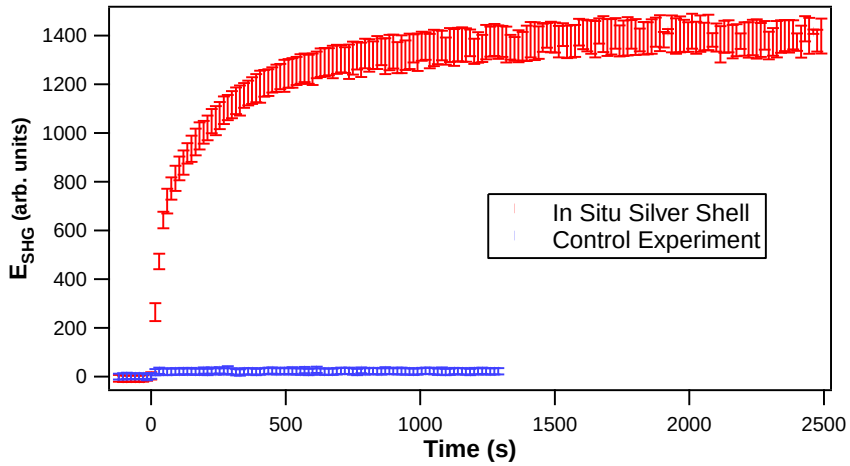

Figure 3.3. (red dots) SHG time-profiles of the growth of the silver shell on the surface of 65 nm colloidal gold nanoparticles in water achieved by reducing $AgNO_3$ by adding ascorbic acid and sodium hydroxide. (blue dots) SHG time-profiles of the reduction of $AgNO_3$ using the same ascorbic acid and sodium hydroxide concentrations in water.

The gold-silver core-shell nanoparticles have greatly enchanced SHG signal compared to gold nanoparticles and silver nanoparticles of approximately the same size. Figure 3.4 shows the SHG spectra of 65 nm gold nanoparticles, 70 nm silver nanoparticles, and 65-11 nm gold-silver core-shell nanoparticles in water, where all three samples have the same nanoparticle concentration. The incident laser beam is centered at 800 nm and the generated SHG signal is detected at approximately 400 nm. An

8-fold and 3-fold enhancement in the E_{SHG} signal is observed from the surface of the core-shell sample compared to gold nanoparticles and silver nanoparticles, respectively, corresponding to an enhancement of 64-folds and 25-folds in the intensity of the SHG signal, respectively. This remarkable enhancement in the SHG signal is due to the optical field enhancement generated at the gold and silver interface. However, additional theoretical work is still needed to accurately model the optical properties of these core-shell nanoparticles. This optical field enhancement is very advantageous for various applications using surface optical field enhancement of nanoparticles.

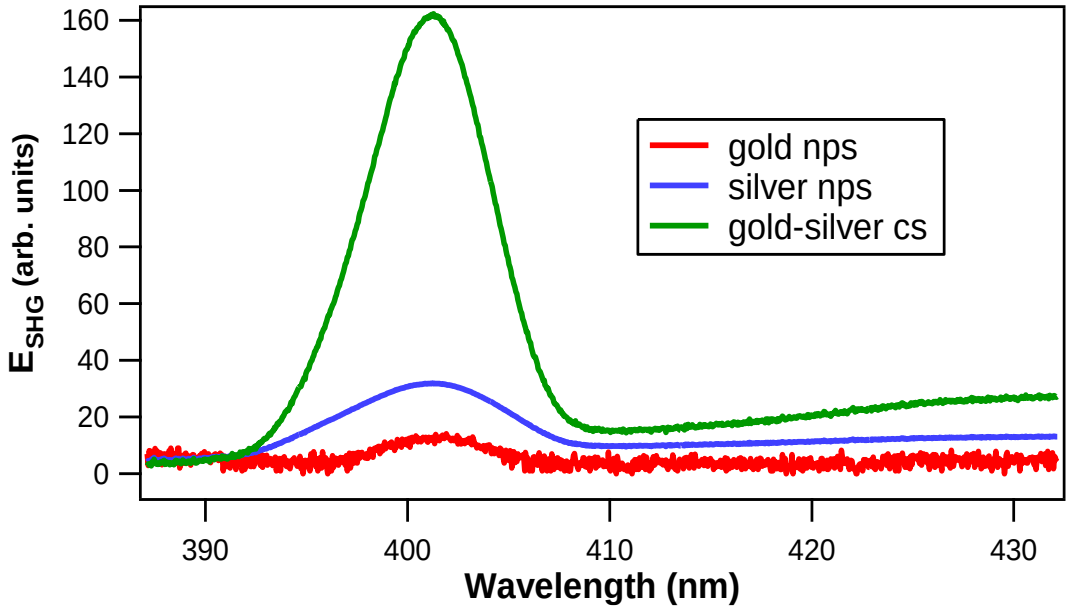

Figure 3.4. SHG spectra of (red line) 65 nm gold nanoparticles, (blue line) 70 nm silver nanoparticles, and (green line) 65-11 nm gold-silver core-shell nanoparticles in water at the same nanoparticle concentration. The SHG peak is detected near 400 nm.

3.4 Conclusion

In-situ SHG is used to monitor the growth of an 11 nm silver shell on the surface of 65 nm gold nanoparticles. The SHG signal of the growth mechanism is monitored over time at different stages of the silver reduction reaction. High-resolution TEM and SAXS are used to additionally characterize the size and surface structure of the gold-silver core-shell nanoparticles. Gold-silver core-shell nanoparticles show a remarkable SHG enhancement of 64-folds and 25-folds compared to gold nanoparticles and silver nanoparticles, respectively. This large nonlinear enhancement makes these core-shell nanoparticles very

promsing for potential applications in molecular sensing such as surface-enhanced Raman spectroscopy, surface-enhanced fluorescence, and resonance coupling, as well as for labelling in two-photon optical microscopy investigations. Additionally, the in-situ SHG measurements demonstrate a sensitive technique for real-time monitoring of core-shell growth mechanisms in hybrid colloidal nanoparticle synthesis.

3.5 References

(1) El-Sayed, I.; Huang, X.; El-Sayed, M. Surface Plasmon Resonance Scattering and Absorption of Anti-EGFR Antibody Conjugated Gold Nanoparticles in Cancer Diagnostics: Applications in Oral Cancer. *Nano Lett.* **2005**, *5*, 829−834.

(2) El-Sayed, I.; Huang, X.; El-Sayed, M. Selective Laser Photothermal Therapy of Epithelial Carcinoma Using Anti-EGFR Antibody Conjugated Gold Nanoparticles. *Cancer Lett.* **2006**, *239*, 129−135.

(3) Kamat, P. V. Photophysical, Photochemical and Photocatalytic Aspects of Metal nanoparticles. *J. Phys. Chem. B* **2002**, *106*, 7729−7744.

(4) Narayanan, R.; El-Sayed, M. A. Catalysis with Transition Metal Nanoparticles in Colloidal Solution: Nanoparticle Shape Dependence and Stability. *J. Phys. Chem. B* **2005**, *109*, 12663−12676.

(5) Haes, A. J.; Van Duyne, R. P. A Nanoscale Optical Biosensor: Sensitivity and Selectivity of an Approach Based on the Localized Surface Plasmon Resonance Spectroscopy of Triangular Silver Nanoparticles. *J. Am. Chem. Soc.* **2002**, *124*, 10596−10604.

(6) Sperling, R. A.; Gil, P. R.; Zhang, F.; Zanella, M.; Parak, W. J. Biological Applications of Gold Nanoparticles. *Chem. Soc. Rev.* **2008**, *37*, 1896−1908.

(7) Freddi, S.; D'Alfonso, L.; Collini, M.; Caccia, M.; Sironi, L.; Tallarida, G.; Caprioli, S.; Chirico, G. Excited-State Lifetime Assay for Protein Detection on Gold Colloids− Fluorophore Complexes. *J. Phys. Chem. C* **2009**, *113*, 2722−2730.

(8) Prigodich, A. E.; Lee, O.-S.; Daniel, W. L.; Seferos, D. S.; Schatz, G. C.; Mirkin, C. A. Tailoring DNA Structure to Increase Target Hybridization Kinetics on Surfaces. *J. Am. Chem. Soc.* **2010**, 132, 10638−10641.

(9) Kamat, P. V. Meeting the Clean Energy Demand: Nanostructure Architectures for Solar Energy Conversion. *J. Phys. Chem. C* **2007**, 111, 2834−2860.

(10) Karam, T. E.; Haber, L. H. Molecular Adsorption and Resonance Coupling at the Colloidal Gold Nanoparticle Interface. *J. Phys. Chem. C* **2014**, *118*, 642−649.

(11) Stiles, P. L.; Dieringer, J. A.; Shah, N. C.; Van Duyne, R. P. Surface-Enhanced Raman Spectroscopy. *Annu. Rev. Anal. Chem.* **2008**, *1*, 601−626.

(12) Brus, L. Noble Metal Nanocrystals: Plasmon Electron Transfer Photochemistry and Single Molecule Raman Spectroscopy. *Acc. Chem. Res.* **2008**, *41*, 1742−1749.

(13) Tam, F.; Goodrich, G. P.; Johnson, B. R.; Halas, N. J. Plasmonic Enhancement of Molecular Fluorescence. *Nano Lett.* **2007**, *7*, 496−501.

(14) Lakowics, J. R.; Geddes, C. D.; Gryczynski, I.; Malicka, J.;Gryczynski, Z.; Aslan, K.; Lukomska, J.; Matveeva, E.; Zhang, J.; Badugu, R.; et al. Advances in Surface-Enhance Fluorescence. *J. Fluoresc.* **2004**, *14*, 425−441.

(15) Baldelli, S.; Eppler, A. S.; Anderson, E.; Shen, Y.-R.; Somorjai, G. A. Surface Enhanced Sum Frequency Generation of Carbon Monoxide Adsorbed on Platinum Nanoparticle Arrays. *J. Chem. Phys.* **2000**, *113*, 5432−5438.

(16) Bordnyuk, A. N.; Weeraman, C.; Yatawara, A.; Jayathilake, H. D.; Stiopkin, I.; Liu, Y.; Benderskii, A. V. Vibrational Sum Frequency Generation Spectroscopy of Dodecanethiol on Metal Nanoparticles. *J. Phys. Chem. C* **2007**, *111*, 8925−8933.

(17) Vance, F. W.; Lemon, B. J.; Hupp, J. T. Enormous HyperRayleigh Scattering from Nanocrystalline Gold Particle Suspensions. *J. Phys. Chem. B* **1998**, *102*, 10091−10093.

(18) Butet, J.; Bachelier, G.; Russier-Antoine, I.; Jonin, C.; Benichou,E.; Brevet, P.-F. Interference between Selected Dipoles and Octupoles in the Optical Second-Harmonic Generation from Spherical Gold Nanoparticles. *Phys. Rev. Lett.* **2010**, *105*, 077401.

(19) Hao, E. C.; Schatz, G. C.; Johnson, R. C.; Hupp, J. T. Hyper-Rayleigh Scattering from Silver Nanoparticles. *J. Chem. Phys.* **2002**, *117*, 5963−5966.

(20) Duboisset, J.; Russier-Antoine, I.; Benichou, E.; Bachelier, G.; Jonin, C.; Brevet, P. F. Single Metallic Nanoparticle Sensitivity with Hyper-Rayleigh Scattering. *J. Phys. Chem. C* **2009**, *113*, 13477−13481.

(21) Chandra, M.; Knappenberger, K. L. Nanoparticle Surface Electromagnetic Fields Studied by Single-Particle Nonlinear Optical Spectroscopy. *Phys. Chem. Chem. Phys.* **2013**, *15*, 4177−4182.

(22) Dadap, J. I.; Shan, J.; Eisenthal, K. B.; Heinz, T. F. Second-Harmonic Rayleigh Scattering from a Sphere of Centrosymmetric Material. *Phys. Rev. Lett.* **1999**, *83*, 4045−4048.

(23) Walsh, G. F.; Dal Negro, L. Enhanced Second Harmonic Generation by Photonic−Plasmonic Fano-Type Coupling in Nanoplasmonic Arrays. *Nano Lett.* **2013**, *13*, 3111−3117.

(24) Shen, S.; Meng, L.; Zhang, Y.; Han, J.; Ma, Z.; Hu, S.; He, Y.; Li, J.; Ren, B.; Shih, T. –M.; Wang, Z.; Yang, Z.; Tian, Z. Plasmon-Enhanced Second-Harmonic Generation Nanorulers with Ultrahigh Sensitivities. *Nano Lett.* **2015**, *15*, 6716−6721.

(25) Thyagarajan, K.; Butet, J.; Martin, O. J. F. Augmenting Second Harmonic Generation Using Fano Resonances in Plasmonic Systems. *Nano Lett.* **2013**, *13*, 1847−1851.

(26) Nikoobakht B.; El-Sayed, M. A. Preparation and Growth Mechanism of Gold Nanorods (NRs) Using Seed-Mediated Growth Method. *Chem. Mater.* **2003**, *15*, 1957–1962.

(27) Huang, X.; El-Sayed, I. H.; Qian, W.; El-Sayed, M. A. Cancer Cell Imaging and Photothermal Therapy in the Near-Infrared Region by Using Gold Nanorods. *J. Am. Chem. Soc.* **2006**, *128*, 2115–2120.

(28) Grzelczak, M.; Sánchez-Iglesias, A.; Mezerji, H. H.; Bals, S.; Pérez-Juste, J.; Liz-Marzán, L. M. Steric Hindrance Induces crosslike Self-Assembly of Gold Nanodumbbells. *Nano Lett.* **2012**, *12*, 4380–4384.

(29) Li, W.; Camargo, P. H. C.; Lu, X.; Xia, Y. Dimers of Silver Nanospheres: Facile Synthesis and Their Use as Hot Spots for Surface-Enhanced Raman Scattering. *Nano Lett.* **2009**, *9*, 485–490.

(30) Bachelier, G.; Russier-Antoine, I.; Benichou, E.; Jonin, C.; Del Fatti, N.; Vallée, F.; Brevet, P. –F. Fano Profiles Induced by Near-Field Coupling in Heterogeneous Dimers of Gold and Silver Nanoparticles. *Phys. Rev. Lett.* **2008**, *101*, 197401.

(31) Talley, C. E.; Jackson, J. B.; Oubre, C.; Grady, N. K.; Hollars, C. W.; Lane, S. M.; Huser, T. R.; Nordlander, P.; Halas, N. J. Surface-Enhanced Raman Scattering from Individual Au Nanoparticles and Nanoparticle Dimer Substrates. *Nano Lett.* **2005**, *5*, 1569–1574.

(32) Liz-Marzán, L. M.; Giersig, M.; Mulvaney, P. Synthesis of Nanosized Gold−Silica Core−Shell Particles. *Langmuir* **1996**, *12*, 4329–4335.

(33) Lu, Y.; Yin, Y.; Li, Z. –Y.; Xia, Y. Synthesis and Self-Assembly of Au@SiO2 Core−Shell Colloids. *Nano Lett.* **2002**, *2*, 785–788.

(34) Samal, A. K.; Polavarapu, L.; Rodal-Cedeira, S.; Liz-Marzan, L. M.; Perez-Juste, J.; Pastoriza-Santos, I. Size Tunable Au@Ag Core–Shell Nanoparticles: Synthesis and Surface-Enhanced Raman Scattering Properties. *Langmuir* **2013**, *29*, 15076−15082.

(35) Pande, S.; Ghosh, S. K.; Praharaj, S.; Panigrahi, S.; Basu, S.; Jana, S.; Pal, A.; Tsukuda, T.; Pal, T. Synthesis of Normal and Inverted Gold−Silver Core−Shell Architectures in β-Cyclodextrin and Their Applications in SERS. *J. Phys. Chem. C* **2007**, *111*, 10806–10813.

(36) Karam, T. E.; Smith, H. T.; Haber, L. H. Enhanced Photothermal Effects and Excited-State Dynamics of Plasmonic Size-Controlled Gold–Silver–Gold Core–Shell–Shell Nanoparticles. *J. Phys. Chem. C* **2015**, *119*, 18573–18580.

(37) Eisenthal, K. Second Harmonic Spectroscopy of Aqueous Nano- and Microparticle Interfaces. *Chem. Rev.* **2006**, *106*, 1462−1477.

(38) Boyd, R. Nonlinear Optics; Academic Press: New York, 2010.

(39) Yan, E. C. Y.; Liu, Y.; Eisenthal, K. B. New Method for Determination of Surface Potential of Microscopic Particles by Second Harmonic Generation. *J. Phys. Chem. B* **1998**, *102*, 6331−6336.

(40) Kumal, R. R.; Karam, T. E.; Haber, L. H. Determination of the Surface Charge Density of Colloidal Gold Nanoparticles Using Second Harmonic Generation. *J. Phys. Chem. C* **2015**, *119*, 16200–16207.

(41) Subir, M.; Liu, J.; Eisenthal, K. B. Protonation at the Aqueous Interface of Polymer Nanoparticles with Second Harmonic Generation. *J. Phys. Chem. C* **2008**, *112*, 15809−15812.

(42) Sauerbeck, C.; Haderlein, M.; Schürer, B.; Braunschweig, B.; Peukert, W.; Klupp Taylor, R. N. Shedding Light on the Growth of Gold Nanoshells. ACS Nano 2014, 8, 3088–3096.

(43) Brown, K. R.; Walter, D. G.; Natan, M. J. Seeding of Colloidal Au Nanoparticle Solutions. 2. Improved Control of Particle Size and Shape. *Chem. Mater.* **2000**, *12*, 306−313.

(44) Perrault, S.; Chan, W. Synthesis and Surface Modification of Highly Monodispersed, Spherical Gold Nanoparticles of 50−200 nm. *J. Am. Chem. Soc.* **2009**, *131*, 17042−17043.

(45) Jana, N. R.; Gearheart, L.; Murphy, C. J. Evidence for Seed-Mediated Nucleation in the Chemical Reduction of Gold Salts to Gold Nanoparticles. *Chem. Mater.* **2001**, *13*, 2313−2322.

(46) Li, H.; Xia, H.; Wang, D.; Tao, X. Simple Synthesis of Monodisperse, Quasi-spherical, Citrate-Stabilized Silver Nanocrystals in Water. *Langmuir*, **2013**, *29*, 5074–5079.

CHAPTER 4 – ENHANCED PHOTOTHERMAL EFFECTS AND EXCITED-STATE DYNAMICS OF PLASMONIC SIZE-CONTROLLED GOLD-SILVER-GOLD CORE-SHELL-SHELL NANOPARTICLES*

4.1 Introduction

Metallic nanoparticles composed of gold and silver possess unique chemical, electronic, and optical properties that are useful for applications in the fields of molecular sensing, catalysis, and biologically-relevant technologies.[1-10] Localized surface plasmon resonances, characterized by the coherent oscillations of free electrons at the nanoparticles surface[11-13] are highly dependent on the nanoparticle composition, size, shape and surrounding medium. Plasmonic gold and silver nanoparticles can be functionalized with biological molecules and polymers through thiolation for applications in biolabeling,[14, 15] drug delivery,[16, 17] and photothermal therapy.[18-20] Plasmon-enhanced absorption in the near-infrared (NIR) photon energies, corresponding to the optical window in biological tissues, is advantageous for biological applications such as photothermal therapy and non-invasive bio-imaging.[6]

Several different types of plasmonic nanoparticles have been extensively studied due to their potential use in photothermal therapy including gold nanorods,[21,22] gold nanocages,[23] silica-gold core-shell nanoparticles,[20, 21] hollow spherical nanoshells,[24,25] and gold nanoparticles coated with reduced graphene oxide.[26] These nanoparticles can absorb light in the NIR wavelengths and convert it to heat through nonradiative processes leading to a localized photothermal effect that can be used for selective killing of cancer cells. Methods to increase the NIR photothermal efficiency of plasmonic nanoparticles can provide more effective photothermal cancer therapies.[27, 28] For example, gold-silica-gold nanomatryoshkas were shown to be more efficient as photothermal transducers than gold-silica core-shell.[29] Au@Ag/Au nanospheres composed of a gold nanorod core and a silver/gold alloy shell demonstrated higher photothermal efficiencies and lower citotoxities than gold nanorods.[30]

Another type of nanoparticle called gold-silver-gold core-shell-shell nanoparticles have been studied for potential applications in sensing and labeling,[31,] and represent a new direction for plasmonic engineering for highly efficient photothermal therapies at NIR wavelengths.

In this chapter, we describe the synthesis, characterization, photothermal measurements, and transient absorption investigations of colloidal gold-silver-gold core-shell-shell nanoparticles. These nanoparticles exhibit plasmonic enhancement and controllable extinction spectra extending from the ultraviolet (UV) to the NIR wavelengths. The ratio of the outer gold shell thickness to the overall particle size shows a linear dependence with the position of the plasmon extinction peak wavelength. Temperature measurements after laser irradiation demonstrate that the colloidal gold-silver-gold core-shell-shell nanoparticles have a higher photothermal effect compared to colloidal gold nanospheres and gold nanorods. The excited-state dynamics of these plasmonic nanoparticles are studied using pump-probe transient absorption spectroscopy. The lifetime associated with phonon-phonon scattering is shown to be remarkably faster in core-shell-shell nanoparticles than in gold nanospheres and nanorods, which is an important contributing factor leading to their higher photothermal efficiencies. In addition, the synthesis of extended core-shell architectures with alternating gold/silver shells and controllable core and shell dimensions is reported for advanced plasmonic engineering.

4.2 Experimental Section

4.2.1 Nanoparticle Synthesis

For the nanoparticle syntheses, all chemicals are purchased from Sigma Aldrich and used without further purification in ultrapure water. For the synthesis of 12 nm gold nanoparticle seeds for the gold core, 30 mL of 290 μM gold chloride in water is brought to reflux under vigorous stirring conditions, followed by the addition of 900 μL of 34 mM sodium citrate. The colloidal solution undergoes a color change from pale yellow to bright red after 20 minutes and is removed from heat and cooled to room temperature. For the growth of the first silver shell, 300 μL of the gold seeds are added to 10 mL ultrapure water. The mixture is kept at room temperature under vigorous stirring with additions of 60 μL of 100 mM ascorbic acid, 15 μL of 100 mM silver nitrate, and 75 μL of 100 mM sodium hydroxide. Ascorbic

acid is a mild reducing agent that reduces Ag^+ onto the gold core under basic conditions.[32] The size of the silver shell can be controlled by selecting the number of ascorbic acid, silver nitrate, and sodium hydroxide sequential additions. The gold-silver core-shell colloidal nanoparticles are centrifuged at 2,400 rpm for 20 minutes and redispersed in 10 mL of ultrapure water. Different sizes of outer gold shells are then grown by adding 100 μL, 200 μL, or 300 μL of 29 mM gold chloride, followed by the addition of 25 μL of 34 mM sodium citrate and 100 μL of 0.03 M hydroquinone under vigorous stirring at room temperature for 60 minutes. These gold-silver-gold core-shell-shell nanoparticles can be easily thiolated and functionalized for potential biochemical applications. The three steps involved in the synthesis are depicted in Scheme 4.1.

Spherical gold nanoparticles and gold nanorods are used for comparison studies of the photothermal effects of the colloidal core-shell-shell nanoparticles. The gold nanospheres of diameter 54 ± 6 nm are prepared using a seeding growth technique reported previously.[33-36] Here, 250 μL of the 12 nm seed solution, 100 μL of 0.03 M hydroquinone, and 22 μL of 34 mM sodium citrate are added consecutively to 10.0 mL of 2.9 mM gold chloride solution. The solution is left at room temperature and under vigorous stirring conditions for 60 minutes. The gold nanorod sample is purchased from Nanopartz, has a 10 ± 1 nm width, a 35 ± 6 nm length, and is capped with CTAB in aqueous colloidal suspension. All

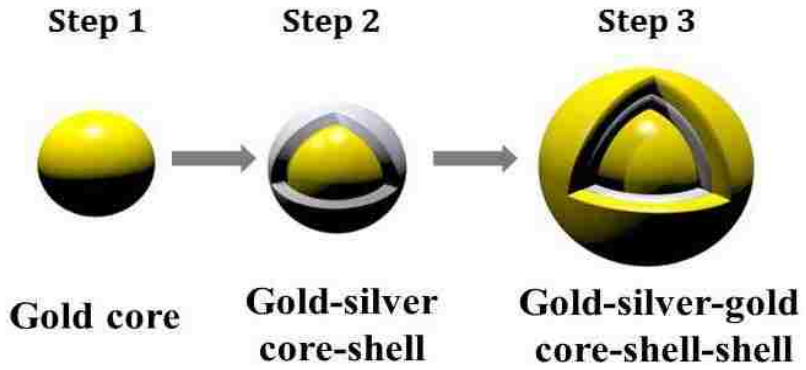

Scheme 4.1. The three steps involved in the synthesis of colloidal gold-silver-gold core-shell-shell nanoparticles.

gold nanosphere and gold nanorod studies reported here use these samples with 54 nm diameter nanospheres and 10 nm width, 35 nm length gold nanorods, respectively.

4.2.2 Characterization

High-resolution transmission electron microscopy (HR-TEM), extinction spectroscopy, emission spectroscopy, and photothermal measurements are used to characterize the nanoparticles. The average sizes and size distributions are determined using greater than 100 HR-TEM images for each sample. HR-TEM images and extinction spectra of the gold core and gold-silver core-shell nanoparticles are shown in the Appendix 3. The core-shell-shell concentration is determined using inductively coupled plasma optical emission spectroscopy (ICP-OES). Energy dispersive X-ray spectroscopy (EDS) is performed to investigate the elemental composition of the core-shell-shell nanoparticles.

4.2.3 Photothermal Analysis

The photothermal performance of 12-12-30 nm colloidal gold-silver-gold core-shell-shell nanoparticles at a concentration of 3.6×10^{10} nanoparticles/mL is studied in solution under NIR light. A 0.8 mL volume of the colloidal sample is placed in a 1.0 mm path-length quartz cuvette and irradiated with a laser beam centered at 800 nm with an average power of 1.7 W, a beam size of 1.2 ± 0.2 mm, a pulse width of 75 fs, and a repetition rate of 80 MHz. The temperature change is measured using a K type thermocouple connected to a computer using a data acquisition card. The results are compared to an ultrapure water sample, the colloidal gold nanosphere sample in water, and the colloidal gold nanorod sample in water. The gold nanosphere concentration determined using ICP-OES and Mie Theory is 3.1×10^{10} nanoparticles/mL and 2.9×10^{10} nanoparticles/mL respectively. The concentration of the gold nanorods samples determined using ICP-OES is 2.7×10^{11} nanoparticles/mL. The optical density (OD = 0.26) of the plasmon peak of the colloidal gold nanospheres at 540 nm is equal to the optical density of the plasmon peak of the gold-silver-gold core-shell-shell nanoparticle sample at 800 nm as well as the gold nanorod sample at 800 nm for a quantitative comparison of the photothermal effects of the different nanoparticle samples.

4.2.4 Transient Absorption Setup

The transient absorption setup consists of an amplified titanium:sapphire laser system, an optical parametric amplifier (OPA), an optical setup, and a fiber optic spectrometer with a charge-coupled device detector.[37] The laser produces 0.7 mJ, 75 fs pulses centered at 800 nm with a repetition rate of 10 kHz. The fundamental beam is split using a beamsplitter to separate the pump and probe pulses. The pump pulses are passed through an OPA to generate 400 nm, 5 μJ pump pulses that are reflected by a retroreflector on a computer-controlled translation stage to control the pump-probe temporal delay. The probe beam is focused into a 1 cm fused quartz flow cell containing water to generate femtosecond white light probe pulses that are refocused to a spatial overlap with the pump pulse at the sample. The colloidal sample is contained in a 3 mm fused quartz cell under constant stirring. Several time-resolved spectral scans are taken for statistical analysis. A schematic diagram of the optical setup is included in the Appendix 3.

4.3 Results and Discussion

The extinction spectra of the gold-silver-gold nanoparticles as a function of the silver and gold shell sizes are first investigated. The different average sizes and distributions of the gold-silver-gold core-shell-shell nanoparticles studied are listed in the Appendix 3. Figure 4.1, a-c show selected HR-TEM images of the gold-silver-gold core-shell-shell nanoparticles with a 12.0 ± 0.9 nm gold core and various silver and gold shell thicknesses. After the addition of the silver shell, the surface plasmon resonance peak blueshifts from 513 nm for the gold core to approximately 420 nm for the gold-silver core-shell nanoparticles. The plasmon extinction peak broadens and increases in intensity as the thickness of the silver shell is increased, as shown in Appendix 3. Figure 4.2 shows the extinction spectra of the colloidal gold-silver-gold core-shell-shell nanoparticles with a 12.0 ± 0.9 nm gold core and various silver and gold shell thicknesses. After the formation of the outer gold shell, the plasmon peak redshifts leading to enhanced extinction in the near-infrared region. Figure 4.2 (a) shows the normalized extinction spectra of gold-silver-gold core-shell-shell nanoparticles with a 12.0 ± 0.9 nm gold core, a 12.0 ± 1.1 nm silver shell, and an outer gold shell of thickness 5.0 ± 0.6 nm, 15.0 ± 0.9 nm, 20.0 ± 1.6 nm, and 30.0 ± 2.4 nm,

respectively. For the thinnest gold shell of 5 nm, the plasmon peak is centered near 565 nm and extends to the near-infrared. As the thickness of the outer gold shell is increased, the plasmon peak broadens and redshifts to the near-infrared. At an outer gold shell thickness of 30.0 ± 2.4 nm, the plasmon peak is centered near 850 nm.

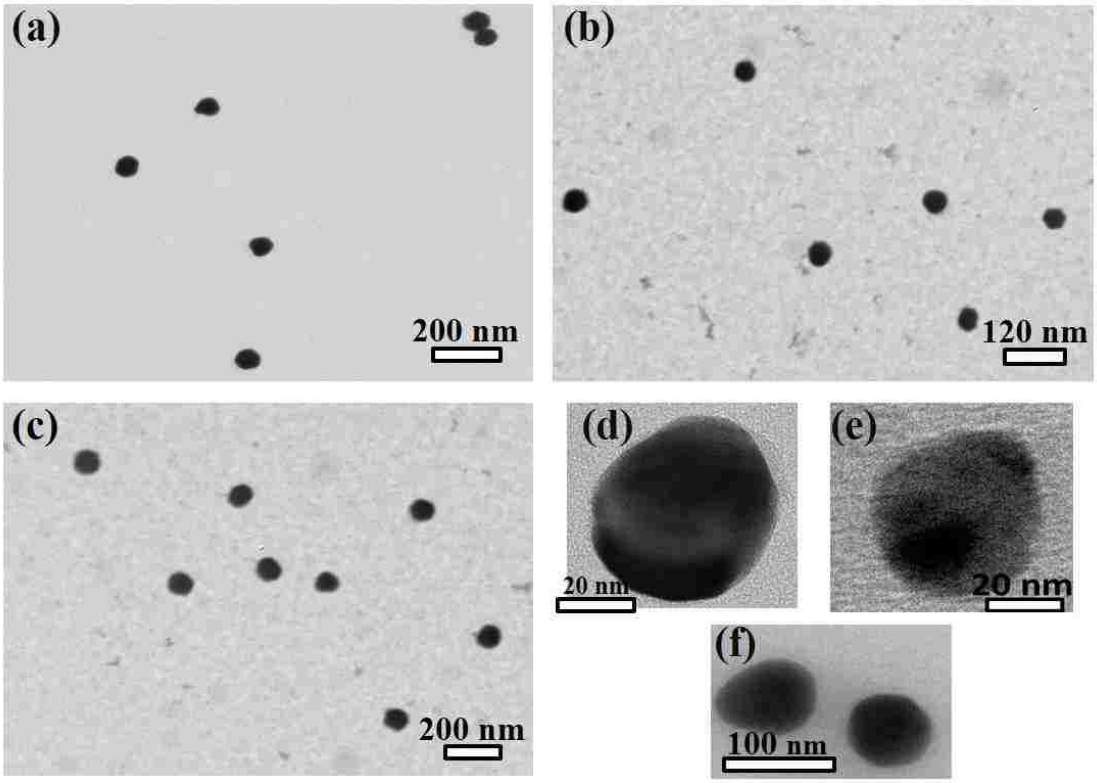

Figure 4.1. TEM images of gold-silver-gold core-shell-shell nanoparticles with (a) 12-12-12 nm, (b) 12-18-10 nm, (c) 12-24-10 nm, (d) 12-12-5 nm, (e) 12-18-10 nm, and (f) 12-24-10 nm core-shell-shell sizes, respectively.

The effect of varying the thickness of the silver shell is also studied. Figure 4.2 (b) shows the extinction spectra of gold-silver-gold core-shell-shell nanoparticles with a 12.0 ± 0.9 nm gold core, a 18.0 ± 1.6 nm silver shell, and an outer gold shell thickness of 5.0 ± 0.6 nm, 7.5 ± 0.8 nm, and 10.0 ± 1.1 nm, respectively. Similarly to Figure 4.2 (a), the gold-shell-shell nanoparticles with the thinnest gold shell of 5 nm has a plasmon peak centered near 565 nm that extends to the near-infrared. Increasing the thickness of the outer gold shell to 10 nm redshifts the plasmon peak wavelength to approximately 585 nm. Figure 4.2 (c) shows the extinction spectra of the gold-silver-gold core-shell-shell nanoparticles with a 12.0 ± 0.9 nm gold core, a 24.0 ± 2.1 nm silver shell, and an outer gold shell thickness of 5.0 ± 0.7 nm, 7.5 ± 0.9 nm,

and 10.0 ± 1.1 nm, respectively. For the thinnest gold shell of 5 nm, the plasmon peak is centered at 610 nm and extends to the near-infrared. As the thickness of the gold shell is increased, the plasmon peak first blueshifts, then an additional peak centered in the NIR rises and increases in intensity. The plasmon-enhanced extinction spectra can be controlled from the UV to the NIR wavelengths by varying the silver and gold shell sizes, making these nanoparticles ideal for many biologically-relevant applications such as photothermal therapy and bioimaging.[6] Importantly, as shown in Figure 4.2 (d), the plasmon extinction peak wavelength depends linearly on the ratio of thickness of the outer gold shell to the overall size of the nanoparticle. The equation of the best fit line is given by a slope of $1.44\times10^{-3} \pm 2.9\times10^{-5}$ nm^{-1} and a y-intercept of -0.64 ± 0.02. This relationship provides a mechanism to control the plasmonic optical properties of the colloidal gold-silver-gold core-shell-shell nanoparticles depending on the desired application. Future studies will compare these experimental results to theoretical modelling to investigate the underlying plasmonic interactions that give rise to these controlled optical properties. The EDS spectrum provided in the Appendix 3 for the 12-12-30 nm gold-silver-gold core-shell-shell nanoparticle sample shows that silver is still present after the formation of outer gold layer.

Figure 4.3 displays the results of the photothermal study of different nanoparticle samples. The temperature of the 12-12-30 nm colloidal gold-silver-gold core-shell-shell nanoparticle sample with a 12 nm core, a 12 nm silver shell, and a 30 nm outer gold shell as a function of time after irradiation with 800 nm laser light is shown. The results are compared to corresponding measurements on colloidal gold nanorods with a 10 nm width and a 35 nm length in water, 54 nm colloidal gold nanospheres in water, and an ultrapure water control sample. The extinction spectra of these samples are shown in the Appendix 3. The water and spherical colloidal gold nanoparticle samples do not exhibit any detectable temperature change after laser irradiation. Here, the negligible extinction at 800 nm corresponds to negligible heating. The colloidal core-shell-shell nanoparticles show a temperature change of 5.2 ± 0.2 ℃ at a rate of 1.5 ℃/min due to the conversion of the absorbed NIR light to heat by the plasmonic nanoparticles. The gold nanorods show a temperature change of 3.7 ± 0.2 ℃ at a rate of 0.75 ℃/min. It is important to note that previous photothermal studies of gold nanorods of these same dimensions were compared to silica-gold

core-shell nanoparticles as well as gold nanoparticles coated with reduced graphene oxide.[26] Our results indicate that gold-silver-gold core-shell-shell nanoparticles have the largest plasmonic photothermal effects in the NIR for potential advances in photothermal cancer therapy.

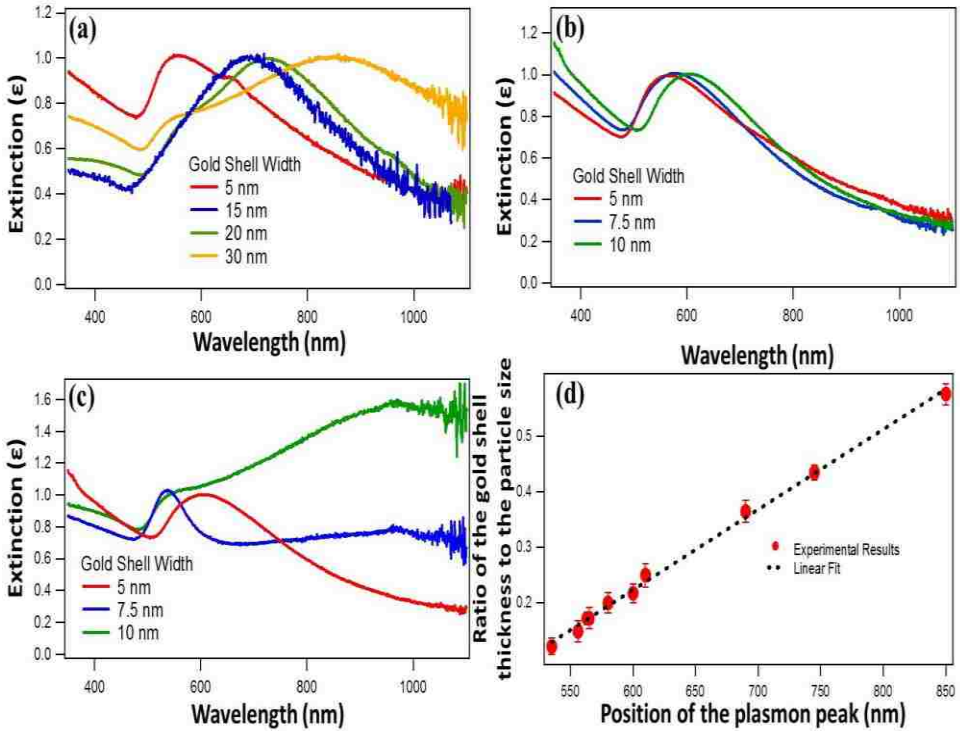

Figure 4.2. Normalized extinction spectra of different samples of the colloidal gold-silver-gold core-shell-shell nanoparticles obtained by varying the thickness of the gold and silver shells. The size of the gold core is 12.0 ± 0.9 nm, and the thickness of the silver shell is (a) 12.0 ± 1.1 nm, (b) 18.0 ± 1.6 nm, and (c) 24.0 ± 2.1 nm, respectively. (d) The position of the plasmon extinction peak wavelength varies linearly with the ratio of the gold shell thickness to the overall particle size.

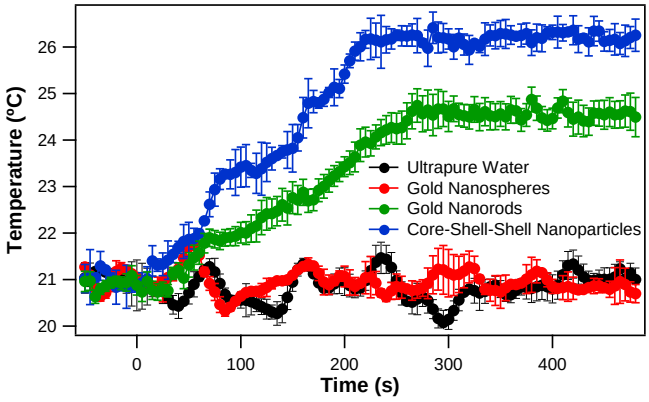

Figure 4.3. Temperature change over time upon irradiation with 1.7 W of 800 nm laser light of (black dots) water, (red dots) 54 nm colloidal gold nanospheres, (green dots) colloidal gold nanorods, and (blue dots) 12-12-30 nm colloidal gold-silver-gold core-shell-shell nanoparticles. The laser beam is unblocked at time 0 s.

Femtosecond transient absorption is used to investigate the excited-state dynamics of gold-silver-gold core-shell-shell nanoparticles for comparison to gold nanosheres and gold nanorods. The excited-state dynamics and spectral features of the transient absorption measurements of gold nanoparticles have been extensively studied.[38, 39] Figure 4.4 displays the transient absorption spectra and time profiles of 54 nm colloidal gold nanospheres at different time delays using 400 nm, 5 μJ pump pulses.

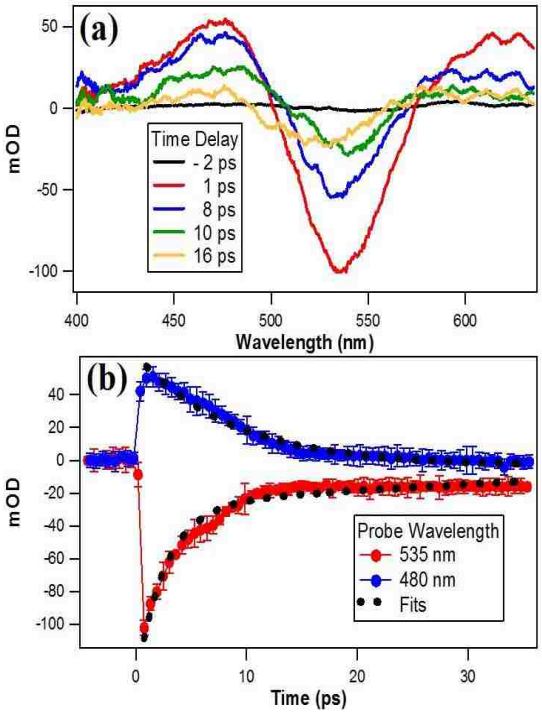

Figure 4.4. (a) Transient absorption spectra of 54 nm colloidal gold nanospheres at different time delays using excitation with a 400 nm pump pulse. (b) Transient absorption time profiles of 54 nm colloidal gold nanospheres at 480 nm and 535 nm probe wavelengths with corresponding fits.

A positive band centered at 480 nm arises from an electronic interband transition. A negative band centered at 535 nm is attributed to the depletion of the plasmon electrons. Another positive band after 578 nm is due to the absorption of thermally excited plasmon electrons. These electrons are excited by lattice vibrations and can relax back to the ground-state through electron-electron scattering, electron-phonon scattering, and phonon-phonon scattering. Representative transient absorption time profiles measured at 480 nm and 535 nm are shown in Figure 4.4 (b). The time-dependent transient absorption profiles are analyzed over the wavelength range of 410 nm to 550 nm using a global analysis technique shown in Appendix 3. Three lifetimes are required to adequately describe the relaxation dynamics of the

gold nanosphere sample. The time profile at 480 nm is characterized by a single exponential function with a lifetime of 8.0 ± 0.6 ps. The time profile corresponding to the plasmon depletion band centered at 535 nm is characterized by two exponential functions with lifetimes of 2.6 ± 0.3 ps and 94.0 ± 7.3 ps attributed to electron-phonon scattering and phonon-phonon scattering respectively.

The excited-state dynamics of gold nanorods show similar excited-state relaxation dynamics. Figure 4.5 a-b display the transient absorption spectra of the colloidal gold nanorods at different pump-probe time delays using 400 nm and 800 nm, 5 μJ pump pulses, respectively. Two negative bands near 530 nm and 750 nm are attributed to the depletion of the transverse and longitudinal plasmon modes, respectively. A positive transient absorption band centered near 625 nm is caused by thermally-excited plasmonic electrons.[40, 41] Representative transient absorption time profiles at 750 nm using 400 nm and 800 nm pump pulse excitation wavelengths are shown in Figure 4.5 (c). The longitudinal and transverse bands have similar excited-state relaxation lifetimes, in concurrence with the same electron-phonon and phonon-phonon relaxation pathways of the two orthogonal oscillations.[40] The time-dependent transient absorption profiles are analyzed over the wavelength range of 490 nm to 770 nm using a global analysis technique shown in Appendix 3. Three lifetimes are required to adequately describe the relaxation dynamics of the gold nanorod sample. The electron-phonon and phonon-phonon scattering lifetimes obtained from global analysis using 400 nm pump pulses are 2.8 ± 0.3 ps, and 102 ± 7 ps The electron-phonon and phonon-phonon scattering lifetimes obtained from global analysis using 800 nm excitation pulses are 3.2 ± 0.4 ps and 104 ± 12 ps. An important observation is that the plasmon depletion dynamics corresponding to the electron-phonon and phonon-phonon scattering lifetimes for the gold nanorod sample is shown to be the same when exciting with either 400 nm or 800 nm, to within experimental uncertainty.

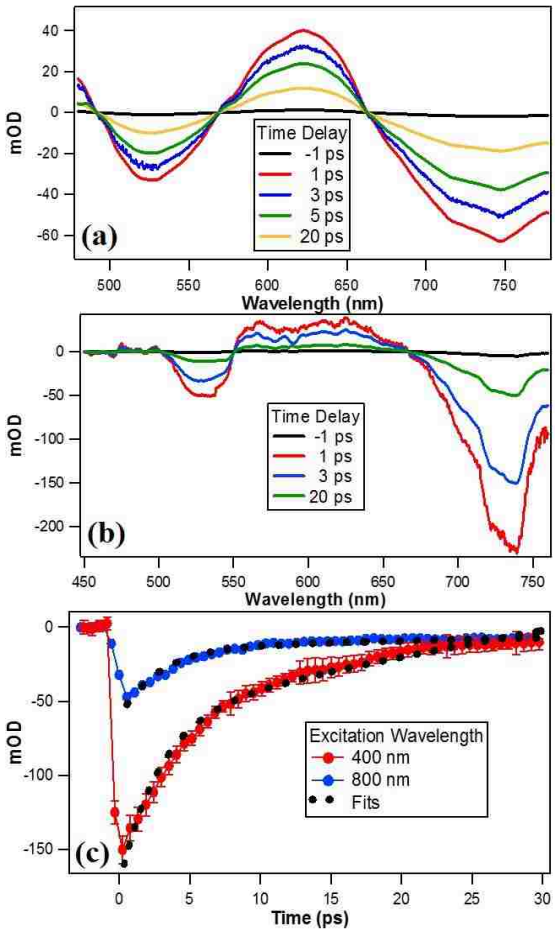

Figure 4.5. Transient absorption spectra of colloidal gold nanorods at different time delays using (a) 400 nm and (b) 800 nm excitation pulses. (c) Transient absorption time profiles of colloidal gold nanorods at a probe wavelength of 750 nm using 400 nm and 800 nm pump pulse excitation wavelengths with corresponding fits.

Pump-probe transient absorption spectroscopy is used to investigate the enhanced photothermal effect of the colloidal gold-silver-gold core-shell-shell nanoparticles. Figure 4.6 shows the transient absorption spectra of 12-12-30 nm colloidal gold-silver-gold core-shell-shell nanoparticles with a 12 nm core, a 12 nm silver shell, and a 30 nm outer gold shell at different time delays using (a) 400 nm and (b) 800 nm, 5 μJ pump pulses. A positive band centered at 470 nm is observed using 400 nm excitation pulses and is attributed to the electronic interband transition. A broad plasmon depletion band is observed for wavelengths greater than 500 nm, extending to the NIR, using 400 nm and 800 nm pump pulse excitation wavelengths. The transient absorption time profiles measured at 750 nm using 400 nm and 800 nm excitation pulses are shown in Figure 4.6 (c). The time-dependent transient absorption profiles are

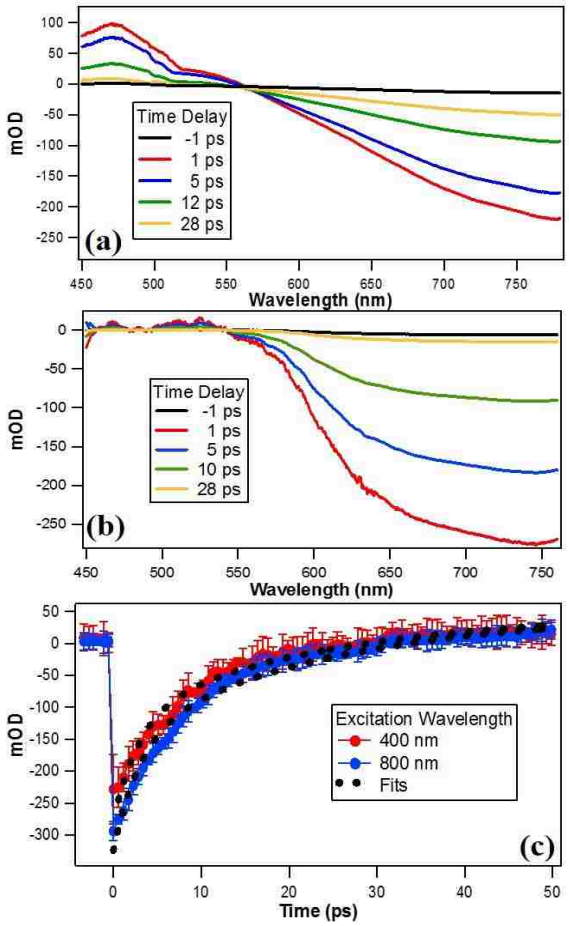

Figure 4.6. Transient absorption spectra of 12-12-30 nm colloidal gold-silver-gold core-shell-shell nanoparticles at different time delays using (a) 400 nm and (b) 800 nm pump pulse excitation wavelengths. (c) Transient absorption time profiles of these nanoparticles measured at 750 nm using 400 nm and 800 nm pump pulse excitation wavelengths with corresponding fits.

analyzed over the wavelength range of 450 nm to 770 nm using a global analysis technique shown in the Appendix 3. Three lifetimes are required to adequately describe the relaxation dynamics of the core-shell-shell nanoparticle sample. The electronic interband transition observed after 400 nm pump pulses is characterized by a lifetimes of 5.0 ± 0.3 ps. The plasmon depletion band is described by the two lifetimes of 3.0 ± 0.2 ps and 23.5 ± 0.6 ps using 400 nm excitation pulses and 2.8 ± 0.2 ps and 23.9 ± 0.5 ps using 800 nm excitation pulses. These two lifetimes are attributed to electron-phonon scattering and phonon-phonon scattering, respectively. Again, we observe that the electron-phonon and phonon-phonon scattering lifetimes are the same using either 400 nm or 800 nm excitation pulses, to within experimental uncertainty. However, the decay lifetimes of the plasmon band are dependent on the fluences of the

excitation pulses.[39,42,43] The power-dependent study of the three samples under study is shown in the Appendix 3. The lifetime associated with the electron-phonon scattering is identical within the standard deviation for the gold nanoparticles, gold nanorods, and gold-silver-gold core-shell-shell nanoparticles under study. Electron-phonon scattering and phonon-phonon scattering in the umklapp processes are known to limit the thermal conductivity of materials.[44-47] Importantly, the lifetimes of the phonon-phonon scattering is remarkably faster in the case of the core-shell-shell nanoparticles, which is a contributing factor that leads to more efficient energy relaxation for the photothermal effect.

This reported synthesis technique also allows for the continuation of alternating gold/silver shells for advanced plasmonic engineering. Figure 4.7 shows the normalized extinction spectra of 12 nm colloidal gold nanoparticles, 30 nm colloidal gold-silver core-shell nanoparticles, 35 nm colloidal gold-silver-gold core-shell-shell nanoparticles, 47 nm colloidal gold-silver-gold-silver core-shell-shell-shell nanoparticles, and 53 nm colloidal gold-silver-gold-silver-gold core-shell-shell-shell-shell nanoparticles, respectively. Each successive sample uses the previous sample as its corresponding core, for direct comparison. Here, the plasmon extinction peak wavelength closely correlates with the composition of the outer shell of the nanoparticle. For example, when the outer shell composition is gold, the plasmon extinction peak wavelength ranges from about 550 to 600 nm. Similarly, when the outer shell is silver, the plasmon extinction peak wavelength ranges from about 400 to 450 nm. In addition, every sequential shell of alternating gold or silver composition broadens the plasmon extinction peak while redshifting it further to the NIR wavelengths. It is also important to point out that the extinction peak wavelength of the extended gold-silver-gold-silver-gold nanoparticles with multiple alternating gold and silver shells does not follow the linear trend reported in Figure 4.2 (d). Therefore, these extended core-shell architectures with controllable core and shell dimensions of alternating gold and silver compositions provide additional spectral tunability for advanced plasmonic nanoparticle engineering. Several approaches were used for the synthesis of non-plasmonic core-multiple nanocrystals. [48,49] However, to our knowledge, this is the first report of extended core–shell architectures with controllable core and shell dimensions of alternating gold/silver shells. This synthesis strategy allows for the control of the optical properties of the plasmonic

nanoparticles with extinction peaks extending from the near ultraviolet to the infrared for various potential applications.

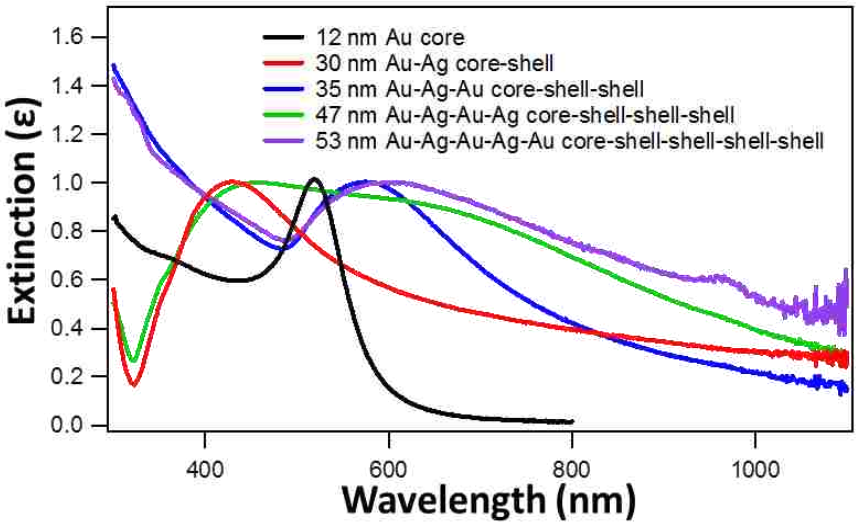

Figure 4.7. Normalized extinction spectra of 12 nm colloidal gold nanoparticles (black line), 30 nm colloidal gold-silver core-shell nanoparticles (red line), 35 nm colloidal gold-silver-gold core-shell-shell nanoparticles (blue line), 47 nm colloidal gold-silver-gold-silver core-shell-shell-shell nanoparticles (green line), and 53 nm colloidal gold-silver-gold-silver-gold core-shell-shell-shell-shell nanoparticles (purple line).

4.4 Conclusion

In summary, the development of a new synthesis technique for colloidal gold-silver-gold core-shell-shell nanoparticles is reported. These nanoparticles exhibit plasmon enhancement and controllable NIR absorption that are very advantageous for biologically-relevant applications such as photothermal cancer therapy and biosensing. The plasmon extinction peak wavelength of the gold-silver-gold core-shell-shell nanoparticles depends linearly on the ratio of the thickness of the outer gold shell to the overall size of the nanoparticle. A photothermal study shows a significant temperature increase of colloidal 12-12-30 nm gold-silver-gold core-shell-shell nanoparticle sample upon irradiation with NIR laser light, demonstrating a larger photothermal effect compared to gold nanorods and gold nanospheres. Transient absorption measurements show that the phonon-phonon scattering lifetime for colloidal gold-silver-gold core-shell-shell nanoparticles is much faster than the corresponding lifetimes for gold nanospheres and nanorods, which contributes to the higher photothermal efficiencies of the core-shell-shell nanoparticles.

4.5 References

(1) El-Sayed, I.; Huang, X.; El-Sayed, M. Surface Plasmon Resonance Scattering and Absorption of Anti-EGFR Antibody Conjugated Gold Nanoparticles in Cancer Diagnostics: Applications in Oral Cancer. *Nano Lett.* **2005**, *5*, 829−834.

(2) El-Sayed, I.; Huang, X.; El-Sayed, M. Selective Laser Photothermal Therapy of Epithelial Carcinoma Using Anti-EGFR Antibody Conjugated Gold Nanoparticles. *Cancer Lett.* **2006**, *239*, 129−135.

(3) Kamat, P. V. Photophysical, Photochemical and Photocatalytic Aspects of Metal Nanoparticles. *J. Phys. Chem. B* **2002**, *106*, 7729−7744.

(4) Narayanan, R.; El-Sayed, M. A. Catalysis with Transition Metal Nanoparticles in Colloidal Solution: Nanoparticle Shape Dependence and Stability. *J. Phys. Chem. B* **2005**, *109*, 12663−12676.

(5) Haes, A. J.; Van Duyne, R. P. A Nanoscale Optical Biosensor: Sensitivity and Selectivity of an Approach Based on the Localized Surface Plasmon Resonance Spectroscopy of Triangular Silver Nanoparticles. *J. Am. Chem. Soc.* **2002**, *124*, 10596−10604.

(6) Sperling, R. A.; Gil, P. R.; Zhang, F.; Zanella, M.; Parak, W. J. Biological Applications of Gold Nanoparticles. *Chem. Soc. Rev.* **2008**, *37*, 1896−1908.

(7) Freddi, S.; D'Alfonso, L.; Collini, M.; Caccia, M.; Sironi, L.; Tallarida, G.; Caprioli, S.; Chirico, G. Excited-State Lifetime Assay for Protein Detection on Gold Colloids− Fluorophore Complexes. *J. Phys. Chem. C* **2009**, *113*, 2722−2730.

(8) Prigodich, A. E.; Lee, O.-S.; Daniel, W. L.; Seferos, D. S.; Schatz, G. C.; Mirkin, C. A. Tailoring DNA Structure to Increase Target Hybridization Kinetics on Surfaces. *J. Am. Chem. Soc.* **2010**, *132*, 10638−10641.

(9) Kamat, P. V. Meeting the Clean Energy Demand: Nanostructure Architectures for Solar Energy Conversion. *J. Phys. Chem. C* **2007**, *111*, 2834−2860.

(10) Bardhan, R.; Grady, N. K.; Cole, J. R.; Joshi, A.; Halas, N. J. Fluorescence Enhancement by Au Nanostructures: Nanoshells and Nanorods. *ACS Nano* **2009**, *3*, 744–752.

(11) Link, S.; El-Sayed, M. Shape and Size Dependence of Radiative, Non-radiative and Photothermal Properties of Gold Nanocrystals. *Int. Rev. Phys. Chem.* **2000**, *19*, 409−453.

(12) Daniel, M.-C.; Astruc, D. Gold Nanoparticles: Assembly, Supramolecular Chemistry, Quantum-Size-Related Properties, and Applications toward Biology, Catalysis, and Nanotechnology. *Chem. Rev.* **2004**, *104*, 293−346.

(13) Chandra, M.; Dowgiallo, A. M.; Knappenberger, K. L. Controlled Plasmon Resonance Properties of Hollow Gold Nanosphere Aggregates. *J. Am. Chem. Soc.* **2010**, *132*, 15782−15789.

(14) Eck, W.; Craig, G.; Sigdel, A.; Ritter, G.; Old, L. J.; Tang, L.; Brennan, M. F.; Allen, P. J.; Mason, M. D. Conjugated to Monoclonal F19 Antibodies as Targeted Labeling Agents for Human Pancreatic Carcinoma Tissue. *ACS Nano* **2008**, *2*, 2263–2272.

(15) Maxwell, D. J.; Taylor, J. R.; Nie, S. Self-Assembled Nanoparticle Probes for Recognition and Detection of Biomolecules. *J. Am. Chem. Soc.* **2002**, *124*, 9606–9612.

(16) Brown, S. D.; Nativo, P.; Smith, J. –A.; Stirling, D.; Edwards, P. R.; Venugopal, B.; Flint, D. J.; Plumb, J. A.; Graham, D.; Wheate, N. J. Gold Nanoparticles for the Improved Anticancer Drug Delivery of the Active Component of Oxaliplatin. *J. Am. Chem. Soc.* **2010**, *132*, 4678–4684.

(17) Song, J., Zhou, J., Duan, H. Self-Assembled Plasmonic Vesicles of SERS-Encoded Amphiphilic Gold Nanoparticles for Cancer Cell Targeting and Traceable Intracellular Drug Delivery. *J. Am. Chem. Soc.* **2012**, *134*, 13458–13469.

(18) Huang, X.; El-Sayed, I. H.; Qian, W.; El-Sayed, M. A. Cancer Cell Imaging and Photothermal Therapy in the Near-Infrared Region by Using Gold Nanorods. *J. Am. Chem. Soc.* **2006**, *128*, 2115–2120.

(19) Qian, X.; Peng, X.-H.; Ansari, D. O.; Yin-Goen, Q.; Chen, G. Z.; Shin, D. M.; Yang, L.; Young, A. N.; Wang, M. D.; Nie, S. In Vivo Tumor Targeting and Spectroscopic Detection with Surface-Enhanced Raman Nanoparticle Tags. *Nat. Biotechnol.* **2008**, *26*, 83–90.

(20) Bardhan, R.; Lal, S.; Joahi, A.; Halas, N. J. Theranostic Nanoshells: From Probe Design to Imaging and Treatment of Cancer. *Acc. Chem. Res.* **2011**, *44*, 936–946.

(21) Cole, J. R.; Mirin, N. A.; Knight, M. W.; Goodrich, G. P.; Halas, N. J. Photothermal Efficiencies of Nanoshells and Nanorods for Clinical Therapeutic Applications. *J. Phys. Chem. C* **2009**, *113*, 12090–12094.

(22) Huang, X.; El-Sayed, I. H.; Qian, W.; El-Sayed, M. A. Cancer Cell Imaging and Photothermal Therapy in the Near-Infrared Region by Using Gold Nanorods. *J. Am. Chem. Soc.* **2006**, *128*, 2115–2120.

(23) Skrabalak, S. E.; Chem, J.; Au, L.; Lu, X.; Li, X.; Xia, Y. N. Gold Nanocages for Biomedical Applications. *Adv. Mater.* **2007**, *19*, 3177–3184.

(24) Schwartzberg, A. M.; Olson, T. Y.; Talley, C. E.; Zhang, J. Z. Synthesis, Characterization, and Tunable Optical Properties of Hollow Gold Nanospheres. *J. Phys. Chem. B*, **2006**, *110*, 19935–19944.

(25) Melancon, M. P.; Lu, W.; Yang, Z.; Zhang, R.; Cheng, Z.; Elliot, A. M.; Stafford, J.; Olson, T.; Zhang, J. Z.; Li, C. In Vitro and in Vivo Targeting of Hollow Gold Nanoshells Directed at Epidermal Growth Factor Receptor for Photothermal Ablation Therapy. *Mol. Caner Ther.* **2008**, *7*, 1730-1739.

(26) Lim, D. –K.; Barhoumi, A.; Wylie, R. G.; Reznor, G.; Langer, R. S.; Kohane, D. S. Enhanced Photothermal Effect of Plasmonic Nanoparticles Coated with Reduced Graphene Oxide. *Nano Lett.* **2013**, *13*, 4075–4079.

(27) Bardhan, R.; Grady, N. K.; Cole, J. R.; Joshi, A.; Halas, N. J. Fluorescence Enhancement by Au Nanostructures: Nanoshells and Nanorods. *ACS Nano* **2009**, *3*, 744−752.

(28) Nguyen, S. C.; Zhang, Q.; Manthiram, K.; Ye, X.; Lomont, J. P.; Harris, C. B.; Weller, H.; Alivisatos, A. P. Study of Heat Transfer Dynamics from Gold Nanorods to the Environment via Time-Resolved Infrared Spectroscopy. *ACS Nano*, **2016**, *10*, 2144–2151.

(29) Ayala-Orozco, C.; Urban, C.; Knight, M. W.; Urban, A. S.; Neumann, O.; Bishnoi, S. W.; Mukherjee, S.; Goodman, A. M.; Charron, H.; Mitchell, T.; et al. Au Nanomatryoshkas as Efficient Transducers for Cancer Treatment: Benchmarking against Nanoshells. *ACS Nano* **2014**, *8*, 6372−6381.

(30) Ye, X.; Shi, H.; He, X.; Wang, K.; Lia, D.; Qiua, P. Gold Nanorod-Seeded Synthesis of Au@Ag/Au Nanospheres with Broad and Intense Near-Infrared Absorption for Photothermal Cancer Therapy. *J. Mater. Chem. B*, **2014**, *2*, 3667-3673.

(31) Zhang, J.; Tang, Y.; Weng, L.; Ouyang, M. Versatile Strategy for Precisely Tailored Core@Shell Nanostructures with Single Shell Layer Accuracy: The Case of Metallic Shell. *Nano Lett.* **2009**, *9*, 4061–4065.

(32) Zhang, J.; Tang, Y.; Lee, K.; Ouyang, M. Nonepitaxial Growth of Hybrid Core-Shell Nanostructures with Large Lattice Mismatches. Science 2010, 327, 1634–1638.

(33) Knauer, A.; Thetea, A.; Li, S.; Romanus, H.; Csáki, A.; Fritzsche, W.; Köhler, J. M. Au/Ag/Au Double Shell Nanoparticles With Narrow Size Distribution Obtained by Continuous Micro Segmented Flow Synthesis. *Chem. Eng. J.* **2011**, *166*, 1164–1169.

(34) Samal, A. K., Polavarapu, L., Rodal-Cedeira, S., Liz-Marzán, L. M., Pérez-Juste, J., Pastoriza-Santos, I. Size Tunable Au@Ag Core−Shell Nanoparticles: Synthesis and Surface-Enhanced Raman Scattering Properties. *Langmuir* **2013**, *29*, 15076−15082.

(35) Brown, K. R.; Walter, D. G.; Natan, M. J. Seeding of Colloidal Au Nanoparticle Solutions. 2. Improved Control of Particle Size and Shape. *Chem. Mater.* **2000**, *12*, 306−313.

(36) Perrault, S.; Chan, W. Synthesis and Surface Modification of Highly Monodispersed, Spherical Gold Nanoparticles of 50−200 nm. *J. Am. Chem. Soc.* **2009**, *131*, 17042−17043.

(37) Karam, T. E.; Siraj, N.; Warner, I. M.; Haber L. H. Anomalous Size-Dependent Excited-State Relaxation Dynamics of NanoGUMBOS. *J. Phys. Chem. C*, **2015**, *119*, 28206–28213.

(38) Jana, N. R.; Gearheart, L.; Murphy, C. J. Evidence for Seed-Mediated Nucleation in the hemical Reduction of Gold Salts to Gold Nanoparticles. *Chem. Mater.* **2001**, *13*, 2313−2322.

(39) Karam, T. E.; Haber, L. H.; Molecular Adsorption and Resonance Coupling at the Colloidal Gold Nanoparticle Interface. *J. Phys. Chem. C* **2014**, *118*, 642−649.

(40) Ahmadi, T.; Logunov, S. L.; El-Sayed, M. A. Picosecond Dynamics of Colloidal Gold Nanoparticles. *J. Phys. Chem.* **1996**, *100*, 8053.

(41) Logunov, S. L.; Ahmadi, T. S.; El-Sayed, M. A.; Khoury, J. T.; Whetten, R. L. Electron Dynamics of Passivated Gold Nanocrystals Probed by Subpicosecond Transient Absorption Spectroscopy. *J. Phys. Chem. B.* **1997**, *101*, 3713-3719.

(42) Link, S.; Burda, C.; Mohamed, M. B.; Nikoobakht, B.; El-Sayed, M. A. Femtosecond Transient-Absorption Dynamics of Colloidal Gold Nanorods: Shape Independence of the Electron-Phonon Relaxation Time. *Phys. Rev. B* **2000**, *61*, 6086–6090.

(43) Dai, H. –W.; Yu, Y.; Wang, X.; Ma, Z. –W.; Chen, C.; Zhou, Z. K.; Han, J. B.; Han, Y. –B.; Liu, S. –D.; Li, L. Study of Surface Plasmon Induced Hot Electron Relaxation Process and Third-Order Optical Nonlinearity in Gold Nanostructures. *J. Phys. Chem. C* **2015**, *119*, 27156−27161.

(44) Yu, K.; Polavarapu, L.; Xu, Q. –H. Excitation Wavelength and Fluence Dependent Femtosecond Transient Absorption Studies on Electron Dynamics of Gold Nanorods. *J. Phys. Chem. A* **2011**, *115*, 3820–3826.

(45) Hodak, J. K.; Martini, I.; Hartland, G. V. Spectroscopy and Dynamics of Nanometer-Sized Noble Metal Particles. *J. Phys. Chem. B* **1998**, *102*, 6958–6967.

(46) Callaway, J. Model for Lattice Thermal Conductivity at Low Temperatures. *Phys. Rev.* **1959**, *113*, 1046–1051.

(47) Kim, W.; Singer, S. L.; Majumdar, A.; Zide, J. M. O.; Klenov, D.; Gossard, A. C.;Stemmer, S. Reducing Thermal Conductivity of Crystalline Solids at High Temperature Using Embedded Nanostructures. *Nano Lett.* **2008**, *8*, 2097-2099.

(48) Lauhon, L. J.; Gudiksen, M. S.; Wang, D.; Lieber, C. M. Epitaxial Core–Shell and Core–Multishell Nanowire Heterostructures. *Nature* **2002**, *420*, 57–61.

(49) Talapin, D. V.; Mekis, I.; Götzinger, I.; Kornowski, A.; Benson, O.; Weller, H. CdSe/CdS/ZnS and CdSe/ZnSe/ZnS Core-Shell-Shell Nanocrystals. *J. Phys. Chem. B* **2004**, *108*, 18826-18831.

CHAPTER 5 – ENHANCED PLASMON-EXCITON RESONANCE AND FLUORESCENCE AT THE SURFACE OF COLLOIDAL GOLD-SILVER-GOLD CORE-SHELL-SHELL NANOPARTICLES

5.1 Introduction

Plasmonic nanomaterials have been widely studied due to their various applications in molecular sensing, catalysis, nanomedicine, and photovoltaics.[1-10] Particular interest arises from the localized surface plasmon resonances from the coherent oscillations of free electrons[11-13] that can lead to significant optical enhancement of processes such as surface-enhanced Raman scattering (SERS),[14, 15] surface-enhanced fluorescence,[16, 17] second harmonic generation (SHG),[18, 19] and sum frequency generation (SFG).[20–25] Recently, we reported the synthesis, the enhanced photothermal properties, and the excited-state dynamics of plasmonic gold-silver-gold core-shell-shell nanoparticles.[26] The higher photothermal efficiency of these nanoparticles was attributed to faster phonon-phonon scattering lifetimes and lower fluorescence signals.

Second harmonic generation is a powerful tool for the study of colloidal centrosymmetric nanoparticles such as gold and silver.[27] SHG is a second order nonlinear technique where two incident photons of frequency ω add coherently to scatter a photon of frequency 2ω. SHG is typically forbidden in bulk media with a center of inversion, which makes it a surface-specific technique that is ideal for the study of colloidal nanoparticle surfaces.[28] The adsorption isotherms of triphenylmethane dyes at the gold nanoparticle surface have been previously investigated and the free energies of adsorption and the number of adsorbate sites per nanoparticle have been obtained by analyzing the experimental results using a modified Langmuir model.[29, 30] In general, the molecular adsorption properties are shown to be governed by the adsorbate molecular structure, as well as interactions involving electrostatic and hydrophobic/hydrophilic forces at the nanoparticle surface.

The resonance coupling of plasmonic nanoparticles with organic adsorbates can give rise to strong optical interactions that can be measured by extinction spectroscopy.[30, 31] New exciton-plasmon

polariton peaks and Fano-type profiles have been observed due to the resonance coupling of molecules to the plasmon band. These quantum mechanical states are described by a coupled-oscillator Hamiltonian and are separated by Rabi splitting energy $h\omega_c$.[32] Resonance coupling has been observed between organic dye molecules and various plasmonic nanomaterials such as silver nanoparticles on a substrate,[33] noble metal nanovoids,[34] gold nanorods in colloidal suspension, [31] and colloidal gold nanoparticles.[30] Additionally, fluorescence quenching or enhancement of organic molecules due to the weak coupling to plasmonic nanoparticles were also reported.[35-37] showing that the fluorescence intensity of the dye-nanoparticle complex depends on its spectral overlap with the plasmonic band.[37]

In this chapter, the adsorption isotherms of three triphenylmethane dyes malachite green, brilliant green, and methyl green, as well as rhodamine 110, are measured using SHG at the surface of 65-11-9 nm colloidal gold-silver-gold core-shell-shell nanoparticles in water. A modified Langmuir model is used to fit the adsorption isotherms in order to obtain the free energies of adsorption as well as the number of adsorbate sites per nanoparticle. Enhanced resonance coupling between the dye molecules and the core-shell-shell nanoparticles is reported and can be described by the formation of new exciton-plasmon polariton states and Fano-type profiles. The fluorescence of the triphenylmethane dyes is remarkably enhanced at the core-shell-shell nanoparticle surface while that of rhodamine 110 is significantly quenched. Additionally, transient absorption is used to probe the excited-state dynamics of the various dyes adsorbed on the core-shell-shell nanoparticle surface. The excited-state relaxation decays of brilliant green are slightly slower on the colloidal nanoparticle surface then in solution due to molecular confinement and electrostatic hindrance of the torsional dynamics of the molecule at the nanoparticle surface. On the other hand, the excited-state relaxation dynamics of rhodamine 110 at the colloidal core-shell-shell nanoparticle surface are much faster than those measured in solution due to energy transfer from the dye molecule to the core-shell-shell plasmonic band. Additional transient absorption spectra show the excited-state relaxation dynamics of the exciton-plasmon polariton states at the surface of the core-shell-shell nanoparticles.

5.2 Experimental Section

5.2.1 Nanoparticle Synthesis and Characterization

The gold nanoparticle sample is prepared using a two-step seeding growth technique.[38, 39] All chemicals are purchased from Sigma-Aldrich and used without further purification in ultrapure water. The first step of the synthesis involves the preparation of gold seeds by adding 900 μL of 34 mM sodium citrate to 30 mL of 290 μM gold chloride in water under boiling and vigorous stirring conditions. The colloidal solution is removed from heat and cooled down after 15 min or when a deep red color is reached. In a second step, the gold nanoparticles are prepared by adding 100 μL of 29 mM gold chloride and 75 μL of the prepared gold colloidal seeds to 9.7 mL of water. 25 μL of 34 mM sodium citrate and 100 μL of 0.03 M hydroquinone are added to the mixture, which is then maintained under vigorous stirring at room temperature for 60 min. Colloidal gold-silver core-shell nanoparticles are prepared by the consecutive additions of 60 μL of 100 mM ascorbic acid, 30 μL of 100 mM $AgNO_3$, and 80 μL of 100 mM of NaOH to 10 mL of the prepared colloidal gold sample. The final mixture is left stirring at room temperature for 30 min. The colloidal gold-silver core-shell sample is centrifuged and washed twice, then redispersed in 10 mL ultrapure water. The core-shell-shell nanoparticles are prepared by adding 100 μL of 29 mM gold chloride and 22 μL of 34 mM sodium citrate to the colloidal gold-silver core-shell sample. The mixture is then vortexed for 5 min, followed by the dropwise addition of 100 μL of 0.03 M hydroquinone. The colloidal gold-silver-gold core-shell-shell nanoparticles are left under vigorous stirring at room temperature for 60 min. Finally, the colloidal core-shell-shell sample is centrifuged and washed twice then redispersed in a mixture of 10 mL water and 20 μL of 34 mM sodium citrate. Transmission electron microscopy (TEM), extinction spectroscopy, and inductively coupled plasma optical emission spectroscopy (ICP-OES) are used to characterize the nanoparticle samples. The average size distribution is determined using more than 100 nanoparticles for each sample. TEM images and extinction spectra of the gold core and the gold-silver core-shell nanoparticles are shown in Appendix 4. The measured nanoparticle sizes are 65 ± 4 nm, 88 ± 6 nm, and 103 ± 7 nm for the gold nanoparticles, gold-silver core-shell nanoparticles, and gold-silver-gold core-shell-shell nanoparticles, respectively. The core−shell−shell

nanoparticle bulk concentration determined with ICP-OES using both gold and silver atomic emission measurements is 9.6×10^9 nanoparticles/mL. The relative gold to silver concentration is in agreement with the TEM results. Figure 5.1 (a) shows a representative TEM image of 105 ± 7 nm gold-silver-gold core-shell-shell nanoparticles composed of a 62 nm gold core, 8 nm silver shell, and 4 nm gold outer shell. Figure 5.1 (b) shows the extinction spectra of colloidal 106 nm gold-silver-gold core-shell-shell. The experimental spectrum is fit using Mie theory.

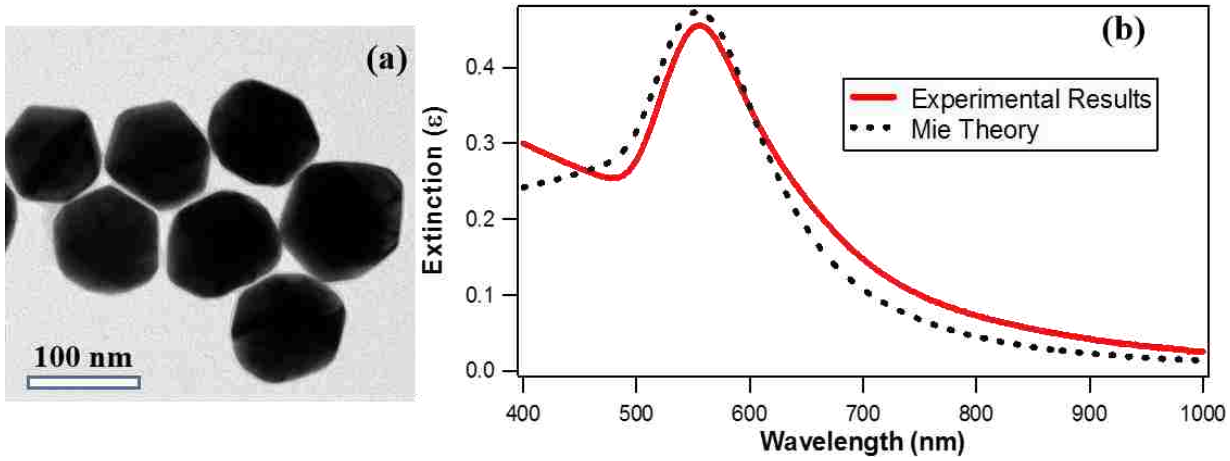

Figure 5.1. (a) TEM image and (b) extinction spectrum of 105 ± 7 nm gold-silver-gold core-shell-shell nanoparticles. The experimental spectrum are fit using Mie theory.

5.2.2 Second Harmonic Generation

The second harmonic generation optical setup has been previously reported elsewhere.[30, 29, 41] Briefly, a titanium:sapphire oscillator produces 70 fs pulses centered at 800 nm with a repetition rate of 80 MHz and an average power of 3.0 W. The generated laser pulses pass through an optical filter to remove any SHG residual light prior to the sample. A 20 mm focal length lens is used to focus the incident beam into a 1 cm quartz cuvette containing the colloidal nanoparticle sample. The generated SHG signal is collected in the forward direction and refocused to a monochromator connected to a high-sensitivity spectroscopy charge coupled device detector (CCD). An additional filter is placed before the CCD to remove any fundamental laser light while transmitting the SHG signal generated from the sample. A computer-controlled burette is used for the addition of the different dye solutions and the sample is

automatically stirred after each addition. Each spectrum and background is acquired 50 times for statistical analysis for each concentration measured for each sample.

5.2.3 Transient Absorption Setup

The transient absorption optical setup has been previously reported.[26,42] An amplified titanium:sapphire laser system generates 0.7 mJ, 70 fs pulses centered at 800 nm with a repetition rate of 10 KHz. The fundamental beam is split using a beam splitter into two separated pump and probe pulses. The pump pulses are passed through an optical parametric amplifier (OPA) to selectively generate the excitation wavelength, which are then reflected through a retroreflector on a computer-controlled delay stage. The probe beam passes through a β-barium borate crystal to generate 400 nm pulses through frequency doubling. The 400 nm and the residual 800 nm pulses are then focused into a 1 cm fused quartz flow cell containing water to generate a stable femtosecond white light probe pulses. The pump beam is focused to a spatial overlap with the probe beam at a 3 mm fused quartz cell containing the sample under constant stirring.

5.3 Results and Discussion

SHG is used to investigate the adsorption properties of malachite green, brilliant green, methyl green, and rhodamine 110 at the surface of 105 ± 7 nm colloidal gold-silver-gold core-shell-shell nanoparticles. Figure 5.2, a-c show representative SHG spectra of the core-shell-shell nanoparticles at 1.6×10^9 nanoparticles/mL in water at various added malachite green, brilliant green, and methyl green concentrations. The lower wavelength peak centered at 400 nm is assigned to SHG while the rise at higher wavelength is attributed to two-photon fluorescence.[43, 44] The position of the SHG peak remains constant within experimental uncertainties for all added dye concentrations. The SHG intensities are shown to increase with the added dye concentration reaching maxima as the adsorbates at the core-shell-shell nanoparticle interface reach their saturation values. Figure 5.2 (d) shows representative SHG spectra of the core-shell-shell nanoparticles at 1.6×10^9 nanoparticles/mL in water at various added rhodamine 110 concentrations. The fluorescence contribution to the measured spectra is significant in this case.

Thus, these spectra are fit with a sum of a Gaussian and a third order polynomial functions to deconvolute the SHG and the two-photon fluorescence signal, respectively. The SHG peaks are centered at 399.8 ± 0.1 nm and full width at half-maxima of 4.5 ± 0.2 nm. The peak centers and widths stay constant to within experimental uncertainty for all added dye concentrations. As shown in Figure 5.2 (d) using solid black lines, the corresponding fits all accurately describe the measured spectra. Similarly to the triphenylmethane dyes, the SHG intensities are shown to increase with the added dye concentration reaching maxima as the adsorbates at the core-shell-shell nanoparticle interface reach their saturation values.

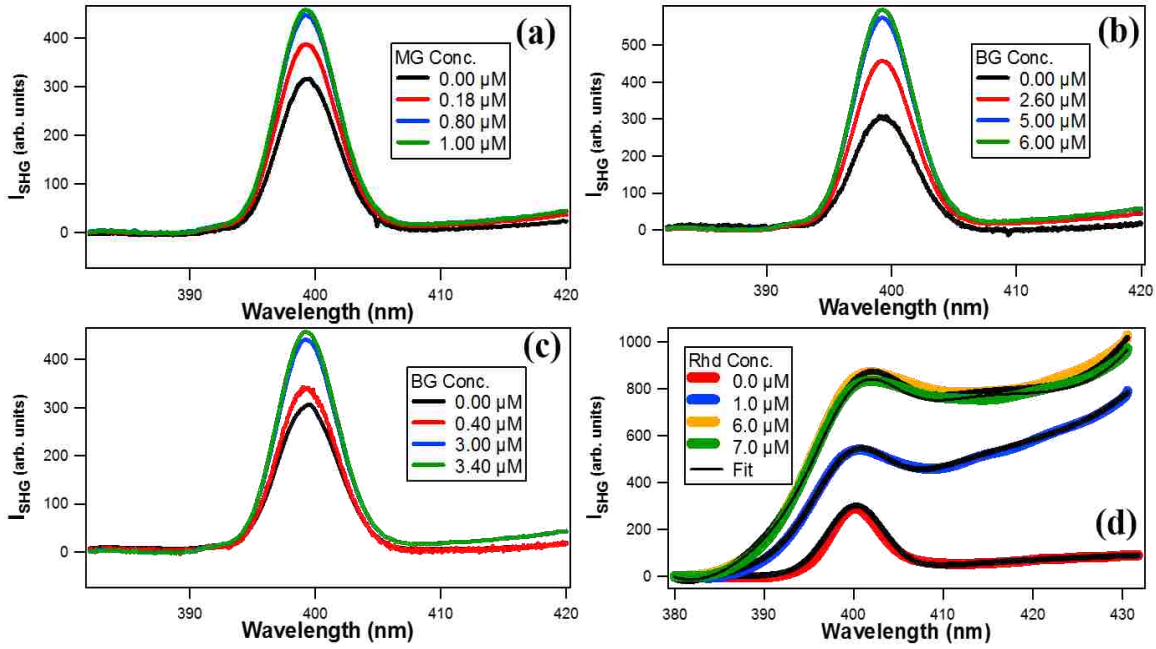

Figure 5.2. SHG spectra of the colloidal 106 ± 7 nm gold-silver-gold core-shell-shell nanoparticles at different (a) malachite green, (b) brilliant green, (c) methyl green, and (d) rhodamine 110 concentrations.

The adsorption isotherms obtained from the SHG spectra from the addition malachite green, brilliant green, methyl green, and rhodamine 110 to colloidal gold-silver-gold core-shell-shell nanoparticles are shown in Figure 5.3. The experimental data are corrected by subtracting the added hyper-Rayleigh scattering arising from the free dye molecules in solution.[30] Additional information on the correction method is described in Appendix 4. The concentration-dependent hyper-Rayleigh scattering

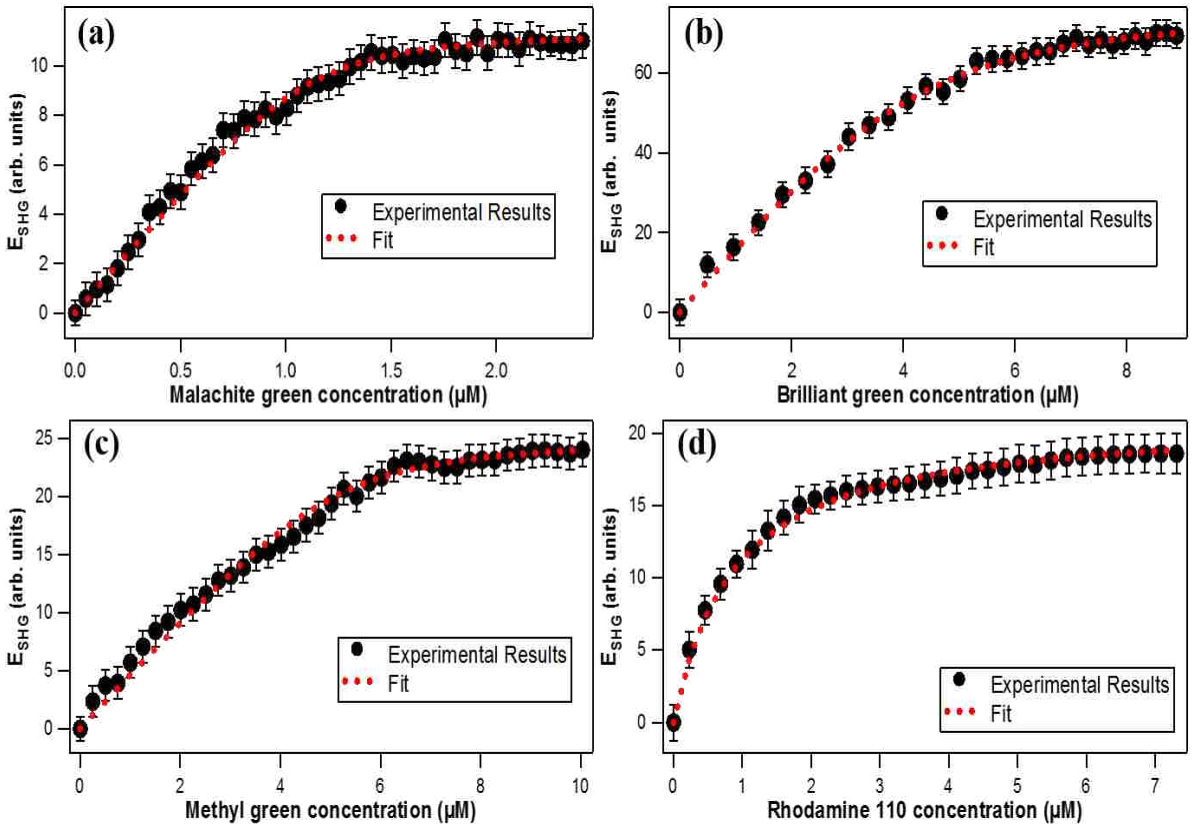

Figure 5.3. Adsorption isotherm results (black dots) obtained from second harmonic generation measurements as a function of (a) malachite green, (b) brilliant green, (c) methyl green, and (d) rhodamine 110 concentrations to the surface of colloidal 106 ± 7 nm gold nanoparticles at a concentration of 1.6×10^9 nanoparticles/mL. The experimental data are compared with the best fits from the modified Langmuir model (dotted red lines).

signal of the four dye solutions is shown in Appendix 4, where the hyper-Rayleigh scattering signal is proportional to the free dye concentration in water. The corrected experimental data are compared to the modified Langmuir model[29, 45] given by

$$\frac{N}{N_{max}} = \frac{\left(C + N_{max} + \frac{55.5}{K}\right) - \sqrt{(C + N_{max} + \frac{55.5}{K})^2 - 4CN_{max}}}{2N_{max}} \quad (1)$$

where N is the adsorbate population on the nanoparticle surface, N_{max} is the maximum number of adsorbate sites on the nanoparticle surface multiplied by the concentration of nanoparticles in the solution, C is the adsorbate bulk concentration added, and K is the adsorption equilibrium constant. The free energy of adsorption is calculated using the equation $\Delta G^o = -RT \ln K$, where R is the ideal gas constant and T is temperature. The free energies of adsorption obtained from the best fit of the adsorption

isotherms are -13.9 ± 0.1 kcal/mol, -13.0 ± 0.2 kcal/mol, -13.6 ± 0.1 kcal/mol, -10.7 ± 0.3 kcal/mol for malachite green, brilliant green, methyl green, and rhodamine 110 adsorbed on the surface of core-shell-shell nanoparticles, respectively. The corresponding number of adsorption sites per particle for the four different molecules is determined to be $(5.46 \pm 0.01) \times 10^4$, $(1.39 \pm 0.02) \times 10^4$, $(4.87 \pm 0.01) \times 10^4$, $(1.12 \pm 0.01) \times 10^4$ sites per particle, respectively. The adsorption site areas are $148 \pm 6\ A^2$, $96 \pm 9\ A^2$, $118 \pm 6\ A^2$, $63 \pm 9\ A^2$. These values are dependent on the adsorbate interactions with the nanoparticle surface as well as adsorbate−adsorbate repulsions.[30] Of the four molecular dyes, rhodamine have the lowest magnitude of free energy of adsorption and the smallest adsorption site areas. The positively charged molecular dyes have a very strong electrostatic attraction to the negatively charged nanoparticle surface. However, the adsorption properties are highly dependent on the molecular structure of the adsorbate, especially around the charged nitrogen center, which in turn affects the image-charge attractions with the metal center. The same trend of the free energy of adsorption and site area obtained from the adsorption of these four molecular dyes on the surface of 85 nm colloidal gold nanoparticles is shown in Appendix 4. The free energies of adsorption obtained from the best fit of the adsorption isotherms are -15.3 ± 0.2 Kcal/mol, -14.8 ± 0.1 Kcal/mol, -15.0 ± 0.2 Kcal/mol, -12.7 ± 0.3 Kcal/mol for malachite green, brilliant green, methyl green, and rhodamine 110 adsorbed on the surface of 85 nm colloidal gold nanoparticles, respectively. The corresponding number of adsorption sites per particle for the four different molecules is determined to be $(9.4 \pm 0.02) \times 10^3$, $(8.8 \pm 0.03) \times 10^3$, $(9.0 \pm 0.02) \times 10^3$, $(7.8 \pm 0.03) \times 10^3$ sites per particles, respectively. The adsorption site areas are $79 \pm 3\ A^2$, $68 \pm 4\ A^2$, $72 \pm 4\ A^2$, $53 \pm 4\ A^2$. However, the free energies of adsorption of the four molecular dyes studied are higher and the site areas are smaller when they are adsorbed on the surface of gold nanoparticles compared to the core-shell-shell nanoparticles. The corresponding SHG spectra and adsorption isotherms of the dyes adsorbed on the surface of 85 nm colloidal gold nanoparticles capped in citrate are shown in Appendix 4. The effect of added NaCl on the SHG signal of the core-shell-shell nanoparticles is investigated and the corresponding SHG spectra are shown in Appendix 4. A decrease in the SHG signal

with the salt concentration is observed due to dilution effects and the change in the electrostatic potential at the nanoparticle surface, which leads to a change in the corresponding $\chi^{(3)}$.[46, 47] The SHG signal remained stable for added NaCl concentrations higher than 65 μM, showing that aggregation does not occur at the added dye concentrations of this study. This remarkable decrease in the SHG signal of the core-shell-shell nanoparticle sample after the addition of salt will be further investigated in future studies.

The effect of the plasmonic nanoparticles on the quenching or enhancement of the fluorescence signal of the dye molecules is shown in Figure 5.4. In addition to the effect of the core-shell-shell nanoparticles on the fluorescence of the molecular dyes, spectral resonance coupling between the molecules and the plasmonic core-shell-shell nanoparticles is investigated. Figure 5.5 shows the difference spectra obtained after subtracting the core-shell-shell nanoparticle and the dye extinction spectra alone in water from the spectra measured from mixtures of both at the same corresponding concentrations. The dye concentrations are chosen to span the relevant concentrations of the adsorption isotherms determined from the SHG measurements above for each triphenylmethane dye. Several additional features are observed that can be attributed to enhanced exciton-plasmon polaritons and Fano-type resonances at the core-shell-shell surface. Positive and negative extinction peaks are observed and can be attributed to super-radiant and sub-radiant spectra regions, respectively. Resonance coupling between triphenylmethane dyes and gold nanoparticles has been previously reported.[30] However, the resonance coupling signal at the surface of the colloidal core-shell-shell nanoparticles is around 40 times more enhanced than at the surface of gold nanoparticles. The Fano-type resonance is due to the coupling between a spectral continuum and a narrow discrete resonance. The spectral resonance of the core-shell-shell nanoparticles is broader than that of gold nanoparticles, which leads to the enhanced Fano-type resonance peaks.

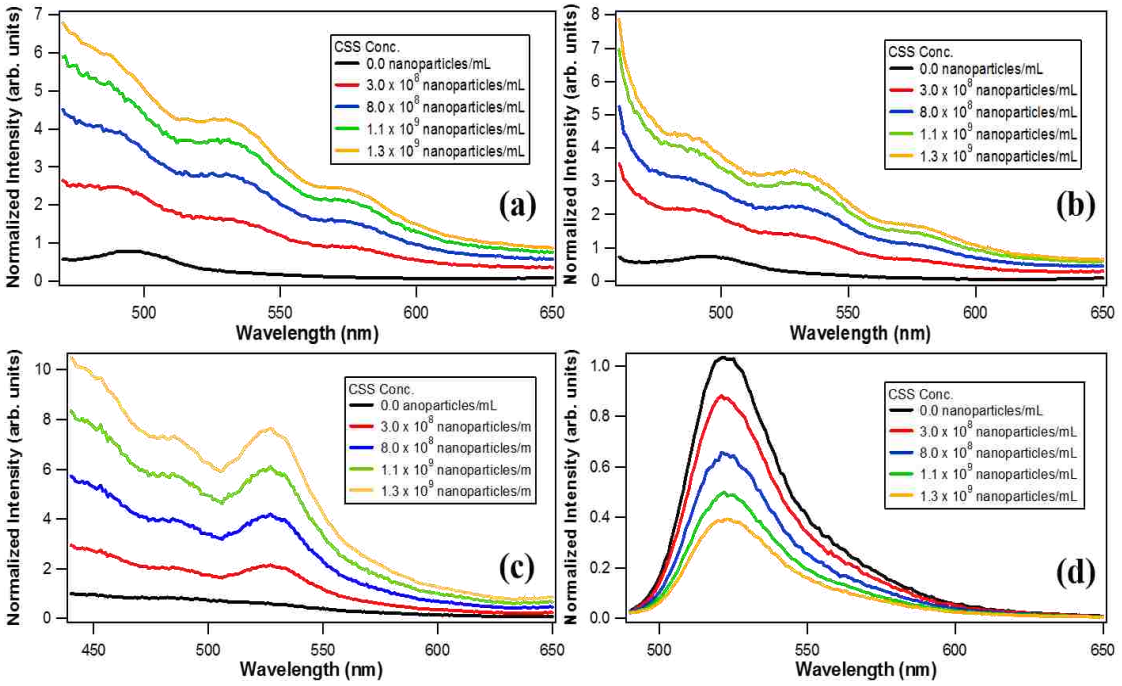

Figure 5.4. Fluorescence spectra of 1.0 μM (a) malachite green, (b) brilliant green, (c) methyl green, and (d) rhodamine 110 at different added core-shell-shell nanoparticle concentrations. The spectra are normalized to the fluorescence intensity of the dyes alone.

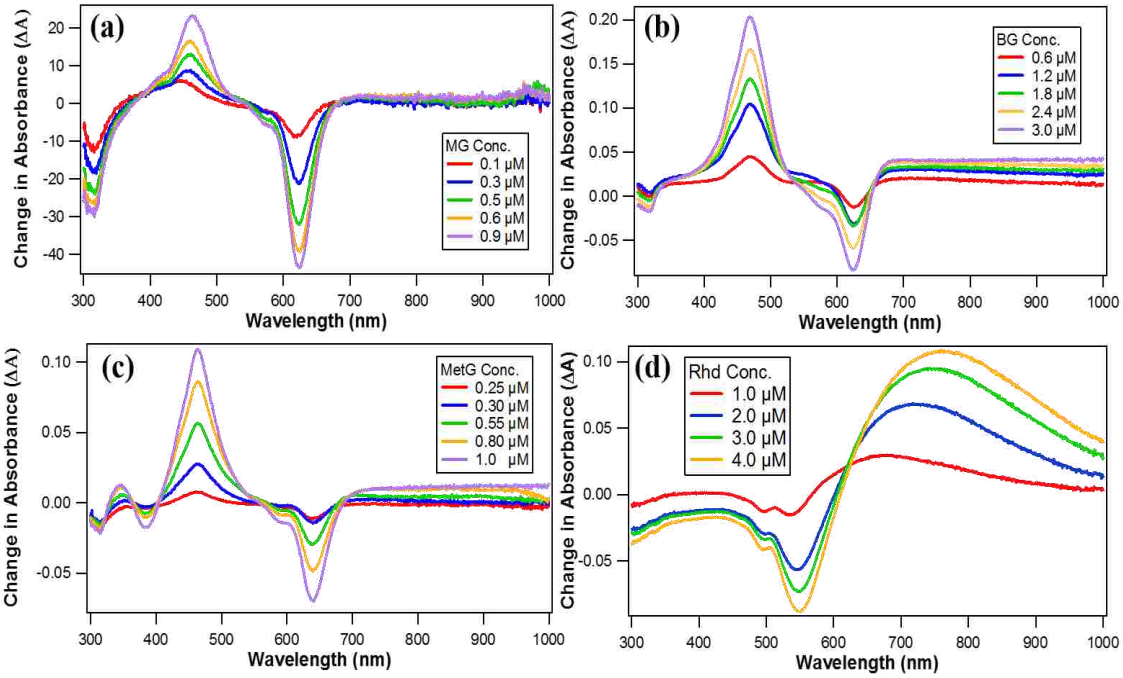

Figure 5.5. Difference spectra obtained from subtracting core-shell-shell nanoparticle and dye molecule extinction spectra alone in water from the spectra measured from mixtures of both at corresponding concentrations for (a) malachite green, (b) brilliant green, (c) methyl green, and (d) rhodamine 110.

Femtosecond transient absorption is used to investigate the excited-state dynamics of 105 ± 7 nm colloidal gold-silver-gold core-shell-shell nanoparticles. Figure 5.6 (a) shows representative transient absorption spectra of the colloidal gold-silver-gold core-shell-shell nanoparticles at different time delays using 400 nm, 5 μJ pump pulses. A positive band centered at 480 nm is attributed to the excited-state absorption of the interband transition electrons. A broad plasmon depletion band is observed for wavelengths greater than 500 nm, extending past 700 nm and is centered at 550 nm. The corresponding time-profiles integrated at 480 and 550 nm are shown in Figure 5.6 (b). Similarly to gold nanoparticles, three lifetimes are required to adequately describe the excited-state dynamics of the core-shell-shell nanoparticles.[26, 48, 49] As shown in Figure 5.6 (c) from the decay spectra obtained using a global analysis technique,[50] a lifetime of 7.0 ± 0.2 ps is associated with the interband transition. The electron-phonon and the phonon-phonon scattering relaxation decay are characterized by lifetimes of 5.4 ± 0.1 ps and 21 ± 0.4 ps, respectively. The phonon-phonon scattering lifetime has been reported to be significantly faster in core-shell-shell nanoparticles than gold nanoparticles, which enhances the photothermal effect of the nanoparticles.[26] Figure 5.6 (d) shows the residual signals from the transient absorption time profiles measured at 550 nm after subtracting the biexponential best fits, showing oscillations that are attributed to acoustic phonons. The damping lifetime and oscillation period of the acoustic phonons are 13.5 ± 0.4 ps and 2.9 ± 0.2 ps, respectively. However, additional size-dependent studies are still needed to accurately model the acoustic phonons of three-layered plasmonic nanoparticles.

In order to better understand the coupling between molecules and the nanoparticle plasmon resonance, the excited-state dynamics of brilliant green and rhodamine 110 adsorbed on the surface of gold-silver-gold core-shell-shell nanoparticles are investigated and compared to those of the dye molecules in water. The excited-state dynamics of triphenylmethane dyes have been previously investigated in bulk solution and at the air/water interface.[51, 52] Representative transient absorption spectra of brilliant green in water and adsorbed on the surface of colloidal core-shell-shell nanoparticles are shown in Figure 5.7, a-b, respectively. A positive band centered at 480 nm is attributed to excited-state

absorption, followed by a negative band attributed to ground-state depletion centered at 580 nm and 600 nm for brilliant green in water and at the core-shell-shell nanoparticle surface, respectively.

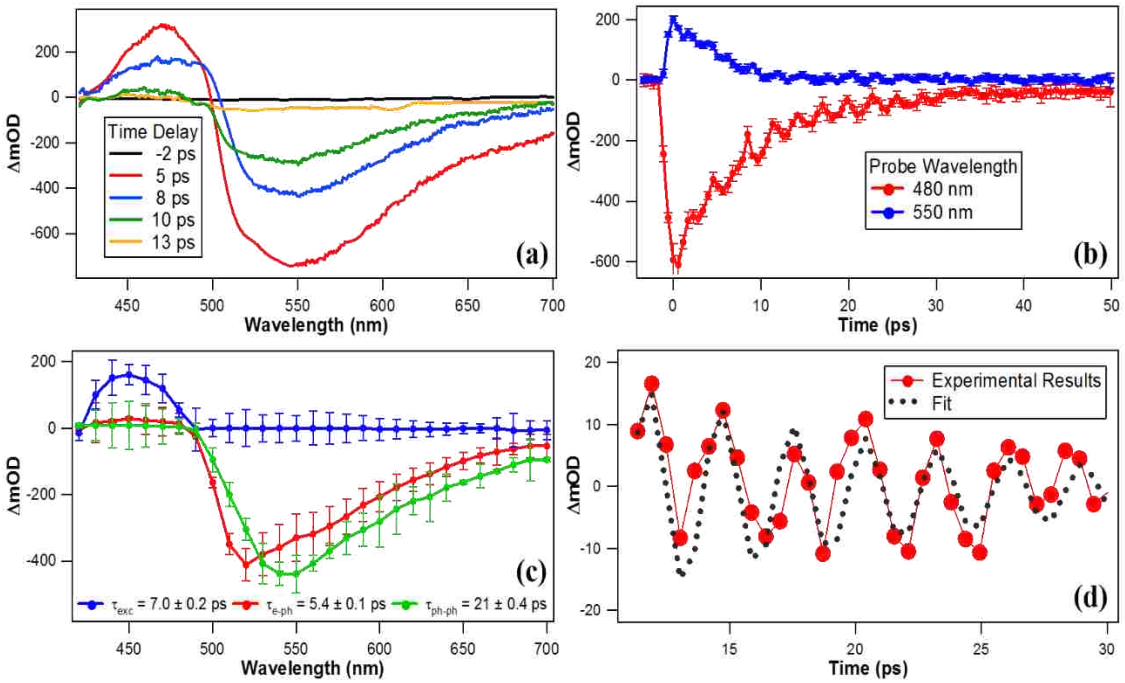

Figure 5.6. (a) Transient absorption spectra of 105 ± 7 nm colloidal gold−silver−gold core−shell−shell nanoparticles at different time delays using 400 nm pump pulse excitation wavelength. (b) Transient absorption time profiles of these nanoparticles measured at 480 and 550 nm. (c) Decay spectra obtained using a sum of exponential fits for the time-dependent transient absorption spectra of the core-shell-shell nanoparticles. (d) Residual signals from the transient absorption time profiles measured at 550 nm after subtracting the biexponential best fits, showing the phonon oscillations.

Representative transient absorption time-profiles measured of malachite green in water and at the core-shell-shell nanoparticle surface are shown in Figure 5.7, b-e, respectively. The global analysis of the transient absorption time-profiles of brilliant green in water and at the core-shell-shell nanoparticle surface are shown in Figure 5.7 (c) and (f), respectively. Three lifetimes are needed to accurately describe the excited-state relaxation dynamics of brilliant green. These lifetimes are 0.82 ± 0.04 ps, 0.63 ± 0.03 ps, and 3.18 ± 0.07 ps for brilliant green in water compared to 0.32 ± 0.02 ps, 0.98 ± 0.08 ps, and 3.85 ± 0.11 ps for brilliant green at the core-shell-shell nanoparticle surface. The first lifetime is faster while the other two are slower at the core-shell-shell nanoparticle surface. The three lifetimes of brilliant green in solution are known to describe the propeller-like torsional dynamics of the phenyl rings about the central

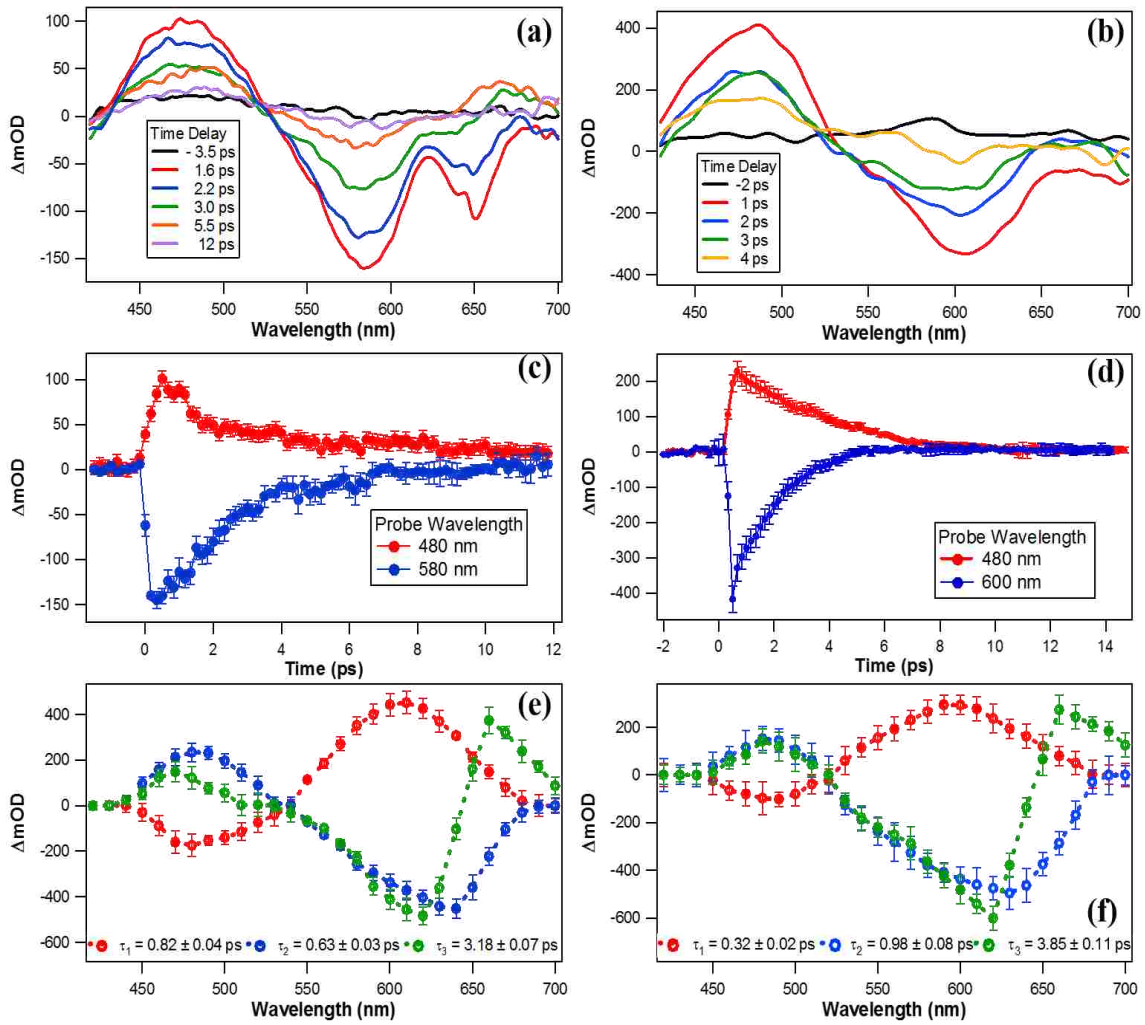

Figure 5.7. Transient absorption spectra of 8 μM brilliant green (a) in water and (b) adsorbed on the surface of 106 ± 7 nm colloidal core-shell-shell nanoparticles at a concentration of 1.6×10^9 nanoparticles/mL at different time delays using 400 nm pump pulse excitation wavelength. Transient absorption time profiles of brilliant green (c) in water and (d) adsorbed on the surface of core-shell-shell nanoparticles measured at 480 and 580 nm. Decay spectra obtained using a sum of exponential fits for the time-dependent transient absorption spectra of brilliant green (e) in water and (f) adsorbed on the surface of core-shell-shell nanoparticles.

carbon, as the excited-state molecule first torsionally twists away from the ground state configuration, then more slowly twists back again to the ground state geometry. The slower lifetimes of the molecule at the nanoparticle surface indicates a molecular confinement and electrostatic hindrance of the molecular torsional dynamics. It is important to point out that these mesaurements are an average of molecules in solution and adsorbed to the nanoparticle surface. However, in this case, the optical field enhancement of the plasmon causes a much larger sampling of the adsorbed molecules. The decay lifetimes of brilliant

green adsorbed on the surface of 85 ± 7 nm colloidal gold nanoparticles shown in Appendix 4 are 0.71 ± 0.05 ps, 0.75 ± 0.04 ps, and 3.33 ± 0.07 ps. The change in the excited-state relaxation lifetimes of brilliant green is more significant at the core-shell-shell surface than at the gold surface. This may be a consequence of greater optical field enhancement in the core-shell-shell nanoparticle causing greater weighting to the ensemble of adsorbed molecules over free molecules compared to the gold nanoparticle which has a lower optical field enhancement. This agrees with the observation that the fluorescence signal of brilliant green is much more enhanced when it is adsorbed to the core-shell-shell nanoparticle surface compared to the colloidal gold nanoparticle surface.

The excited-state dynamics of rhodamine 110 in water and rhodamine 110 adsorbed on the core-shell-shell nanoparticle surface are shown in Figure 5.8, a-b, respectively. A negative band centered at 500 nm is attributed to electronic ground-state depletion. Two positive bands are observed on both sides of the depletion peak and are attributed to absorption of the excited-state. Figure 5.8 (c) shows the transient absorption time-profiles of rhodamine 110 in water and at the core-shell-shell nanoparticle surface measured at 500 nm. Rhodamine 110 has excited-state dynamics that are longer-lived than our experimental pump-probe time delay range. Therefore, no relaxation decays are observed for rhodamine 110 in water. However, when rhodamine is adsorbed at the colloidal core-shell-shell surface, much faster excited-state relaxation dynamics are observed. The time-profile can be fit with a sum of two exponential functions with a first lifetime that is longer than 10 ns and a second lifetime of 30 ± 6 ps. The shorter lifetime is due to energy transfer from rhodamine to the plasmon, which can explain the quenched fluorescence of rhodamine at the core-shell-shell nanoparticle surface. The first lifetime is attributed to free rhodamine 110 in water. As shown in Appendix 4, for rhodamine adsorbed on the surface of colloidal gold nanoparticles, the shorter lifetime becomes 60 ± 8 ps. The fluorescence of rhodamine is more quenched when it is adsorbed on the surface of the core-shell-shell than the gold nanoparticles as a greater overlap between the molecular energy transition and the broad plasmon band allows for more efficient energy transfer from the excited molecular state to the plasmon.

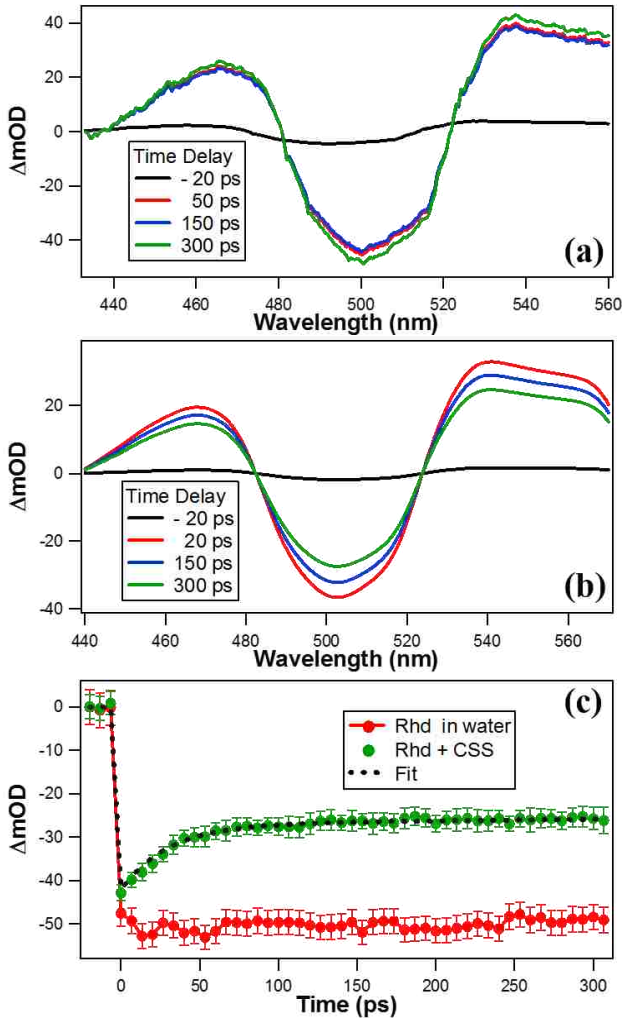

Figure 5.8. Transient absorption spectra of 7 μM rhodamine 110 (a) in water and (b) adsorbed on the surface of 106 ± 7 nm colloidal core-shell-shell nanoparticles at a concentration of 1.6×10^9 nanoparticles/mL at different time delays using 400 nm pump pulse excitation wavelength. (c) Transient absorption time profiles of rhodamine 110 (red dots) in water and (green dots) adsorbed on the surface of core-shell-shell nanoparticles measured at 500 nm.

Femtosecond transient absorption is used to investigate the ultrafast dynamics of brilliant green adsorbed to the colloidal core-shell-shell nanoparticle surface using 470 nm excitation pulses, which are on resonance with the peak due to the exciton-plasmon resonance coupling shown in Figure 5.5 (b). Figure 5.9 (a) shows representative transient absorption spectra of brilliant green adsorbed on the colloidal core-shell-shell surface using 470 nm excitation pulses. A sharp negative band is observed at 470 nm due to the depletion of exciton-plasmon polaritons. Two positive band are observed before 450 nm and after 490 nm and are attributed to excited-state absorption. Representative transient absorption

time-profiles measured at 470 nm and 510 nm are shown in Figure 5.9 (b). From the global analysis shown in Figure 5.9 (c), two lifetimes of 377 ± 15 fs and 187 ± 13 fs are needed to accurately describe these excited-state relaxation dynamics. These lifetimes describe to the excited-state relaxation dynamics of exciton-plasmon polaritons.

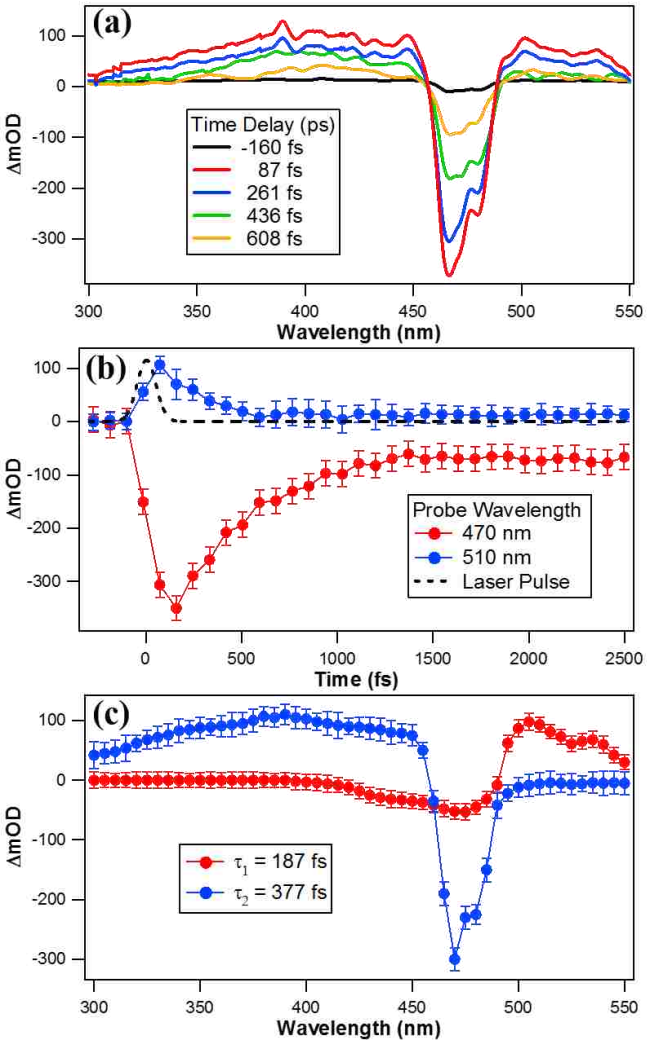

Figure 5.9. (a) Transient absorption spectra of 8 μM brilliant green adsorbed on the surface of 105 ± 7 nm colloidal core-shell-shell nanoparticles at a concentration of 1.6×10^9 nanoparticles/mL at different time delays using 470 nm pump pulse excitation wavelength. (b) Transient absorption time profiles of brilliant green adsorbed on the surface of core-shell-shell nanoparticles measured at 470 and 510 nm. (c) Decay spectra obtained using a sum of exponential fits for the time-dependent transient absorption spectra of brilliant green adsorbed on the surface of core-shell-shell nanoparticles.

5.4 Conclusion

SHG is used to investigate the adsorption isotherms of malachite green, brilliant green, methyl green, and rhodamine 110 on the surface of 105 nm colloidal gold-silver-gold core-shell-shell nanoparticles. The adsorption isotherms are fit using a modified Langmuir model to determine the free energies of adsorption and the adsorption site densities. These results are compared to the adsorption properties at the surface of 85 nm gold nanoparticles. Overall, the free adsorption energies of the molecular dyes are lower at the core-shell-shell surface than the gold nanoparticle surface, while the site densities are higher for core-shell-shell. Complementary measurements from extinction spectroscopy show remarkably enhanced plasmonic and molecular resoanance coupling leading to the formation of new polaritonic states and Fano-type profiles. Additionally, the fluorescence of the malachite green, brilliant green, and methyl green is significantly enhanced at the core-shell-shell surface, while the fluorescence of rhodamine is significantly quenched. These results can be explained from the optical field enhancements, molecular confinement, torsional hindrance, energy transfer between the core-shell-shell nanoparticles and the adsorbates observed with the transient absorption measurements. Finally, transient absorption is used to investigate the excited-state relaxation dynamics of exciton-plasmon polaritons generated at the surface of the colloidal core-shell-shell nanoparticles. These gold-silver-gold core-shell-shell nanoparticles can be very beneficial for various biloigcal applications such as photothermal drug delivery, biosensing, and labeling.

5.5 References

(1) El-Sayed, I.; Huang, X.; El-Sayed, M. Surface Plasmon Resonance Scattering and Absorption of Anti-EGFR Antibody Conjugated Gold Nanoparticles in Cancer Diagnostics: Applications in Oral Cancer. *Nano Lett.* **2005**, *5*, 829−834.

(2) El-Sayed, I.; Huang, X.; El-Sayed, M. Selective Laser Photothermal Therapy of Epithelial Carcinoma Using Anti-EGFR Antibody Conjugated Gold Nanoparticles. *Cancer Lett.* **2006**, *239*, 129−135.

(3) Kamat, P. V. Photophysical, Photochemical and Photocatalytic Aspects of Metal Nanoparticles. *J. Phys. Chem. B* **2002**, *106*, 7729−7744.

(4) Narayanan, R.; El-Sayed, M. A. Catalysis with Transition Metal Nanoparticles in Colloidal Solution: Nanoparticle Shape Dependence and Stability. *J. Phys. Chem. B* **2005**, *109*, 12663−12676.

(5) Haes, A. J.; Van Duyne, R. P. A Nanoscale Optical Biosensor: Sensitivity and Selectivity of an Approach Based on the Localized Surface Plasmon Resonance Spectroscopy of Triangular Silver Nanoparticles. *J. Am. Chem. Soc.* **2002**, *124*, 10596−10604.

(6) Sperling, R. A.; Gil, P. R.; Zhang, F.; Zanella, M.; Parak, W. J. Biological Applications of Gold Nanoparticles. *Chem. Soc. Rev.* **2008**, *37*, 1896−1908.

(7) Freddi, S.; D'Alfonso, L.; Collini, M.; Caccia, M.; Sironi, L.; Tallarida, G.; Caprioli, S.; Chirico, G. Excited-State Lifetime Assay for Protein Detection on Gold Colloids− Fluorophore Complexes. *J. Phys. Chem. C* **2009**, *113*, 2722−2730.

(8) Prigodich, A. E.; Lee, O.-S.; Daniel, W. L.; Seferos, D. S.; Schatz, G. C.; Mirkin, C. A. Tailoring DNA Structure to Increase Target Hybridization Kinetics on Surfaces. *J. Am. Chem. Soc.* **2010**, *132*, 10638−10641.

(9) Kamat, P. V. Meeting the Clean Energy Demand: Nanostructure Architectures for Solar Energy Conversion. *J. Phys. Chem. C* **2007**, *111*, 2834−2860.

(10) Atwater, H. A.; Polma, A. Plasmonics for Improved Photovoltaic Devices. *Nat. Mater.* **2010**, *9*, 205–213.

(11) Link, S.; El-Sayed, M. Shape and Size Dependence of Radiative, Non-radiative and Photothermal Properties of Gold Nanocrystals. *Int. Rev. Phys. Chem.* **2000**, *19*, 409−453.

(12) Daniel, M.-C.; Astruc, D. Gold Nanoparticles: Assembly, Supramolecular Chemistry, Quantum-Size-Related Properties, and Applications toward Biology, Catalysis, and Nanotechnology. *Chem. Rev.* **2004**, *104*, 293−346.

(13) Chandra, M.; Dowgiallo, A. M.; Knappenberger, K. L. Controlled Plasmon Resonance Properties of Hollow Gold Nanosphere Aggregates. *J. Am. Chem. Soc.* **2010**, *132*, 15782−15789.

(14) Stiles, P. L.; Dieringer, J. A.; Shah, N. C.; Van Duyne, R. P. Surface-Enhanced Raman Spectroscopy. *Annu. Rev. Anal. Chem.* **2008**, *1*, 601−626.

(15) Brus, L. Noble Metal Nanocrystals: Plasmon Electron Transfer Photochemistry and Single Molecule Raman Spectroscopy. *Acc. Chem. Res.* **2008**, *41*, 1742−1749.

(16) Tam, F.; Goodrich, G. P.; Johnson, B. R.; Halas, N. J. Plasmonic Enhancement of Molecular Fluorescence. *Nano Lett.* **2007**, *7*, 496−501.

(17) Lakowics, J. R.; Geddes, C. D.; Gryczynski, I.; Malicka, J.; Gryczynski, Z.; Aslan, K.; Lukomska, J.; Matveeva, E.; Zhang, J.; Badugu, R.; et al. Advances in Surface-Enhanced Fluorescence. *J. Fluoresc.* **2004**, *14*, 425−441.

(18) Baldelli, S.; Eppler, A. S.; Anderson, E.; Shen, Y.-R.; Somorjai, G. A. Surface Enhanced Sum Frequency Generation of Carbon Monoxide Adsorbed on Platinum Nanoparticle Arrays. *J. Chem. Phys.* **2000**, *113*, 5432−5438.

(19) Bordnyuk, A. N.; Weeraman, C.; Yatawara, A.; Jayathilake, H. D.; Stiopkin, I.; Liu, Y.; Benderskii, A. V. Vibrational Sum Frequency Generation Spectroscopy of Dodecanethiol on Metal Nanoparticles. *J. Phys. Chem. C* **2007**, *111*, 8925−8933.

(20) Vance, F. W.; Lemon, B. J.; Hupp, J. T. Enormous Hyper-Rayleigh Scattering from Nanocrystalline Gold Particle Suspensions. *J. Phys. Chem. B* **1998**, *102*, 10091−10093.

(21) Butet, J.; Bachelier, G.; Russier-Antoine, I.; Jonin, C.; Benichou, E.; Brevet, P.-F. Interference between Selected Dipoles and Octupoles in the Optical Second-Harmonic Generation from Spherical Gold Nanoparticles. *Phys. Rev. Lett.* **2010**, *105*, 077401.

(22) Hao, E. C.; Schatz, G. C.; Johnson, R. C.; Hupp, J. T. Hyper-Rayleigh Scattering from Silver Nanoparticles. *J. Chem. Phys.* **2002**, *117*, 5963−5966.

(23) Duboisset, J.; Russier-Antoine, I.; Benichou, E.; Bachelier, G.; Jonin, C.; Brevet, P. F. Single Metallic Nanoparticle Sensitivity with Hyper Rayleigh Scattering. *J. Phys. Chem. C* **2009**, *113*, 13477−13481.

(24) Chandra, M.; Knappenberger, K. L. Nanoparticle surface electromagnetic fields studied by single-particle nonlinear optical spectroscopy. *Phys. Chem. Chem. Phys.* **2013**, *15*, 4177−4182.

(25) Dadap, J. I.; Shan, J.; Eisenthal, K. B.; Heinz, T. F. SecondHarmonic Rayleigh Scattering from a Sphere of Centrosymmetric Material. *Phys. Rev. Lett.* **1999**, *83*, 4045−4048.

(26) Karam, T. E.; Smith, H. T.; Haber, L. H. Enhanced Photothermal Effects and Excited-State Dynamics of Plasmonic Size-Controlled Gold−Silver−Gold Core−Shell−Shell Nanoparticles. *J. Phys. Chem. C* **2015**, *119*, 18573−18580.

(27) Eisenthal, K. Second Harmonic Spectroscopy of Aqueous Nano- and Microparticle Interfaces. *Chem. Rev.* **2006**, *106*, 1462−1477.

(28) Boyd, R. Nonlinear Optics; Academic Press: New York, 2010.

(29) Haber, L. H.; Kwok, S. J. J.; Semeraro1, M.; Eisenthal, K. B. Probing the Colloidal Gold Nanoparticle/Aqueous Interface with Second Harmonic Generation. *Chem. Phys. Lett.* **2011**, *507*, 11–14.

(30) Karam, T. E.; Haber, L.H. Molecular Adsorption and Resonance Coupling at the Colloidal Gold Nanoparticle Interface. *J. Phys. Chem. C* **2014**, *118*, 642−649.

(31) Ni, W.; Chen, H.; Su, J.; Sun, Z.; Wang, J.; Wu, H. Effects of Dyes, Gold Nanocrystals, pH, and Metal Ions on Plasmonic and Molecular Resonance Coupling. *J. Am. Chem. Soc.* **2010**, *132*, 4806−4814.

(32) Hutchison, J. A.; Liscio, A.; Schwartz, T.; Canaguier-Durand, A.; Genet, C.; Palermo, V.; Samori, P.; Ebbesen, T. Tuning the WorkFunction via Strong Coupling. *Adv. Mater.* **2013**, *25*, 2481−2485.

(33) Cade, N. I.; Ritman-Meer, T.; Richards, D. Strong Coupling of Localized Plasmons and Molecular Excitons in Nanostructured Silver Films. *Phys. Rev. B* **2009**, *79*, 241404(R).

(34) Sugawara, Y.; Kelf, T. A.; Baumber, J. J.; Abdelsalam, M. E.; Bartlett, P. N. Strong Coupling between Localized Plasmons and Organic Excitons in Metal Nanovoids. *Phys. Rev. Lett.* **2006**, *97*, 266808.

(35) Dulkeith, E.; Morteani, A. C.; Niedereichholz, T.; Klar, T. A.; Feldmann, J.; Levi, S. A.; van Veggel, F. C. J. M.; Reinhoudt, D. N.; Möller, M.; Gittins, D. I. Fluorescence Quenching of Dye Molecules near Gold Nanoparticles: Radiative and Nonradiative Effects. *Phys. Rev. Lett.* **2002**, *89*, 203002.

(36) Tam, F.; Goodrich, G. P.; Johnson, B. R.; Halas, N. J. Plasmonic Enhancement of Molecular Fluorescence. *Nano Lett.* **2007**, *7*, 496–501.

(37) Chen, Y.; Munechika, K.; Ginger, D. S. Dependence of Fluorescence Intensity on the Spectral Overlap between Fluorophores and Plasmon Resonant Single Silver Nanoparticles. *Nano Lett.* **2007**, *7*, 690–696.

(38) Brown, K. R.; Walter, D. G.; Natan, M. J. Seeding of Colloidal Au Nanoparticle Solutions. 2. Improved Control of Particle Size and Shape. *Chem. Mater.* **2000**, *12*, 306−313.

(39) Perrault, S.; Chan, W. Synthesis and Surface Modification of Highly Monodispersed, Spherical Gold Nanoparticles of 50−200 nm. *J. Am. Chem. Soc.* **2009**, *131*, 17042−17043.

(40) Jana, N. R.; Gearheart, L.; Murphy, C. J. Evidence for Seed-Mediated Nucleation in the Chemical Reduction of Gold Salts to Gold Nanoparticles. *Chem. Mater.* **2001**, *13*, 2313−2322.

(41) Haber, L. H.; Eisenthal, K. B. Molecular Excited-State Relaxation Dynamics at the Colloidal Microparticle Interface Monitored with Pump−Probe Second Harmonic Generation. *J. Phys. Chem. B* **2013**, *117*, 4249−4253.

(42) Karam, T. E.; Smith, H. T.; Haber, L. H. Enhanced Photothermal Effects and Excited-State Dynamics of Plasmonic Size-Controlled Gold−Silver−Gold Core−Shell−Shell Nanoparticles. *J. Phys. Chem. C* **2015**, *119*, 18573−18580.

(43) Bhasikuttan, A. C.; Sapre, A. V.; Okada, T. Ultrafast Relaxation Dynamics from the S2 State of Malachite Green Studied with Femtosecond Upconversion Spectroscopy. *J. Phys. Chem. A* **2003**, *107*, 3030−3035.

(44) Denk, W.; Strickler, J. H.; Webb, W. W. Two-Photon Laser Scanning Fluorescence Microscopy. *Science* **1990**, *248*, 73−76.

(45) Wang, H.; Yan, E.; Liu, Y.; Eisenthal, K. B. Energetics and Population of Molecules at Microscopic Liquid and Solid Surfaces. *J. Phys. Chem. B* **1998**, *102*, 4446−4450.

(46) Yan, E. C. Y.; Liu, Y.; Eisenthal, K. B. New Method for Determination of Surface Potential of Microscopic Particles by Second Harmonic Generation. *J. Phys. Chem. B* **1998**, *102*, 6331−6336.

(47) Kumal, R. R.; Karam, T. E.; Haber, L. H. Determination of the Surface Charge Density of Colloidal Gold Nanoparticles Using Second Harmonic Generation. *J. Phys. Chem. C*, **2015**, *119*, 16200–16207.

(48) Ahmadi, T.; Logunov, S. L.; El-Sayed, M. A. Picosecond Dynamics of Colloidal Gold Nanoparticles. *J. Phys. Chem.* **1996**, *100*, 8053.

(49) Logunov, S. L.; Ahmadi, T. S.; El-Sayed, M. A.; Khoury, J. T.; Whetten, R. L. Electron Dynamics of Passivated Gold Nanocrystals Probed by Subpicosecond Transient Absorption Spectroscopy. *J. Phys. Chem. B* **1997**, *101*, 3713−3719.

(50) Duvanel, G.; Grilj, J.; Vauthey, E. Ultrafast Long-Distance Excitation Energy Transport in Donor–Bridge–Acceptor Systems. *J. Phys. Chem. A* **2013**, *117*, 918–928.

(51) Punzi, A.; Martin-Gassinm, M.; Grilj, J.; Vauthey, E. Effect of Salt on the Excited-State Dynamics of Malachite Green in Bulk Aqueous Solutions and at Air/Water Interfaces: a Femtosecond Transient Absorption and Surface Second Harmonic Generation Study. *J. Phys. Chem. C* **2009**, *113*, 11822–11829.

(52) Bhasikuttan, A. C.; Sapre, A. V.; Okada, T. Ultrafast Relaxation Dynamics from the S2 State of Malachite Green Studied with Femtosecond Upconversion Spectroscopy. *J. Phys. Chem. A* **2003**, *107*, 3030−3035.

CHAPTER 6 – EXCITED-STATE DYNAMICS OF SIZE-DEPENDENT COLLOIDAL TiO_2-Au NANOCOMPOSITES

6.1 Introduction

Gold nanoparticles have been widely studied due to their various potential applications in sensing, photovoltaics, catalysis, imaging, and photothermal therapy.[1-10] The size- and shape-dependent localized surface plasmon resonances from coherent oscillations of free electrons[11-13] can lead to large optical field enhancements. Ultrafast pump-probe spectroscopy has been used to investigate the excited-state relaxation dynamics of gold nanoparticles, which can be characterized by different spectral regions that correspond to different relaxation processes.[14-17] A higher-energy, excited-state absorption spectral region near 480 nm is attributed to the interband excitation of electrons from the gold *d* band to the *sp* band above the Fermi level, with excited-state dynamics specified by the electronic interband transition lifetime. A lower-energy depletion spectrum near 550 nm corresponds to the plasmon resonance region with relaxation dynamics described by electron-phonon and phonon-phonon scattering lifetimes. The electron-phonon scattering lifetime is observed to increase as the pump pulse intensity is increased due to heating of the electron gas.[11, 16, 18] At even spectral lower energies, excited-state absorption centered near 600 nm is attributed to nonequilibrium "hot" electron distributions, with lifetimes that are also governed by the plasmon dynamics.[19]

Semiconductor-metal nanocomposites are of great interest for plasmon-induced photocatalytic applications such as the production of hydrogen,[20-22] the reduction of thiocyanate,[23] and the oxidation of carbon monoxide.[24] The oxidation of CO to CO_2 at the surface of semiconductor-supported gold nanoclusters depends on the nanocluster size as well as the size and material of the semiconductor.[25, 26] Several studies reported ultrafast electron transfer into the conduction band of TiO_2 nanocrystals after an excitation on resonance with the plasmon band.[27 - 29] Excitation above the Fermi level permits excited electrons to cross the Schottky barrier leading to electron transfer from gold to TiO_2.[30] Excitation above the TiO_2 band gap in colloidal suspensions of gold nanoclusters adsorbed to TiO_2 nanoparticles in

ethanol-toluene causes electron transfer from TiO_2 to gold for photocatalytic reduction reactions and size-dependent Fermi level shifts with larger shifts for smaller nanocluster sizes.[31, 32] An opposite size-dependent trend is observed for gold-TiO_2 nanocomposites in water, where a more negative Fermi energy shift occurs for larger gold nanocluster sizes.[33] Understanding the relationship between the semiconductor-metal nanocomposite size and morphology with the resulting excited-state dynamics is critical for the development, control, and optimization of the nanomaterial catalytic properties.[34]

In this chapter, we report investigations on the ultrafast excited-state dynamics of size-dependent colloidal gold nanoclusters at the surface of 10 nm TiO_2 nanoparticles. The electron-phonon and phonon-phonon scattering lifetimes are found to be constant for the different nanocluster sizes. The decay of the induced excitation band centered at 480 nm is characterized by two lifetimes corresponding to excited-state electrons from the gold interband transition and size-dependent electron transfer between the gold nanoclusters and the TiO_2 nanoparticle. In addition, size-dependent periodic oscillations are observed at the plasmon depletion band and are attributed to coherent acoustic phonons of the gold nanoclusters.

6.2 Experimental Section

6.2.1 Synthesis and Characterization of TiO_2-Au Nanocomposites

The TiO_2-Au nanocomposites are prepared by hydrolysis of titanium (IV) tetraisopropoxide ($Ti[OCH(CH_3)_2]_4$) (TTIP) followed by the reduction of gold chloride ($HAuCl_4$) at the TiO_2 nanoparticle surface.[34] All chemicals are purchased from Sigma-Aldrich and are used without further purification in ultrapure water. Briefly, the TiO_2 colloidal suspension is produced by acidifying 200 mL of water with perchloric acid ($HClO_4$) to a final pH of 1.5 under vigorous stirring followed by the dropwise addition of 3.0 mL of 0.35 M TTIP in ethanol (EtOH). The reaction flask is then covered with parafilm and stirred vigorously for 20 minutes. Three different suspensions of gold-capped TiO_2 nanocomposites are prepared by adding 4 mL of the TiO_2 colloid suspension to 0.7 mL, 1.4 mL, and 2.0 mL, respectively, of 30 mM gold chloride solution, with the total volume of the solution subsequently adjusted to 100 mL by adding ultrapure water. The relative concentrations of $HAuCl_4$ are varied in these solutions to achieve molar concentration ratios [TiO_2]:[Au] of 1:1, 1:2, and 1:3, respectively. Finally, 5 mL of a 1 mM solution of

the reducing agent, sodium borohydride ($NaBH_4$) in water, is added dropwise under vigorous stirring over approximately 20 minutes to each solution until a deep red color change is observed.

Transmission electron microscopy (TEM) images and the corresponding extinction spectra of the different TiO_2-Au nanocomposite samples are shown in Figure 6.1. The size distributions of the nanoparticles are obtained after surveying more than 100 nanoparticles for each sample. Additional TEM images of the nanoparticles are shown in Appendix 5. All nanoparticles and nanocomposites are observed to be very spherical in shape. The average diameter of the TiO_2 nanoparticles is measured to be 9.9 ± 0.4 nm. The average diameters of the 1:1, 1:2, and 1:3 [TiO_2]:[Au] nanocomposites are measured to be 19.1 ± 0.4 nm, 21.9 ± 0.3 nm, and 24.3 ± 0.4 nm, respectively. Although the spatial resolution of the electron microscopy used in this study is insufficient to clearly resolve individual gold nanoclusters on the TiO_2 nanoparticle surface, the average gold nanocluster sizes can be estimated from the increases of the nanoparticle sizes by the TEM measurements, following previous comparative investigations.[34] Using this approach, the sizes of the gold nanoclusters are estimated to be 4.6 ± 0.3 nm, 6.0 ± 0.3 nm, and 7.2 ± 0.3 nm for the 1:1, 1:2, and 1:3 [Au]:[TiO_2] nanocomposite samples, respectively.

6.2.2 Transient Absorption Setup

The transient absorption setup consists of an amplified titanium:sapphire laser system, an optical parametric amplifier (OPA), an optical setup, and a fiber optic spectrometer with a charge-coupled device detector.[18] The laser produces 0.7 mJ, 75 fs pulses centered at 800 nm with a repetition rate of 10 kHz. A 90/10 beamsplitter is used to separate the pump and probe beams. The pump beam is passed through an OPA to generate 400 nm, 5 μJ pump pulses at a 10 kHz repetition rate. The probe beam is focused into a fused quartz flow cell containing water to generate the femtosecond white light probe pulses that are refocused to a spatial overlap with the pump pulse at the sample, which is contained in a 3 mm fused quartz cell under constant stirring. The pump-probe temporal delay is controlled using a retroreflector on a computer-controlled translation stage. A computer-controlled beam block opens and shuts on the pump pulse in synchronization with an automated file saving program, and sixty spectra at 1 second acquisitions

are taken for each time step. Several time-resolved transient absorption spectral scans are taken for each sample for statistical analysis.

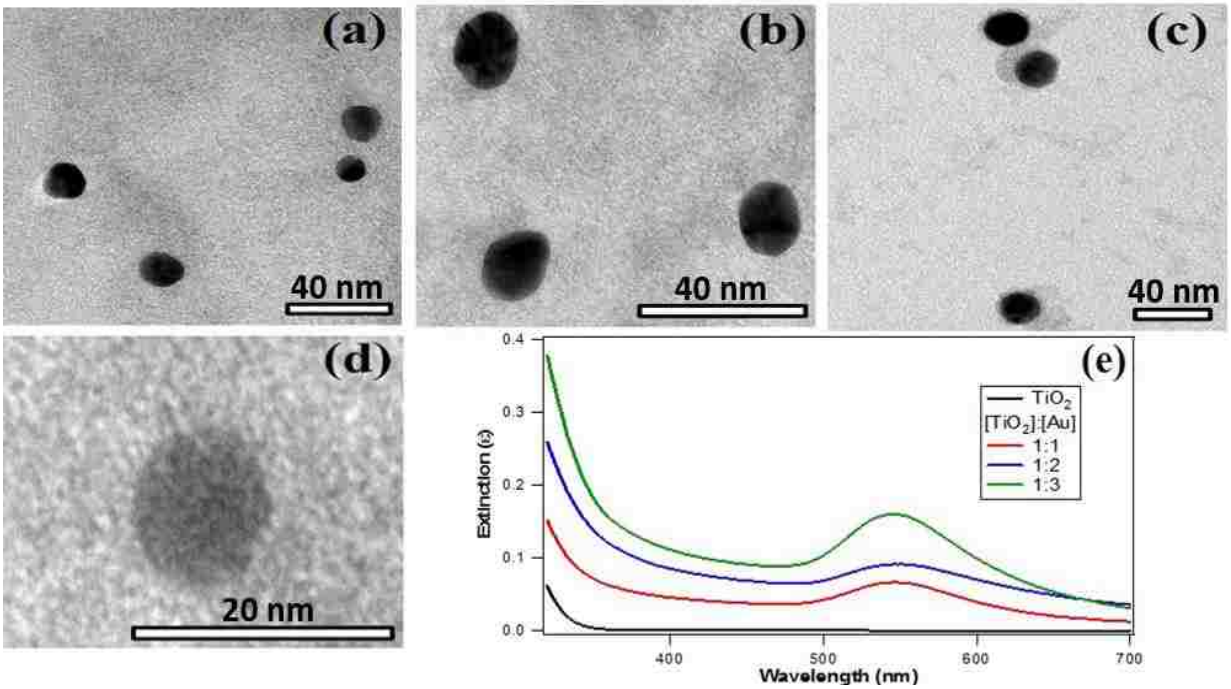

Figure 6.1. Transmission electron microscopy images of (a) 1:1, (b) 1:2, (c) 1:3 TiO_2-Au nanocomposites and (d) precursor TiO_2 nanoparticles. (e) Extinction spectra of colloidal TiO_2 nanoparticles (black) and TiO_2-Au nanocomposites with 1:1 (red), 1:2 (blue), and 1:3 (green) [TiO_2]:[Au] ratios, respectively.

6.3 Results and Discussion

Pump-probe transient absorption spectroscopy is used to investigate the excited-state dynamics of the colloidal TiO_2-Au nanocomposites. Figure 6.2 shows the transient absoprtion spectra of the colloidal samples at different pump-probe time delays using 400 nm excitation pulses for the (a) 1:1, (b) 1:2, and (c) 1:3 [TiO_2]:[Au] ratios, respectively. As in the case of free colloidal gold nanoparticles, the transient absorption spectra are described by a positive excited-state absorption band centered near 480 nm followed by a negative depletion band centered near 550 nm.[14, 15] The positive band centered near 480 nm is consistent with the well-established interband transition region in the gold nanoclusters. The negative depletion band centered near 550 nm is consistent with the depletion of plasmon electrons.[14, 15] By careful analysis of the transient absorption data, information on the optical and electronic intertactions between the gold nanoclusters and the TiO_2 nanoparticle surface can be obtained.

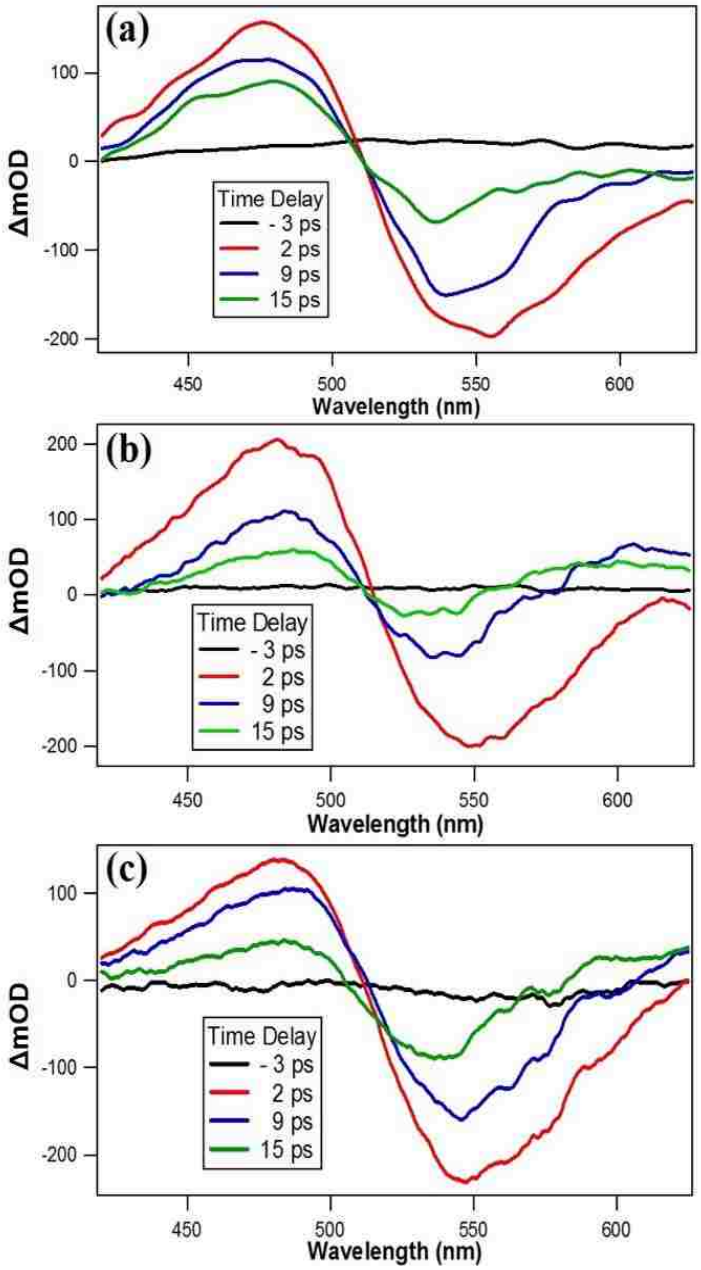

Figure 6.2. Transient absorption spectra of colloidal TiO_2-Au nanocomposites at different time delays using 400 nm excitation pulses with (a) 1:1, (b) 1:2, and (c) 1:3 [TiO_2]:[Au] ratios, respectively.

Figure 6.3 shows the time-dependent transient absorption profiles of the colloidal TiO_2-Au nanocomposites with (a) 1:1, (b) 1:2, and (c) 1:3 [TiO_2]:[Au] ratios, respectively, at probe wavelengths of 480 nm (blue data points) and 550 nm (red data points). The time-dependent transient absorption profiles

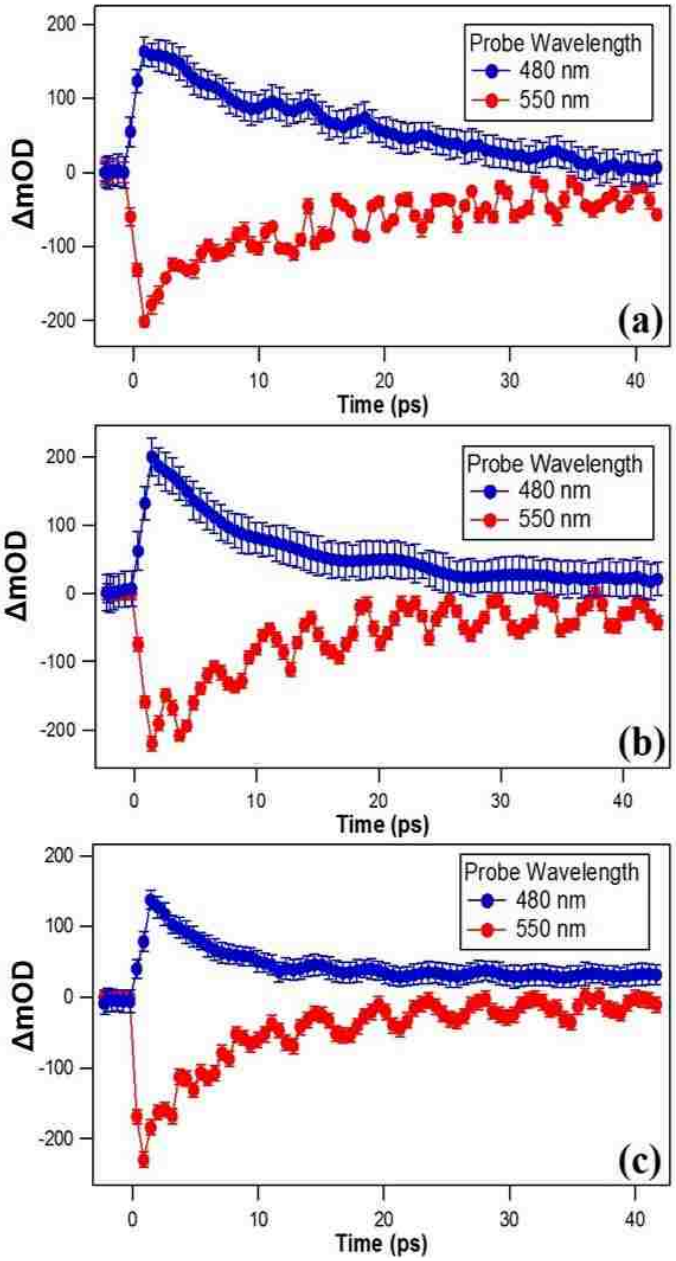

Figure 6.3. Transient absorption time profiles of colloidal TiO_2-Au nanocomposites at 480 nm and 550 nm with (a) 1:1, (b) 1:2, and (c) 1:3 [TiO_2]:[Au] ratios, respectively.

measured at 550 nm are fit with a biexponential function to determine the excited-state lifetimes due to electron-phonon scattering and phonon-phonon scattering.[14, 15] The electron-phonon scattering lifetimes are 3.0 ± 0.3 ps, 3.3 ± 0.5 ps, and 3.2 ± 0.2 ps for the 1:1, 1:2, and 1:3 [TiO_2]:[Au] ratio, respectively. The phonon-phonon scattering lifetimes are 49 ± 6 ps, 53 ± 8 ps, and 55 ± 8 ps for the 1:1, 1:2, and 1:3 [TiO_2]:[Au] ratio, respectively. The lifetimes corresponding to the electron-phonon and phonon-phonon

scaterring are similar for the three samples to within experimental uncertainty. These results agree with previous work that showed the electron-phonon scattering lifetime is generally independent of the size and shape of the gold nanoparticles.[17, 35, 36] The size-dependent superimposed oscillations are due to acoustic phonons and will be discussed later. Previous measurements on 54 nm gold nanospheres obtained electron-phonon and phonon-phonon scattering lifetimes of approximately 3 ps and 100 ps, respectively.[18] The electron-phonon scattering lifetimes from the TiO_2-Au nanocomposites agree with previous measurements in gold nanoparticles. However, the phonon-phonon scattering lifetimes from the TiO_2-Au nanocomposites are considerably faster than the corresponding lifetime in gold nanoparticles. The phonon-phonon scattering lifetime is known to depend on the surrounding medium of the gold nanoclusters caused by differences in the rate of heat transfer.[37, 38] The faster phonon-phonon scattering lifetimes of TiO_2-Au nanocomposites compared to gold nanoparticles can be explained due to the much higher thermal conductivity of TiO_2 compared to water, leading to faster heat transfer, although additional factors such as the surface to volume ratio, the relative TiO_2 to water surface coverage, the precise chemical stucture of the interface, and the resulting molecular and material dynamics should also influence these results.

The transient absorption time profiles measured at 480 nm are fit with biexponential functions with corresponding lifetimes attributed to the excited-state decay of electrons in the gold interband transition with an additional lifetime attributed to electron transfer between the gold nanoclusters and the TiO_2 conduction band. The lifetimes associated with the interband transition in gold are measured to 7.9 ± 0.3 ps, 8.2 ± 0.2 ps, and 8.5 ± 0.3 ps for the 1:1, 1:2, and 1:3 [TiO_2]:[Au] ratios, respectively. These lifetimes are the same to within the experimental uncertainty. The lifetimes associated with the electron transfer between the gold and TiO_2 nanomaterials are determined to be 33.1 ± 0.4 ps, 7.5 ± 0.1 ps, and 4.2 ± 0.1 ps for the 1:1, 1:2, and 1:3 [TiO_2]:[Au] ratios, respectively. These lifetimes become faster as the gold nanocluster size increases. The net electron transfer from the gold to the TiO_2 conduction band at the metal-semiconductor junction occurs upon photoexcitation at time zero on the time scale of the electron-electron scattering, which occurs faster than the current experimental temporal

resolution. As the pump-probe time increases, back electron transfer from the TiO_2 to the gold nanoclusters occurs, corresponding to an eventual relaxation back to the global ground state. Larger gold nanoclusters have a larger density of states near the Fermi level leading to a faster electron-hole recombination rate and a shorter electron transfer lifetime.[39]

The Figure 6.4 shows the decay spectra obtained using the global analysis technique[40, 41] for a more detailed analysis of the transient absorption spectroscopy of the colloidal (a) 1:1, (b) 1:2, and (c) 1:3 [TiO_2]:[Au] nanocomposites, respectively. The transient absorption time-profiles are fit using four exponential functions and an offset, given by $I(t) = y_0 + A_{ib}e^{\left(-\frac{t}{\tau_{ib}}\right)} + A_{et}e^{\left(-\frac{t}{\tau_{et}}\right)} + A_{ep}e^{\left(-\frac{t}{\tau_{ep}}\right)} + A_{pp}e^{\left(-\frac{t}{\tau_{pp}}\right)}$ where $I(t)$ is the time-dependent transient absorption intensity at a given wavelength, y_0 is a constant offset, and A_{ib}, A_{et}, A_{ep}, and A_{pp} are the wavelength-dependent amplitudes of the excited-state decays of the interband transition, the electron-transfer, the electron-phonon scattering, and phonon-phonon scattering, respectively, with the corresponding lifetimes, $\tau_{ib}, \tau_{et}, \tau_{ep}$, and τ_{pp} that describe these dynamics. The electron-phonon scattering lifetimes obtained from the global analysis fit for the 1:1, 1:2, and 1:3 [TiO_2]:[Au] nanocomposites are 3.0 ± 0.3 ps, 3.3 ± 0.5 ps, and 3.2 ± 0.2 ps, respectively. Additionally, the phonon-phonon scattering lifetimes are 49 ± 6 ps, 53 ± 8 ps, and 55 ± 8 ps, for the 1:1, 1:2, and 1:3 [TiO_2]:[Au] nanocomposites, respectively. The interband transition lifetimes are 7.9 ± 0.3 ps, 8.2 ± 0.2 ps, and 8.5 ± 0.3 ps, respectively, and the electron transfer lifetimes are 33.1 ± 0.4 ps, 7.5 ± 0.1 ps, and 4.2 ± 0.1 ps, respectively for the 1:1, 1:2, and 1:3 [TiO_2]:[Au] nanocomposites. These values are all in agreement with the results from the transient absorption time profiles.

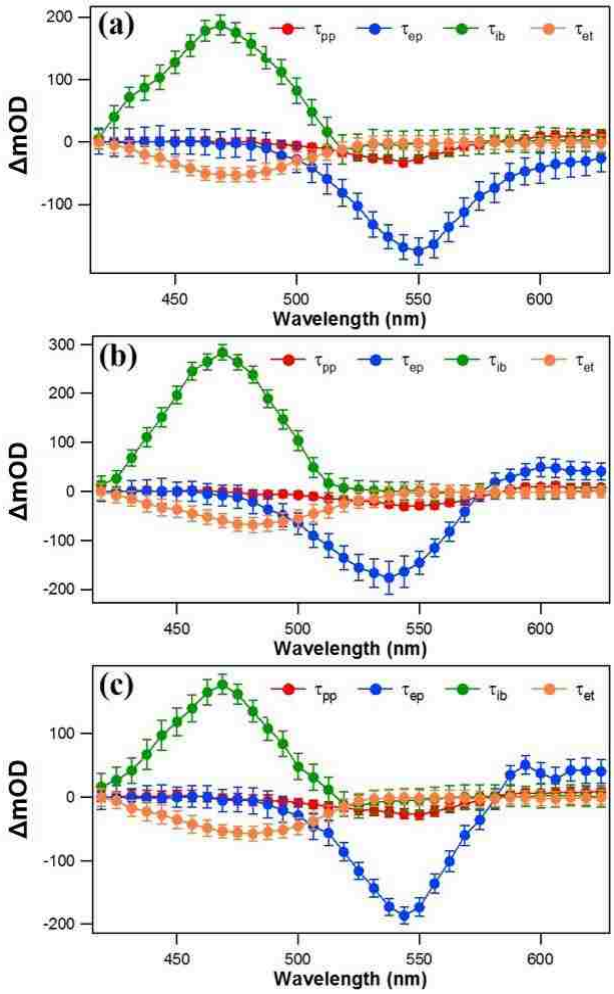

Figure 6.4. Decay spectra obtained using a sum of exponential fits for global analysis of the transient absorption results from (a) 1:1, (b) 1:2, and (c) 1:3 [TiO_2]:[Au] nanocomposites, respectively.

The global analysis decay spectra associated with each dynamic process provides important spectral characterizations of the TiO_2-Au nanomaterial. The interband transition decay spectrum is centered near 480 nm, followed by the electron transfer decay spectrum centered near 485 nm. These decay spectra approach zero amplitude, to within the experimental uncertainty, for wavelengths greater than 520 nm. The electron-phonon scattering and phonon-phonon scattering decay spectra are both centered near 550 nm. The amplitudes of these electron-phonon and phonon-phonon decay spectra approach zero to within experimental uncertainty at wavelengths below 500 nm. This separation in the decay spectra allows the 480 nm and 550 nm time profiles to be accurately treated using separate biexponential fits with different lifetimes. The interband transition decay spectra obtained from global

analysis are positive in amplitude while the electron transfer decay spectra are negative. This indicates that the electron transfer causes a net depletion from the electronic population of the *sp* band associated with the interband transition. A positive excited-state absorption band at wavelengths longer than 600 nm, attributed to thermally-excited plasmon electron distributions, is observed for the 1:2 and 1:3 sample. However, this positive band is not observed for the 1:1 sample. This agrees with previous measurements that observe more prominant hot electron excited-state absorption in this spectral region for larger nanoparticle sizes.[15]

Figure 6.5 shows the time-dependent differences between the experimental measurements and the biexponential best fits for the TiO_2-Au nanocomposites with (a) 1:1, (b) 1:2, and (c) 1:3 [TiO_2]:[Au] ratios. The resulting oscillations are attributed to acoustic phonons that persist longer than 50 ps, which is concurrent with previous reported results on the acoustic lattice vibrations in gold nanoparticles and provide additional information on the gold nanoclusters.[18,42,43] The residual oscillations of the phonons that are fit using a sine function given by $I(t) = y_0 + Aexp\left(-\frac{t}{\tau_d}\right)\sin(2\pi ft + \varphi)$, where f, φ, and τ_d are the frequency, phase shift, and phonon damping time, respectively. The phonon frequencies obtained from the best fits are 0.35 ± 0.02 ps^{-1}, 0.26 ± 0.02 ps^{-1}, 0.22 ± 0.01 ps^{-1} for the 1:1, 1:2, and 1:3 samples, respectively. The corresponding phonon damping times are 108 ± 7 ps, 106 ± 8 ps, and 110 ± 7 ps for the 1:1, 1:2, and 1:3 samples, respectively.

The acoustic phonon oscillation frequencies can be compared to different size-dependent models for additional characterization of the gold nanocluster morphologies. Three different TiO_2-Au nanocomposite architectures are considered which are described by gold nanospheres tangentially adsorbed to the TiO_2 surface, gold nanorods adsorbed to the TiO_2 surface, and TiO_2-Au core-shell nanoparticles. These acoustic phonon models and the results of the corresponding calculated sizes are discussed in more detail in the Appendix 5. The sizes calculated using the gold nanosphere model are found to be approximately two times larger than the sizes obtained by the corresponding TEM

measurements, indicating that the nanocluster morphologies are not perfect spheres tangentially adsorbed to the surface, but may be more accurately described as hemispherical in shape, especially at lower gold

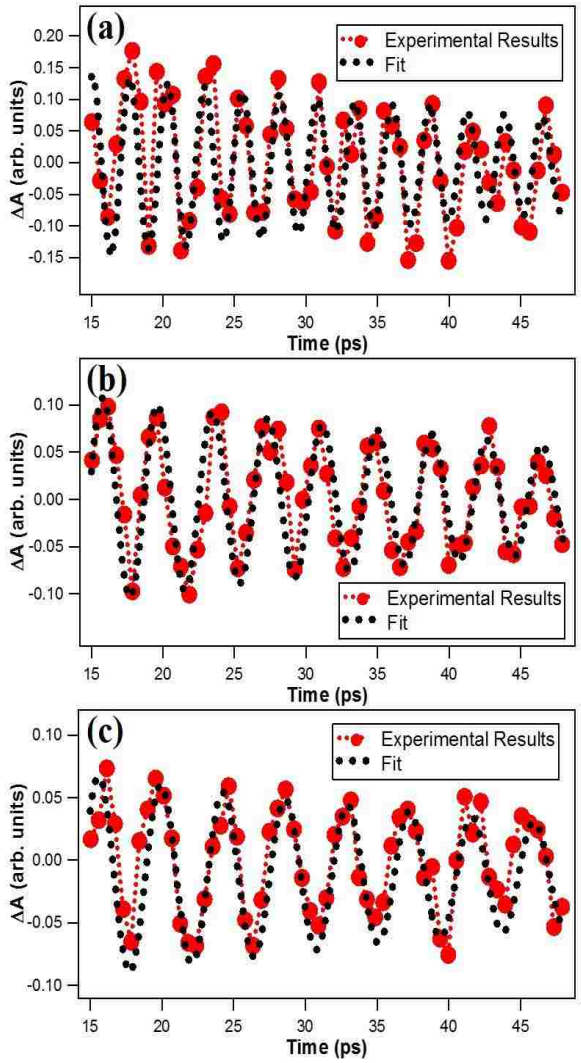

Figure 6.5. Residual signals from the transient absorption time profiles measured at 550 nm after subtracting the biexponential best fits, showing the phonon oscillations for the different TiO_2-Au nanocomposites samples with (a) 1:1, (b) 1:2, and (c) 1:3 [TiO_2]:[Au] ratios, respectively, along with the corresponding fits.

concentrations. The acoustic phonon oscillation frequencies do not agree with expected values from either nanorod morphologies or fully-formed gold shells. However, the frequencies may be consistent with an inhomogeneous, porous gold shell structure composed of aggregated nanoclusters. Individual hemispherical nanoclusters may form at lower gold concentrations, and then the nanoclusters may interconnect with neighboring nanoclusters to form extended porous shells at higher gold concentrations.

Overall, more work is still needed to accurately determine the nanocluster morphologies and size distributions.

The damping times of the acoustic are known to depend on factors such as energy transfer to the surrounding environment, acoustic phonon coupling to other phonon modes in the nanoparticle, and dephasing of the phonon frequencies due to polydispersity of the sample.[43] When the damping is dominated by either polydispersity dephasing or energy transfer to a homogenous surrounding medium, the damping time τ_d is expected to be proportional to the nanoparticle radius.[43,44] However, these descriptions may breakdown under the size and morphology distributions considered in the TiO_2-Au nanocomposites studied here. The phonon damping times of the gold nanoculsters adsorbed at the surface of TiO_2 nanoparticles are measured to be constant for the different nanocomposite sizes, to within experimental uncertainty, indicating that phonon damping is not controlled by either polydispersity dephasing or a simple energy transfer process. Since the gold nanoclusters have surface contact with both TiO_2 and water, and may form aggregated contact with neighboring nanoclusters in a porous shell architecture, the effect of a heterogenous surrounding could result in deviations from an ideal model.

6.4 Conclusion

The ultrafast excited-state dynamics of size-dependent gold nanoclusters reduced on the surface of TiO_2 nanoparticles are investigated using transient absorption spectroscopy. The average sizes of the gold nanoclusters are estimated using high-resolution transmission electron microscopy for different molar concentration ratios of TiO_2 to Au. The transient absorption time profiles measured at the peak of the plasmon depletion band are fit to biexponential functions to obtain the lifetimes of the electron-phonon and phonon-phonon scattering processes. These plasmonic dynamics are shown to be independent of the size of the gold nanoclusters adsorbed to the colloidal TiO_2 nanoparticle surface. The relaxation dynamics of the excited-state absorption band centered at 480 nm are fit with different biexponential functions to determine the lifetimes associated with the electronic interband tranition in gold and the electron transfer between the gold and TiO_2 nanomaterials. While the interband transition lifetime is observed to remain constant under changing nanocluster size, the electron transfer lifetimes are shown to

decrease significantly as the adsorbed gold nanocluster sizes increase due to increased density of states near the Fermi level of the gold nanoclusters. Additionally, size-dependent oscillations of the gold nanoclusters are observed and are attributed to acoustic phonon breathing modes with frequencies that decrease and damping times that remain constant as the nanocluster sizes increase. These findings provide important information that can be useful for improving catalytic efficiencies in plasmonic TiO_2-Au nanocomposites.

6.5 References

(1) El-Sayed, I. H.; Huang, X.; El-Sayed, M. A. Surface Plasmon Resonance Scattering and Absorption of Anti-EGFR Antibody Conjugated Gold Nanoparticles in Cancer Diagnostics: Applications in Oral Cancer. *Nano Lett.* **2005**, *5*, 829–834.

(2) El-Sayed, I. H.; Huang, X.; El-Sayed, M. A. Selective Laser Photo-Thermal Therapy of Epithelial Carcinoma Using Anti-EGFR Antibody Conjugated Gold Nanoparticles. *Cancer Lett.* **2006**, *239*, 129–135.

(3) Kamat, P. V. Photophysical, Photochemical and Photocatalytic Aspects of Metal Nanoparticles. *J. Phys. Chem. B* **2002**, *106*, 7729–7744.

(4) Narayanan r.; El-Sayed, M. A. Catalysis with Transition Metal Nanoparticles in Colloidal Solution: Nanoparticle Shape Dependence and Stability. *J. Phys. Chem. B* **2005**, *109*, 12663–12676.

(5) Haes, A. J.; Van Duyne, R. P. A. A Nanoscale Optical Biosensor: Sensitivity and Selectivity of an Approach Based on the Localized Surface Plasmon Resonance Spectroscopy of Triangular Silver Nanoparticles. *J. Am. Chem. Soc.* **2002**, *124*, 10596–10604.

(6) Sperling, R. A.; Gil, P. R.; Zhang, F.; Zanella, M.; Parak, W. J. Biological Applications of Gold Nanoparticles. *Chem. Soc. Rev.* **2008**, *37*, 1896–1908.

(7) Karam, T. E.; Haber, L. H. Molecular Adsorption and Resonance Coupling at the Colloidal Gold Nanoparticle Interface. *J. Phys. Chem. C* **2014**, *118*, 642–649.

(8) Prigodich, A. E.; Lee, O. –S.; Daniel, W. L.; Seferos, D. S.; G. C. Schatz, G. C.; Mirkin, C. A. Tailoring DNA Structure To Increase Target Hybridization Kinetics on Surfaces. *J. Am. Chem. Soc.* **2010**, *132*, 10638–10641.

(9) Kamat, P. V. Meeting the Clean Energy Demand: Nanostructure Architectures for Solar Energy Conversion. *J. Phys. Chem. C* **2007**, *111*, 2834–2860.

(10) Kholmicheva, N.; Moroz, P.; Rijal, U.; Bastola, E.; Uprety, P.; Liyanage, G.; Razgoniaev, A.; Ostrowski, A. D.; Zamkov, M. Plasmonic Nanocrystal Solar Cells Utilizing Strongly Confined Radiation. *ACS Nano* **2014**, *8*, 12549–12559.

(11) Link, S.; El-Sayed, M. A. Shape and Size Dependence of Radiative, Non-Radiative and Photothermal Properties of Gold Nanocrystals. *Int. Rev. Phys. Chem.* **2000**, *19*, 409–453.

(12) Daniel, M. –C.; Astruc, D. Gold Nanoparticles: Assembly, Supramolecular Chemistry, Quantum-Size-Related Properties, and Applications toward Biology, Catalysis, and Nanotechnology. *Chem. Rev.* **2004**, *104*, 293–346.

(13) Chandra, M.; Dowgiallo, A. M.; Knappenberger, K. L. Controlled Plasmon Resonance Properties of Hollow Gold Nanosphere Aggregates. *J. Am. Chem. Soc.* **2010**, *132*, 15782–15789.

(14) Ahmadi, T.S.; Logunov, S.L.; El-Sayed, M.A.; Picosecond Dynamics of Colloidal Gold Nanoparticles. *J. Phys. Chem.* **1996**, *100*, 8053–8056.

(15) Logunov, S. L.; Ahmadi, T. S.; El-Sayed, M. A.; Khoury, J. T.; Whetten, R. L.; Electron Dynamics of Passivated Gold Nanocrystals Probed by Subpicosecond Transient Absorption Spectroscopy. *J. Phys. Chem. B* **1997**, *101*, 3713–3719.

(16) Hodak, J. H.; Martini, I.; Hartland, G. V. Spectroscopy and Dynamics of Nanometer-Sized Noble Metal Particles. *J. Phys. Chem. B* **1998**, *102*, 6958–6967.

(17) Link, S.; Burda, C.; Mohamed, M. B.; Nikoobakht, B.; El-Sayed, M.A. Femtosecond Transient-Absorption Dynamics of Colloidal Gold Nanorods: Shape Independence of the Electron-Phonon Relaxation Rime. *Phys. Rev. B* **2000**, *61*, 6086.

(18) Karam, T. E.; Smith, H. T.; Haber, L. H. Enhanced Photothermal Effects and Excited-State Dynamics of Plasmonic Size-Controlled Gold–Silver–Gold Core–Shell–Shell Nanoparticles. *J. Phys. Chem. C* **2015**, *119*, 18573–18580.

(19) Dulkeith, E.; Niedereichholz, T.; Klar, T. A.; Feldmann, J.; Von Plessen, G.; Gittins, D. I.; Mayya, K. S.; Caruso, F. Plasmon Emission in Photoexcited Gold Nanoparticles. *Phys. Rev. B* **2004**, *70*, 205424.

(20) Murdoch, M.; Waterhouse, G. I. N.; Nadeem, M. A.; Metson, J. B.; Keane, M. A.; Howe, R. F.; Llorca, J.; Idriss, H. The Effect of Gold Loading and Particle Size on Photocatalytic Hydrogen Production from Ethanol over Au/TiO_2 Nanoparticles. *Nat. Chem.* **2011**, *3*, 489–492.

(21) Maeda, K.; Domen, K. Photocatalytic Water Splitting: Recent Progress and Future Challenges. *J. Phys. Chem. Lett.* **2010**, *1*, 2655–2661.

(22) Joshi, U. A.; Palasyuk, A.; Arney, D.; Maggard, P. A. Semiconducting Oxides to Facilitate the Conversion of Solar Energy to Chemical Fuels. *J. Phys. Chem. Lett.* **2010**, *1*, 2719–2726.

(23) Kamat, P. V.; Flumiani, M.; Dawson, A. Metal–Metal and Metal–Semiconductor Composite Nanoclusters. *Colloids Surf. A Physicochem. Eng. Asp.* **2002**, *202*, 269–279.

(24) Chen, M.; Goodman, D. W. Catalytically Active Gold on Ordered Titania Supports. *Chem. Soc. Rev.* **2008**, *37*, 1860–1870.

(25) Meier, D. C.; Goodman, D. W. The Influence of Metal Cluster Size on Adsorption Energies: CO Adsorbed on Au Clusters Supported on TiO_2. *J. Am. Chem. Soc.* **2004**, *126*, 1892–1899.

(26) Comotti, M.; Li, W. C.; Spliethoff, B.; Schüth, F. Support Effect in High Activity Gold Catalysts for CO Oxidation. *J. Am. Chem. Soc.* **2006**, *128*, 917–924.

(27) Furube, A.; Du, L.; Hara, K.; Katoh, R.; Tachiya, M. Ultrafast Plasmon-Induced Electron Transfer from Gold Nanodots into TiO_2 Nanoparticles. *J. Am. Chem. Soc.* **2007**, *129*, 14852–14853.

(28) Tian, Y.; Tatsuma, T. Mechanisms and Applications of Plasmon-Induced Charge Separation at TiO_2 Films Loaded with Gold Nanoparticles. *J. Am. Chem. Soc.* **2005**, *127*, 7632–7637.

(29) Du, L.; Furube, A.; Yamamoto, K.; Hara, K.; Katoh, R.; Tachiya, M. Plasmon-Induced Charge Separation and Recombination Dynamics in Gold− TiO_2 Nanoparticle Systems: Dependence on TiO_2 Particle Size. *J. Phys. Chem. C* **2009**, *113*, 6454–6462.

(30) McFarland, E. W.; Tang, J. A Photovoltaic Device Structure Based on Internal Electron Emission. *Nat.* **2003**, *421*, 616–618.

(31) Jakob, M.; Levanon, H.; Kamat, P. V. Charge Distribution between UV-Irradiated TiO_2 and Gold Nanoparticles: Determination of Shift in the Fermi Level. *Nano Lett.* **2003**, *3*, 353–358.

(32) Subramanian, V.; Wolf, E. E.; Kamat, P. V. Catalysis with TiO_2/Gold Nanocomposites. Effect of Metal Particle Size on the Fermi Level Equilibration. *J. Am. Chem. Soc.* **2004**, *126*, 4943–4950.

(33) Kiyonaga, T.; Fujii, M.; Akita, T.; Kobayashi, H.; Tada, H. Size-Dependence of Fermi Energy of Gold Nanoparticles Loaded on Titanium (IV) Dioxide at Photostationary State. *Phys. Chem. Chem. Phys.* **2008**, *10*, 6553–6561.

(34) Dawson, A.; and Kamat, P. V. Semiconductor-Metal Nanocomposites. Photoinduced Fusion and Photocatalysis of Gold-Capped TiO_2 (TiO_2/gold) Nanoparticles. *J. Phys. Chem. 2001* **B**, *105*, 960–966.

(35) Hodak, J.; Martini, I.; Hartland, G. V. Ultrafast Study of Electron–Phonon Coupling in Colloidal Gold Particles. *Chem. Phys. Lett.* **1998**, *284*, 135–141.

(36) Link, S.; Burda, C.; Wang, Z. L.; El-Sayed, M. A. Electron Dynamics in Gold and Gold–Silver Alloy Nanoparticles: The Influence of a Nonequilibrium Electron Distribution and the Size Dependence of the Electron–Phonon Relaxation. *J. Chem. Phys.* **1999**, *111*, 1255–1264.

(37) Mohamed, M. B.; Ahmadi, T. S.; Link, S.; Braun, M.; El-Sayed, M.A. Hot Electron and Phonon Dynamics of Gold Nanoparticles Embedded in a Gel Matrix. *Chem. Phys. Lett.* **2001**, *343*, 55–63.

(38) Dowgiallo, A. M.; Knappenberger, K. L. Influence of Confined Fluids on Nanoparticle-to-Surroundings Energy Transfer. *J. Am. Chem. Soc.* **2011**, *134*, 19393–19400.

(39) Anger, P.; Bharadwaj, P.; Novotny, L. Enhancement and Quenching of Single-Molecule Fluorescence. *Phys. Rev. Lett.* **2006**, *96*, 113002.

(40) Banerji, N.; Cowan, S.; Leclerc, M.; Vauthey, E.; Heeger, A. J. Exciton Formation, Relaxation, and Decay in PCDTBT. *J. Am. Chem. Soc.* **2010**, *132*, 17459–17470.

(41) Duvanel, G.; Grilj, J.; Vauthey, E. Ultrafast Long-Distance Excitation Energy Transport in Donor–Bridge–Acceptor Systems. *J. Phys. Chem. A* **2013**, *117*, 918–928.

(42) Pelton, M.; Sader, J. E.; Burgin, J.; Liu, M.; Guyot-Sionnest, P.; Gosztola, D. Damping of Acoustic Vibrations in Gold Nanoparticles. *Nat. Nanotech.* **2009**, *4*, 492–495.

(43) Hodak, J. H.; Henglein, A.; Hartland, G. V. Size Dependent Properties of Au Particles: Coherent Excitation and Dephasing of Acoustic Vibrational Modes. *J. Chem. Phys.* **1999**, *111*, 8613–8621.

(44) Del Fatti, N.; Voisin, C.; Chevy, F.; Vallée, F.; Flytzanis, C. Coherent Acoustic Mode Oscillation and Damping in Silver Nanoparticles. *J. Chem. Phys.* **1999**, *110*, 11484–11487.

CHAPTER 7 – ANOMALOUS SIZE-DEPENDENT EXCITED-STATE RELAXATION DYNAMICS OF NANOGUMBOS*

7.1 Introduction

Frozen ionic liquids[1-3] with melting points ranging from 25 °C to 100 °C, and related organic salts with melting points up to 250 °C, have a wide range of chemical and material variability for controlled properties and are categorized using the term, group of uniform materials based on organic salts (GUMBOS).[4] Colloidal nanoparticles prepared from GUMBOS are known as nanoGUMBOS and are particularly interesting due to their optical and electronic properties, as well as their facile syntheses and highly diverse chemical functionalities. In this regard, nanoGUMBOS have been shown to be promising candidates for an extended list of potential applications including biomedical imaging,[5] antibiotics,[6,7] cancer therapy,[8] molecular sensing,[9-11] organic light-emitting diodes,[12,13] and photovoltaics.[14]

NanoGUMBOS provide exciting new opportunities for potential advances in optoelectronic applications due to their multifaceted photodynamic properties. In order to develop nanoGUMBOS for improved optoelectronic technologies, a more complete understanding of the fundamental mechanisms involving photoexcitation and excited-state relaxation dynamics of these nanomaterials is required. Processes such as intermolecular energy transfer, charge transfer, vibrational and phonon assisted relaxation, singlet to triplet state transitions, fluorescence, and hindered molecular conformational motions[15-18] are all expected to play an important role in the overall photophysics of nanoGUMBOS. The excited-state relaxation dynamics of molecules and nanostructures can be selectively probed using transient absorption spectroscopy, where the change in absorption is measured due to a pump pulse photoexcitation as a function of the pump-probe time delay with sub-picosecond resolution. Literature on recent transient absorption research has revealed studies of ionic liquid based systems,[19,20] single-walled carbon nanotubes,[21] electron- and hole-doped cuprates,[22] and dye-sensitized TiO_2.[23,24] In addition, short-lived

*"Reprinted with permission from [Karam, T. E.; Siraj, N.; Warner, I. M.; Haber, L. H. J. Phys. Chem. C 2015, 119, 28206−28213]. Copyright [2015] American Chemical Society."

quasiparticle dynamics of polaritonic states,[25] excitons,[26,27] and phonons[28] have been recently investigated using transient absorption measurements.

It is well established that ruthenium bipyridine and its derivatives are important as efficient sensitizers for dye-sensitized solar cells (DSSCs) because these molecules can bind to titanium dioxide surfaces and inject electrons into this high-band gap semiconductor upon photoexcitation for light harvesting and inexpensive, clean energy generation.[29–31] Time-resolved optical spectroscopy has been used to investigate the charge injection from ruthenium bipyridine derivatives into TiO_2 substrates.[32-34] Alternative DSSC technology utilizes recent advances in solid-state Perovskite $CH_3NH_3PbI_3$-sensitized solar cells[35,36] which show improved solar energy efficiencies since these designs avoid depletion in the electrical current due to losses at the nanostructured semiconductor interface. Another promising strategy for improved photovoltaic efficiencies relies on hot-carrier extraction, where photon energies above the band gap can be converted to electricity before the excited states of the electrons and holes are lost to heat.[37,38] This approach is proposed to improve light-to-electricity efficiency limits and possibly surpass the Shockley-Quiesser limit,[39] although additional research is needed to study these new optoelectronic materials with long-lived phonon states for hot-carrier extraction photovoltaic implementation.

In this chapter, we investigate the excited-state relaxation dynamics of size-selected ruthenium(II)-tris-(2,2'-bipyridine)-bis(pentafluoroethylsulfonyl)imide ($[Ru(bipy)_3][BETI]_2$) nanoGUMBOS in aqueous media using pump-probe time-resolved transient absorption spectroscopy. The results of these studies are compared to corresponding measurements of $Ru(bipy)_3Cl_2$ dissolved in water, and show spectral shifts and size-dependent relaxation dynamics for nanoGUMBOS with diameters varying from 20 nm to 100 nm. The excited-state dynamics of these nanoGUMBOS are similar to those of the parent compound at high pump pulse energies. Furthermore, the excited-state lifetimes increase with increasing size of these nanoGUMBOS. An additional and much faster relaxation pathway is measured and is attributed to intermolecular energy transfer (IMET), which increases with increasing nanoparticle size. An anomalous behavior of large, size-dependent phonon oscillations is also observed and persists during the entire relaxation dynamics timescales, suggesting very low coupling between the electronic and phonon states.

Thus, these colloidal $[Ru(bipy)_3][BETI]_2$ nanoGUMBOS display fascinating photodynamic properties, which make them potential candidates for highly efficient dye-sensitized solar cells and other optoelectronic devices, including hot-carrier extraction photovoltaics.

7.2 Experimental Section

7.2.1 NanoGUMBOS Synthesis

Tris (2,2'-bipyridyl)dichlororuthenium (II) hexahydrate (Ru(bipy)3Cl2.6H2O) and lithium bis (pentafluoroethylsulfonyl)imide (LiBETI) are purchased from Sigma Aldrich and are used as received, while methanol (MeOH) is purchased from OmniSolv. Triply deionized water (18.2 MΩ. cm) is obtained by use of an Elga model PURELAB ultra water-filtration system and is used for all ion exchange reactions and nanoGUMBOS preparation. An anion exchange reaction is performed using 0.13 mol of $Ru(bipy)_3Cl_2$ and 0.27 mol of LiBETI dissolved separately in equal volumes of water. These solutions are mixed and stirred for a few hours, followed by ultrafast centrifugation at 3800 rpm to separate the $[Ru(bipy)_3][BETI]_2$ orange precipitate. The product precipitate is washed several times with fresh deionized distilled water to remove the lithium chloride byproduct. The product is then freeze-dried overnight to remove trace water, providing an overall product yield of approximately 99%.

The size-selected colloidal $[Ru(bipy)_3][BETI]_2$ nanoparticle samples in aqueous suspension are prepared using an additive reprecipitation method[5,1240,41] by adding 1.05 mL of 2 mM $[Ru(bipy)_3][BETI]_2$ in methanol to a vial containing 30 mL of deionized distilled water in an ice bath, followed by 5 min of sonication. A variable power ultrasonic processor (model VCX 750, Sonics and Materials Inc.) with a 6.5 mm tapered microtip is used for preparation of 23 nm ± 5 nm and 56 nm ± 13 nm nanoGUMBOS under 40% (25 W) and 25% (13 W) power, respectively. Another ultrasonic processor (model 08849-00 cleaner, Cole-Parmer Instrument Company) is used to prepare 97 nm ± 19 nm nanoGUMBOS. The crystal structure of the $[Ru(bipy)_3][BETI]_2$ nanoGUMBOS is shown in Figure 7.1 and is determined to be monoclinic with a C2/c space group using X-ray crystallography. Such crystallinity differs from nanoGUMBOS studied to date since most have been observed to be amorphous. Additional information on the synthesis and

characterization of the nanoGUMBOS samples, including transmission electron microscopy, thermogravimetric analysis, and extinction spectroscopy, is provided in the Appendix 6.

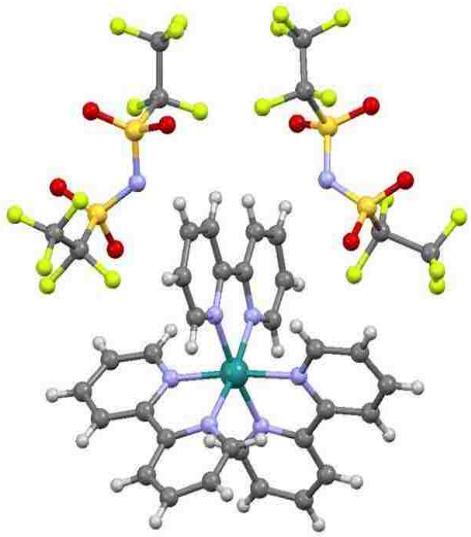

Figure 7.1. Crystal structure of $[Ru(bipy)_3][BETI]_2$ GUMBOS obtained from X-ray crystallography.

7.2.2 Transient Absorption Setup

The transient absorption spectroscopy setup consists of an ultrafast laser system, an optical setup, and a fiber optic spectrometer detector.[42] An amplified titanium:sapphire laser system produces 0.7 mJ, 75 fs pulses centered at 800 nm with a repetition rate of 10 kHz. The optical setup includes a beam splitter to separate the pump and probe pulses and a retroreflector on a computer-controlled translation stage to control the pump-probe temporal delay. Pump-probe transient absorption spectroscopy is used to measure the ultrafast dynamics of the sample by monitoring a change in absorption (ΔA) due to the pump pulse at different pump-probe time delays. The pump beam is used to generate the 400 nm pump pulse by frequency doubling with a nonlinear beta barium borate crystal, followed by an optical filter to remove the fundamental 800 nm light before focusing to the sample. The probe beam is focused into a fused quartz flow cell containing water to generate the femtosecond white light probe pulses that are refocused to a spatial overlap with the pump pulse at the sample, which is contained in a 3 mm fused quartz flow cell. The linear polarizations of the pump and probe electric field vectors are aligned. Spectra are acquired from 400 nm to 1000 nm using the fiber optic spectrometer detector. A computer-controlled beam block opens and

shuts on the pump pulse in synchronization with an automated file saving program, and several time-resolved spectral scans are taken for each sample for statistical analysis.

7.3 Results and Discussion

Pump-probe transient absorption measurements are first taken on a 0.4 mM solution of $Ru(bipy)_3Cl_2$ in water in order to determine the excited-state relaxation dynamics of the $Ru(bipy)_3^{2+}$ cation. Figure 7.2 (a) shows transient absorption spectra of aqueous $Ru(bipy)_3Cl_2$ measured at different time delays using 400 nm excitation with a pump pulse energy of 15 μJ. The band centered at 450 nm is due to ground state depletion and the broad spectrum after 490 nm is attributed to excited-state absorption.[43,44] An isosbestic point between the two peaks is observed near 490 nm. The time-dependent transient absorption profiles are shown in Figure 7.2 (b) at a probe wavelength of 450 nm with different pump pulse energies. The magnitudes of the transient absorption signals increase with increasing pump pulse energies, and the time profiles are normalized for comparison. Under lower pump pulse energies of 10 and 15 μJ, very slow relaxation dynamics are observed which are consistent with the standard long-lived triplet metal to ligand charge transfer (MLCT) state, with a lifetime of approximately 600 ns,[45] which is much longer than the temporal range available in our optical setup. The standard ruthenium bipyridine excited-state dynamics are characterized by electronic population of the singlet MLCT excited state upon excitation followed by an ultrafast intersystem crossing to the long-lived triplet MLCT excited-state previously observed using transient absorption[43] and time-resolved fluorescence measurements.[46-48] Under higher pump pulse powers, significantly faster relaxation dynamics are observed. The time-dependent transient absorption profiles are analyzed over the wavelength range of 410 nm to 550 nm using a global analysis technique[17,44] described by a sum of exponentials to recover the lifetimes and corresponding spectra of the relaxation dynamics under higher pump pulse energies. Representative decay spectra obtained from the global analysis of the transient absorption time profiles of aqueous ruthenium bipyridine at pump pulse energy of 32 μJ are shown in Figure 7.2 (c), with corresponding lifetimes of 8020 ± 76 ps and 3590 ± 56 ps. These two decay spectra correspond to specific non-standard excited states that are accessed through multi-photon excitation, and

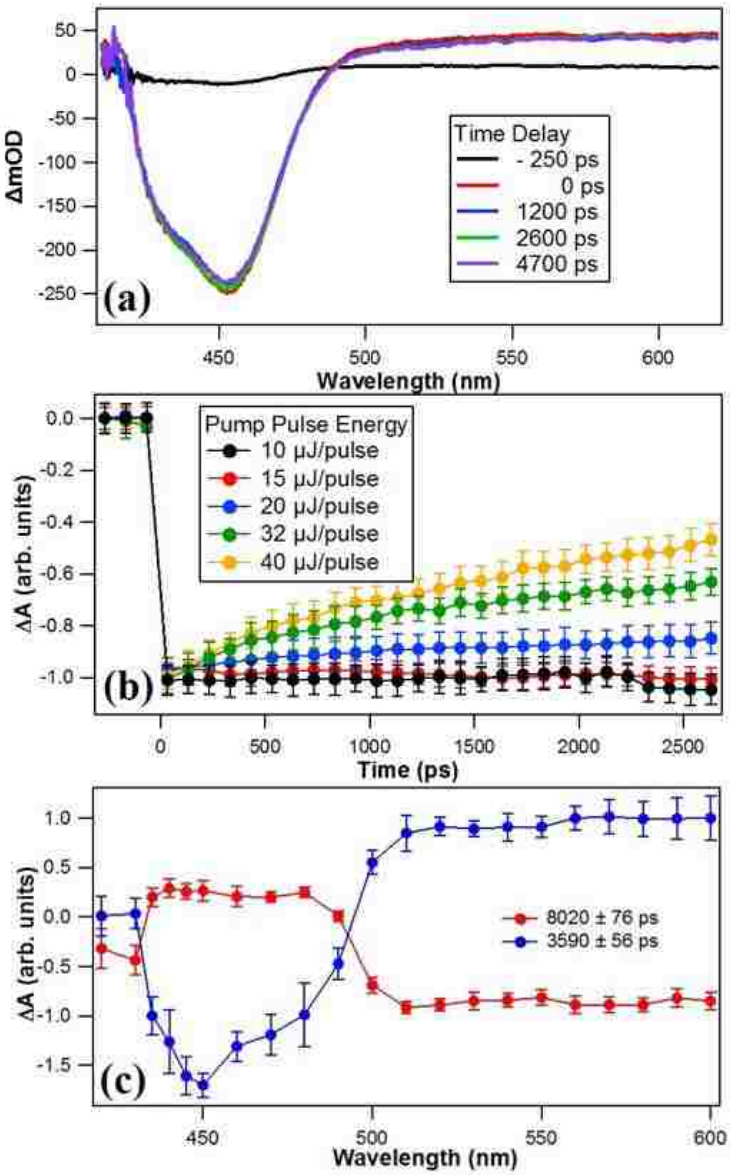

Figure 7.2. (a) Transient absorption spectra of 0.4 mM aqueous Ru(bipy)3Cl2 at different times delays using 400 nm excitation with an energy of 10 μJ/pulse. (b) Time profiles of the transient absorption spectra of 0.4 mM aqueous $Ru(bipy)_3Cl_2$ at 450 nm using different pump pulse energies. The spectra are normalized for clarity. (c) Representative decay spectra obtained using a sum of exponential fits of time-dependent transient absorption spectra of aqueous ruthenium bipyridine at pump pulse energy of 32 μJ.

can be tentatively assigned as a non-standard MLCT state and a non-standard metal centered (MC) state, respectively, due to their spectral features. The longer-lived state resembles the standard MLCT spectrum.[43,47] Triplet MC states are known to decay through intramolecular vibrational relaxation,[49-52] which is consistent with the shorter-lived decay spectrum.

Transient absorption spectroscopy measurements on the $[Ru(bipy)_3][BETI]_2$ nanoGUMBOS in water show significantly different excited-state relaxation dynamics as compared to the $Ru(bipy)_3Cl_2$ in water, and vary as a function of nanoparticle size. Additionally, time-dependent baseline shifts are observed due to heating dynamics of the nanoGUMBOS. Figure 7.3 displays the shift of the transient absorption baseline as a function of the pump-probe time delay for the three different $[Ru(bipy)_3][BETI]_2$ nanoGUMBOS sizes of 23 nm, 56 nm, and 97 nm using 400 nm excitation pulses at an energy of 10 μJ/pulse. The pump pulse causes the nanoparticles to heat, inducing a structural rearrangement in the crystal lattice. This results in a baseline shift that grows in magnitude and then decreases back to zero as the nanoparticle cools and returns to the original structure at longer time delays. The baseline shift is dependent on the nanoparticle size, where smaller nanoparticles show a maximum shift at shorter times and more rapid subsequent cooling as compared to the larger nanoparticles. Consequently, as expected, larger nanoparticles have slower heating and cooling dynamics following the pump pulse initialization.

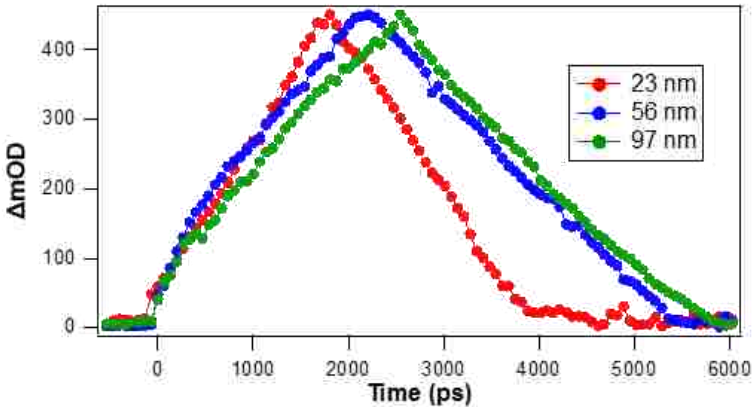

Figure 7.3. Shift in the baseline of the transient absorption spectra as a function of delay times for 23 ± 5 nm, 56 ± 13 nm, and 97 ± 19 nm $[Ru(bipy)_3][BETI]_2$ nanoGUMBOS using 400 nm pump pulse energy of 10 μJ.

Figure 7.4 shows the transient absorption spectra of 23, 56, and 97 nm $[Ru(bipy)_3][BETI]_2$ nanoGUMBOS at different pump-probe time delays using a pump pulse energy of 10 μJ after subtracting the baseline shift. A band centered at 420 nm is due to ground-state depletion, showing a spectral shift compared to $Ru(bipy)_3Cl_2$ in water. The broad spectra from 440 nm to 500 nm is from excited-state absorption, which is similar to $Ru(bipy)_3Cl_2$ in water. An isosbestic point is observed near 428 nm at

different time intervals for the different nanoparticle sizes. Figure 7.5 displays representative time profiles of the transient absorption spectra of (a) 23 ± 5 nm, (b) 56 ± 13 nm, and (c) 97 ± 19 nm $[Ru(bipy)_3][BETI]_2$ nanoGUMBOS at probe wavelengths of 420, 430, and 445 nm. The spectra are normalized and offset for clarity. These time profiles show that $[Ru(bipy)_3][BETI]_2$ nanoGUMBOS have more complicated relaxation dynamics than corresponding $Ru(bipy)_3Cl_2$ in water, as characterized by wavelength-dependent increases and decreases with superimposed periodic oscillations.

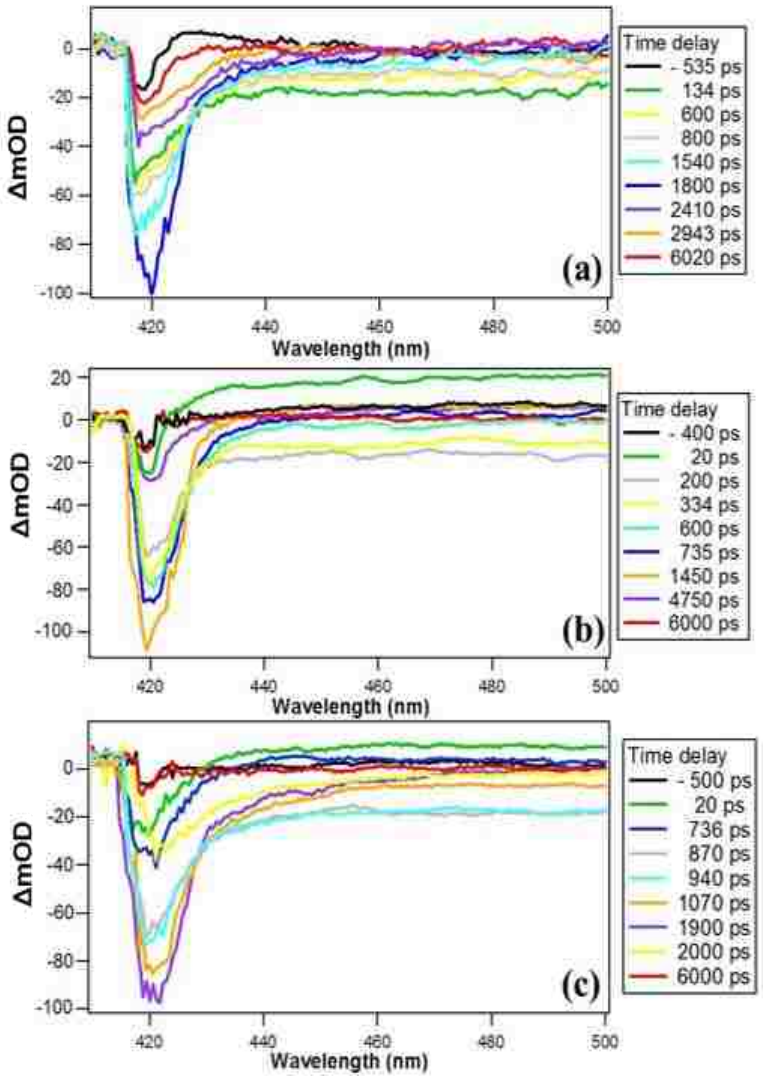

Figure 7.4. Transient absorption spectra of (a) 23 ± 5 nm, (b) 56 ± 13 nm, and (c) 97 ± 19 nm $[Ru(bipy)_3][BETI]_2$ nanoGUMBOS at different pump-probe time delays using a 400 nm pump pulse energy of 10 μJ and after correcting for the baseline shift.

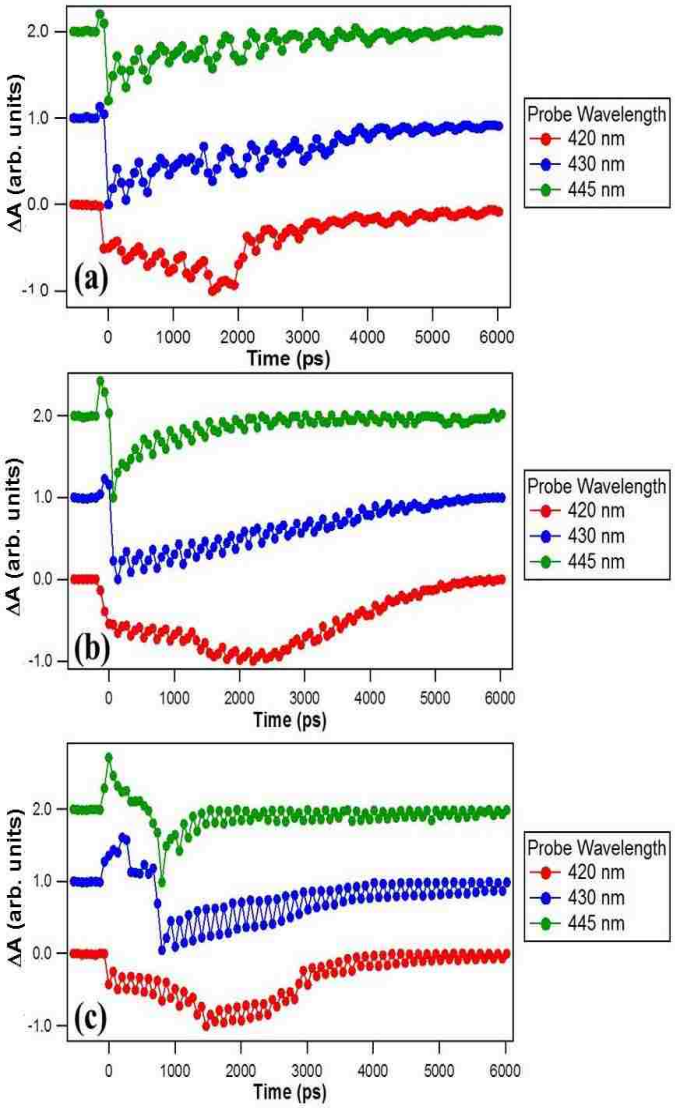

Figure 7.5. Time profiles of transient absorption spectra of (a) 23 ± 5 nm, (b) 56 ± 13 nm, and (c) 97 ± 19 nm $[Ru(bipy)_3][BETI]_2$ nanoGUMBOS. The time-dependent signals are integrated over 420 nm (red line), 430 nm (blue line), and 445 nm (green line). The time profiles are normalized and offset for clarity.

The time-dependent transient absorption profiles of the different nanoGUMBOS samples are analyzed over the wavelength range of 410 nm to 550 nm using a global analysis technique. Three lifetimes are required to adequately describe the relaxation dynamics of the nanoGUMBOS. Two of the resulting lifetimes have similar values as compared to the non-standard excited-state lifetimes from the $Ru(bipy)_3^{2+}$ cation under higher pump pulse energies, while the third lifetime is drastically shorter. The resulting decay spectra and corresponding lifetimes are plotted in Figure 7.6 for (a) 23 ± 5 nm, (b) 56 ± 13 nm, and (c) 97 ± 19 nm $[Ru(bipy)_3][BETI]_2$ nanoGUMBOS. As shown in Figure 7.6 (a) for 23 nm particles, the spectrally-

resolved time profiles are described by a convolution of three processes with lifetimes of 8364 ± 65 ps, 3702 ± 41 ps, and 431.5 ± 76 ps. In the case of 56 nm particles, shown in Figure 7.6 (b), the three processes have corresponding lifetimes of 8775 ± 136 ps, 4104 ± 55 ps, and 761 ± 22 ps. The spectrally-resolved time profiles for 97 nm particles, shown in Figure 7.6 (c), have corresponding lifetimes of 9502 ± 74 ps, 4516 ± 72 ps, and 1135 ± 122 ps.

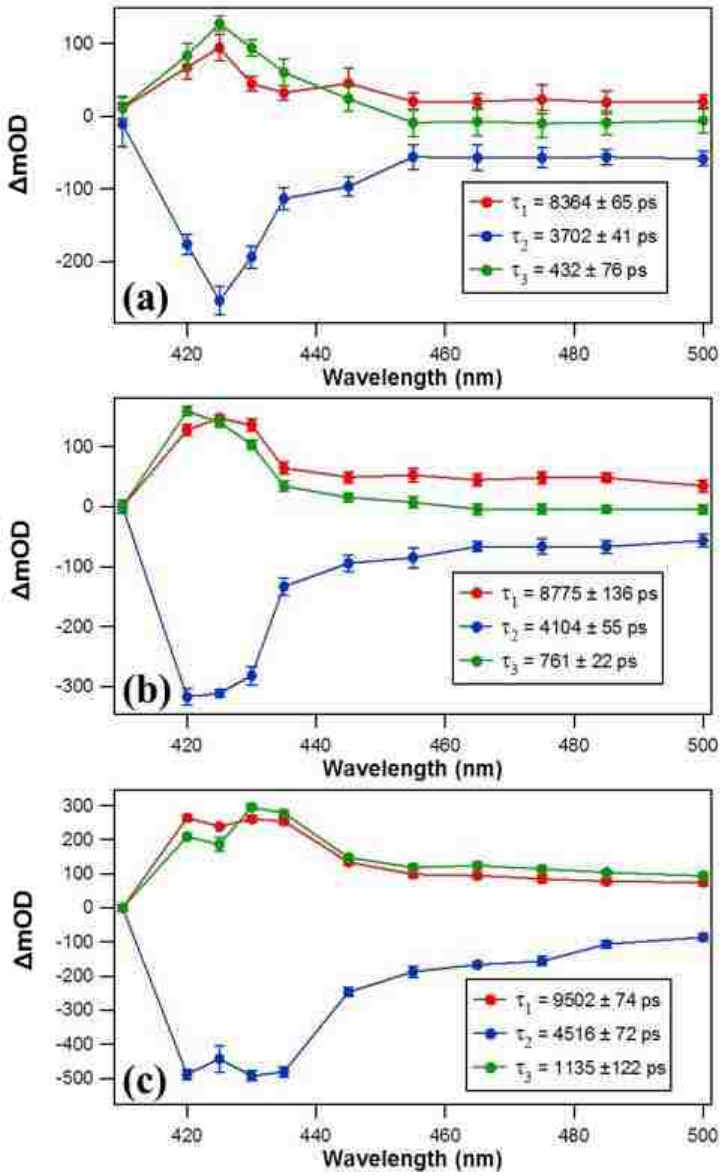

Figure 7.6. Decay spectra obtained using a sum of exponential fits of time-dependent transient absorption spectra of (a) 23 ± 5 nm, (b) 56 ± 13 nm, and (c) 97 ± 19 $[Ru(bipy)_3][BETI]_2$ nanoGUMBOS.

The time constants obtained from fits of the experimental data using sums of exponential functions show that relaxation dynamics of these nanoGUMBOS are size dependent. The first two excited-state lifetimes, τ_1 and τ_2, are similar to the specific non-standard excited-states observed at higher pump pulse energies in the parent compound. Both lifetimes are observed to be faster than corresponding values obtained at higher pump pulse energies in the aqueous dye and increase as nanoGUMBOS size increases. These results suggest that the decay lifetimes in these nanoGUMBOS are slightly altered due to molecular confinement leading to increased lifetimes, with larger nanoparticles having larger confinement effects. The third lifetime, τ_3, is not observed in aqueous $Ru(bipy)_3Cl_2$ dynamics and is attributed to intermolecular energy transfer (IMET) from excited-state dipole-dipole coupling between nearby $Ru(bipy)_3^{2+}$ cations in the nanoGUMBOS material. The shorter IMET lifetimes varies from 0.43 ns, 0.76 ns, and 1.14 ns for the three increasing nanoGUMBOS sizes, which is consistent with the concept that larger nanoGUMBOS volumes require longer times for intermolecular energy transfer to reach equilibrium in energy redistribution. The IMET decay spectra suggest that this process includes a net population transfer from the non-standard triplet MLCT state to the non-standard triplet MC state. Thus, the size-dependent excited-state dynamics of these $[Ru(bipy)_3][BETI]_2$ nanoGUMBOS suggest a new capability for control and optimization of optoelectronic photodynamics in applications such as dye-sensitized solar cells and other optoelectronic devices.

Oscillations are observed to be superimposed on excited-state relaxation dynamics of nanoGUMBOS and are attributed to coherent phonons. These oscillations are persistent through the entire time profiles for all nanoparticle sizes, but, as expected, are not present in the aqueous $Ru(bipy)_3Cl_2$ dynamics. The oscillations of phonons from residuals of time profiles are fit using an exponentially decaying sine function given by $I(t) = y_0 + A\exp(-t/\tau_4)\sin(2\pi ft + \varphi)$, where f, φ, and τ_4 are the frequency, the phase shift, and phonon lifetime, respectively. Representative residual signal oscillations of phonons and their corresponding fits are shown in the Appendix 6. The very low frequencies of the phonon oscillations indicate that they are likely acoustic phonon modes associated with the crystal lattice. The phonon oscillation periods are determined to be 334 ps ± 6 ps, 209 ps ± 5 ps, and 140 ps ± 4 ps for the 23

nm, 56 nm, and 97 nm nanoGUMBOS, respectively. Similar long-lived phonon oscillations have been previously investigated in molecular solids with frequencies on the order of a few GHz.[53,54] This size-dependent frequency trend is opposite to the case of phonons in metallic and semiconductor nanocrystals where the acoustic phonon breathing mode oscillation frequencies decrease with increasing nanoparticle size.[55, 56] The increase of phonon frequencies of these nanoGUMBOS with increasing nanoparticle size is attributed to effects from bulk and sheer viscosity.[57,58] [Ru(bipy)3][BETI]2 nanoGUMBOS have crystalline structures that are held together by much weaker forces compared to closely-packed metallic and semiconductor materials and thus the interaction with the solvent is expected to play a much more significant role. The size-dependent phonon frequencies can be described using a model based on the size-dependent force constant of the nanocrystals,[59,60] which indicates that the phonon frequency can increase as the nanoparticle size increases when a strong surface stress between the nanomaterial at the solvent causes a lattice contraction. Using estimates for the nanoGUMBOS in water including the compressibility, the surface stress, and the size-dependent bond distances provides a theoretical description of the size-dependent phonon frequencies that agrees with our experimental measurements. More details about this theoretical model are included in the Appendix 6.

The phonon lifetimes vary from 3.4 ns ± 0.4 ns, 4.1 ns ± 0.5 ns, and 5.2 ns ± 0.6 ns for the three nanoGUMBOS sizes, respectively. These very long phonon lifetimes demonstrate that there is a very low coupling between the acoustic phonon motion and other electronic or phonon degrees of freedom, leading to a very slow phonon relaxation and dephasing rate. Additional work is needed to determine the different possible phonon modes of the crystal structure which can couple to these coherent acoustic phonons. The excited electronic states are understood to be first localized on the $Ru(bipy)_3^{2+}$ molecular ion, then energy transfer occurs through dipole-dipole coupling. This contrasts with nanoparticles composed of semiconductor materials, such as quantum dots, where excited conduction electrons and the corresponding holes interact through electrostatic forces, and where increased phonon lifetimes are attributed to the bottleneck effect.[61-64] In quantum dots, the bottleneck effect describes conditions where the electron-phonon scattering rates are suppressed due to quantum confinement. In the nanoGUMBOS studied here, a

fundamentally different process leads to the long phonon lifetimes, where the excited electronic states of the $Ru(bipy)_3^{2+}$ molecular ion are largely decoupled from the phonon oscillations of the crystal lattice. Additional work is needed to determine the mechanisms behind the phonon lifetimes, which may have contributions from both damping and dephasing. Larger nanoGUMBOS may have longer phonon lifetimes, suggesting that phonon damping and dephasing occurs faster at the nanoparticle surface due to interactions with the solvent. Additionally, the IMET occurs much faster in nanoGUMBOS than corresponding excited-state relaxation lifetimes of the dye molecule. The observed long-lived phonons and fast IMET suggest these nanoGUMBOS as potential materials for hot carrier solar cells that may have significantly increased efficiencies through extraction of extra photon energy above the band gap before dissipation into heat.

7.4 Conclusion

This investigation presents the first transient absorption studies of the ultrafast dynamics of nanoGUMBOS. These $[Ru(bipy)_3][BETI]_2$ nanoGUMBOS are shown to have size dependent excited-state relaxation dynamics, with two lifetimes that are similar to the non-standard excited-state lifetimes of the ruthenium bipyridine cation in water under high pump pulse energies, and with an additional faster relaxation pathway that is attributed to intermolecular energy transfer. The non-standard excited-state lifetimes and the IMET dynamics increase as the nanoparticle diameters increase over the range of 20 nm to 100 nm. In addition, long-lived phonon oscillations are observed with frequencies that increase as the nanoparticle size is increased due to effects of bulk and sheer viscosity. The efficient photoexcitation, controllable energy transfer, and excited-state relaxation dynamics suggest that these particles are promising candidates for applications in optoelectronics and DSSC sensitizers with the possibility of achieving higher solar energy conversions due to size-dependent photodynamics and long-lived phonon states.

7.5 References

(1) Armand, M.; Endres, F.; MacFarlane, D. R.; Ohno, H.; Scrosati, B.; Ionic-Liquid Materials for the Electrochemical Challenges of the Future. *Nat. Mat.* **2009**, *8*, 621–629.

(2) Rogers, R. D.; Seddon, K. R.; Ionic Liquids – Solvents of the Future? *Science* **2003**, *302*, 792–793.

(3) Plechkova, N. V.; Seddon, K.R.; Applications of Ionic Liquids in the Chemical Industry. *Chem. Soc. Rev.* 2008, 37, 123–150.

(4) Warner, I.M.; El-Zahab, B.; Siraj, N. Perspectives on Moving Ionic Liquid Chemistry into the Solid Phase. *Anal. Chem.* **2014**, *86*, 7184–7191.

(5) Bwambok, D. K.; El-Zahab, B.; Challa, S. K.; Li, M.; Chandler, L.; Baker, G. A.; Warner, I. M.; Near-Infrared Fluorescent NanoGUMBOS for Biomedical Imaging. *ACS Nano* 2009, *3*, 3854–3860.

(6) Cole, M. R.; Li, M.; Jadeja, R.; El-Zahab, B.; Hayes, D.; Hobden, J. A.; Janes, M. E.; Warner, I. M.; Minimizing Human Infection from Escherichia Coli O157:H7 Using GUMBOS. *J. Antimicrob. Chemother.* **2013**, *68*, 1312–1318.

(7) Cole, M. R.; Li, M.; El-Zahab, B.; Janes, M. E.; Hayes, D.; Warner, I. M.; Design, Synthesis, and Biological Evaluation of β-Lactam Antibiotic-Based Imidazolium- and Pyridinium-Type Ionic Liquids. *Chem. Biol. Drug. Des*. **2011**, *78*, 33–41.

(8) Magut, P. K. S.; Das, S.; Fernand, V. E.; Losso, J.; McDonough, K.; Naylor, B. M.; Aggarwal, S.; Warner, I. M.; Tunable Cytotoxicity of Rhodamine 6G via Anion Variations. *J. Am. Chem. Soc.* **2013**, *135*, 15873–15879.

(9) Das, S.; Magut, P. K. S.; de Rooy, S. L.; Hasan, F.; Warner, I. M. Ionic Liquid-Based Fluorescein Colorimetric pH Nanosensors. *RSC Adv.* **2013**, *3,* 21054–21061.

(10) Lu, C.; Das.; Magut, P. K. S.; Li, M.; El-Zahab, B.; Warner, I. M.; Irradiation Induced Fluorescence Enhancement in PEGylated Cyanine-Based NIR Nano- and Mesoscale GUMBOS. *Langmuir* **2012**, *28*, 14415–14423.

(11) Regmi, B. P.; Monk, J.; El-Zahab, B.; Das, S.; Hung, F. R.; Hayes, D.J.; Warner, I. M. A Novel Composite Film for Detection and Molecular Weight Determination of Organic Vapors. *J. Mater. Chem.* **2012***, 22*, 13732–13741.

(12) Das, S.; Bwambok, D.; El-Zahab, B.; Monk, J.; de Rooy, S. L.; Challa, S.; Li, M.; Hung, F. R.; Baker, G. A.; Warner, I. M.; Nontemplated Approach to Tuning the Spectral Properties of Cyanine-Based Fluorescent NanoGUMBOS. *Langmuir* **2010**, *26*, 12867–12876.

(13) Siraj, N.; Hasan, F.; Das, S.; Kiruri, L. W.; Gall, K. E. S.; Baker, G.A.; Warner, I. M. Carbazole-Derived Group of Uniform Materials Based on Organic Salts: Solid State Fluorescent Analogues of Ionic Liquids for Potential Applications in Organic-Based Blue Light-Emitting Diodes. *J. Phys. Chem. C* **2014**, *118*, 2312–2320.

(14) Jordan, A. N.; Das, S.; Siraj, N.; de Rooy, S. L.; Li, M.; El-Zahab, B.; Chandler, L.; Baker, G. A.; Warner, I. M. Anion-controlled Morphologies and Spectral Features of Cyanine-Based NanoGUMBOS – an Improved Photosensitizer. *Nanoscale* **2012**, *4*, 5031–5038.

(15) Duncan, W. R.; Prezhdo, O. V. Theoretical Studies of Photoinduced Electron Transfer in Dye-Sensitized TiO2. *Annu. Rev. Phys. Chem.* **2007**, *58*, 143–184.

(16) Haber, L. H.; Eisenthal, K. B. Molecular Excited-State Relaxation Dynamics at the Colloidal Microparticle Interface Monitored with Pump–Probe Second Harmonic Generation. *J. Phys. Chem. B* **2013**, *117*, 4249–4253.

(17) Duvanel, G.; Grilj, J.; Vauthey, E. Ultrafast Long-Distance Excitation Energy Transport in Donor–Bridge–Acceptor Systems. *J. Phys. Chem. A* **2013**, *117*, 918–928.

(18) Wilson, M. W. B.; Roa, A.; Ehrler, B.; Friend, A. H. Singlet Exciton Fission in Polycrystalline Pentacene: From Photophysics toward Devices. *Acc. Chem. Res.* **2013**, *46*, 1330–1338.

(19) Wang, P.; Zakeeruddin, S. M.; Moser, J. E.; Humphry-Baker, R.; Grätzel, M. A. Solvent-Free, $SeCN^-$/$(SeCN)^{3-}$ Based Ionic Liquid Electrolyte for High-Efficiency Dye-Sensitized Nanocrystalline Solar Cells. *J. Am. Chem. Soc.* **2004**, *126*, 7164–7165.

(20) Nese, C.; Unterreiner, A –N. Photochemical Processes in Ionic Liquids on Ultrafast Timescales. *Phys. Chem. Chem. Phys.* **2010**, *12*, 1698–1708.

(21) Koyama, T.; Yoshimitsu, S.; Miyata, Y.; Shinohara, H.; Kishida, H.; Nakamura, A. Transient Absorption Kinetics Associated with Higher Exciton States in Semiconducting Single-Walled Carbon Nanotubes: Relaxation of Excitons and Phonons. *J. Phys. Chem. C* **2013**, *117*, 20289–20299.

(22) Okamoto, H.; Miyagoe, T.; Kobayashi, K.; Uemura, H.; Nishioka, H.; Matsuzaki, H.; Sawa, A.; Tokura, Y. Ultrafast Charge Dynamics in Photoexcited Nd2CuO4 and La2CuO4 Cuprate Compounds Investigated by Femtosecond Absorption Spectroscopy. *Phys. Rev. B* **2012**, *82*, 060513 (R).

(23) Wenger, S.; Bouit, P –A.; Chen, Q.; Teuscher, J.; Di Censo, D.; Humphry-Baker, R.; Moser, J. –E.; Delgado, J. L.; Martin, N.; Zakeeruddin, S. M et al, Efficient Electron Transfer and Sensitizer Regeneration in Stable π-Extended Tetrathiafulvalene-Sensitized Solar Cells. *J. Am. Chem. Soc.* **2012**, *132*, 5165–5169.

(24) Mahanta, S.; Furube, A.; Matsuzaki, H.; Murakami, T. N. Electron Injection Efficiency in Ru-Dye Sensitized TiO2 in the Presence of Room Temperature Ionic Liquid Solvents Probed by Femtosecond Transient Absorption Spectroscopy: Effect of Varying Anions. *J. Phys. Chem. C* **2012**, *116*, 20213–20219.

(25) Hutchison, J.; Shwartz, T.; Genet, C.; Devaux, E.; Ebbesen, T. W. Modifying Chemical Landscapes by Coupling to Vacuum Fields. *Angew. Chem. Int. Ed.* **2012***, 51*, 1592–1596.

(26) Reid, O. G.; Rumbles, G. Quantitative Transient Absorption Measurements of Polaron Yield and Absorption Coefficient in Neat Conjugated Polymers. *J. Phys. Chem. Lett.* **2013**, *4*, 2348–2355.

(27) Guo, J.; Ohkita, H.; Benten, H.; Ito, S. Near-IR Femtosecond Transient Absorption Spectroscopy of Ultrafast Polaron and Triplet Exciton Formation in Polythiophene Films with Different Regioregularities. *J. Am. Chem. Soc.* **2009**, *131*, 16869–16880.

(28) Staleva, H.; Hartland, G. V. Transient Absorption Studies of Single Silver Nanocubes. *J. Phys. Chem. C* **2008**, *112*, 7535–7539.

(29) Wang, P.; Zakeeruddin, S. M.; Moser, J. E.; Nazeeruddin, M. L.; Sekiguchi, T.; Grätzel, M. A Stable Quasi-Solid-State Dye-Sensitized Solar Cell with an Amphiphilic Ruthenium Sensitizer and Polymer Gel Electrolyte. *Nat. Mater.* **2003**, *2*, 402–407.

(30) Chen, C. –Y.; Wang, M.; Li, J. –Y.; Pootrakulchote, N.; Alibabaei, L.; Ngoc-le, C.; Decoppet, J. –D.; Tsai, J. –H.; Grätzel, C.; Wu, C. –G.; et al. Highly Efficient Light-Harvesting Ruthenium Sensitizer for Thin-Film Dye-Sensitized Solar Cells. *ACS Nano* **2009**, *3*, 3103–3109.

(31) Cao, Y.; Bai, Y.; Yu, Q.; Cheng, Y.; Liu, S.; Shi, D.; Gao, F.; Wang, P. Dye-Sensitized Solar Cells with a High Absorptivity Ruthenium Sensitizer Featuring a 2-(Hexylthio)thiophene Conjugated Bipyridine. *J. Phys. Chem. C* **2009**, *113*, 6290–6297.

(32) Merrins, A.; Kleverlaan, C.; Will, G.; Nagaraja Rao.; S.; Scandola, F.; Fitzmaurice, D. Time-Resolved Optical Spectroscopy of Heterosupramolecular Assemblies Based on Nanostructured TiO2 Films Modified by Chemisorption of Covalently Linked Ruthenium and Viologen Complex Components. *J. Phys. Chem. B* **2001**, *105*, 2998–3004.

(33) Vinodgopal, K.; Hua, X.; Dahlgren, R. L.; Lappin, A. G.; Patterson, L. K.; Kamat, P. V. Photochemistry of $Ru(bpy)_2(dcbpy)^{2+}$ on Al_2O_3 and TiO_2 Surfaces. An Insight into the Mechanism of Photosensitization. *J. Phys. Chem.* **1995**, *99*, 10883–10889.

(34) Heimer, T. A.; Heilweil, E. J. Direct Time-Resolved Infrared Measurement of Electron Injection in Dye-Sensitized Titanium Dioxide Films. *J. Phys. Chem. B* **1997**, *101*, 10990–10993.

(35) Park, N. –G. Organometal Perovskite Light Absorbers toward a 20% Efficiency Low-Cost Solid State Mesoscopic Solar Cell. *J. Phys. Chem. Lett.* **2013**, *4*, 2412–2429.

(36) Kin, H. –S.; Lee, J. –W.; Yantara, N.; Boix, P. P.; Kulkarni, S. A.; Mhaisalkar, S.; Gratzel, M. Park, N. –G. High Efficiency Solid-State Sensitized Solar Cell-Based on Submicrometer Rutile TiO2 Nanorod and CH3NH3PbI3 Perovskite Sensitizer. *Nano Lett.* **2013**, *13*, 2412–2417.

(37) Tisdale, W. A.; Williams, K. J.; Timp, B. A.; Norris, D. J.; Aydil, E. S.; Zhu, X, -Y. Hot-Electron Transfer from Semiconductor Nanocrystals. *Science* **2010**, *328,* 1543–1547.

(38) Shockley, W.; Queisser, H. J. Detailed Balance Limit of Efficiency of p-n Junction Solar Cells. *J. Appl. Phys.* **1961**, *32*, 510–519.

(39) Nelson, C. A.; Monahan, N. R.; Zhu, X. –Y. Exceeding the Shockley–Queisser Limit in Solar Energy Conversion. *Energy Environ. Sci.* **2013**, *6*, 3508–3519.

(40) Tesfai, A.; El-Zahab, B.; Kelley, A. T.; Li, M.; Garno, J. C.; Baker, G. A.; Warner, I. M. Magnetic and Nonmagnetic Nanoparticles from a Group of Uniform Materials Based on Organic Salts. *ACS Nano* **2009**, *3*, 3244–3250.

(41) Tesfai, A.; El-Zahab, B.; Bwambok, D. K.; Baker, G. A.; Fakayode, S. O.; Lowry, M.; Warner, I. M. Controllable Formation of Ionic Liquid Micro- and Nanoparticles via a Melt–Emulsion–Quench Approach. *Nano Lett* **2008**, *8*, 897–901.

(42) Karam, T. E.; Smith, H. T.; Haber, L. H. Enhanced Photothermal Effects and Excited-State Dynamics of Plasmonic Size-Controlled Gold–Silver–Gold Core–Shell–Shell Nanoparticles. *J. Phys. Chem. C* **2015**, *119*, 18573–18580.

(43) Tarnovsky, A. N.; Gawelda, W.; Johnson, M.; Bressler, C.; Chergui, M. Photexcitation of Aqueous Ruthenium(II)-tris-(2,2‘-bipyridine) with High-Intensity Femtosecond Laser Pulses. *J. Phys. Chem. B* **2006**, *110*, 26497–26505.

(44) Sun, Q.; Mosquera-Vazquez, S.; Daku, L. M. L.; Guénée, L.; Goodwin, H. A.; Vauthey, E.; Hauser, A. Experimental Evidence of Ultrafast Quenching of the ^{3}MLCT Luminescence in Ruthenium(II) Tris-bipyridyl Complexes via a 3dd State. *J. Am. Chem. Soc.* **2013**, *135*, 13660–13663.

(45) Bradely, P. G.; Kress, N.; Hornberger, B. A.; Dallinger, R. F.; Woodruff, W. H. Vibrational Spectroscopy of the Electronically Excited State. 5. Time-Resolved Resonance Raman Study of Tris(bipyridine)ruthenium(11) and Related Complexes. Definitive Evidence for the "Localized" MLCT State. *J. Am. Chem. Soc.* **1981**, *103*. 1441–1446.

(46) Bhasikuttan, A. C.; Suzuki, M.; Nakashima, S.; Okada, T. Ultrafast Fluorescence Detection in Tris(2,2'-bipyridine)ruthenium(II) Complex in Solution: Relaxation Dynamics Involving Higher Excited States. *J. Am. Chem. Soc.* **2002**, *124*, 8398–8405.

(47) Browne, W. R.; Coates, C. G.; Brady, C.; Matousek, P.; Towrie, M.; Botchway, S. W.; Parker, A. W.; Vos, J. G.; McGarvey, J. J. Isotope Effects on the Picosecond Time-Resolved Emission Spectroscopy of Tris(2,2'-bipyridine)ruthenium (II). *J. Am. Chem. Soc.* **2003**, *125*, 1706–1707.

(48) Cannizzo, A.; van Mourik, F.; Gawelda, W.; Zgrablic, G.; Bressler, C.; Chergui, M. Broadband Femtosecond Fluorescence Spectroscopy of $[Ru(bpy)_3]^{2+}$. *Angew. Chem. Int. Ed.* **2006**, *45*, 3174–3176.

(49) Balzani, V.; Sabbatini, N.; Scandola, F. "Second-Sphere" Photochemistry and Photophysics of Coordination Compounds. *Chem. Rev.* **1986***, 86*, 319–337.

(50) Jakubikova, E.; Chen, W.; Dattelbaum, D. M.; Rein, F. N.; Rocha, R. C.; Martin, R. L.; Batista, E. R. Electronic Structure and Spectroscopy of $[Ru(tpy)_2]^{2+}$, $[Ru(tpy)(bpy)(H_2O)]^{2+}$, and $[Ru(tpy)(bpy)(Cl)]^{+}$. *Inorg. Chem.* **2009***, 48*, 10720–10725.

(51) Breivogel, A.; Meister, M.; Förster, C.; Laquai, F.; Heinze, K. Excited State Tuning of Bis(tridentate) Ruthenium(II) Polypyridine Chromophores by Push–Pull Effects and Bite Angle Optimization: A Comprehensive Experimental and Theoretical Study. *Chem. Eur. J.* **2013**, *19*, 13745–13760.

(52) Adamson, A. W.; Demas, J. N. New Photosensitizer Tris(2,2'-bipyridine)Ruthenium(II) Chloride. *J. Am. Chem. Soc.* **1971,** *93*, 1800–1801.

(53) Nelson, K. A.; Fayer, M. D. Laser Induced Phonons: A Probe of Intermolecular Interactions in Molecular Solids. *J. Phys. Chem.* **1980**, *72*, 5202–5218.

(54) Kim, H.; Dlott, D. D. Theory of Ultrahot Molecular solids: Vibrational Cooling and Shock-Induced Multiphonon Up Pumping in Crystalline Naphthalene. *J. Chem. Phys.* **1990**, *93*, 1695–1709.

(55) Mahmoud, M. A.; O'Niel, D.; El-Sayed, M. A. Shape- and Symmetry-Dependent Mechanical Properties of Metallic Gold and Silver on the Nanoscale. *Nano Lett.* **2013**, *12*, 743–748.

(56) Huxter, V. M.; Lee, A.; Lo, S. S.; Scholes, G. D. CdSe Nanoparticle Elasticity and Surface Energy. *Nano Lett.* **2009**, *9*, 405–409.

(57) Saviot, L.; Netting, C. H.; Murray, D. B. Damping by Bulk and Shear Viscosity of Confined Acoustic Phonons for Nanostructures in Aqueous Solution. *J. Phys. Chem. B* **2007**, *111*, 7457–7461.

(58) Major, T. A.; Lo, S. S.; Yu, K.; Hartland, G. V. Time-Resolved Studies of the Acoustic Vibrational Modes of Metal and Semiconductor Nano-Objects. *J. Phys. Chem. Lett.* **2014**, *5*, 866–874.

(59) Liang, L. –H.; Shen, C. –M.; Chen, X.-P.; Lui, W. –M.; Gao, H. –J. The Size-Dependent Phonon Frequency of Semiconductor Nanocrystals. *J. Phys: Condens. Matter* **2004**, 16, 267–272.

(60) Jiang, Q.; Liang, L. –H.; Zhao, D. –S.; Lattice Contraction and Surface Stress of fcc Nanocrystals. *J. Phys. Chem. B* **2001**, *105*, 6275–6277.

(61) Nozik, A. J. Spectroscopy and Hot Electron Relaxation Dynamics in Semiconductor Quantum Wells and Quantum Dots. *Annu. Rev. Phys. Chem.* **2001**, *52*, 193–231.

(62) Guyot-Sionnest, P.; Pandey, A. Slow Electron Cooling in Colloidal Quantum Dots. *Science* **2008**, *332*, 929–932.

(63) Kilina, S.V.; Neukirch, A. J.; Habenicht, B. F.; Kilin, D. S.; Prezhdo, O. V. Quantum Zeno Effect Rationalizes the Phonon Bottleneck in Semiconductor Quantum Dots. *Phys. Rev. Lett.* **2013**, 110, 180404.

(64) Pipa, V. I.; Mitin, V. V.; Stroscio, M. Acoustic Phonon Bottleneck in Quantum Dots: Role of Deformation Variation of Electron Effective Mass. *Solid State Commun.* **2001**, *117*, 713–717.

CHAPTER 8 – EFFICIENT PHOTOINDUCED ENERGY TRANSFER IN PORPHYRIN-BASED NANOGUMBOS

8.1 Introduction

Organic nanomaterials are of great interest due to their many potential applications including photothermal cancer therapy,[1,2] biosensing,[3] and optoelectronics.[4] Solid phase organic materials composed of molecular ions are described as a group of uniform materials based on organic salts or GUMBOS. These emerging class of organic materials provide a wide range of controllable chemical and physical properties.[5] Colloidal nanoparticles prepared from GUMBOS are given the term of nanoGUMBOS and are promising nanomaterials due to their facile syntheses and their extended list of potential applications such as biomedical imaging,[6] antibiotics,[7,8] cancer therapy,[9] molecular sensing,[10-12] organic light-emitting diodes,[13,14] and photovoltaics.[15] A better understanding of the fundamental physical properties of these nanomaterials is needed for the design of potential applications. Femtosecond transient absorption provides a valuable spectroscopic technique to study excited-state relaxation dynamics of nanomaterials by measuring the change in absorption due to photoexcitation by a pump pulse in resonance with the electronic transition of the sample as a function of the pump-probe time delay.

M-porphyrin molecular dyes, with M = H or Zn, are particularly attractive due to their tunable spectral and optical properties as well as their highly efficient electron transfer in a donor-acceptor configuration. These photodynamic properties which makes them potential candidates for advances in dye sensitized solar cells and optoelectronics.[16-19] These porphyrin-based dyes can be used for the development of artificial light-harvesting antennas that mimic photosynthesis by transferring the absorbed photon energy to a reaction center.[20] In addition, zinc porphyrin-sensitized solar cells with a cobalt(II/III)-based redox electrolyte previously recorded an excellent conversion efficiency of 12.3%.[21] Several porphyrin-based synthetic strategies have been utilized for photovoltaics including configurations based on arrays,[22,23] dimers,[24] dendrimers,[25] controlled aggregation,[26] and supramolecular assemblies.[27,28] These synthetic designs must possess several essential properties required for the design of efficient light

harvesting antennas such as strong absorbance in the visible region and enhanced electron transfer.[29,30] Porphyrin hexamers have also been reported for their near-infrared luminescence for organic light emitting diodes.[31] The wide interest in porphyrin-based materials is due to the fact that they possess many reaction sites that can be functionalized providing tunability of their optical, physical, and electrochemical properties for optimal energy conversion.[19] Another promising approach is the synthesis of porphyrin C_{60} dyads as an electron donor configuration for applications in photovoltaics [32–35] and near-infrared photodetectors.[36]

Efficient energy and electron transfer between Zn-porphyrin-based systems and various substrate was previously investigated.[25] Time-resolved terahertz spectroscopy was used to study the interfacial electron transfer from Zn-porphyrin dyes into TiO_2 nanoparticles after photoexcitation with 400 nm.[18] It was shown that the electron injection efficiency is dependent on the conductance of the linker employed. The energy and electron transfer from Zn-porphyrin dimers into TiO_2 films was observed using femtosecond transient absorption after excitation in resonance with the Q bands.[24] Time-resolved fluorescence upconversion measurements were used to investigate the enhanced energy and electron transfer from Zn-porphyrin aggregates to nanocrystalline semiconductor films when a coadsorbed chenodeoxycholic acid is added.[26] All these studies show the various strategies for the enhancement of energy and electron transfer from Zn-porhpyrin and semiconductor substrates, which is advantageous for advances in dye-sensitized solar cells.

In this chapter, we report the study of the excited-state relaxation dynamics of colloidal $[P66614]_4$[M-TCPP], with M = H and Zn, using pump-probe time-resolved transient absorption spectroscopy using pump pulse excitation centered at 400 nm and white light continuum ultrafast probe pulses. The transient absorption results obtained for the nanoGUMBOS are compared to corresponding results acquired from aqueous solutions of the M–porphyrin molecular dyes. The M–porphyrin dyes have long-lived excited-states on the order a several nanoseconds. In the corresponding nanoGUMBOS samples, efficient electron transfer and energy transfer is observed between the porphyrin groups leading to shorter excited-state lifetimes. In addition, the excited-state dynamics of $[P66614]_4$[Zn-TCPP]

nanoGUMBOS are faster than those of $[P66614]_4$[H-TCPP] nanoGUMBOS due to increase of the electronic delocalization caused by the metal center. The rate of electron transfer between Zn-TCPP molecules in the $[P66614]_4$[Zn-TCPP] nanoGUMBOS is significantly increased. This remarkable change in the excited-state relaxation dynamics shows that these nanoGUMBOS present a simple synthetic strategy for the design of efficient light harvesting antennas. In addition, the use of nanoparticles in this type of solar cells is advantageous due to their large surface to volume ratio leading to higher expected energy conversion efficiencies.

8.2 Experimental Section

8.2.1 NanoGUMBOS Synthesis

The GUMBOS are synthesized using a metathesis reaction carried out in a binary solvent mixture. Briefly, meso-tetra(4-carboxyphenyl)porphyrin (TCPP) or Zn–TCPP is neutralized using an excess of aqueous sodium hydroxide to obtain water soluble tetrasodium salt in 10% excess. The other reactant [P66614][Cl] is dissolved in DCM. The two solutions are then mixed and stirred for 40 hours. After the reaction is complete, the product is washed several times with water followed by the removal of the DCM by rotary evaporation under reduced pressure. The residual water is removed by freeze drying and the final yield of the $[P66614]_4$[M-TCPP] GUMBOS product is approximately 96%. NanoGUMBOS are synthesized via reprecipitation of the GUMBOS in water by adding 50 μL of a 1 mM GUMBOS stock ethanolic solution into 5 mL of water under sonication for 30 minutes. The reaction scheme is shown in Appendix 7. The reprecipitation of $[P66614]_4$[M-TCPP] in water produces spherical nanoparticles with an average sizes of 49 ± 25 nm for $[P66614]_4$[H-TCPP] nanoGUMBOS and 52 ± 15 nm for $[P66614]_4$[Zn-TCPP] nanoGUMBOS. The absorbance and fluorescence spectra of aqueous M-TCPP molecular dyes as well as the colloidal $[P66614]_4$[M-TCPP] nanoGUMBOS are shown in Appendix 7. The absorbance and luminescence bands of H-TCPP and Zn-TCPP are red-shifted in the nanoGUMBOS compared to the free dye molecule in water due to the presence of four bulky hydrophobic cation, leading to the formation of loosely packed aggregate.[37] Representative TEM images of the nanoGUMBOS samples are also shown in Appendix 7.

8.2.2 Transient Absorption Setup

Ultrafast transient absorption is a powerful technique for the investigation of excited-state relaxation dynamics of molecules and nanomaterials.[38] Our home-built transient absorption setup consists of an ultrafast laser system, an optical setup, and a fiber optic spectrometer detector.[38, 39] The laser pulses are generated by a titanium:sapphire laser system that produces 75 fs pulses centered at 800 nm with a 10 kHz repetition rate and an average power of 0.7 mJ/pulse. The initial laser beam was separated into pump and probe beams using a beam splitter. The 400 nm pump pulsed light is generated by frequency doubling by focusing the beam into a nonlinear beta barium borate crystal. An optical filter is then used to remove any 800 nm residual light yielding an excitation power of 0.16 μJ/pulse. The probe pulses are focused into a fused quartz flow cell containing water to generate the femtosecond white light probe pulses. The pump and probe beams are refocused to a spatial overlap in the sample which is contained in a 3 mm fused quartz flow cell. The pump-probe optical delay is enabled by a computer-controlled delay stage. More than 150 spectral scans are acquired for spectral analysis.

8.3 Results and Discussion

The excited-state dynamics of different samples of the M-TCPP molecular dyes are measured to a time delay of 6 ns using 400 nm excitation pulses and the results are compared to the nanoGUMBOS samples. Figure 8.1 (a) shows transient absorption spectra of 20 μM aqueous HTCPP measured at different time delays using 400 nm excitation. A depletion band centered at 422 nm is due to depletion of the ground state population followed by a broad spectrum after 425 nm attributed to excited-state absorption. An isosbestic point separating the ground state depletion band and the excited-state absorption region is observed at 424 nm. Representative time-profiles of the transient absorption spectra of aqueous HTCPP integrated at 422 nm and 430 nm are shown in Figure 8.1 (b). The excited-state dynamics are long-lived corresponding to a triplet state with much longer electronic decays than the 6 ns time delay of the experiment.

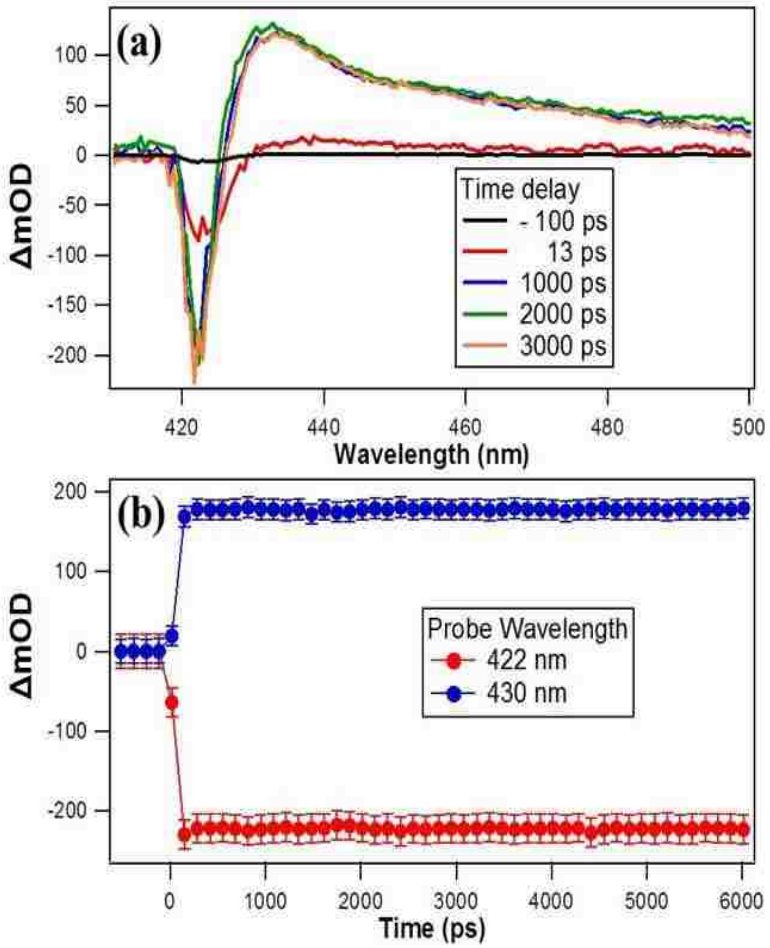

Figure 8.1. (a) Transient absorption spectra of 20 μM TCPP molecular dye in water at different time delays using 400 nm excitation. (b) Time-profiles of the transient absorption spectra of aqueous TCPP molecular dye. The time-dependent signals are measured at 422 nm and 430 nm.

In order to unravel the photophysical properties of HTCPP-based nanoGUMBOS and investigate their potential applications, the excited-state dynamics of $[P66614]_4$[HTCPP]nanoGUMBOS are studied and compared to those obtained from HTCPP molecular dye. Figure 8.2 (a) displays the transient absorption spectra of colloidal $[P66614]_4$[HTCPP] nanoGUMBOS at different time delays using 400 nm excitation pulses. A negative depletion band is centered at 423 nm followed by a broad positive spectrum attributed to induced excitation band after 440 nm. The two spectral features are separated by an isosbestic point at 438 nm. Representative time-profiles of the transient absorption spectra of colloidal $[P66614]_4$[HTCPP] nanoGUMBOS integrated at 423 nm and 460 nm are shown in Figure 8.2 (b). As shown in Figure 8.2 (c), the experimental data are fit with a global analysis technique using a sum of

exponential functions.[38-42] The equation used in the global analysis fit is of the form $I(t) = y_0 + \sum_{i=1}^{n} A_i \exp\left(-\frac{t}{\tau_i}\right)$, where n is the number of lifetimes required to accurately fit the time-profiles obtained

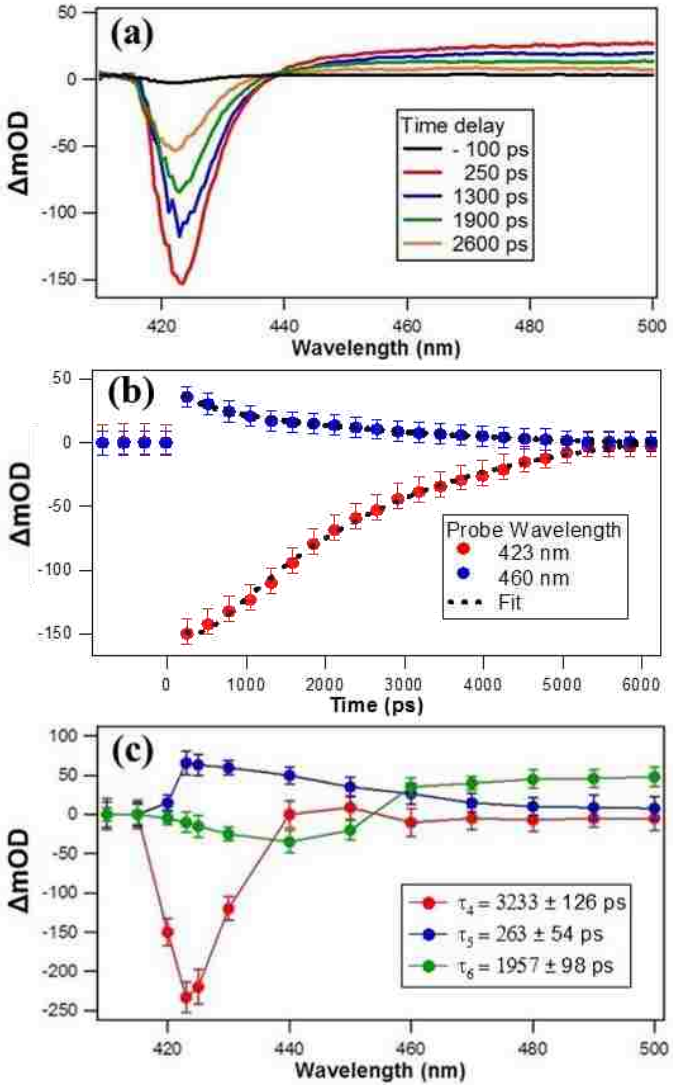

Figure 8.2. (a) Transient absorption spectra of colloidal [TCPP][P66614]$_2$ nanoGUMBOS at different time delays using 400 nm excitation. (b) Time-profiles of the transient absorption spectra of colloidal [TCPP][P66614]$_2$ nanoGUMBOS. The time-dependent signals are measured at 423 nm and 460 nm. (c) Decay spectra obtained using a sum of exponential fits of time-dependent transient absorption spectra of colloidal [TCPP][P66614]$_2$ nanoGUMBOS.

from the transient absorption spectra. Three lifetimes are required to accurately fit the temporal evolution of transient signal over the wavelengths range of the experiment with lifetimes of $\tau_1 = 3233 \pm 126$ ps, $\tau_2 = 263 \pm 54$ ps, and $\tau_3 = 1957 \pm 98$ ps. The transient absorption results demonstrate that the excited-state dynamics of the [P66614]$_4$[HTCPP] nanoGUMBOS are faster than those of the aqueous

HTCPP dye. In the nanoparticle, TCPP acts as an efficient electron donor due to its delocalized electronic structure where electron and energy transfer between porphyrin groups is possible. In this case, excited electrons from the singlet state can transfer to the lower-energy band leading to a charge separated state, followed by relaxation to the ground-state through charge recombination. This electron transfer is confirmed from the global analysis where the lifetimes of TCPP in the colloidal nanostructures can be determined with our experimental time delays as observed in Figure 8.2. Luminescence data shown in Appendix 7 indicates an increase in the intensity of the band centered at 650 nm due to this electron transfer. Energy transfer takes place due to the proximity of the TCPP groups in the nanosphere.

The effect of a zinc center on the excited-state dynamics of aqueous Zn-TCPP and colloidal $[P66614]_4$[Zn-TCPP] nanoGUMBOS are investigated. Figure 8.3 (a) shows the transient absorption spectra of aqueous Zn-TCPP molecular dye at different time delays using 400 nm excitation pulses. A depletion band centered at 426 nm is attributed to ground-state depletion and is followed by a broad spectrum after 435 nm attributed to excited-state absorption. The two spectral regions are separated by an isosbestic point at 433 nm. Representative time-dependent transient absorption spectra integrated at 428 nm and 450 nm are shown is Figure 8.3 (b). Global analysis of the decay spectra shown in Figure 8.3 (c) are generated using a sum of two exponential function with lifetimes $\tau_4 = 14.9 \pm 0.9$ ns and $\tau_5 = 1100 \pm 98$ ps. These longer-lived lifetime most probably corresponds to the electronic decay from a triplet state. The time-profile of Zn-TCPP molecular dye in water at short time delays shown in Figure 8.3 (d), can be fit with an exponential function with a lifetime $\tau_6 = 75 \pm 2$ ps. Due to their relatively short lifetimes, these excited-state decay paths can be attributed to singlet state or charge transfer state.

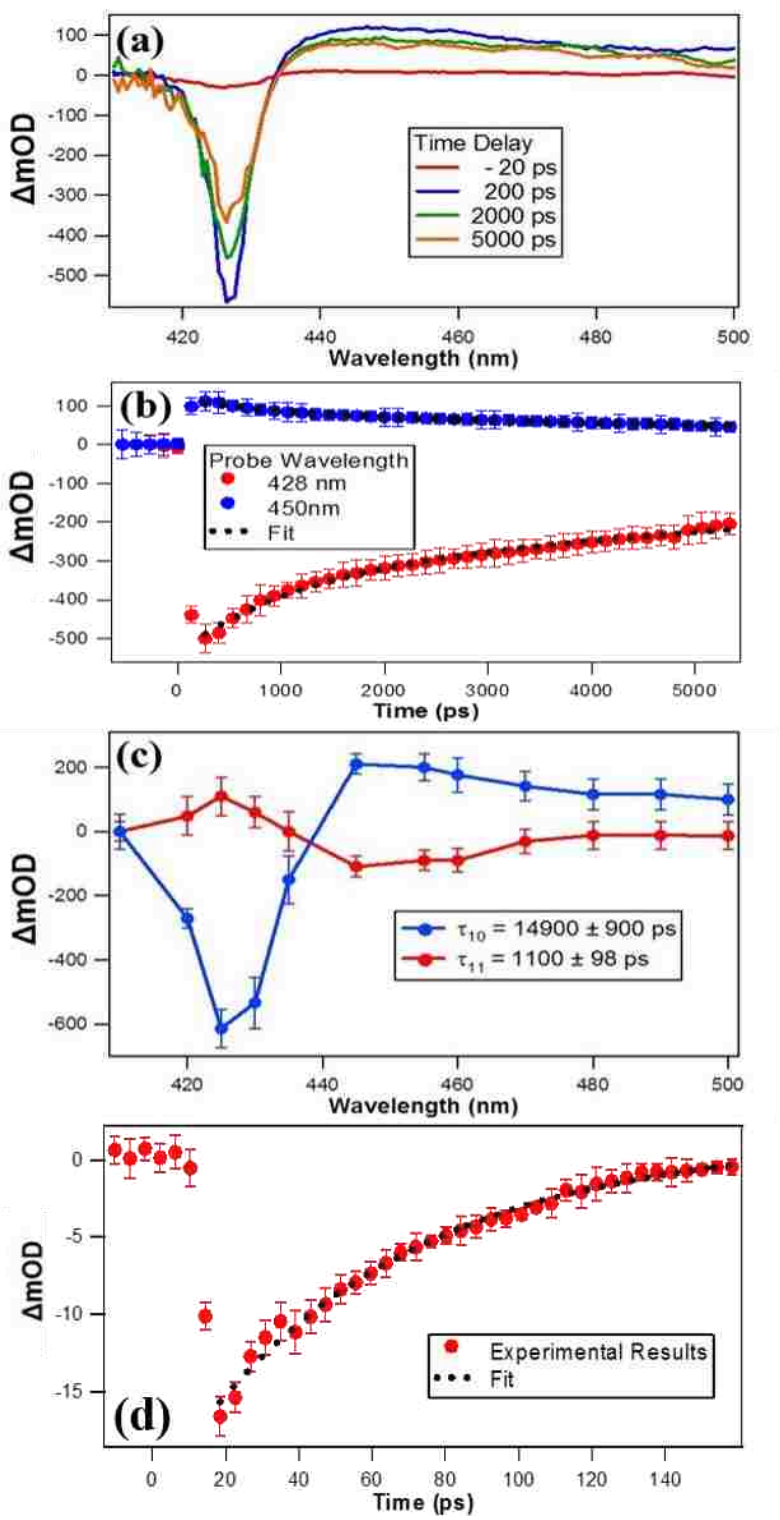

Figure 8.3. (a) Transient absorption spectra of 20 μL aqueous Zn-TCPP molecular dye at different time delay using 400 nm excitation. (b) Time-profiles of the transient absorption spectra of aqueous Zn-TCPP molecular dye. The time-dependent signals are measured at 428 nm and 450 nm. (c) Decay spectra obtained using a sum of exponential fits of time-dependent transient absorption spectra of aqueous Zn-TCPP molecular dye. (d) Time-profiles of Zn-TCPP molecular dye at short time delays.

Transient absorption measurements are also performed on a sample of colloidal $[P66614]_4$[Zn-TCPP] nanoGUMBOS. Figure 8.4 (a) displays the transient absorption spectra of colloidal $[P66614]_4$[Zn-TCPP] nanoGUMBOS at different time delays using 400 nm excitation. A depletion band centered at 425 attributed to ground-state depletion is followed by a broad spectrum after 450 nm attributed to induced excitation. The time-dependent transient absorption spectra integrated at 420 nm and 458 nm are shown in Figure 8.4 (b). The decay spectra from the global analysis of the time-profiles are shown in Figure 8.4 (c).

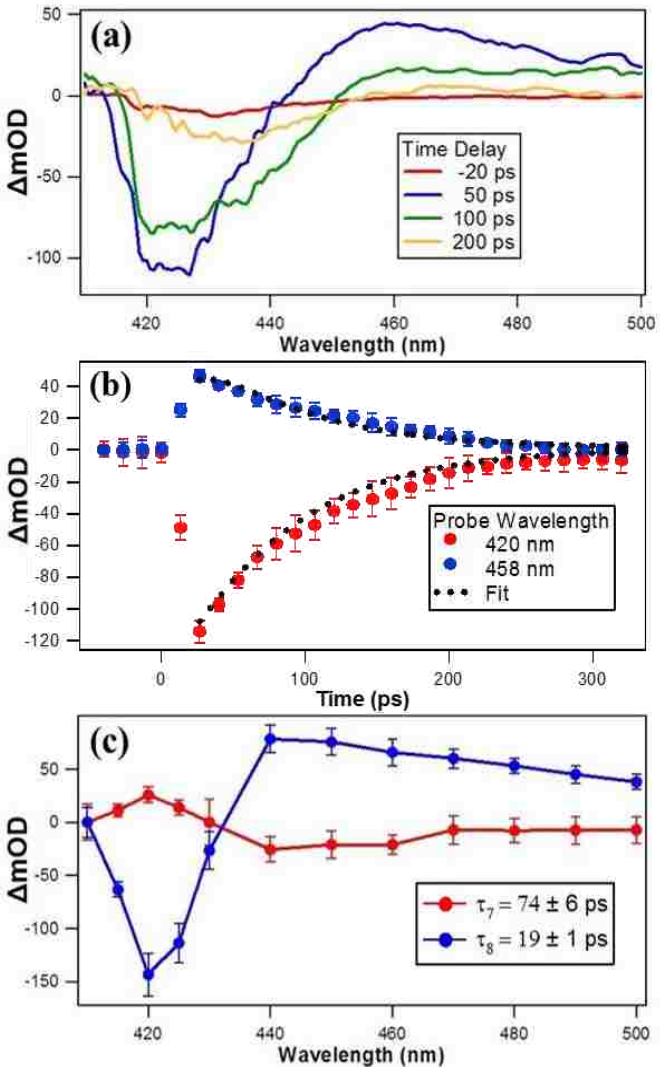

Figure 8.4. (a) Transient absorption spectra of colloidal [Zn-TCPP]$[P66614]_2$ nanoGUMBOS at different time delays using 400 nm excitation. (b) Time-profiles of the transient absorption spectra of colloidal [Zn-TCPP]$[P66614]_2$ nanoGUMBOS. The time-dependent signals are measured at 428 nm and 450 nm. (c) Decay spectra obtained using a sum of exponential fits of time-dependent transient absorption spectra of colloidal [Zn-TCPP]$[P66614]_2$ nanoGUMBOS.

The time-profiles are fit using a sum of two exponential functions with lifetimes $\tau_7 = 74 \pm 6$ ps and $\tau_8 = 19 \pm 1$ ps. The shorter lifetimes in the case of $[P66614]_4$[Zn-TCPP] nanoGUMBOS are concurrent with enhanced electron transfer between Zn-TCPP molecules. As shown in the Appendix 7, the intensity of the high-energy emission band centered at around 620 nm decreases while the intensity of the lower energy band centered at around 670 nm increases for the $[P66614]_4$[Zn-TCPP] nanoGUMBOS sample. This is concurrent with enhanced electron transfer between singlet states of Zn-TCPP groups in the nanosphere, which leads to quenching of the fluorescence from the singlet state. This long-lived excited-state is not detected in the transient absorption measurements of $[P66614]_4$[Zn-TCPP] nanoGUMBOS due to its low electronic population.

8.4 Conclusion

The transient absorption study of aqueous M-TCPP (M = H and Zn) molecular dye shows relatively long-lived excited-states dynamics. In contrast, the excited-state dynamics of colloidal $[P66614]_4$[M-TCPP] nanoGUMBOS are characterized by faster lifetimes compared to the dynamics of the initial molecular dye. In the case of [TCPP]$[P66614]_4$ nanoGUMBOS, the faster lifetimes are due to efficient electron and energy transfer between M-TCPP molecules in the nanoGUMBOS. In addition, the excited-state dynamics of $[P66614]_4$[Zn-TCPP] nanoGUMBOS are faster than those of $[P66614]_4$[Zn-TCPP] nanoGUMBOS due to increase of the electronic delocalization caused by the metal center. The electron transfer between Zn-TCPP molecules in $[P66614]_4$[Zn-TCPP] nanoGUMBOS in particular is remarkably enhanced. This ultra-efficient electron transfer is very promising for possible applications in light-harvesting solar cells and optoelectronics.

8.5 References

(1) Yang, K.; Xu, H.; Cheng, L.; Sun, C.; Wang, J.; Liu, Z. In Vitro and In Vivo Near Infrared Photothermal Therapy of Cancer Using Polypyrrole Organic Nanoparticles. *Adv. Mater.* **2012**, *24*, 5586–5592.

(2) Yang, J.; Choi, J.; Bang, D.; Kim, E.; Lim, E. –K.; Park, H.; Suh, J. –S.; Lee, K.; Yoo, K. –H.; Kim, E. –K.; Huh, Y. –M.; Haam, S. Convertible Organic Nanoparticles for Near-Infrared Photothermal Ablation of Cancer Cells. *Angew. Chem.* **2011**, *123*, 461 –464.

(3) Petkau, K.; Kaeser, A.; Fischer, I.; Brunsveld, L.; Schenning, A. P. H. J. Pre- and Postfunctionalized Self-Assembled π-Conjugated Fluorescent Organic Nanoparticles for Dual Targeting. *J. Am. Chem. Soc.* **2011**, *133*, 17063–17071.

(4) Kwan An, B. –K.; Kwon, S. –K.; Jung, S. –D.; Park, S. Y. Enhanced Emission and Its Switching in Fluorescent Organic Nanoparticles. *J. Am. Chem. Soc.* **2002**, *124*, 14410-14415.

(5) Warner, I. M.; El-Zahab, B.; Siraj, N. Perspectives on Moving Ionic Liquid Chemistry into the Solid Phase. *Anal. Chem.* **2014**, *86*, 7184−7191.

(6) Bwambok, D. K.; El-Zahab, B.; Challa, S. K.; Li, M.; Chandler, L.; Baker, G. A.; Warner, I. M. Near-Infrared Fluorescent NanoGUMBOS for Biomedical Imaging. ACS Nano 2009, 3, 3854-3860.

(7) Cole, M. R.; Li, M.; Jadeja, R.; El-Zahab, B.; Hayes, D.; Hobden, J. A..; Janes, M. E.; Warner, I. M. Minimizing human infection from Escherichia coli O157:H7 using GUMBOS. *J. Antimicrob. Chemother.* **2013**, *68*, 1312-1318.

(8) Cole, M. R.; Li, M.; El-Zahab, B.; Janes, M. E.; Hayes, D.; Warner, I. M. Design, Synthesis, and Biological Evaluation of β-Lactam Antibiotic-Based Imidazolium- and Pyridinium-Type Ionic Liquids. *Chem. Biol. Drug Des.* **2011**, *78*, 33-41.

(9) Magut, P. K. S.; Das, S.; Fernand, V. E.; Losso, J.; McDonough, K.; Naylor, B. M.; Aggarwal, S.; Warner, I. M. Tunable Cytotoxicity of Rhodamine 6G via Anion Variations. *J. Am. Chem. Soc.* **2013**, *135*, 15873–15879.

(10) Das, S.; Magut, P. K. S.; de Rooy, S. L.; Hasan, F.; Warner, I. M. Ionic Liquid-Based Fluorescein Colorimetric pH Nanosensors. *RSC Adv.* **2013**, *3*, 21054-21061.

(11) Lu, C.; Das, S.; Magut, P. K. S.; Li, M.; El-Zahab, B.; Warner, I. M. Irradiation Induced Fluorescence Enhancement in PEGylated Cyanine-Based NIR Nano- and Mesoscale GUMBOS. *Langmuir* **2012**, *28*, 14415-14423.

(12) Regmi, B. P.; Monk, J.; El-Zahab, B.; Das, S.; Hung, F. R.; Hayes D. J.; Warner, I. M. A Novel Composite Film for Detection and Molecular Weight Determination of Organic Vapors. *J. Mater. Chem.* **2012**, *22*, 13732-13741.

(13) Das, S.; Bwambok, D.; El-Zahab, B.; Monk, J.; de Rooy, S. L.; Challa, S.; Li, M.; Hung, F. R.; Baker, G. A.; Warner, I. M. Nontemplated Approach to Tuning the Spectral Properties of Cyanine-Based Fluorescent NanoGUMBOS. *Langmuir* **2010**, *26*, 12867-12876.

(14) Siraj, N.; Hasan, F.; Das, S.; Kiruri, L. W.; Gall, K. E. S.; Baker, G. A.; Warner, I. M. Carbazole-Derived Group of Uniform Materials Based on Organic Salts: Solid State Fluorescent Analogues of Ionic Liquids for Potential Applications in Organic-Based Blue Light-Emitting Diodes. *J. Phys. Chem. C* **2014**, *118*, 2312–2320.

(15) Jordan, A. N.; Das, S.; Siraj, N.; de Rooy, S. L.; Li, M.; El-Zahab, B.; Chandler, L.; Baker G. A.; Warner, I. M. Anion-controlled Morphologies and Spectral Features of Cyanine-Based NanoGUMBOS – an Improved Photosensitizer. *Nanoscale* **2012**, *4*, 5031-5038.

(16) Yella, A.; Lee, H.-W.; Tsao, H. N.; Yi, C.; Chandiran, A. K.; Nazeeruddin, M. K.; Diau, E. W.-G.; Yeh, C.-Y.; Zakeeruddin, S. M.; Grätzel, M. Porphyrin-Sensitized Solar Cells with Cobalt (II/III)−Based Redox Electrolyte Exceed 12% Efficiency. *Science* **2011**, *334*, 629−634.

(17) Bessho, T.; Zakeeruddin, S. M.; Yeh, C.-Y.; Diau, E. W.-G.; Grätzel, M. Highly Efficient Mesoscopic Dye-Sensitized Solar Cells Based on Donor−Acceptor-Substituted Porphyrins. *Angew. Chem., Int. Ed.* **2010**, *49*, 6646−6649.

(18) Negre, C. F. A.; Milot. R. L.; Martini, L. A.; Ding, W.; Crabtree, R. H.; Schmuttenmaer, C. A.; Batista, V. S. Efficiency of Interfacial Electron Transfer from Zn-Porphyrin Dyes into TiO_2 Correlated to the Linker Single Molecule Conductance. *J. Phys. Chem. C* **2013**, *117*, 24462–24470.

(19) Li, L. –L.; Diau, E. W. –G. Porphyrin-Sensitized Solar Cells. *Chem. Soc. Rev.* **2013**, *42*, 291–304.

(20) Wasielewski, M. R. Self-Assembly Strategies for Integrating Light Harvesting and Charge Separation in Artificial Photosynthetic Systems. *Acc. Chem. Res.* **2009**, *42*, 1910–1921.

(21) Yella, A.; Lee, H. –W.; Tsao, H. N.; Yi, C.; Chandiran, A. K.; Nazeeruddin, M. K.; Diau, E. W. –G.; Yeh, C. –Y.; Zakeeruddin, S. M.; Grätzel, M. Porphyrin-Sensitized Solar Cells with Cobalt (II/III)–Based Redox Electrolyte Exceed 12 Percent Efficiency. *Science* **2011**, *334*, 629–334.

(22) Choi, M. –S.; Yamazaki, T.; Yamazaki, I.; Aida, T. Bioinspired Molecular Design of Light-Harvesting Multiporphyrin Arrays. *Angew. Chem. Int. Ed.* **2004**, *43*, 150 –158.

(23) Mickley Conron, S. M.; Shoer, L. E.; Smeigh, A. L.; Butler Ricks, A.; Wasielewski, M. R. Photoinitiated Electron Transfer in Zinc Porphyrin−Perylenediimide Cruciforms and Their Self-Assembled Oligomers. *J. Phys. Chem. B* **2013**, *117*, 2195−2204.

(24) Mozer, A. J.; Griffith, M. J. Tsekouras, G.; Wagner, P.; Wallace, G. G.; Mori, S.; Sunahara, K.; Miyashita, M.; Earles, J. C.; Gordon, K. C.; Du, L.; Katoh, R.; Furube, A.; Officer, D. L. Zn–Zn Porphyrin Dimer-Sensitized Solar Cells: Toward 3-D Light Harvesting. *J. Am. Chem. Soc.* **2009**, *131*, 1562–15623.

(25) Du. B.; Fortin, D.; Harvey, P. D. Singlet and Triplet Energy Transfers in Tetra-(meso-truxene)zinc(II)- and Tetra-(meso-tritruxene)zinc(II) Porphyrin and Porphyrin-Free Base Dendrimers. *Inorg. Chem* **2011**, *50*, 11493–11505.

(26) Lu, H. –P.; Tsai, C. –Y.; Yen, W. –N.; Hsieh, C. –P.; Lee, C. –W.; Yeh, C. –Y.; Diau, E. W. –G. Control of Dye Aggregation and Electron Injection for Highly Efficient Porphyrin Sensitizers on Semiconductor Films with Varying Ratios of Coadsorbate. *J. Phys. Chem. C* **2009**, *113*, 20990–20997.

(27) Uetomo, A.; Kozaki, M.; Suzuki, S.; Yamanaka, K.; Ito, O.; Okada, K. Efficient Light-Harvesting Antenna with a Multi-Porphyrin Cascade. *J. Am. Chem. Soc.* **2011**, *133*, 13276–13279.

(28) Hosabe, T. Porphyrin-Based Supramolecular Nanoarchitectures for Solar Energy Conversion. *J. Phys. Chem. Lett.* **2013**, *4*, 1771–1780.

(29) Hippius, C.; van Stokkum, I. H. M.; Gsänger, M.; M. Groeneveld, M. M.; Williams, R. M.; Würthner, F. Sequential FRET Processes in Calix[4]arene-Linked Orange-Red-Green Perylene Bisimide Dye Zigzag Arrays. *J. Phys. Chem. C* **2008**, *112*, 2476-2486.

(30) Diring, S.; Puntoriero, F.; Nastasi, F.; Campagna, S.; Ziessel, R. Star-Shaped Multichromophoric Arrays from Bodipy Dyes Grafted on Truxene Core. *J. Am. Chem. Soc.* **2009**, *131*, 6108–6110.

(31) Fenwick, O.; Sprafke, J. K.; Binas, J.; Kondratuk, D. V.; Di Stasio, F.; Anderson, H. L.; Cacialli, F. Linear and Cyclic Porphyrin Hexamers as Near-Infrared Emitters in Organic Light-Emitting Diodes. *Nano Lett.* **2011**, *11*, 2451–2456.

(32) Imahori, H.; Fukuzumi. S. Porphyrin- and Fullerene-Based Molecular Photovoltaic Devices. *Adv. Funct. Mater.* **2004**, *14*, 525–536.

(33) Hasobe, T.; Kamat, P. V.; Absalom, M. A.; Kashiwagi, Y.; Sly, J.; Crossley, M. J.; Hosomizu, K.; Imahori, H.; Fukuzumi, F. Supramolecular Photovoltaic Cells Based on Composite Molecular Nanoclusters: Dendritic Porphyrin and C_{60}, Porphyrin Dimer and C_{60}, and Porphyrin-C_{60} Dyad. *J. Phys. Chem. B* **2004**, *108*, 12865–12872.

(34) Hosabe, T.; Kashiwagi, Absalom, M. A.; Sly, J.; Hosomizu, K.; Crossley, M. J.; Imahori, H.; Kamat, P. V.; Fukuzumi, S. Supramolecular Photovoltaics Cells Using Porphyrin Dendrimers and Fullerenes. *Adv. Mater.* **2004**, *16*, 975–979.

(35) Charvet, R.; Yamamoto, Y.; Sasaki, T.; Kim, J.; Kato, K.; Takata, M.; Saeki, A.; Seki, S,; Aida, T. Segregated and Alternately Stacked Donor/Acceptor Nanodomains in Tubular Morphology Tailored with Zinc Porphyrin−C_{60} Amphiphilic Dyads: Clear Geometrical Effects on Photoconduction. *J. Am. Chem. Soc.* **2012**, *134*, 2524−2527.

(36) Zimmerman, J. D.; Diev, V. V.; Hanson, K.; Lunt, R. R.; Yu, E. K.; Thompson, M. E.; Forrest, S. R. Porphyrin-Tape/C60 Organic Photodetectors with 6.5% External Quantum Efficiency in the Near Infrared. *Adv. Mater.* **2010**, *22*, 2780–2783.

(37) Karam, T. E.; Smith, H. T.; Haber, L. H. Enhanced Photothermal Effects and Excited-State Dynamics of Plasmonic Size-Controlled Gold–Silver–Gold Core–Shell–Shell Nanoparticles. *J. Phys. Chem. C* **2015**, *119*, 18573–18580.

(38) Punzi, A.; Martin-Gassin, G.; Grilj, J.; Vauthey, E. Effect of Salt on the Excited-State Dynamics of Malachite Green in Bulk Aqueous Solutions and at Air/Water Interfaces: a Femtosecond Transient Absorption and Surface Second Harmonic Generation Study. *J. Phys. Chem. C* **2009**, *113*, 11822–11829.

(39) Fita, P.; Punzi, A.; Vauthey, E. Local Viscosity of Binary Water+Glycerol Mixtures at Liquid/Liquid Interfaces Probed by Time-Resolved Surface Second Harmonic Generation. *J. Phys. Chem. C* **2009**, *113*, 20705–20712.

(40) Fita, P.; Fedoseeva, M.; Vauthey, E. Ultrafast Excited-State Dynamics of Eosin B: A Potential Probe of the Hydrogen-Bonding Properties of the Environment. *J. Phys. Chem. A* **2011**, *115*, 2465–2470.

CHAPTER 9 – BRILLIANT GREEN NANOGUMBOS WITH ENHANCED SECOND HARMONIC GENERATION AND NEAR-INFRARED EMISSION

9.1 Introduction

Triphenylmethane dyes such as malachite green and brilliant green have been widely studied for potential applications in protein labeling.[1, 2] These dark molecules are capable of generating an enhanced fluorescence signal when they are specifically bound to proteins or nucleic acids.[3-5] The low fluorescence yield of malachite green in solution is due to the ultrafast nonradiative relaxation dynamics of the first singlet state as a result of the strong coupling between the electronic states and the torsional degrees of freedom of the phenyl ring.[6-8] Additionally, several strategies have been employed for the enhancement of the near-infrared (NIR) emission of triphenyl methane dyes, corresponding to the optical window in biological tissues. This enhancement is very advantageous for applications in non-invasive bio-imaging and bio-sensing.[9, 10]

Second harmonic generation (SHG) is a nonlinear optical technique where two photons of frequency ω coherently add to generate a photon of frequency 2ω.[11] Nonlinear optical harmonic generation and SHG, in particular, is of increasing interest for various applications such as photonics,[12-14] materials chemistry,[15] biosensing,[16] and biomedical imaging.[17] Additionally, molecules and nanomaterials with enhanced SHG signal are useful for as probes in second harmonic generation microscopy and imaging.[18-21] SHG microscopy is uniquely suited for biological micrsocopy due to the narrow and stable nonlinear signal generated at the laser focus, the surface sensitivity of the spectroscopy, and the upconversion of NIR incident light to visible signals.[22]

In this chapter, we report the synthesis, characterization, excited-state dynamics, and SHG signal of thermally stable brilliant green–BETI [BG][BETI] nanoGUMBOS. These thermally stable colloidal nanomaterials exhibit enhanced NIR fluorescence compared to the molecular dye in water. Ultrafast spectroscopy shows that the two excited-state lifetimes of brilliant green in the nanoGUMBOS are longer, which leads to the enhanced fluorescence. Here, the torsional degrees of freedom of the phenyl ring in

brilliant green are hindered in the nanoGUMBOS environment. Additionally, the SHG signal of [BG][BETI] nanoGUMBOS is remarkably enhanced due to the increase of the second order susceptibility tensor $\chi^{(2)}$ of the nanoGUMBOS.

9.2 Experimental Section

Brilliant green ($BG.HSO_4$) and lithium bis (pentafluoroethylsulfonyl)imide (LiBETI) are purchased from Sigma Aldrich. $BG.HSO_4$ is used as received. Ethanol (EtOH) is purchased from OmniSolv. Triply deionized water (18.2 MΩ. cm) obtained from an Elga model PURELAB ultra water-filtration system is used for all ion exchange reactions and nanoGUMBOS preparations. An anion exchange reaction is performed using 0.13 mol of $BG.HSO_4$ and 0.14 mol of LiBETI dissolved separately in equal volumes of water. These solutions are mixed and stirred for 24 hours, followed by centrifugation at 3800 rpm to separate the [BG][BETI] blue-green precipitate. The product precipitate is washed several times with fresh deionized distilled water to remove the lithium bisulphate byproduct. The product is then freeze-dried overnight to remove trace water, providing an overall product yield of approximately 99%. The product is characterized by electrospray ionization time-of-flight mass spectrometry (ESI-TOF-MS). Using positive mode ESI-TOF-MS, an m/z peak of 385 is observed, thus confirming the presence of the $[BG]^+$ cation. In negative-ion mode, $[BETI]^-$ anion peak is observed at m/z of 379.9. The [BG][BETI] nanoGUMBOS sample is prepared in water using the reprecipitation method. Briefly, a small aliquot of 1 mM [BG][BETI] ethanolic solution is dissolved in a vial containing 5 mL of deionized distilled water in an ice bath, followed by 5 min of probe sonication. TEM images of the nanoGUMBOS are shown in Figure 9.1. The average nanoGUMBOS diameter is measured to be 29 ± 6 nm. Figure 9.2 (a) shows the extinction spectra of 10 μM brilliant green dye in water and 10 μM colloidal [BG][BETI] nanoGUMBOS. The fluorescence spectra of brilliant green dye and [BG][BETI] nanoGUMBOS after 420 nm excitation are shown in Figure 9.1 (b).

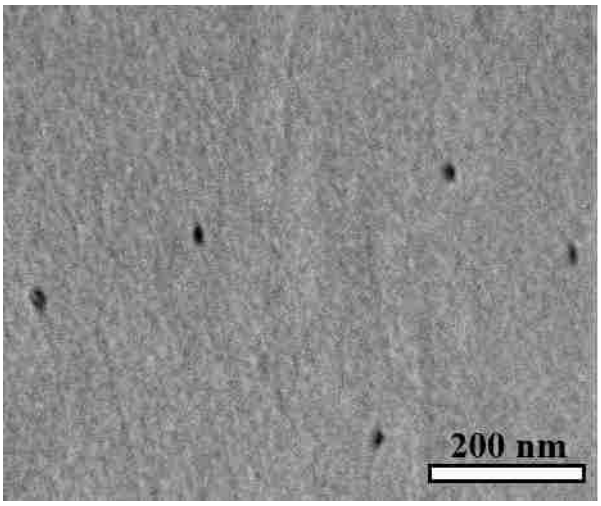

Figure 9.1 TEM image of [BG][BETI] nanoGUMBOS with an average diameter of 29 ± 6 nm.

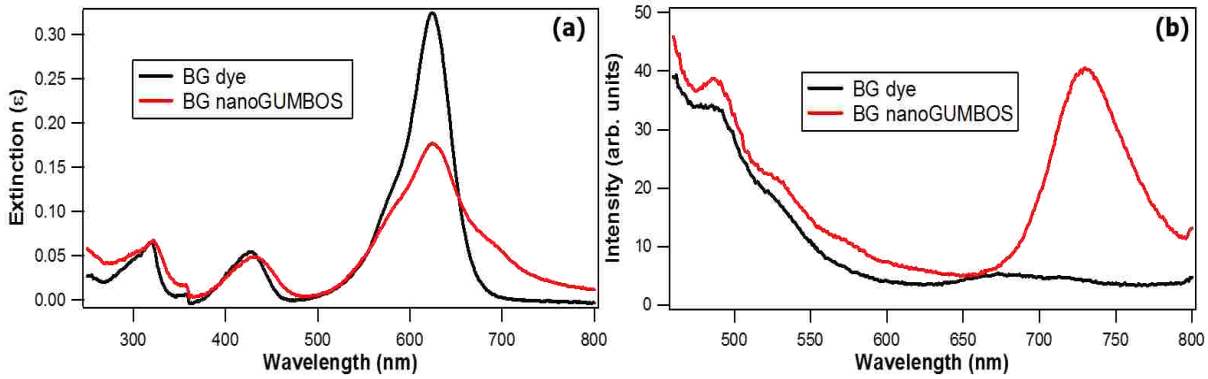

Figure 9.2 (a) Extinction spectra of 10 μM brilliant green dye (red line) and 10 μM [BG][BETI] nanoGUMBOS in water (black line). (b) Fluorescence spectra of 10 μM brilliant green dye (red line) and 10 μM [BG][BETI] nanoGUMBOS in water (black line) after 420 nm excitation.

9.3 Results and Discussion

As shown in Figure 9.2 (b), the fluorescence of [BG][BETI] nanoGUMBOS is significantly enhanced compared to brilliant green dye in water. Particularly, the NIR fluorescence band centered at around 740 nm is enhanced by approximately 6 times. Ultrafast transient absorption is used to investigate the fluorescence enhancement of the nanoGUMBOS. The transient absorption optical setup is described in chapter 5. Figure 9.3 (a) shows representative transient absorption spectra of 10 μM brilliant green dye in water at different time delays using 400 nm excitation. A positive band centered at 480 nm is attributed to excited-state absorption, followed by a negative band attributed to ground-state depletion centered at 580 nm. The time-profiles of brilliant green measured at 480 and 550 nm are shown in Figure 9.3 (b). The

decay spectra obtained from the global analysis of the transient absorption time-profiles of brilliant green dye in water are shown in Figure 9.3 (c). Three lifetimes of 0.82 ± 0.04 ps, 0.63 ± 0.03 ps, and 3.18 ± 0.07 ps are needed to accurately describe the ultrafast excited-state dynamics of brilliant green in water. These fast dynamics are due to the strong coupling of the electronic states to the torsional degrees of freedom of the phenyl ring in the brilliant green structure.[6]

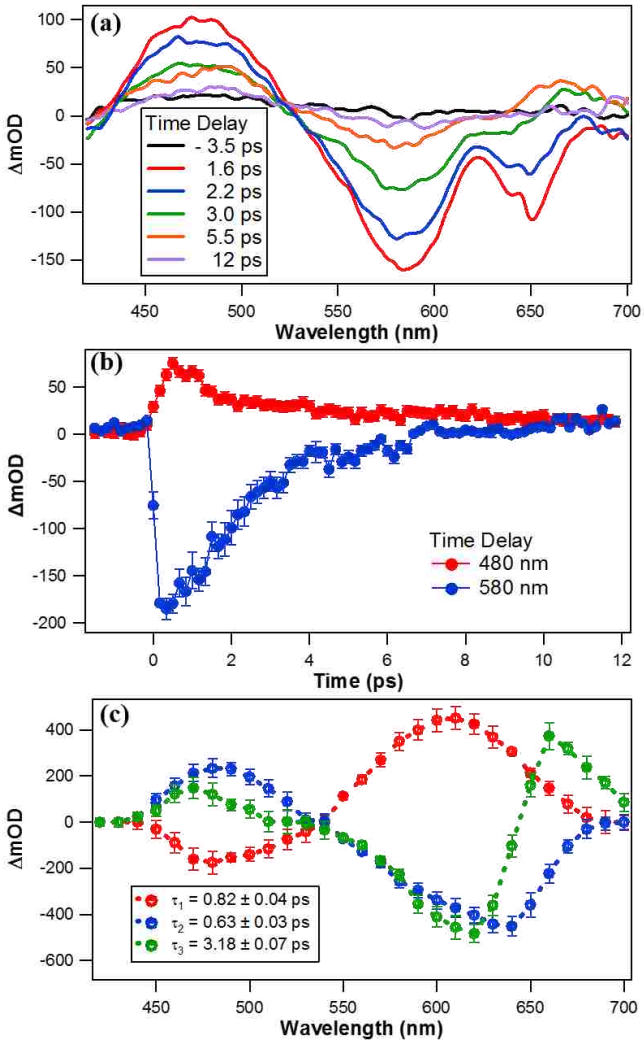

Figure 9.3. (a) Representative transient absorption spectra of 10 μM brilliant green dye in water at different time delays using 400 nm excitation. (b) Representative time-profiles of brilliant green dye measured at 480 and 580 nm. (c) Decay spectra obtained from the global analysis of the transient absorption time-profiles of brilliant green dye.

The excited-state dyanmics of colloidal [BG][BETI] nanoGUMBOS are measured and compared to the dynamics of brilliant green dye in water. Figure 9.4 shows representative transient absorption spectra of 10 μM [BG][BETI] nanoGUMBOS in water at different time delays using 400 nm excitation. A positive band centered at 540 nm is attributed to excited-state absorption, followed by a negative band attributed to ground-state depletion centered at 650 nm. The time-profiles of colloidal [BG][BETI] nanoGUMBOS measured at 540 and 650 nm are shown in Figure 9.4 (b). The decay spectra obtained from the global analysis of the transient absorption time-profiles of [BG][BETI] nanoGUMBOS are shown in Figure 9.4 (c). Three lifetimes of 0.46 ± 0.03 ps, 1.12 ± 0.09 ps, and 4.31 ± 0.13 ps are needed

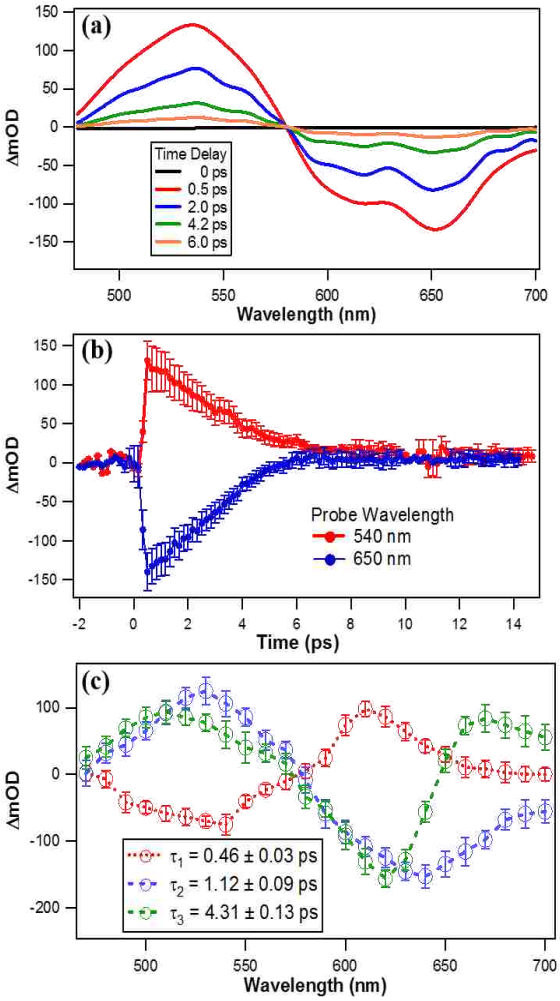

Figure 9.4. (a) Representative transient absorption spectra of 10 μM [BG][BETI] nanoGUMBOS in water at different time delays using 400 nm excitation. (b) Representative time-profiles of [BG][BETI] nanoGUMBOS in water measured at 540 and 650 nm. (c) Decay spectra obtained from the global analysis of the transient absorption time-profiles of [BG][BETI] nanoGUMBOS.

to accurately describe the ultrafast excited-state dynamics of [BG][BETI] nanoGUMBOS in water. Two of these lifetimes are significantly longer in the nanoGUMBOS compared to the molecular dye. These longer lifetimes are attributed to the restriction of the torsional degrees of freedom of the BG phenyl rings about the central carbon atom in the nanoGUMBOS environment compared to the aqueous environment that also leads to the enhanced fluorescence signals.

The SHG signal of [BG][BETI] nanoGUMBOS in water is measured and compared to the signal from BG in water and the signal from 35 ± 3 nm colloidal gold nanospheres at the same nanoparticle concentration. The SHG optical setup is described in details in chapter 5. Figure 9.5 shows the SHG spectra of 10 μM 29 nm [BG][BETI] nanoGUMBOS in water, 35 nm 10 μM gold nanospheres in water, and 10 μM brilliant green molecular dye in water. A 4 and 6-folds enhancement is observed in the SHG signal of the nanoGUMBOS compared to gold nanospheres and the molecular dye, respectively. This enhanced SHG signal is due to the larger $\chi^{(2)}$ of the nanoGUMBOS than the molecular dye. The SHG from the molecular dye dissolved in water is due to hyper Rayleigh scattering (HRS) where random fluctuations of the molecule ensemble at the laser focus leads to incomplete cancellation of the nonlinear signal. SHG from the nanoGUMBOS is due to the coherence length of the SHG process in the nanoparticle medium that is futher enhanced by the large second-order susceptibility of the BG molecule at 800 nm to produce 400 nm. Interestingly, the SHG is of the nanoGUMBOS material is even larger than gold nanoparticles of comparable size, since BG has a two-photon resonance near 400 nm, while the gold plasmon resonance is near 530 nm, so the gold nanoparticle sample has a lower degree of resonance enhancement at 800 nm and 400 nm, while the expected plasmon resonance optical field enhancement is relatively small at these wavelengths.

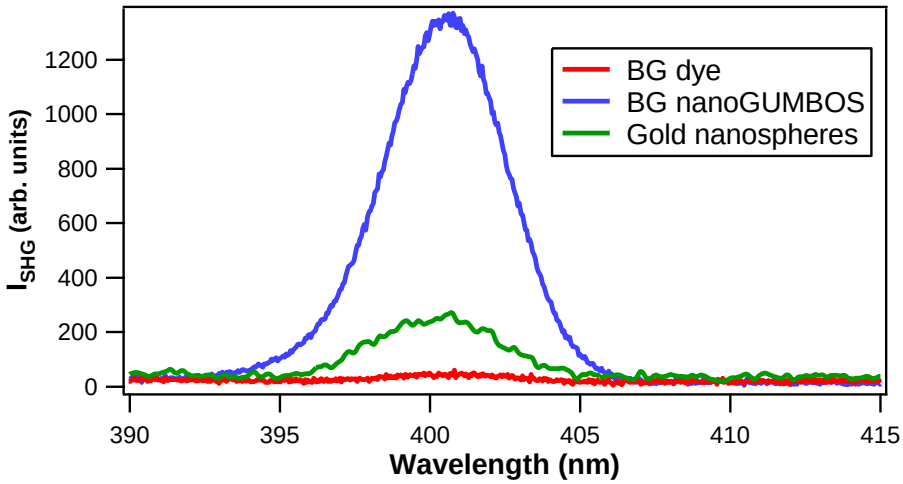

Figure 9.5. SHG spectra of (red line) 10 μM brilliant green dye in water, (blue line) 10 μM 29 nm [BG][BETI] nanoGUMBOS in water, and (green line) 10 μM 35 nm gold nanospehres in water.

9.4 Conclusion

The synthesis, characterization, excited-state dynamics, and SHG measurements of 29 ± 6 nm [BG][BETI] nanoGUMBOS are reported. The nanoGUMBOS sample exhibits enhanced fluorescence signal in the NIR region. This enhanced fluorescence is explained in terms of longer excited-state lifetimes of the nanoGUMBOS sample compared to the molecular dye. Additionally, [BG][BETI] nanoGUMBOS possess an enhanced SHG signal compared to the molecular dye and 35 nm gold nanospheres. These results show that the nanoGUMBOS are excellent candidates for applications in bio-sensing, bio-imaging, and bio-labeling.

9.5 References

(1) Szent-Gyorgyi1, C.; Schmidt, B. F.; Creeger1, Y.; Fisher, G. W.; Zakel, K. L.; Adler, S.; Fitzpatrick, J. A. J.; Woolford, C. A.; Yan, Q.; Vasilev, K. V.; et al. Fluorogen-Activating Single-Chain Antibodies for Imaging Cell Surface Proteins. *Nat. Biotech.* **2007**, *26*, 235–240.

(2) Babendure, J. R.; Adams, S. R.; Tsien, R. Y. Aptamers Switch on Fluorescence of Triphenylmethane Dyes. *J. Am. Chem. Soc.* **2003**, *125*, 14716–14717.

(3) Kolpashchikov, D. M. Binary Malachite Green Aptamer for Fluorescent Detection of Nucleic Acids. *J. Am. Chem. Soc.* **2005**, *127*, 12442–12443.

(4) Fitzpatrick, J. A. J.; Yan, Q.; Sieber, J. J.; Dyba, M.; Schwarz, U.; Szent-Gyorgyi, C.; Woolford, C. A.; Berget, P. B.; Waggoner, A. S.; Bruchez, M. P. STED Nanoscopy in Living Cells Using Fluorogen Activating Proteins. *Bioconjugate Chem.* **2009**, *20*, 1843–1847.

(5) Paige, J. S.; Wu, K. Y.; Jaffrey, S. R. RNA Mimics of Green Fluorescent Protein. *Science* **2011**, *333*, 642–646.

(6) Punzi, A.; Martin-Gassinm, M.; Grilj, J.; Vauthey, E. Effect of Salt on the Excited-State Dynamics of Malachite Green in Bulk Aqueous Solutions and at Air/Water Interfaces: a Femtosecond Transient Absorption and Surface Second Harmonic Generation Study. *J. Phys. Chem. C* **2009**, *113*, 11822–11829.

(7) Bhasikuttan, A. C.; Sapre, A. V.; Okada, T. Ultrafast Relaxation Dynamics from the S2 State of Malachite Green Studied with Femtosecond Upconversion Spectroscopy. *J. Phys. Chem. A* **2003**, *107*, 3030−3035.

(8) Fita, P.; Punzi, A.; Vauthey, E. Local Viscosity of Binary Water+Glycerol Mixtures at Liquid/Liquid Interfaces Probed by Time-Resolved Surface Second Harmonic Generation. *J. Phys. Chem. C* **2009**, *113*, 20705–20712.

(9) Xu, W.; Lu, Y. Label-Free Fluorescent Aptamer Sensor Based on Regulation of Malachite Green Fluorescence. *Anal. Chem.* **2010**, *82*, 574–578.

(10) Funada, T.; Hirose, T.; Tamaib, N.; Yao, H. Organic Nanoparticles of Malachite Green with Enhanced Far-Red Emission: Size-Dependence of Particle Rigidity. *Phys. Chem. Chem. Phys.* **2015**, *17*, 11006–11013

(11) Boyd, R. Nonlinear Optics; Academic Press: New York, **2010**.

(12) Berger, V. Nonlinear Photonic Crystals. *Phys. Rev. Lett.* **1998**, *81*, 4136.

(13) Broderick, N. G. R.; Ross, G. W.; Offerhaus, H. L.; Richardson, D. J.; Hanna, D. C. Hexagonally Poled Lithium Niobate: A Two-Dimensional Nonlinear Photonic Crystal. *Phys. Rev. Lett.* **2000**, *84*, 4345.

(14) Corcoran1, B.; Monat, C.; Grillet, C.; Moss, D. J.; Eggleton, B. J.; White, T. P.; O'Faolain, L.; Krauss, T. F. Green Light Emission in Silicon Through Slow-Light Enhanced Third-Harmonic Generation in Photonic-Crystal Waveguides. *Nat. Photonics* **2009**, *3*, 206–210.

(15) Stupp, S. I.; LeBonheur, V.; Walker, K.; Li, L. S.; Huggins, K. S.; Keser, M.; Amstutz, A. *Science* **1997**, *276*, 384–389.

(16) Campagnola, P. J.; Loew, L. M. *Nat. Biotech.* **2003**, *21*, 1356–1360.

(17) Pu, Y.; Grange, R.; Hsieh, C. L.; Psaltis, D. Nonlinear Optical Properties of Core-Shell Nanocavities for Enhanced Second-Harmonic Generation. *Phys. Rev. Lett.* **2010**, *104*, 207402.

(18) Chen, X.; Nadiarynkh, O.; Plotnikov, S.; Campagnola, P. J. Second Harmonic Generation Microscopy for Quantitative Analysis of Collagen Fibrillar Structure.

(19) Pantazis, P.; Maloney, J.; Wu, D.; Fraser, S. E. Second Harmonic Generating (SHG) Nanoprobes for in Vivo Imaging. *Proc. Natl. Acad. Sci.* **2010**, *107*, 14535–14540.

(20) Wampler, R. D.; Kissick, D. J.; Dehen, C. J.; Gualtieri, E. J.; Grey, J. L.; Wang, H. –F.; Thompson, D. H.; Cheng, J. –X.; Simpson, G. J. Selective Detection of Protein Crystals by Second Harmonic Microscopy. *J. Am. Chem. Soc.* **2008**, *130*, 14076–14077.

(21) Reeve, J. E.; Collins, H. A.; De Mey, K.; Kohl, M. M.; Thorley, K. J.; Paulsen, O.; Clays, K.; Anderson, H. L. Amphiphilic Porphyrins for Second Harmonic Generation Imaging. *J. Am. Chem. Soc.* **2009**, *131*, 2758–2759.

CHAPTER 10 – EXCITED-STATE DYNAMICS OF CARBAZOLE – BETI NANOGUMBOS

10.1 Introduction

Carbazole-BETI GUMBOS and nanoGUMBOS offer exciting new opportunities for potential applications in OLEDs and optoelectronic technologies due to their complex photodynamic properties.[1] Advances in such applications require a complete understanding of the fundamental mechanisms involving the photoexcitation and the excited-state relaxation dynamics of these highly-fluorescent nanomaterials and solutions. More precisely, processes such as charge transfer, energy transfer, metastable states, optical gain, and stimulated emission are expected to have major contributions to the relaxation paths of the excited-state populations of the GUMBOS and nanoGUMBOS.[1-3] Here we use ultrafast time-resolved transient absorption spectroscopy to accurately delineate the excited-state dynamics of these materials and better understand their structural and photodynamic properties.

10.2 Results and Discussion

The synthesis is similar to the one reported in chapter 9 for [BG][BETI] nanoGUMBOS and the transient absorption optical setup is similar to the one reported in chapter 5. The extinction spectrum of carbazole-BETI nanoGUMBOS is shown in Figure 10.1 (b). Using ultrafast spectroscopy, we have investigated several different GUMBOS and nanoGUMBOS samples. Pump-probe transient absorption measurements are taken on a 50 μM carbazole-BETI nanoGUMBOS in water in order to determine the excited-state relaxation dynamics.

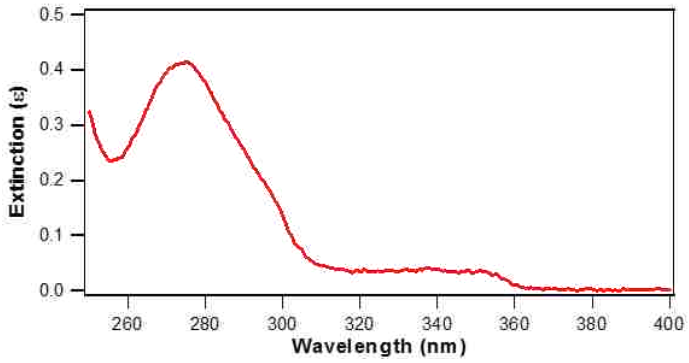

Figure 10.1 Extinction spectrum of carbazole-BETI nanoGUMBOS in water.

Figure 10.2, a-b show the transient absorption spectra of aqueous carbazole-BETI nanoGUMBOS measured at different time delays using 280 nm excitation pulses. The band centered at 320 nm is due to ground-state depletion due to excitation to the S1 excited-state.[1] Two bands centered at 470 nm and 580 nm are attributed to excited-state absorption. The time profiles shown in Figure 10.2 (c) depict the ground-state depletion and the two excited-states absorption bands integrated over 320 nm, 470 nm, and 580 nm respectively. The ground state depletion time profile has an exponential decay with a lifetime of $\tau_1 = 164 \pm 6$ ps. The lifetimes of the excited-states absorption bands are $\tau_2 = 224 \pm 11$ ps at 470 nm and $\tau_3 = 120 \pm 10$ ps at 580 nm. Two sharp depletion peaks are observed at 556 nm and 566 nm and are attributed to optical gain leading to stimulated emission.[2,4] The time-dependent transient absorption profiles are analyzed over the wavelength range of 410 nm to 620 nm using a global analysis technique[5] described by a sum of exponentials to recover the lifetimes and corresponding spectra of the relaxation dynamics. Figure 10.2 (d) displays the spectral results of the global analysis over this wavelength range, showing that the transient absorption is well-represented by a convolution of two excited-state absorption bands with correlated lifetimes of $\tau_2 = 224$ ps and $\tau_3 = 120$ ps.

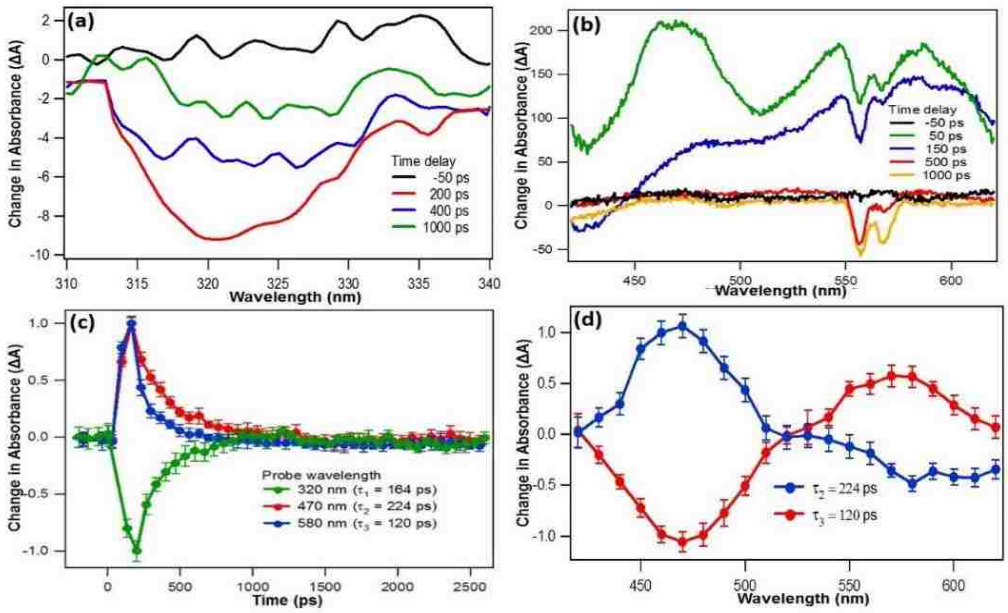

Figure 10.2. (a) and (b) Transient absorption spectra of 50 μM aqueous carbazole-BETI nanoGUMBOS at different time delays using 280 nm excitation pulses. (c) Time profiles of the transient absorption spectra of the nanoGUMBOS at 320 nm (green line), 470 nm (red line), and 580 nm (blue line). (d) Decay spectra obtained by fitting the transient absorption data to sums of exponentials.

Figure 10.3 shows the transient absorption spectra of 50 µL carbazole-BETI nanoGUMBOS in water from (a) 370 nm to 390 nm and (b) 540 nm to 580 nm at different time delays. Three depletion bands attributed to stimulated emission are observed near 380 nm, 556 nm, and 566 nm. The depletion intensities gradually increase with time until a plateau is reached. These three negative bands are fit using a Gaussian function at different time delays and their areas are calculated by integrating over the appropriate Gaussian functions. The obtained time profiles of the different stimulated emission bands are shown in Figure 10.3 (c) and are fit using exponential functions to obtain the corresponding lifetimes of the optical gain. These lifetimes are $\tau_4 = 241 \pm 10$ ps, $\tau_5 = 118 \pm 3$ ps, and $\tau_6 = 810 \pm 5$ ps for the bands centered at 380 nm, 556 nm, and 566 nm respectively.

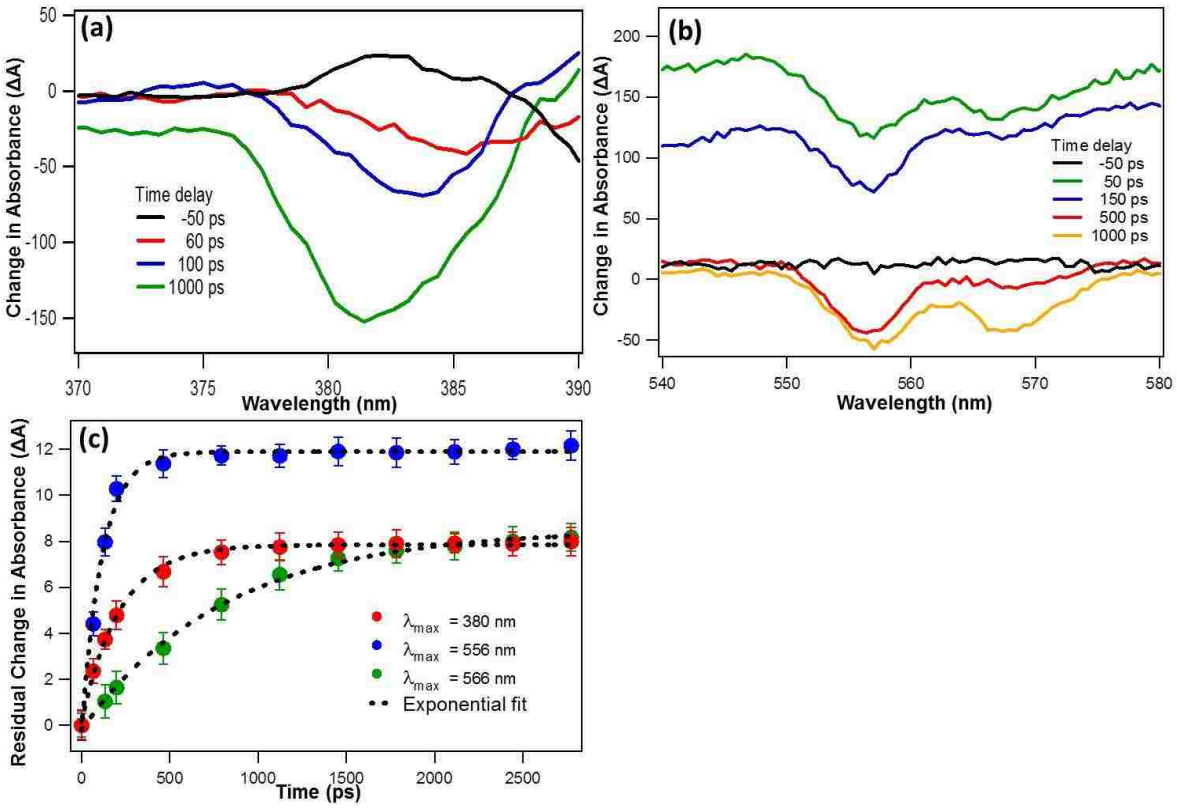

Figure 10.3. Transient absorption spectra of 50 µL aqueous carbazole-BETI nanoGUMBOS at two different wavelength ranges: (a) 370 nm – 390 nm and (b) 540 nm – 580 nm. The spectra show negative peaks attributed to optical gain leading to stimulated emission at (a) 380 nm, (b) 566 and 556 nm. (c) Time profiles of the different stimulated emission bands. The experimental data are fit with an exponential function to obtain the lifetimes of the optical gain.

10.3 Conclusion

These investigations demonstrate the wealth of photodynamic information that transient absorption spectroscopy can provide for these types of GUMBOS and nanoGUMBOS. Many distinct pathways of molecular excited-state relaxation dynamics are identified and measured both spectroscopically and temporally. In addition, stimulated emission bands are seen to exponentially increase and plateau over different characteristic lifetimes, allowing for possible mechanisms for enhanced fluorescence pathways. These results provide detailed information on the photodynamics and excited-state relaxation paths of these novel materials that can help lead towards new designs of advanced OLED devices with increased emission efficiencies and novel optoelectronic applications.

10.4 References

(1) Siraj, N.; Hasan, F.; Das, S.; Kiruri, L. W.; Steege Gall. K. E.; Baker, G. A.; Warner, I. M. Carbazole-Derived Group of Uniform Materials Based on Organic Salts: Solid State Fluorescent Analogues of Ionic Liquids for Potential Applications in Organic-Based Blue Light-Emitting Diodes. *J. Phys. Chem. C*. **2014**, *118*, 2312–2320.

(2) Klimov, V. I.; Mikhailovsky, A. A.; Xu, S.; Malko, A.; Hollingsworth, J. A.; Eisler, H. –J.; Bawendi, M. G. Optical Gain and Stimulated Emission in Nanocrystal Quantum Dots. *Science* **2000**, 290, 314–317.

(3) Sreenath, K.; Yi, C.; Knappenberger, K. L.; Zhu, L. Distinguishing Förster Resonance Energy Transfer and Solvent-Mediated Charge-Transfer Relaxation Dynamics in a Zinc(II) Indicator: a Femtosecond Time-Resolved Transient Absorption Spectroscopic Study. *Phys. Chem. Chem. Phys.* **2014**, *16*, 5088–5092.

(4) Burdett, J. J.; Müller, A. M.; Gosztola, D.; Bardeen, C. J. Excited State Dynamics in Solid and Nonomeric Tetracene: The Roles of Superradiance and Exciton Fission. *J. Chem. Phys.* **2010**, *133*, 144506.

(5) Punzi, A.; Martin-Gassin, G.; Grilj, J.; Vauthey, E. E ffect of Salt on the Excited-State Dynamics of Malachite Green in Bulk Aqueous Solutions and at Air/Water Interfaces: a Femtosecond Transient Absorption and Surface Second Harmonic Generation Study. *J. Phys. Chem. C* **2009**, *113*, 11822–11829.

CHAPTER 11 - CONCLUSION

11.1 Ultrafast and Nonlinear Spectroscopy of Plasmonic Nanoparticles

The nonlinear and ultrafast spectroscopic techniques of second harmonic generation and transient absorption spectroscopy are used to study plasmonic nanoparticles in colloidal suspension. The adsorption properties of triphenylmethane dyes malachite green, brilliant green, and methyl green on the surface of 80 nm colloidal gold nanoparticles are investigated using SHG. The measured isotherms are fit using a modified Langmuir model to obtain the free energies of adsorption and the site densities of the dyes at the colloidal nanoparticle surface. Complementary extinction spectroscopy is used to investigate the plasmon-exciton resonance coupling. Additionally, SHG is used to investigate the growth of a silver shell on the surface of gold nanoparticles in real-time. These results provide valuable information on the time-dependent surface structure and morphology of the nanoshell. The gold-silver core-shell nanoparticles exhibit enhanced SHG signal compared to gold and silver nanoparticles due to the enhanced optical fields.

The synthesis of size-selected novel plasmonic gold-silver-gold core-shell-shell nanoparticles is reported. The extinction peak wavelengths can be controlled over the visible and near-infrared regions by varying the thicknesses of the gold and silver shells. These unique spectroscopic properties make these nanoparticles potential candidates for biologically relevant applications including photothermal cancer therapy and biosensing. The core-shell-shell nanoparticles have a higher photothermal effect compared to gold nanospheres and gold nanorods after irradiation with 800 nm laser pulses. Transient absorption measurements show that the phonon-phonon scattering lifetime is significantly shorter in the core-shell-shell nanoparticles than in gold nanospheres and gold nanorods, which leads to higher photothermal efficiencies.

The adsorption properties of malachite green, brilliant green, methyl green, and rhodamine 110 on the surface of 105 nm colloidal gold-silver-gold core-shell-shell nanoparticles are investigated. The

adsorption isotherms are fit using a modified Langmuir model to obtain the free energies of adsorption and the site densities. Extinction spectroscopy shows that the plasmon-exciton resonance coupling at the core-shell-shell nanoparticle surface is remarkably enhanced. The fluorescence signal of the triphenylmethane dyes is enhanced while the fluorescence signal of rhodamine 110 is quenched at the core-shell-shell nanoparticle surface. Transient absorption measurements reveal that molecular hindrance of the torsional dynamics causes increased excited-state lifetimes for brilliant green adsorbed to the core-shell-shell nanoparticle surface. A very different effect is observed for rhodamine 110, where energy transfer from the dye to the plasmonic nanoparticle results in much faster excited-state lifetimes. The decays of the short-lived excited-states of the plasmon-exciton polaritonic states formed when brilliant green is adsorbed on the core-shell-shell surface are investigated using transient absorption and their decay lifetimes are measured.

The excited-state dynamics of TiO_2-Au nanocomposites are investigated using 400 nm excitation pulses. These nanoparticles have been extensively studied for the potential applications in nanocatalysis. The results show that the relaxation processes of the plasmon depletion band, which are described by electron-phonon and phonon-phonon scattering lifetimes, are independent of the gold nanocluster size adsorbed at the TiO_2 nanoparticle surface. The dynamics corresponding to interfacial charge transfer between the gold nanoclusters and the TiO_2 bandgap are observed to spectrally overlap with the gold interband transition dynamics, and the charge-transfer lifetimes are shown to significantly decrease as the nanocluster size increases. Moreover, size-dependent periodic oscillations attributed to acoustic phonons of the gold nanoclusters are observed. These results provide additional information towards a better understanding of the structure-photocatalytic activity paradigm of the TiO_2-Au nanocomposites.

11.2 Ultrafast and Nonlinear Spectroscopy of NanoGUMBOS

NanoGUMBOS are derived from a group of uniform materials based on organic salts (GUMBOS). These nanomaterials can provide exciting new opportunities for a wide range of applications such as optoelectronics, photovoltaics, OLEDs, and biological applications. The resulting excited-state relaxation dynamics can help in improving potential properties and designs in these developing

nanoGUMBOS applications. Transient absorption is used to investigate the excited-state dynamics of thermally stable crystalline $[Ru(bipy)_3][BETI]_2$ nanoGUMBOS. These nanoGUMBOS show spectral shifts and size-dependent relaxation dynamics for nanoparticle diameters varying from 20 to 100 nm, characterized by excited-state decay dynamics similar to those of the precursor dye at higher pump pulse energies with an additional pathway attributed to intermolecular energy transfer, where all lifetimes increase with increasing nanoparticle size. Long-lived phonons that are persistent for several nanosecond are also observed, where the phonon frequency increases as the nanoparticle size increases. The frequencies of the phonon oscillations are fit using a model based on the size-dependent force constant of the nanocrystals. This anomalous phonon trend is due to very low coupling between electronic and phonon degrees of freedom and a strong hydrophobic interaction with the aqueous solvent. These results suggest that these nanoGUMBOS are very advantageous for dye-sensitized solar cells and other optoelectronic devices, including hot-carrier extraction photovoltaics.

The excited-state dynamics of $[P66614]_4$[M-TCPP] (M = H and Zn) nanoGUMBOS are investigated and compared to those of the corresponding dyes. M-TCPP dyes in water possess very long-lived relaxation decays. $[P66614]_4$[H-TCPP] nanoGUMBOS have much faster lifetimes due to light-induced energy and electron transfer between the porphyrin groups. The decay lifetimes of $[P66614]_4$[Zn-TCPP] nanoGUMBOS are even faster from the increased electronic delocalization of Zn-TCPP. These results show that $[P66614]_4$[M-TCPP] nanoGUMBOS are very promising for potential applications in photovoltaics and optoelectronics.

Colloidal brilliant green–BETI nanoGUMBOS possess enhanced fluorescence signal in the near-infrared region compared to the molecular dye in water. Transient absorption measurements show that the excited-states relaxation lifetimes of the nanoGUMBOS are significantly slower than the corresponding lifetimes of the molecular dye in water. This enhanced fluorescence is due to the restriction of the torsional degrees of freedom of the phenyl ring in brilliant green nanoGUMBOS. A large enhancement of the SHG signal is observed in the nanoGUMBOS samples compared to gold nanoparticles and brilliant

green dye, respectively. These enhanced optical properties make brilliant green – BETI nanoGUMBOS well suited for biological applications in sensing, labeling, and imaging.

Finally, ultrafast spectroscopy is used to study the photophysical properties of carbazole–BETI nanoGUMBOS. There nanoGUMBOS are known to possess enhanced fluorescence signals. Optical gain and stimulated emission are observed as an additional excited-state relaxation pathway in the nanoGUMBOS. These results show that carbazole–BETI GUMBOS and nanoGUMBOS offer exciting new opportunities for potential applications in OLEDs and optoelectronic technologies. The nonlinear and ultrafast spectroscopic techniques of second harmonic generation and transient absorption spectroscopy are demonstrated to be extremely valuable in obtaining important information on molecular adsorption, plasmon enhancement, core-shell growth kinetics, molecular relaxation dynamics, ultrafast photothermal heating, anomolous phonon dynamics, and advanced optoelectronic characterization of colloidal nanoparticles and nanomaterials.

APPENDIX 1 – ADDITIONAL SHG FITS AND RESONANCE COUPLING ANALYSIS

A1.1 Second Harmonic Generation Data and Fits

Second harmonic generation data and fits The adsorption isotherms obtained from the SHG data are fit using an extended modified Langmuir model that takes into account the signal generated from the free dye molecules in water. The total SHG signal is considered to be the sum of the three different contributions including the adsorption of molecules on the surface of gold nanoparticles, the offset from gold nanoparticles in water, and the signal generated from free dye molecules in water. The later term is considered negligible in the case of the adsorption studies on the surface of polystyrene microspheres. The total signal can be written as

$$SHG_{total} = A(\frac{N}{N_{max}})^2 + B + Ma \qquad (A1.1)$$

where N/N_{max} is obtained from the modified Langmuir formula, is the SHG amplitude at the plateau, A is the offset term due to the SHG signal from gold nanoparticles in water without the addition of the dye solution, M is the concentration of free dye molecules in solution, and a is the slope obtained from plotting the SHG signal of dye molecules in water versus dye concentration. Figure A1.1 shows the SHG signal of the different dyes in water at different reduced concentrations, which is the ratio of the concentration over the maximum concentration value. The maximum concentrations used for malachite green, brilliant green, and methyl green are 1.8 μM, 15 μM, and 8 μM respectively. It is shown that the SHG signals of the three dyes in water increase linearly, as expected for hyper Rayleigh scattering. The variation of M as a function of dye concentration, N_{max} , and K are determined using the best fits from the modified Langmuir model. In order to generate the adsorption isotherms, the data are corrected by subtracting the contribution of the free dye molecules in water from the total SHG signal.

By fitting the SHG data as described above using the extended modified Langmuir model, the site densities and the free energies of adsorption of the dye molecules to the surface of polystyrene

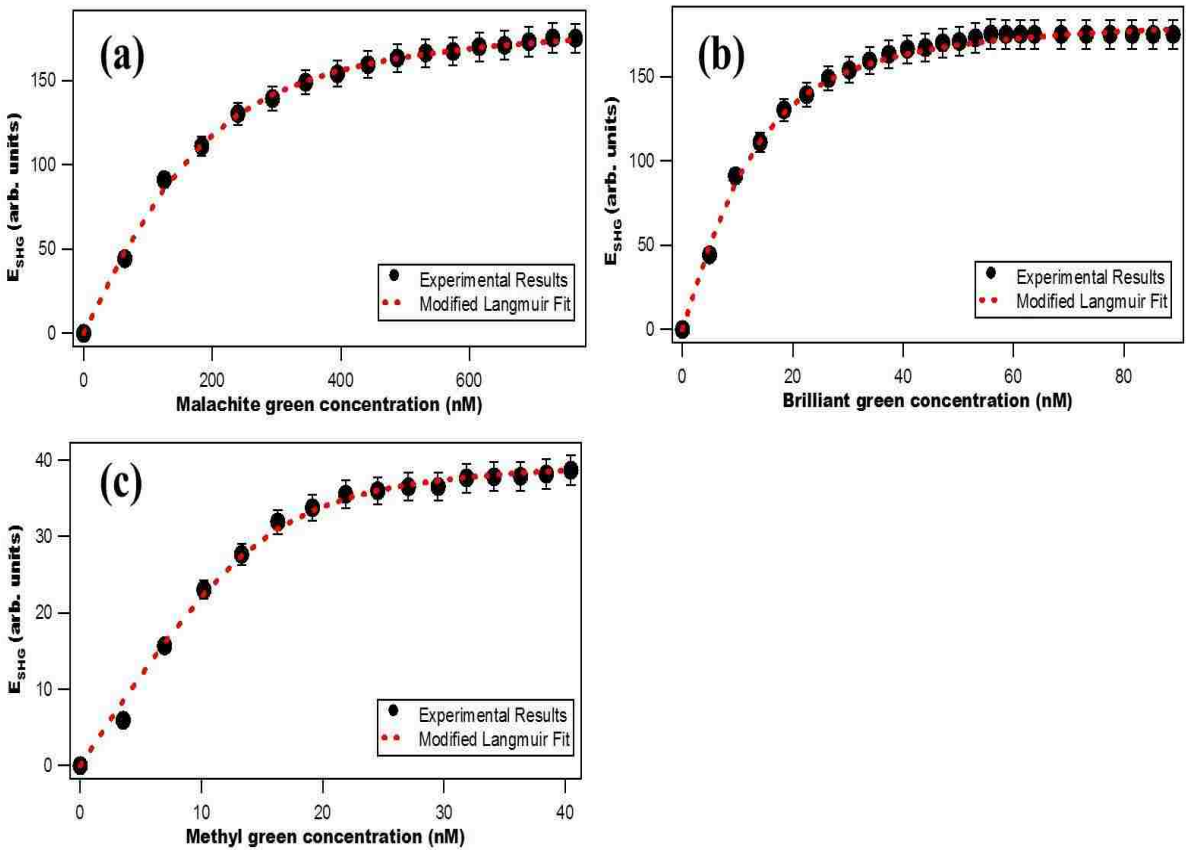

Figure A1.1. Adsorption isotherm results obtained from second harmonic generation data (black dots) from polystyrene microspheres as a function of (a) malachite green, (b) brilliant green, (c) and methyl green concentrations. The experimental data are compared with the best fits from the modified Langmuir model (dotted red lines).

microspheres are determined, as shown in Figure A1.2. The polystyrene sulfate microspheres are purchased from Polysciences and are diluted in nanopure water to a concentration of 4.0×10^8 particles/mL for each SHG adsorption isotherm measurement. The experimental setup is the same as the one used for the gold nanoparticle measurements, with the same data analysis procedure. Using the extended modified Langmuir model, the free energy of adsorption of malachite green to the surface of 1.06 ± 0.03 μm polystyrene microspheres is -11.0 ± 0.2 kcal/mol and the maximum number of sites per particle is $1.80 \pm 0.04 \times 10^6$ where each site occupies 192 ± 9 A^2 . These values are equivalent to the values obtained, under experimental uncertainty, using the modified Langmuir model, which neglects signal from free dye molecules. Using the modified Langmuir model, the corresponding adsorption energy is -11.1 ± 0.4 kcal/mol and the maximum number of sites is $1.83 \pm 0.06 \times 10^6$ per particle where

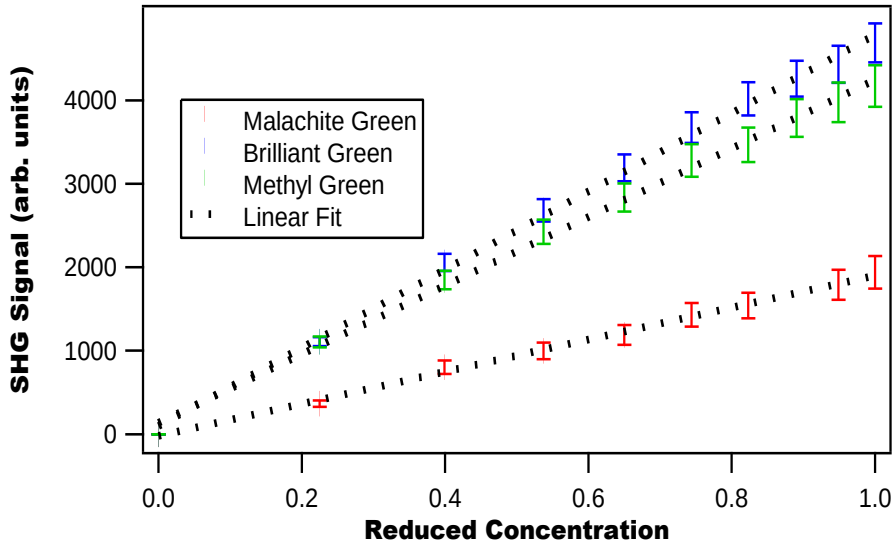

Figure A1.2. Second harmonic generation signal obtained from the addition of malachite green (red line), brilliant green (blue line) and methyl green (green line) to water. The signals are shown to increase linearly, as expected for hyper Raleigh scattering.

each site occupies 193 ± 6 A^2. These results are very similar to values reported in the literature.[1,2] In addition, brilliant green and methyl green molecules bind more strongly to the surface of the polystyrene microspheres than malachite green. The free energy of adsorption of brilliant green is −13.0 ± 0.3 kcal/mol with a maximum of 1.61 ± 0.06 × 10^6 sites per particle where each site occupies 216 ± 9 A^2 , using the extended modified Langmuir model fit. Using the modified Langmuir model, these corresponding values are −12.8 ± 0.2 kcal/mol, 1.57 ± 0.08 ×10^6 sites per particle, and 220 ± 13 A^2, respectively. The free energy of adsorption of methyl green is −14.1 ± 0.5 kcal/mol with a maximum of 1.26 ± 0.10 ×10^6 sites per particle where each site occupies 275 ± 12 A^2, using the extended modified Langmuir model fit. Using the modified Langmuir model, these corresponding values are −14.4 ± 0.5 kcal/mol, 1.30 ± 0.10 ×10^6 sites per particle, and 267 ± 15 A^2, respectively. To our knowledge, no work has previously reported SHG results for brilliant green and methyl green adsorbing to polystyrene microspheres in water.

A1.2 Polaritons and Fano-Type Resonances at the Colloidal Gold Interface Measured Using Absorption Spectroscopy

Extinction measurements of the 80.0 ± 6.1 nm gold nanoparticles are performed at different malachite green and methyl green concentrations, in the same way described for the brilliant green results

shown in the chapter 2. Figure A1.3, a-b display these spectra after subtracting the spectra of the dye solutions in water at the corresponding concentrations. A splitting of the plasmon peak is observed near the molecular resonances, with plasmon and molecular resonance coupling and spectral depletions as the dye concentrations are increased over the range studied in the SHG adsorption isotherm measurements. After subtracting the spectra of gold nanoparticles at the corresponding concentrations from the absorption spectra in Figure A1.3, the difference spectra are obtained and shown in Figure A1.4. The molecule and plasmon depletion fits are displayed in black dashed lines. The residual negative and positive peaks observed are due to a convolution of polaritons and Fano-type resonances. The peaks at higher wavelengths correspond to the lower energy polaritonic state $|P->$ and the peaks at lower wavelengths correspond to the higher energy polaritonic state $|P+>$, respectively. The energy differences between these two peaks are assigned as the Rabi splitting energies. The plasmon peak is depleted as the dye concentrations increase. Figure A1.5 is obtained after subtracting the corresponding depletion fits from the difference spectra in figure A1.4, with offsets added for comparisons. The polariton peaks in Figure A1.5 are fit using the double Gaussian equation A1.2 for the determinations of the peak positions, widths, intensities, and offset values. The results are summarized in Table A1.1.

$$y = y_0 + A_1 \exp\left[-\left(\frac{x - x_1}{w_1}\right)^2\right] + A_2 \exp\left[-\left(\frac{x - x_2}{w_2}\right)^2\right] \qquad (A1.2)$$

The chemical structures and the absorption spectra of the dye molecules are shown in figures A1.6 and A1.7 respectively. A scheme of the SHG optical setup is shown in Figure A1.8.

Table A1.1: Resonance coupling fits of the polariton $|P->$ and $|P+>$ peaks to a double Gaussian function provides the peak positions x_1 and x_2, the peak widths w_1 and w_2, the peak intensities A_1 and A_2, and the offset y_0 at different (a) malachite green, (b) brilliant green and (c) methyl green concentrations.

(a)

MG Conc	131 nM	251 nM	362 nM	465 nM	561 nM
Plasmon Depletion	-1.4E-02 ± 2.0E-03	-2.2E-02 ± 1.2E-03	-3.0E-02 ± 3.1E-03	-4.4E-02 ± 2.1E-03	-5.9E-02 ± 1.1E-03
Molecule Depletion	3.1E-03 ± 1.1E-03	-1.5E-02 ± 3.1E-03	-5.4E-02 ± 2.6E-03	-8.3E-02 ± 3.6E-03	-1.3E-01 ± 2.4E-03
y_0	5.6E-04 ± 3.4E-04	5.9E-04 ± 1.2E-04	3.9E-04 ± 1.5E-04	4.7E-04 ± 1.3E-04	-1.3E-04 ± 1.2E-04
A_1	1.9E-03 ± 3.2E-04	2.3E-03 ± 1.1E-04	2.6E-03 ± 1.4E-04	2.7E-03 ± 1.3E-04	2.87E-03 ± 1.17E-04
x_1	660 ± 0.1	660 ± 0.1	650 ± 0.1	650 ± 0.1	650 ± 0.1
w_1	29 ± 4	28 ± 2	26 ± 2	22 ± 1	24 ± 1
A_2	-2.1E-03 ± 2.6E-04	-2.0E-03 ± 9.3E-05	-2.1E-03 ±1.2E-04	-1.4E-03 ± 8.7E-05	-1.3E-03 ± 6.9E-05
x_2	578 ± 0.1	578 ± 0.1	578 ± 0.1	580 ± 0.1	579 ± 0.1
w_2	23 ± 3	23 ± 1	24 ± 2	19 ± 2	17 ± 1

(b)

BG Conc	1.3 µM	2.5 µM	3.5 µM	4.5 µM	5.45 µM
Plasmon Depletion	-7.9E-02 ± 1.2E-02	-1.0E-01 ± 2.7E-03	-1.4E-01 ± 2.3E-03	-1.8E-01 ± 3.4E-03	-2.3E-01 ± 2.9E-03
Molecule Depletion	-1.2E-02 ± 3.5E-03	-1.6E-02 ± 4.2E-03	-7.5E-03 ± 5.1E-03	-1.0E-03 ± 2.0E-03	1.1E-02 ± 3.1E-03
y_0	4.8E-03 ± 5.9E-04	2.2E-03 ± 4.1E-04	7.6E-03 ± 7.7E-04	4.5E-03 ± 8.2E-04	2.5E-03 ± 4.8E-04
A_1	5.3E-03 ± 1.6E-04	5.3E-03 ± 1.9E-04	4.4E-03 ± 1.6E-04	6.1E-03 ± 4.3E-04	4.9E-03 ± 1.8E-04
x_1	660 ± 0.1	660 ± 0.1	660 ± 0.1	670 ± 0.1	660 ± 0.1
w_1	22 ± 1	21 ± 1	21 ± 1	26 ± 2	21 ± 1
A_2	-5.8E-03 ± 4.4E-04	-6.4E-03 ± 1.8E-04	-7.1E-03 ± 5.0E-04	-8.6E-03 ± 2.1E-04	-6.6E-03 ± 2.9E-04
x_2	570 ± 0.1	570 ± 0.1	570 ± 0.1	570 ± 0.1	570 ± 0.1
w_2	23 ± 1	20 ± 1	22 ± 2	26 ± 5	20 ± 1

(c)

MetG Conc	1.17 µM	2.26 µM	3.25 µM	4.20 µM
Plasmon Depletion	-6.9E-02 ± 9.1E-03	-1.1E-01 ± 9.1E-03	-1.6E-01 ± 8.7E-03	-1.9E-01 ± 7.5E-03
Molecule Depletion	-2.8E-03 ± 9.0E-03	-2.6E-02 ± 9.0E-03	-2.9E-02 ± 1.2E-02	-3.4E-02 ± 1.4E-03
y_0	5.5E-03 ± 2.3E-04	1.4E-03 ± 1.1E-04	1.3E-03 ± 8.9E-05	1.3E-03 ± 2.5E-04
A_1	8.2E-04 ± 1.7E-04	9.1E-04 ± 1.7E-04	7.7E-04 ± 1.3E-04	1.9E-03 ± 1.4E-04
x_1	670 ± 0.1	670 ± 0.1	670 ± 0.1	670 ± 0.1
w_1	10 ± 3	12 ± 3	7 ± 2	13 ± 3
A_2	-4.9E-03 ± 1.2E-04	-1.8E-03 ± 1.2E-04	-1.2E-03 ± 6.4E-05	-1.4E-03 ± 1.1E-04
x_2	580 ± 0.1	580 ± 0.1	570 ± 0.1	570 ± 0.1
w_2	72 ± 2	28 ± 2	21 ± 2	31 ± 3

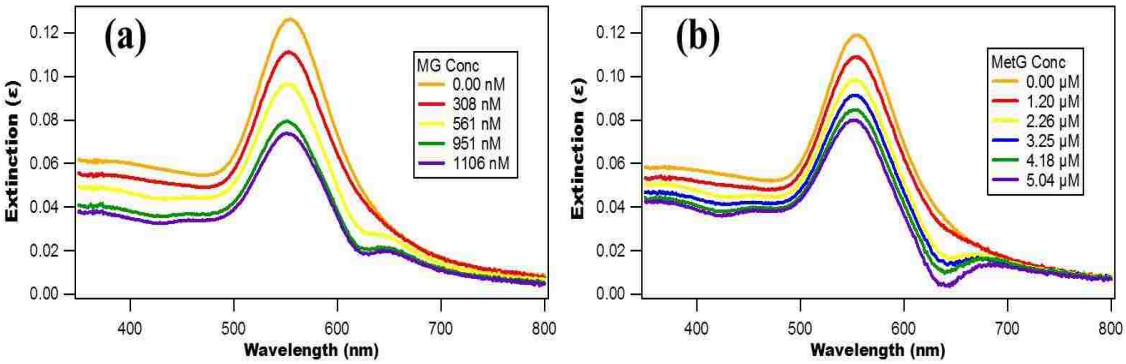

Figure A1.3. Extinction spectra of gold nanoparticles capped with MSA in water at different (a) malachite green and (b) methyl green concentrations after subtracted the corresponding spectra from the dye molecules alone in water. 0.30 mL of the 80.0 nm colloidal gold nanoparticles at a bulk concentration of 4.1×10^9 nanoparticles/mL was added to 3.00 mL water.

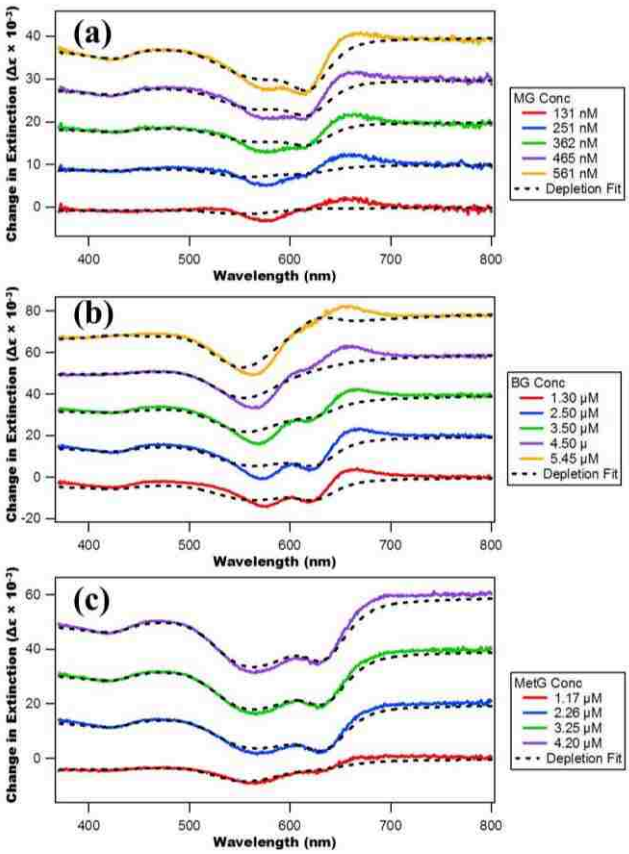

Figure A1.4. Change in extinction obtained from the subtraction of 80.0 ± 6.1 nm gold nanoparticles capped with MSA in water ($d = 9.1 \times 10^9$ nanoparticles per mL) and (a) different malachite green concentrations, (b) different brilliant green concentrations and (c) different methyl green concentrations in water from the spectra of a solution of dye and gold colloid (red solid line). The black dashed line corresponds to the best fit of the plasmon and molecule depletion peaks. A combination of Fano resonance and polaritons is observed. The spectra were offset for better comparison.

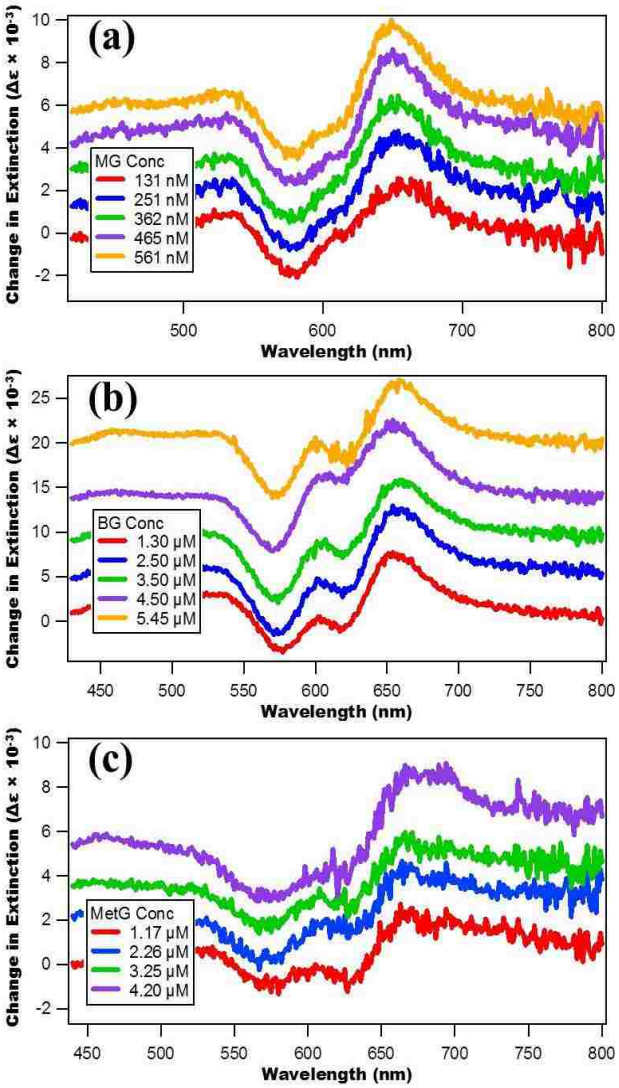

Figure A1.5. Spectra obtained after the subtraction of the depletion fit from the visible extinction difference spectra obtained from 80 nm gold nanoparticles at different dye concentrations (a) malachite green, (b) brilliant green, (c) methyl green in Figure 2.5. The extra remaining peaks are due to a combination of polaritons and Fano resonance.

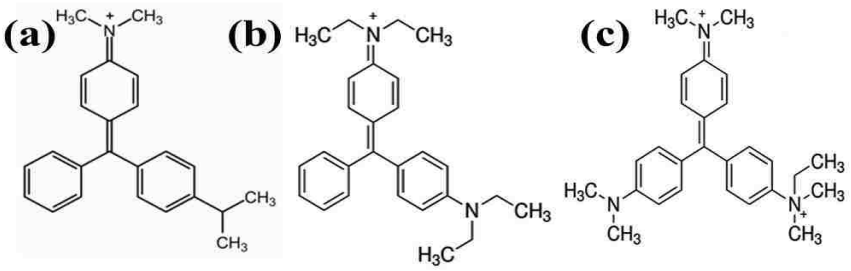

Figure A1.6. Chemical structures of the dye molecules: (a) malachite green, (b) brilliant green, and (c) methyl green.

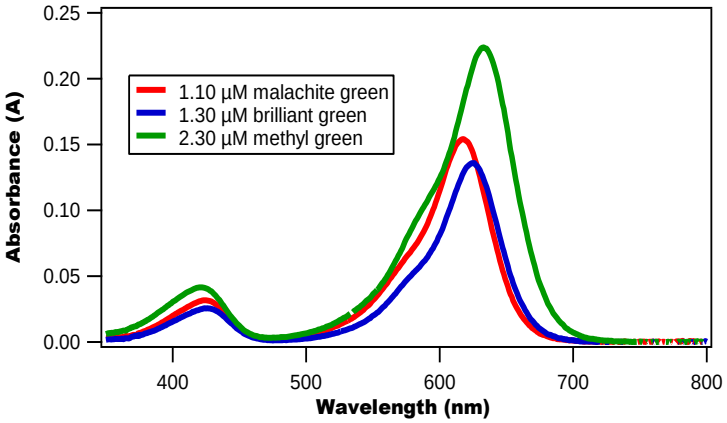

Figure A1.7. The absorption spectra of the three dye molecules: (red line) 1.1 µM malachite green, (blue line) 1.2 µM brilliant green, and (green line) 2.2 µM methyl green.

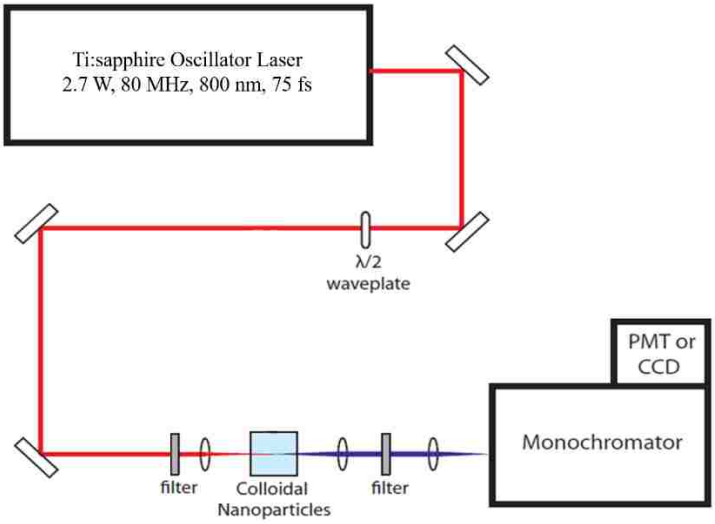

Figure A1.8. Scheme of the SHG optical setup. The computer-controlled burette, beam block, and stir bar are not shown here.

A1.3 References

(1) Wang, H.; Yan, E.; Liu, Y.; Eisenthal, K. B.; *J. Phys. Chem. B* **1998**, *102*, 4446.

(2) Haber, L. H.; Kwok, S. J.; Semeraro, M.; Eisenthal, K. B.; *Chem. Phys. Lett.* **2011**, *507*, 11.

APPENDIX 2 – GOLD-SILVER CORE-SHELL NANOPARTICLE TEM IMAGES AND SHG SPECTRA

Figure A2.1 shows TEM images of (a) 65 nm gold nanoparticles and (b) the 65-11 gold-silver core-shell nanoparticles. Representative SHG spectra of the growth of the silver shell on the surface of 65 nm colloidal gold is shown in Figure A2.2 at different times. At negative times the SHG spectra of 0.5 mL 65 nm gold nanoparticles in 1.0 mL water are measured. At time 0, 3 μL of 100 mM of ascorbic acid, 1.5 μL of 100 mM of $AgNO_3$, and 4 μL of 100 mM NaOH are added to the colloidal gold sample under vigorous stirring at room temperature. The SHG spectra and backgrounds are measured every 15 seconds and the time-profiles are generated. Representative SHG spectra of the reduction of silver nitrate in water is shown in Figure A2.3 at different times. At negative times, the SHG of 1.5 mL water is measured. At time 0, 3 μL of 100 mM of ascorbic acid, 1.5 μL of 100 mM of $AgNO_3$, and 4 μL of 100 mM NaOH are added to the water containing-cuvette. The SHG spectra and backgrounds are measured every 15 seconds and the time-profiles are generated.

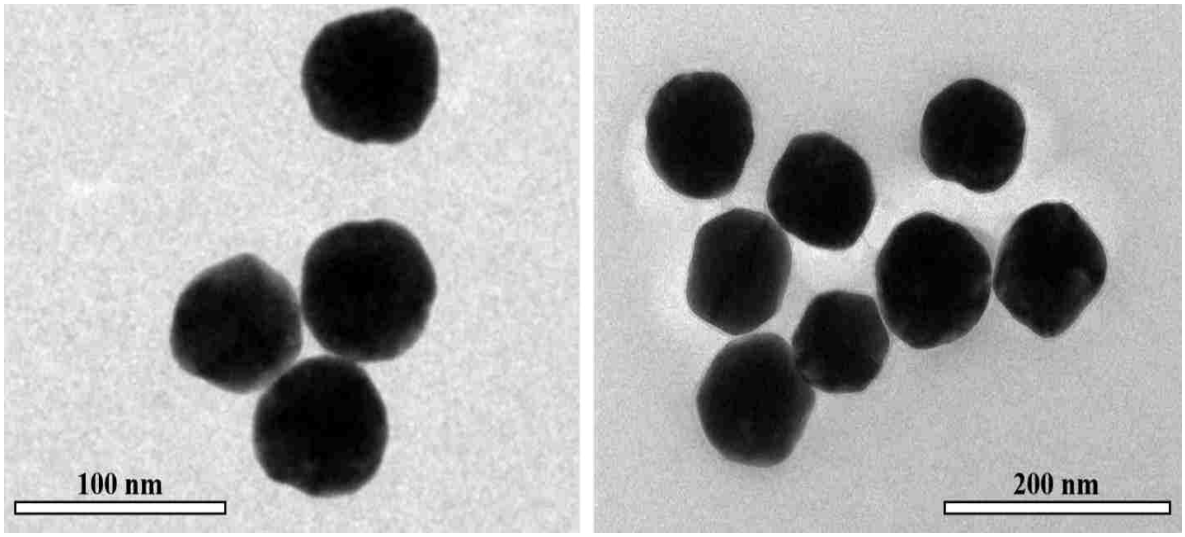

Figure A2.1 TEM images of (a) 65 nm gold nanoparticles and (b) 65-11 nm gold-silver core-shell nanoparticles

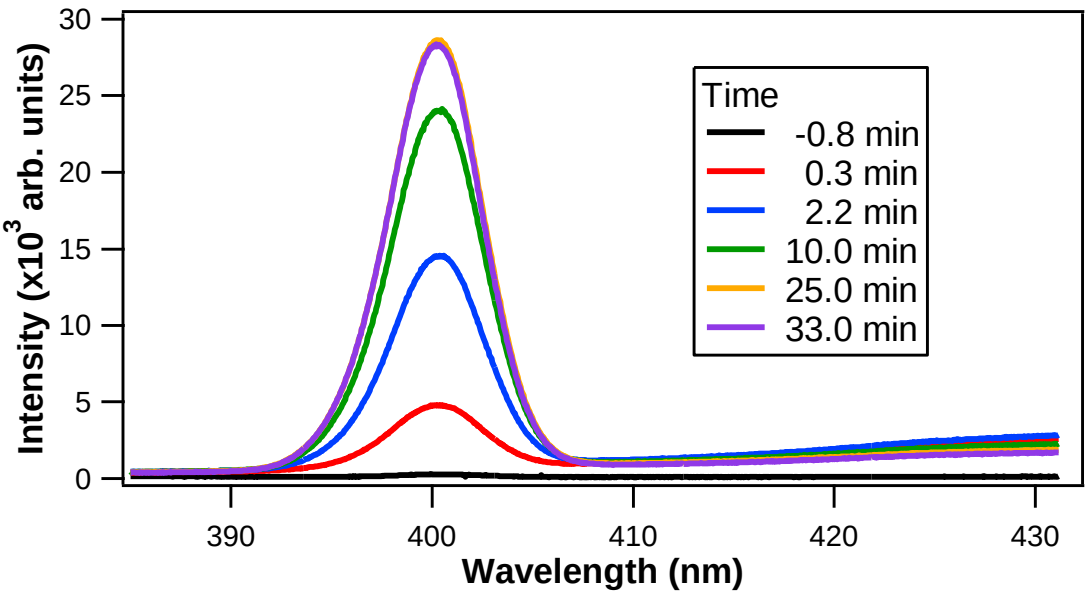

Figure A2.1 SHG spectra of the growth of the silver shell on the surface of 65 nm colloidal gold at different times.

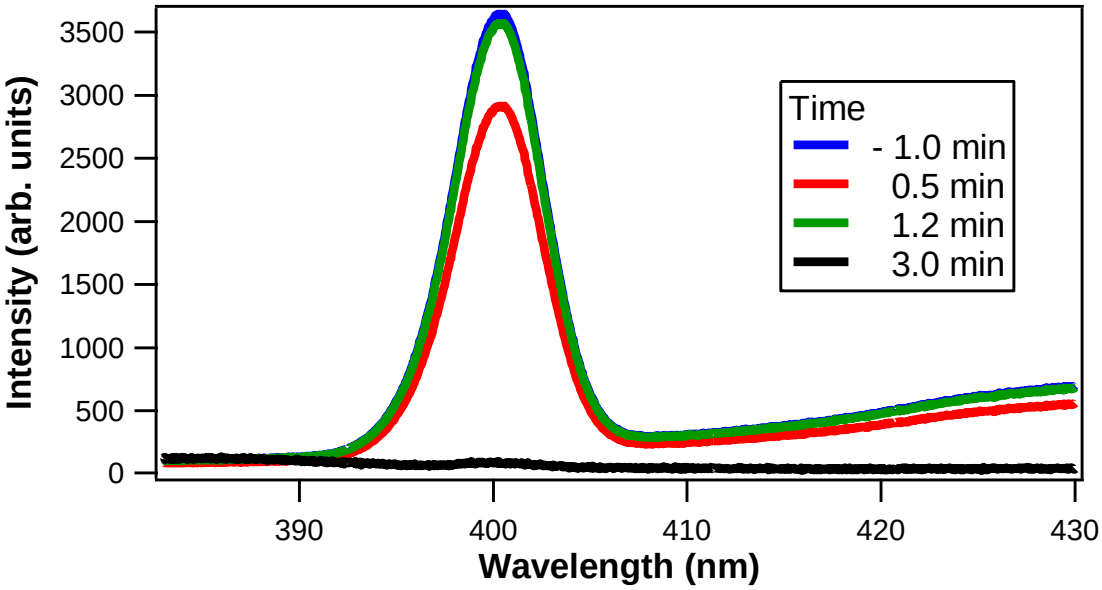

Figure A2.2 SHG spectra of the growth of the control experiment obtained from the reduction of silver nitrate in water.

APPENDIX 3 – GOLD-SILVER-GOLD CORE-SHELL-SHELL NANOPARTICLE CHARACTERIZATION

A3.1 Additional TEM Images and Extinction Spectra

The different average sizes and distributions of the synthesized gold-silver-gold core-shell-shell nanoparticles are shown in Table A3.1. All gold cores presented here have sizes of 12 ± 0.9 nm. Figure A3.1 displays representative HR-TEM images of the 12 nm gold core, and the 36 nm, 48 nm, and 60 nm gold-silver core-shell nanoparticles, as well as their corresponding extinction spectra. The spectrum of the 12 nm gold core is fit using Mie Theory at a concentration of 2.9×10^{11} nanoparticles/mL. Additional HR-TEM images of the gold-silver-gold core-shell-shell nanoparticles, and the gold-silver-gold-silver-gold core-shell-shell-shell-shell nanoparticles are shown in Figures A3.2 and A3.3 respectively.

Table A3.1. Average core and shell sizes of the synthesizied gold-silver-gold core-shell-shell nanoparticles.

Samples	Size of the gold core	Thickness of the silver shell	Thickness of the gold shell
CSS1	12 ± 0.9 nm	12 ± 1.1 nm	5 ± 0.6 nm
CSS2			15 ± 0.9 nm
CSS3			20 ± 1.6 nm
CSS4			30 ± 2.4 nm
CSS5		18 ± 1.6 nm	5 ± 0.6 nm
CSS6			7.5 ± 0.8 nm
CSS7			10 ± 1.1 nm
CSS8		24 ± 2.1 nm	5 ± 0.7 nm
CSS9			7.5 ± 0.9 nm
CSS10			10 ± 1.3 nm

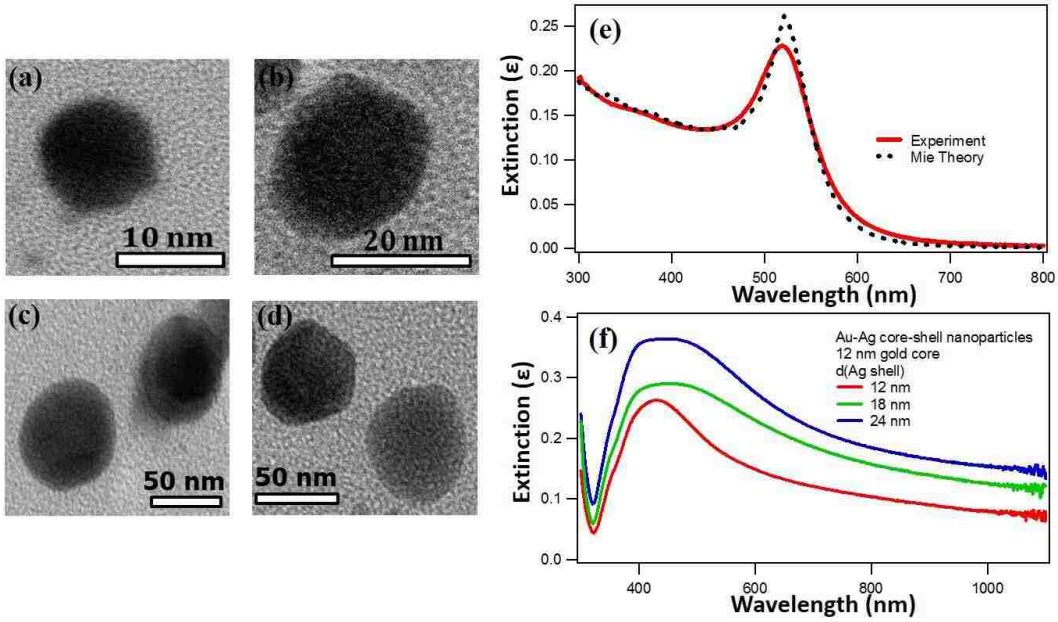

Figure A3.1. TEM images of (a) 12 nm gold nanoparticles, (b) 36 nm gold-silver core-shell nanoparticles, (c) 48 nm gold-silver core-shell nanoparticles, and (d) 60 nm gold-silver core-shell nanoparticles. Extinction spectra of (e) 12 nm gold nanoparticles and (f) 24 nm, 30 nm, and 36 nm gold-silver core-shell nanoparticles are shown. The extinction spectrum of the 12 nm colloidal gold nanoparticles is fit using Mie theory at a concentration is 2.9×10^{11} nanoparticles/mL.

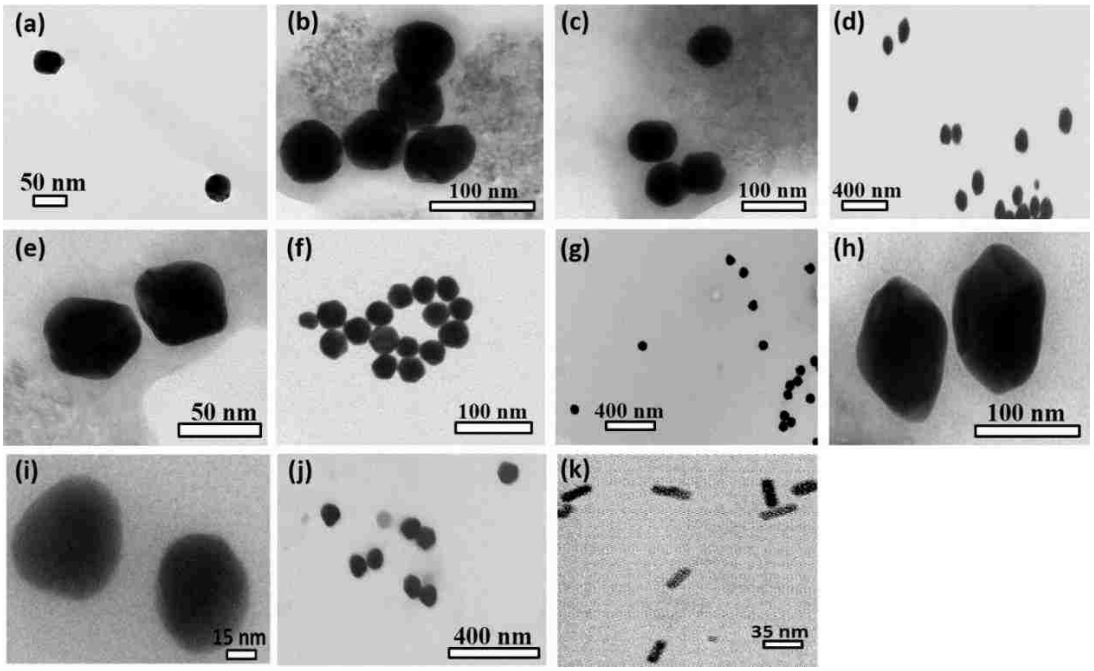

Figure A3.2. TEM images of the gold-silver-gold core-shell-shell nanoparticle samples with sizes of (a) 12-12-5 nm, (b) 12-12-10 nm, (c) 12-12-20 nm, (d) 12-12-30 nm, (e) 12-18-5 nm, (f) 12-18-7.5 nm, (g) 12-18-10 nm, (h) 12-24-5 nm, (i) 12-24-7.5 nm, and (j) 12-24-10 nm. (k) TEM images of gold nanorods of 10 nm width and 35 nm length.

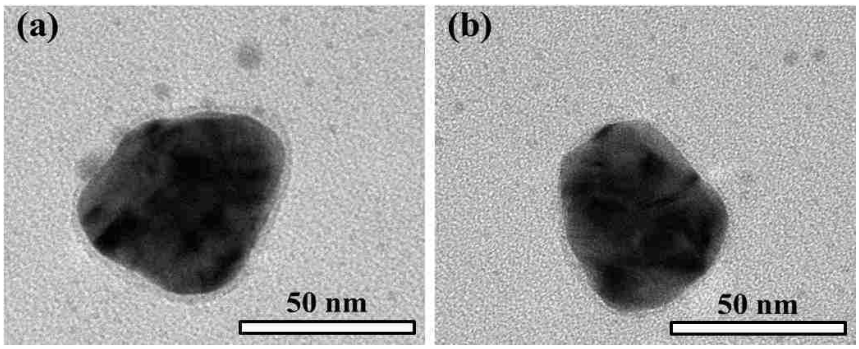

Figure A3.3. (a) and (b) TEM images of the 53 nm gold-silver-gold-silver-gold core-shell-shell-shell-shell nanoparticles.

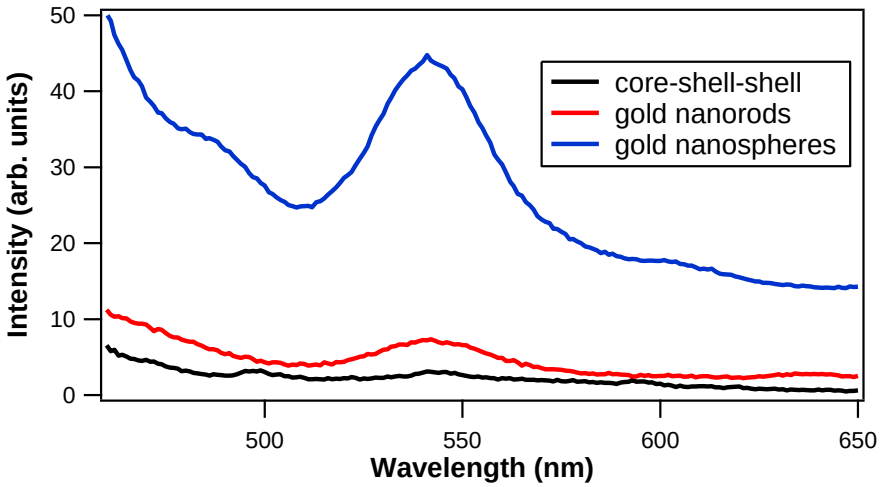

Figure A3.4. Emission spectra of 12-12-30 nm gold-silver-gold core-shell shell nanoparticles, gold nanorods with an average aspect ratio of 3.5, and 54 nm gold nanospheres after 400 nm excitation.

The emission spectra of 12-12-30 nm colloidal gold-silver-gold core-shell-shell nanoparticles, gold nanorods with an average aspect ratio of 3.5, and 54 nm gold nanospheres after 400 nm excitation are shown in Figure A3.4. Gold nanospheres exhibit the highest fluorescence, while gold-silver-gold core-shell-shell nanoparticles exhibit a very low fluorescence.

A3.2 Photothermal Study

Figure A3.5 shows a schematic diagram of the experimental setup used for the photothermal study. Figure A3.6 displays the extinction spectra of the 54 nm spherical colloidal gold nanoparticles, the colloidal gold nanorods (10 nm width and 35 nm length) at a concentration of 3.0 x 10^{11} nanoparticles/mL, and the 12-12-30 nm colloidal gold-silver-gold core-shell-shell nanoparticles (sample CSS4) used in the photothermal study. The extinction of the spherical gold nanoparticles is overlapped with the best fit using Mie theory (dotted black line) at a concentration of 2.8×10^{10} nanoparticles/mL.

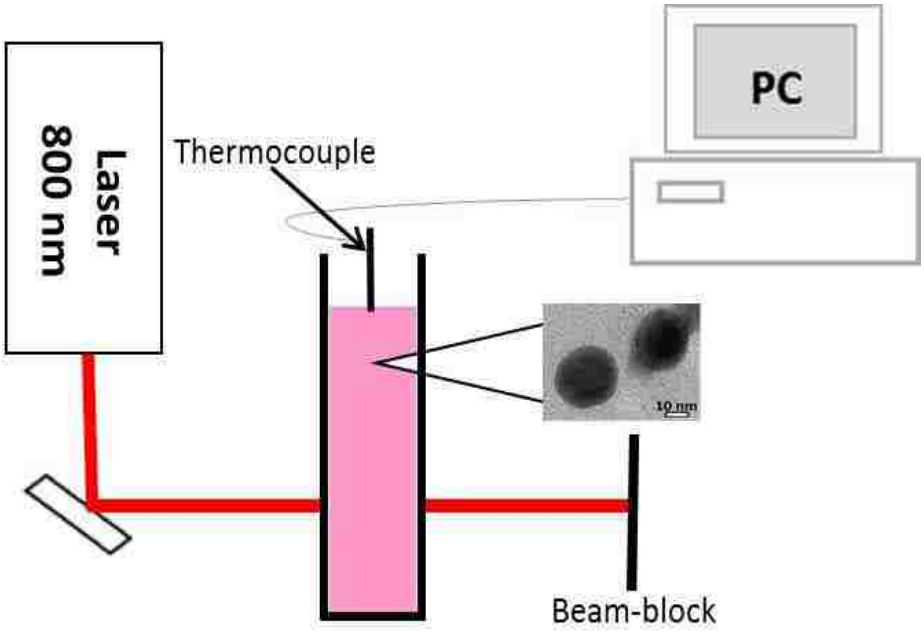

Figure A3.5. Schematic diagram of the experimental setup used for the photothermal study.

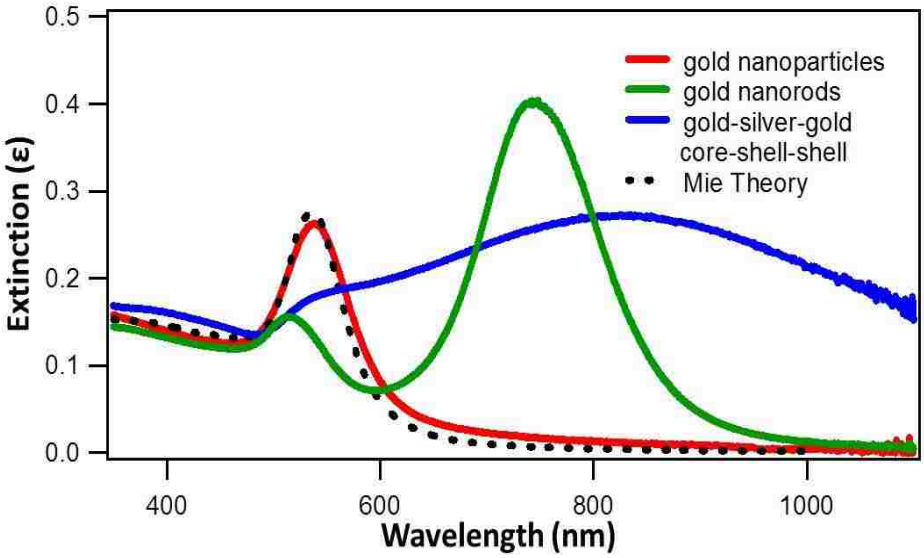

Figure A3.6. Extinction spectra of (red line) 54 nm spherical colloidal gold nanoparticles, (green line) colloidal gold nanorods with a 10 nm width and a 35 nm length, and (blue line) 12-12-30 nm colloidal gold-silver-gold core-shell-shell nanoparticles. The extinction of the spherical gold nanoparticles is overlapped with the best fit using Mie theory (dotted black line).

A3.3 Power-Dependent Transient Absorption Study

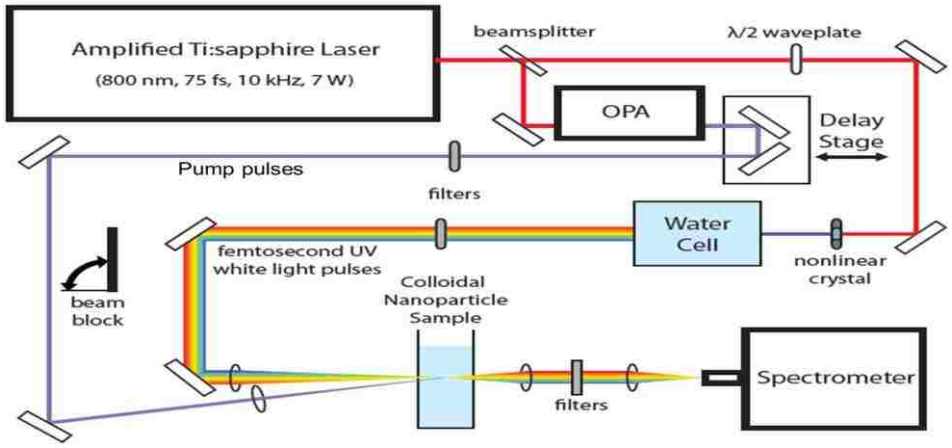

Figure A3.7. Schematic diagram of the femtosecond transient absorption optical setup.

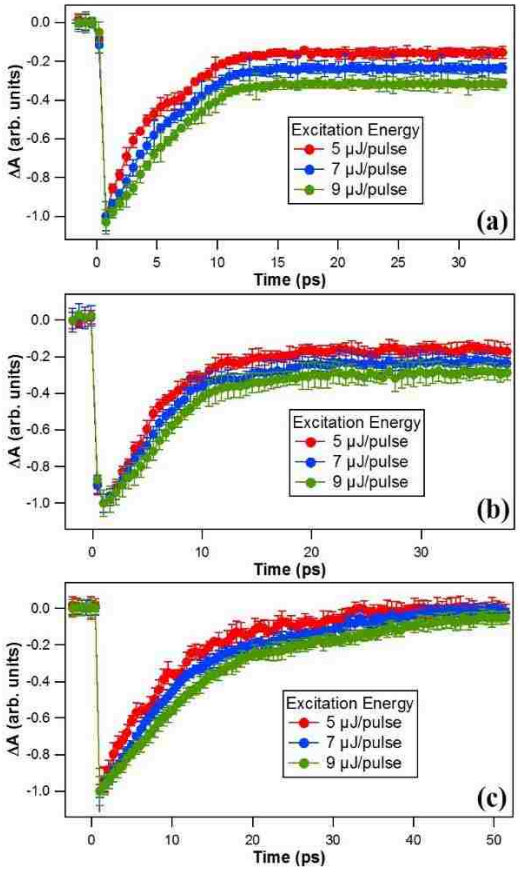

Figure A3.8. Time-dependent transient absorption spectra of (a) 54 nm colloidal gold nanoparticles, (b) colloidal gold nanorods with an average aspect ratio of 3.5, and (c) 12-12-30 nm colloidal gold-silver-gold core-shell-shell nanoparticles after 400 nm excitation pulses at different excitation energies. The transient absorption signal is integrated at 550 nm for the gold nanoparticles and at 750 nm for the gold nanorods and gold-silver-gold core-shell-shell nanoparticles. The time-profiles are all normalized to 1 for clarity.

Figure A3.7 shows a schematic diagram of the femtosecond transient absorption optical setup. Figure A3.8 shows the time-dependent transient absorption spectra of (a) 54 nm colloidal gold nanoparticles, (b) colloidal gold nanorods with an average aspect ratio of 3.5, and (c) 12-12-30 nm colloidal gold-silver-gold core-shell-shell nanoparticles after 400 nm excitation pulses. The magnitude of the transient absorption signal increases with the increase of the excitation power. The time-dependent transient absorption spectra of gold nanoparticles, gold nanorods, and gold-silver-gold core-shell-shell nanoparticles at different excitation energies are normalized to 1 for clarity. The time-profiles are integrated at 550 nm for the gold nanoparticle sample and at 750 nm for gold nanorod and core-shell-shell samples. It was shown that as the excitation is increased, the electron-phonon and phonon-phonon scattering lifetimes become slower due to an increase of the heart capacity of the electron gas.[1,2] The excited-state decay lifetimes shown in Table A3.2 are obtained by fitting the time-dependent transient depletion spectra using a bi-exponential function for the three samples at different excitation energies, the relaxation lifetimes. Figure A3.9 shows the decay spectra obtained using a sum of exponential fits of the time-dependent transient absorption for (a) 54 nm spherical colloidal gold nanoparticles, (b) colloidal gold nanorods with a 10 nm width and a 35 nm length, and (c) 12-12-30 nm colloidal gold-silver-gold core-shell-shell nanoparticles after 400 nm excitation pulses. [3] The lifetimes used to fit the spherical colloidal gold nanoparticles are 8.0 ± 0.6 ps, 2.6 ± 0.3 ps, and 94.0 ± 7.3 ps. The time-traces obtained from the transient absorption measurements of gold nanorods are fit using two lifetimes of 2.8 ± 0.3 ps and 102 ± 7 ps. The time-traces obtained from the transient absorption measurements of core-shell-shell nanoparticles are fit using three lifetimes of 5.0 ± 0.3 ps, 3.0 ± 0.2 ps, and 23.5 ± 0.6 ps.

Table A3.2. The excited-state decay lifetimes are obtained by fitting the time-dependent transient depletion spectra using a bi-exponential function for the three samples at different excitation energies, the relaxation lifetimes.

Excitation Energy	Gold Nanoparticles	Gold Nanorods	Core-Shell-Shell
5 μJ/pulse	2.6 ± 0.3 ps	2.9 ± 0.2 ps	3.0 ± 0.2 ps
	94 ± 7.3 ps	100 ± 9 ps	23.5 ± 0.5 ps
7 μJ/pulse	3.2 ± 0.2 ps	3.2 ± 0.2 ps	3.8 ± 0.2 ps
	114 ± 7.8 ps	116 ± 7 ps	25 ± 0.3 ps
9 μJ/pulse	3.7 ± 0.1 ps	3.5 ± 0.1 ps	4.7 ± 0.3 ps
	121 ± 11 ps	119 ± 9 ps	26.8 ± 0.4 ps

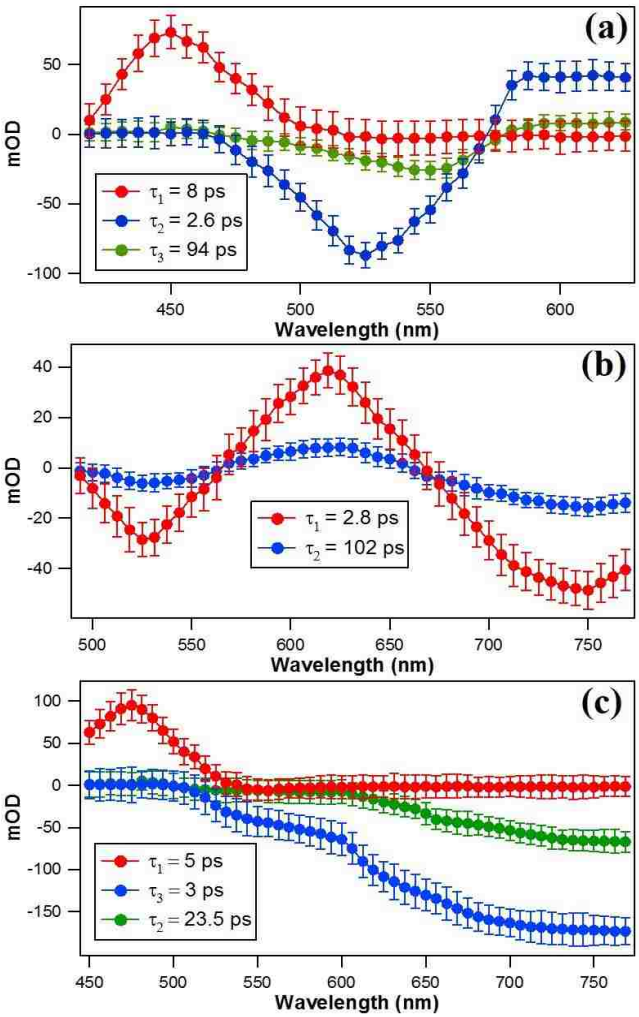

Figure A3.9. Representative decay spectra obtained using a sum of exponential fits of time-dependent transient absorption spectra of (a) 54 nm spherical colloidal gold nanoparticles, (b) colloidal gold nanorods with a 10 nm width and a 35 nm length, and (c) 12-12-30 nm colloidal gold-silver-gold core-shell-shell nanoparticles.

A3.4 References

(1) Logunov, S. L.; Ahmadi, T. S.; El-Sayed, M. A.; Khoury, J. T.; Whetten, R. L. Electron Dynamics of Passivated Gold Nanocrystals Probed by Subpicosecond Transient Absorption Spectroscopy. *J. Phys. Chem. B.* **1997**, *101*, 3713-3719.

(2) Hodak, J. K.; Martini, I.; Hartland, G. V. Spectroscopy and Dynamics of Nanometer-Sized Noble Metal Particles. *J. Phys. Chem. B* **1998**, *102*, 6958–6967.

(3) Duvanel, G.; Grilj, J.; Vauthey, E. Ultrafast Long-Distance Excitation Energy Transport in Donor–Bridge–Acceptor Systems. *J. Phys. Chem. A* **2013**, *117*, 918–928.

APPENDIX 4 – RESONANCE COUPLING AT THE SURFACE OF GOLD-SILVER-GOLD CORE-SHELL-SHELL NANOPARTICLES

A4.1 Additional TEM Images and Spectroscopy

Figure A4.1 shows the high resolution TEM images of (a) 85 ± 7 nm gold nanoparticles, and (b) 65 ± 4 nm gold-silver core-shell nanoparticle. Figure A4.2 shows the extinction spectra of 85 nm gold nanoparticles and 66-11 nm gold-silver core-shell nanoparticles. The extinction spectra of are overlapped with the best fit using Mie theory. Figure A4.3 shows the chemical structures of (a) malachite green, (b) brilliant green, (c) methyl green, and (d) rhodamine 110. The absorption spectra of malachite green, brilliant green, methyl green, and rhodamine 110 are shown in Figure A4.4.

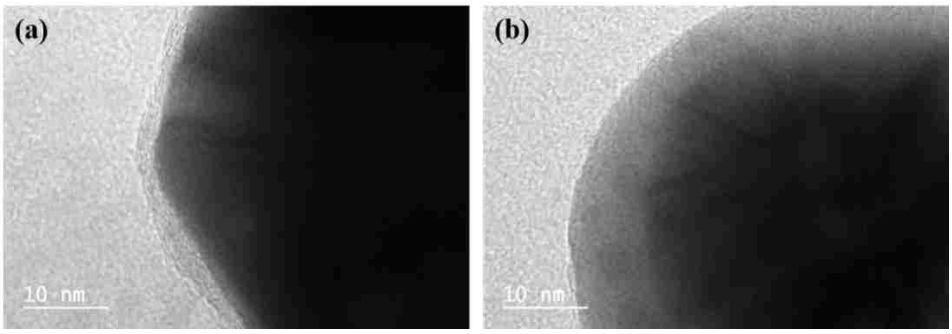

Figure A4.1. High resolution TEM images of (a) 85 ± 7 nm gold nanoparticles and (b) 88 ± 6 nm gold-silver core-shell nanoparticle.

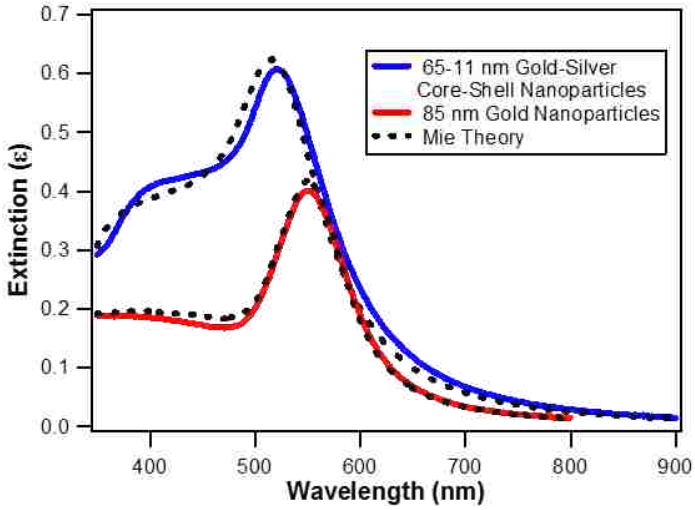

Figure A4.2. Extinction spectra of (red dots) 85 nm gold nanoparticles and (blue dots) 65-11 nm gold-silver core-shell nanoparticles overlapped with the best fit using Mie Theory.

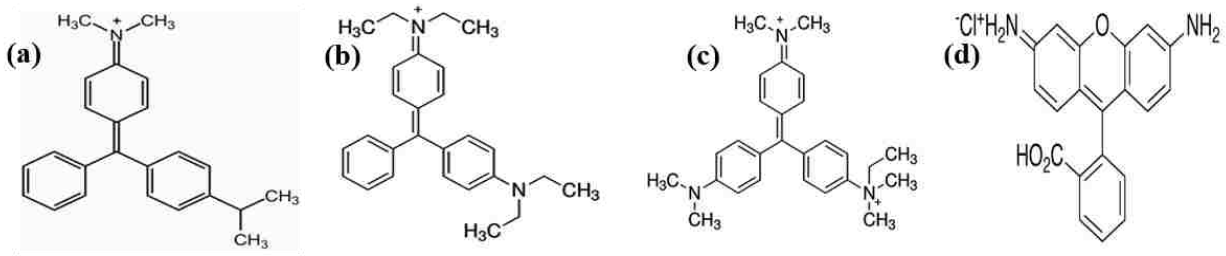

Figure A4.3. Chemical structures of (a) malachite green, (b) brilliant green, (c) methyl green, and (d) rhodamine 110.

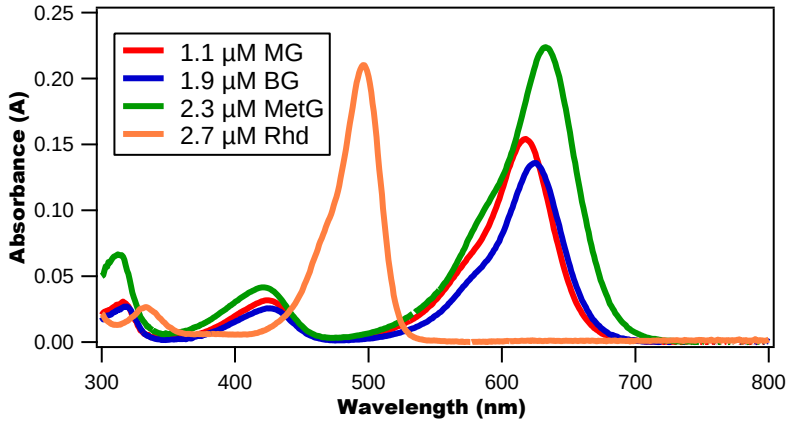

Figure A4.4. Absorption spectra of (red line) 1.1 µM malachite green, (blue line) 1.9 µM brilliant green, (green line) 2.3 µM methyl green, and (orange line) 2.7 µM rhodamine 110.

Figure A4.5 shows the fluorescence signal of (a) malachite green, (b) brilliant green, (c) methyl green, and (d) rhodamine 110 at different added gold nanoparticle concentrations. The fluorescence of malachite green, brilliant green, and methyl green is enhanced when it is adsorbed on the colloidal gold surface. On the other hand the fluorescence of rhodamine 110 is quenched. However, the overall enhancement or quenching intensity of the dye fluorescence is about three times higher on the core-shell-shell surface than the gold surface. These results show a significant enhancement or quenching of the dye molecules adsorbed on the colloidal core-shell-shell surface. The spectral resonance coupling between molecules and the gold-silver-gold core-shell-shell plasmon are investigated using extinction spectroscopy. Figure A4.6 shows the extinction spectra of 106 nm colloidal gold-silver-gold nanoparticles at different adsorbate concentrations. Additional bands due to the resonance coupling between molecules and plasmon are observed.

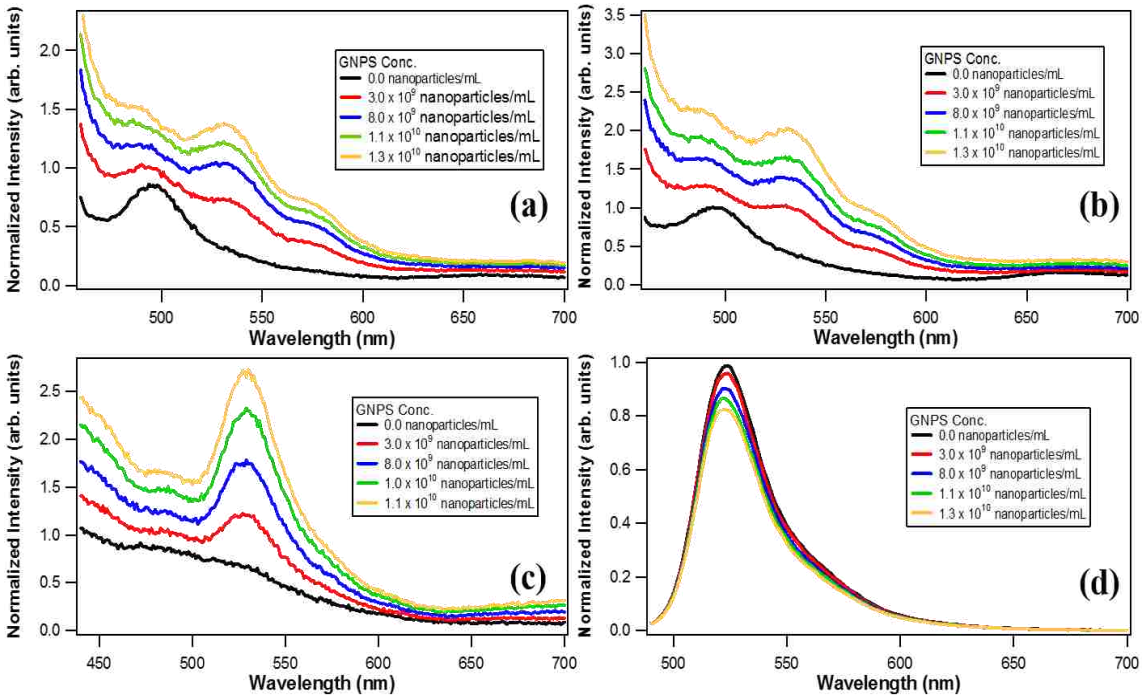

Figure A4.5. Fluorescence spectra of 1.0 μM (a) malachite green, (b) brilliant green, (c) methyl green, and (d) rhodamine 110 at different added 80 nm gold nanoparticle concentrations. The spectra are normalized to the fluorescence intensity of the dyes.

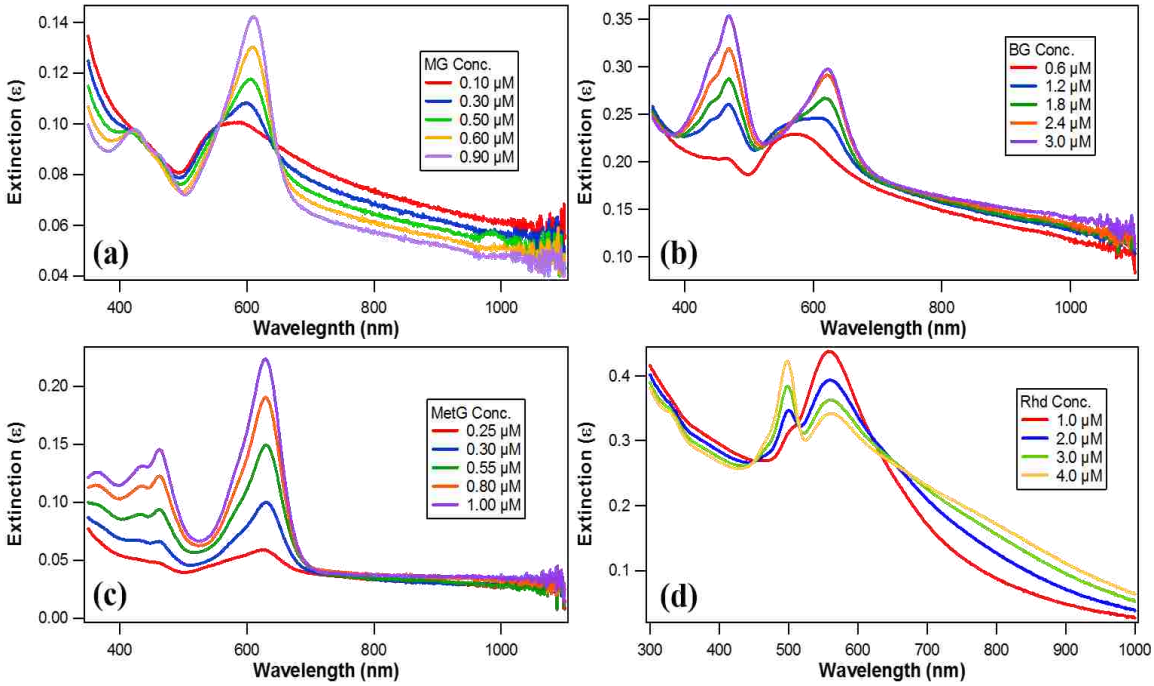

Figure A4.6. Extinction spectra of gold-silver-gold core-shell-shell nanoparticles in water at increasing (a) malachite green, (b) brilliant green, (c) methyl green, and (d) rhodamine 110 concentrations.

A4.2 Additional SHG Data

An extended modified Langmuir model is used to fit the adsorption isotherms obtained from the SHG data. This model takes into the account the signal generated from the dye molecules in water. The total SHG signal measured is the sum of three different contributions, which are the adsorption of molecules on the surface of colloidal nanoparticles, the offset from the nanoparticles in water, and the signal generated from the free dye molecules in water.[1] The total SHG signal is given by

$$SHG_{total} = A(\frac{N}{N_{max}})^2 + B + Ma \qquad (S1)$$

where $^{N}/_{N_{max}}$ is obtained from the modified Langmuir formula, A is the SHG amplitude at the plateau, B is the offset term due to the SHG signal from gold nanoparticles in water without the addition of the dye solution, M is the concentration of free dye molecules in solution, and a is the slope obtained from plotting the SHG signal of dye molecules in water versus dye concentration. Figure A4.7 shows the SHG signal of malachite green, brilliant green, methyl green, and rhodamine 110 in water. The signal is shown to increase linearly, as epxected for hyper-Railegh scattering. The variation of M as a function of dye concentration, N_{max}, and K are obtained from the best fits of the modified Langmuir model. The contribution of the free dye molecule in water is subtracted from the data in order to generate the adsorption isotherms.

Figure A4.8 shows the representative SHG data of 80 nm 9.0×10^9 nanoparticles/mL colloidal gold nanoparticles at different malachite green, brilliant green, methyl green, and rhodamine 110 concentrations. The position of the SHG peak remains constant within experimental uncertainties for all added dye concentrations. The SHG intensities are shown to increase with the added dye concentration reaching maxima as the adsorbates at the core-shell-shell nanoparticle interface reach their saturation values. The fluorescence contribution to the measured spectra of gold nanoparticles at different rhodamine concentrations is significant. Thus, these spectra are fit with a sum of a Gaussian and a third order polynomial functions to deconvolute the SHG and the two-photon fluorescence signal, respectively.

The adsorption isotherms of malachite green, brilliant green, methyl green, and rhodamine 110 on the surface of 80 nm colloidal gold nanoparticles are shown in Figure A4.9. The free energies of adsorption obtained from the best fit of the adsorption isotherms are -15.3 ± 0.2 Kcal/mol, -14.8 ± 0.1 Kcal/mol, -15.0 ± 0.2 Kcal/mol, -12.7 ± 0.3 Kcal/mol for malachite green, brilliant green, methyl green, and rhodamine 110 adsorbed on the surface of 80 nm colloidal gold nanoparticles, respectively. The corresponding number of adsorption sites per particle for the four different molecules is determined to be $(9.4 \pm 0.02) \times 10^3$, $(8.8 \pm 0.03) \times 10^3$, $(9.0 \pm 0.02) \times 10^3$, $(7.8 \pm 0.03) \times 10^3$ sites per particles, respectively. The adsorption site areas are $79 \pm 3\ A^2$, $68 \pm 4\ A^2$, $72 \pm 4\ A^2$, $53 \pm 4\ A^2$.

The effect of added NaCl on the SHG signal of the colloidal core-shell-shell nanoparticles is investigated. The representative SHG spectra of colloidal gold-silver-gold core-shell-shell nanoparticles at different NaCl concentrations are shown in Figure A4.10. A decrease in the SHG signal with the salt concentration is observed due to dilution effects and the change in the electrostatic potential at the nanoparticle surface, which leads to a change in the corresponding $\chi^{(3)}$.[2, 3] The SHG signal remained stable for added NaCl concentrations higher than 65 μM, showing that aggregation does not occur at the added dye concentrations of this study.

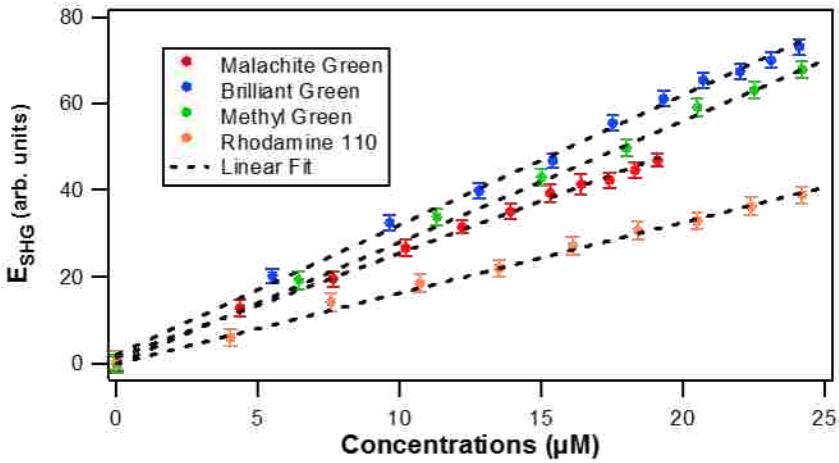

Figure A4.7. Second harmonic generation signal obtained from the addition of malachite green (red dots), brilliant green (blue dots), methyl green (green dots), and rhodamine 110 (orange dots) to water. The signals are shown to increase linearly, as expected for hyper-Raleigh scattering.

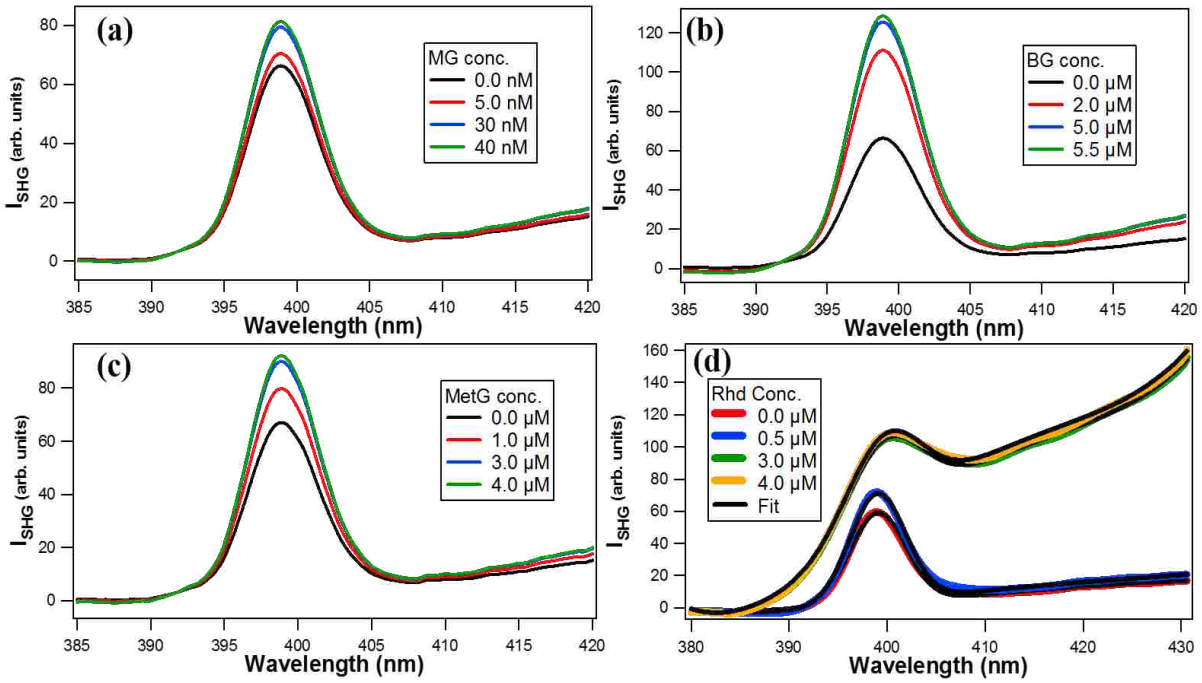

Figure A4.8. SHG spectra of the colloidal 85 ± 7 nm gold nanoparticles at various (a) malachite green, (b) brilliant green, (c) methyl green, and (d) rhodamine 110 concentrations.

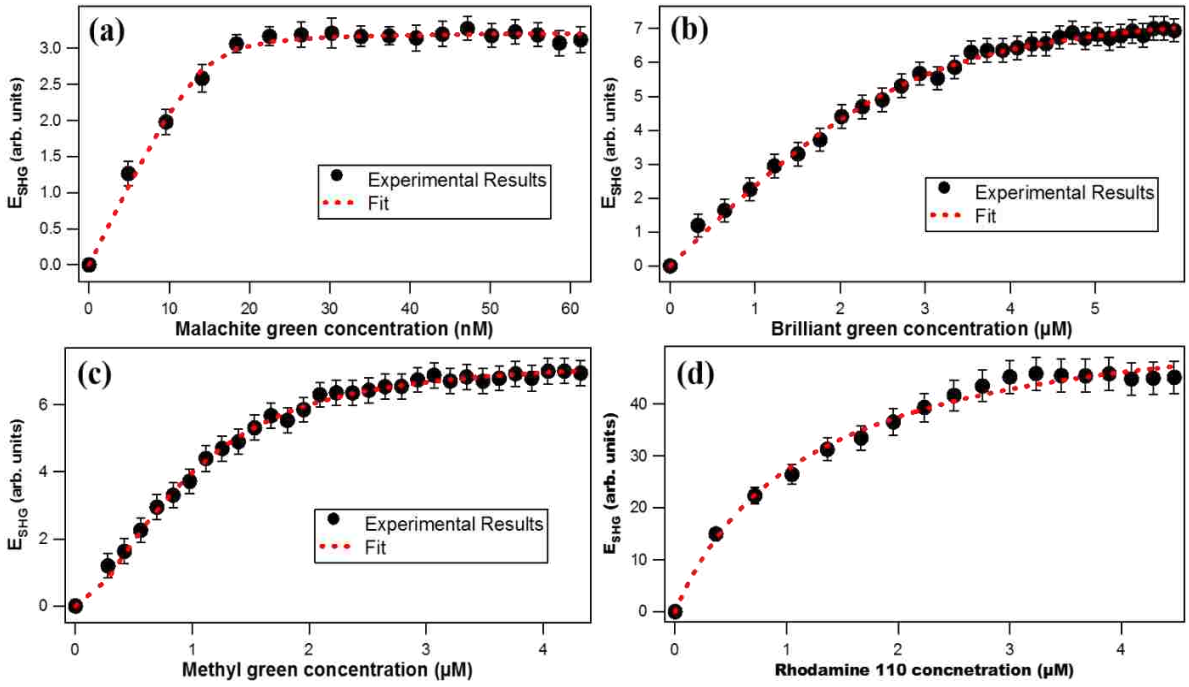

Figure A4.9. Adsorption isotherm results (black dots) obtained from second harmonic generation measurements as a function of (a) malachite green, (b) brilliant green, (c) methyl green, and (d) rhodamine 110 concentrations adsorbed on the surface of 85 ± 7 nm gold nanoparticles 9.0×10^9 nanoparticles/mL. The experimental data are compared with the best fits from the modified Langmuir model (dotted red lines).

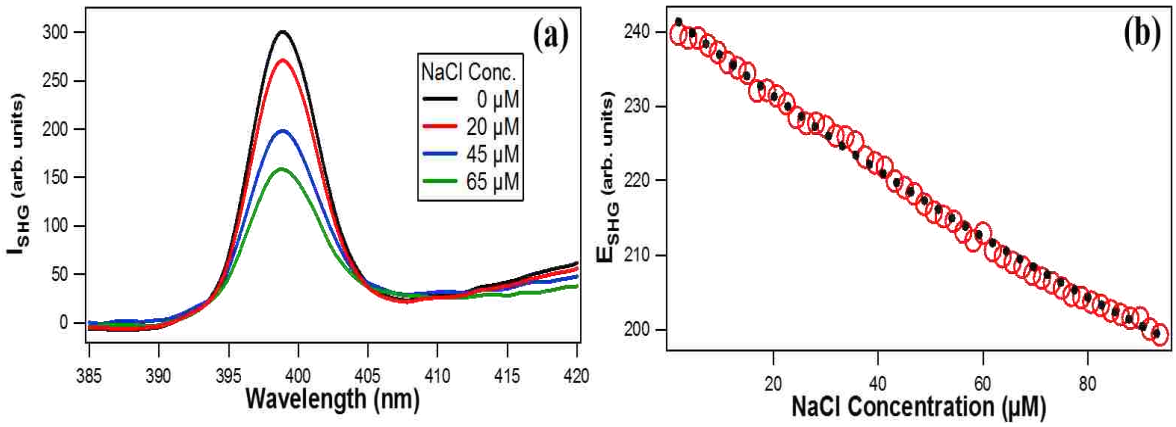

Figure A4.10. (a) SHG spectra of the colloidal 106 ± 7 nm gold-silver-gold core-shell-shell nanoparticles at different NaCl concentration. (b) (red dots) E_{SHG} as a function of the added NaCl concentrations. The black dotted line is a guide to the eye.

A4.3 Additional Transient Absorption Data

Figure A4.11 (a) shows the Transient absorption spectra of 8 μM brilliant green adsorbed on the surface of 85 ± 7 nm colloidal gold nanoparticles at a concentration of 9.6×10^9 nanoparticles/mL at different time delays using 400 nm pump pulse excitation wavelength. (b) The transient absorption time profiles of brilliant green adsorbed on the surface of gold nanoparticles measured at 480 and 600 nm are shown in Figure A4.11 (b). Figure A4.11 (c) shows the decay spectra obtained using a sum of exponential fits for the time-dependent transient absorption spectra of brilliant green adsorbed on the surface of gold nanoparticles. Three lifetimes are needed to accurately describe the excited-state relaxation dynamics of brilliant adsorbed on the surface of colloidal gold nanoparticles. These lifetimes are 0.71 ± 0.05 ps, 0.75 ± 0.04 ps, and 3.33 ± 0.07 ps. Figure A4.12 (a) shows the transient absorption spectra of 7 μM rhodamine 110 adsorbed on the surface of 80 ± 7 nm colloidal core-shell-shell nanoparticles at a concentration of 9.6×10^9 nanoparticles/mL at different time delays using 400 nm pump pulse excitation wavelength. The transient absorption time profiles of rhodamine 110 adsorbed on the surface of core-shell-shell nanoparticles measured at 500 nm are shown in Figure A4.12 (b). The time-profile can be fit with a sum of two exponential functions with a first lifetime longer than 10 ns and a second of 60 ± 8 ps.

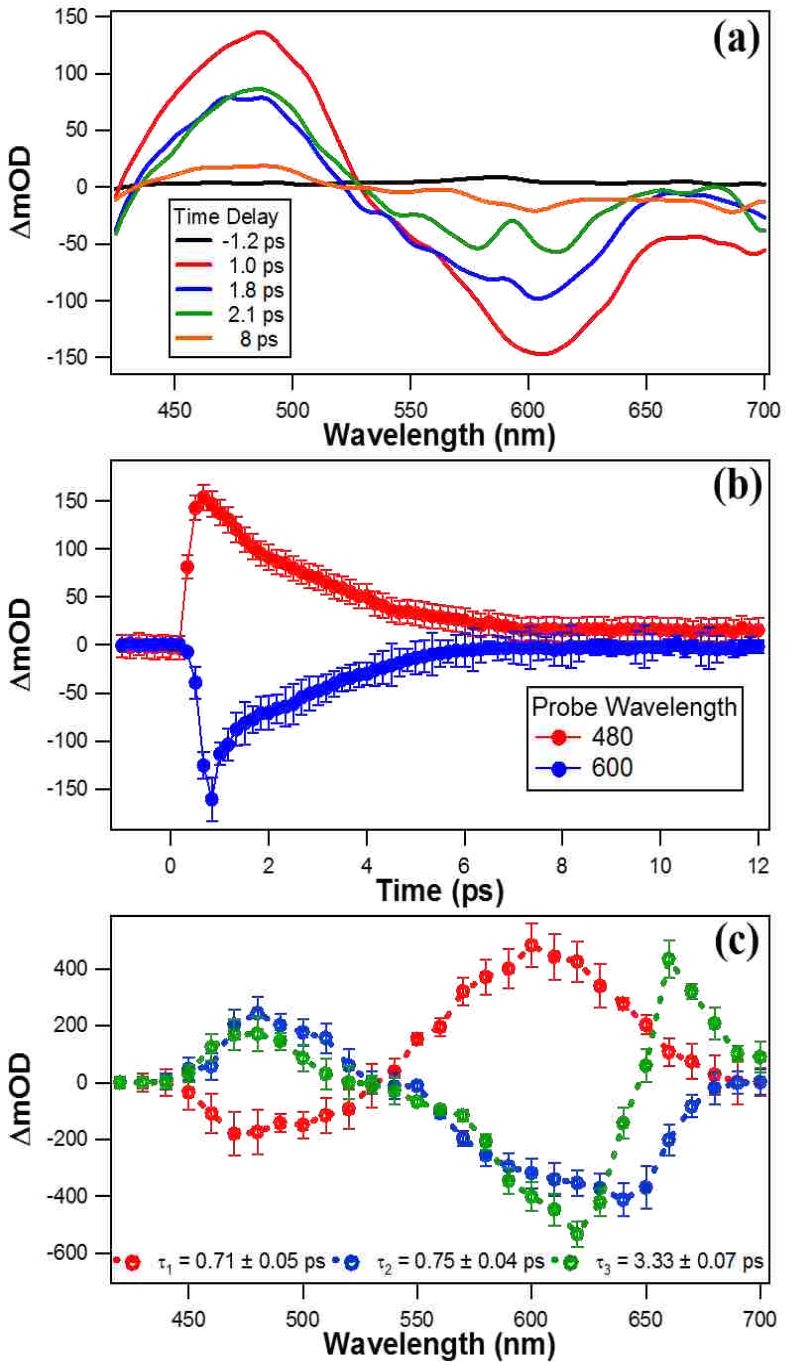

Figure A4.11. (a) Transient absorption spectra of 8 μM brilliant green adsorbed on the surface of 85 ± 7 nm colloidal gold nanoparticles at a concentration of 9.6×10^9 nanoparticles/mL at different time delays using 400 nm pump pulse excitation wavelength. (b) Transient absorption time profiles of brilliant green adsorbed on the surface of gold nanoparticles measured at 480 and 600 nm. (c) Decay spectra obtained using a sum of exponential fits for the time-dependent transient absorption spectra of brilliant green adsorbed on the surface of gold nanoparticles.

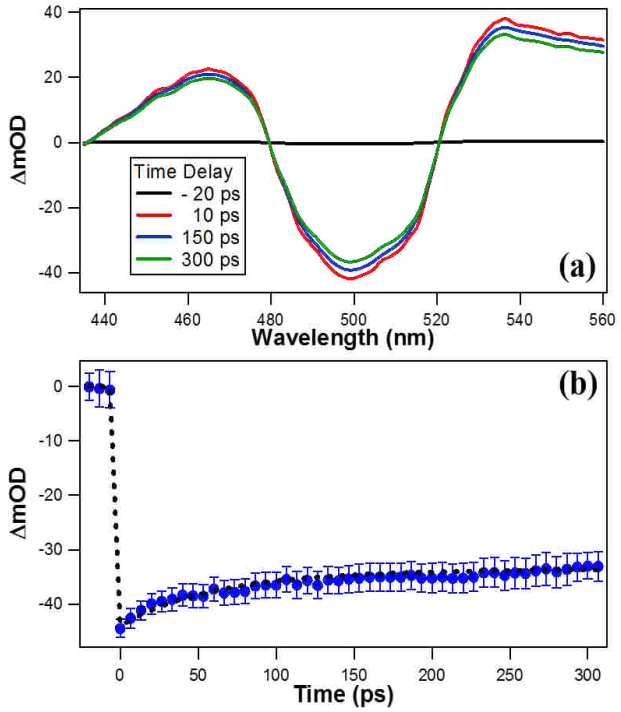

Figure A4.12. (a) Transient absorption spectra of 7 μM rhodamine 110 adsorbed on the surface of 85 ± 7 nm colloidal core-shell-shell nanoparticles at a concentration of 9.6×10^9 nanoparticles/mL at different time delays using 400 nm pump pulse excitation wavelength. (b) Transient absorption time profiles of rhodamine 110 adsorbed on the surface of core-shell-shell nanoparticles measured at 500 nm.

A4.4 References

(1) Karam, T. E.; Haber, L.H. Molecular Adsorption and Resonance Coupling at the Colloidal Gold Nanoparticle Interface. *J. Phys. Chem. C* **2014**, *118*, 642−649.

(2) Yan, E. C. Y.; Liu, Y.; Eisenthal, K. B. New Method for Determination of Surface Potential of Microscopic Particles by Second Harmonic Generation. *J. Phys. Chem. B* **1998**, *102*, 6331−6336.

(3) Kumal, R. R.; Karam, T. E.; Haber, L. H. Determination of the Surface Charge Density of Colloidal Gold Nanoparticles Using Second Harmonic Generation. *J. Phys. Chem. C*, **2015**, *119*, 16200–16207.

APPENDIX 5 – ADDITIONAL CHARACTERIZATION OF TiO_2-Au NANOCOMPOSITES

A5.1 Analysis of TEM Images

Figure A5.1 shows representative TEM images of the 9.9 ± 0.4 nm TiO_2 nanoparticles. The TiO_2 nanoparticles have a significantly lower contrast under TEM compared to gold nanoparticles. The contrast of the TEM images of the TiO_2 nanoparticles is darkened for clarity. The TEM images are taken using a JOEL 100CX microscope with carbon-coated copper grids. Figure A5.2 shows Histogram representing the size distribution of the TiO_2 nanoparticle sample. The experimental results are fit to a lognormal function. Figures A5.3, A5.4, and A5.5 show representative TEM images of the 1:1, 1:2, and 1:3 TiO_2-Au nanocomposites, respectively. Figure A5.6 show the histograms of the size distribution of the 1:1, 1:2, and 1:3 TiO_2:Au nanocomposite samples. The experimental results fit to a lognormal function. These histograms show that the 1:1, 1:2, and 1:3 samples possess distinguishable size distributions.

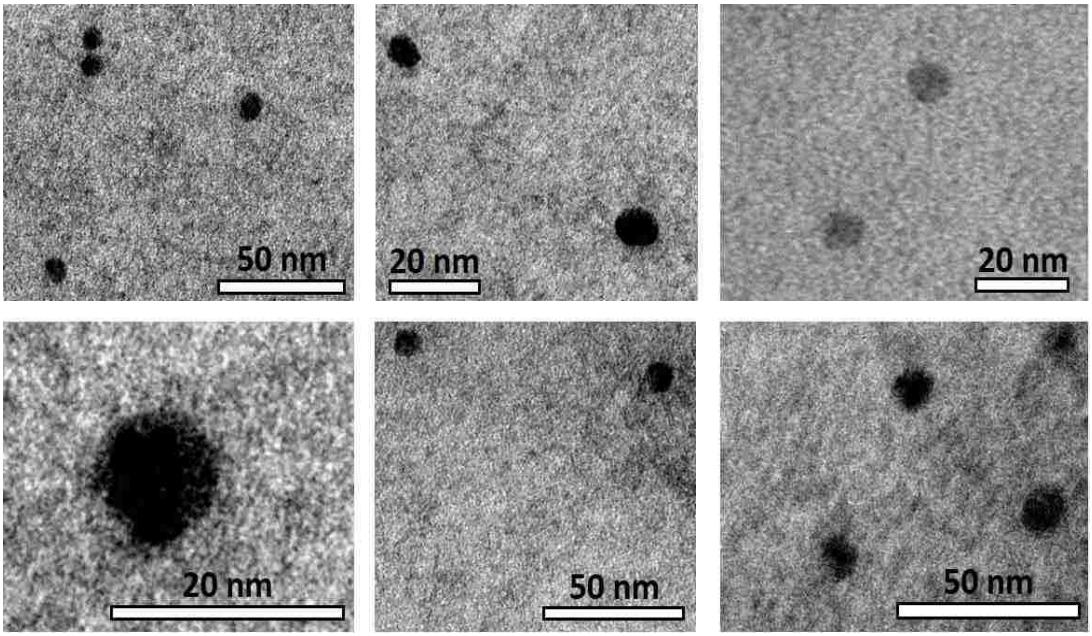

Figure A5.1. Transmission electron microscopy images of the 9.9 nm ± 0.4 nm TiO_2 nanoparticles sample.

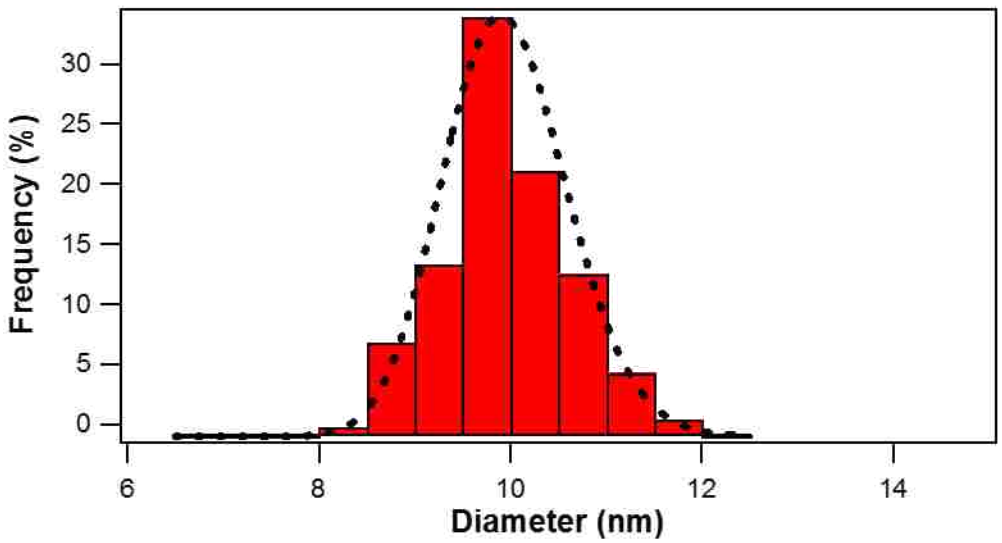

Figure A5.2. Histogram representing the size distribution of the TiO_2 nanoparticle sample. The experimental results are fit to a lognormal function.

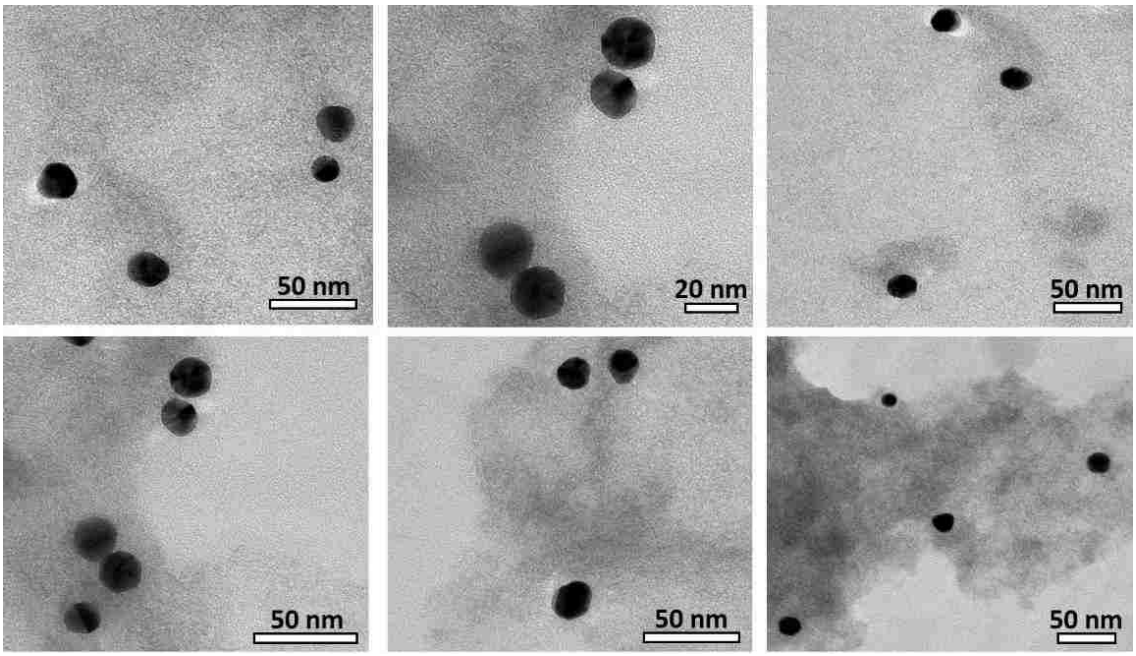

Figure A5.3. Transmission electron microscopy images of the 1:1 TiO_2-Au nanocomposites sample.

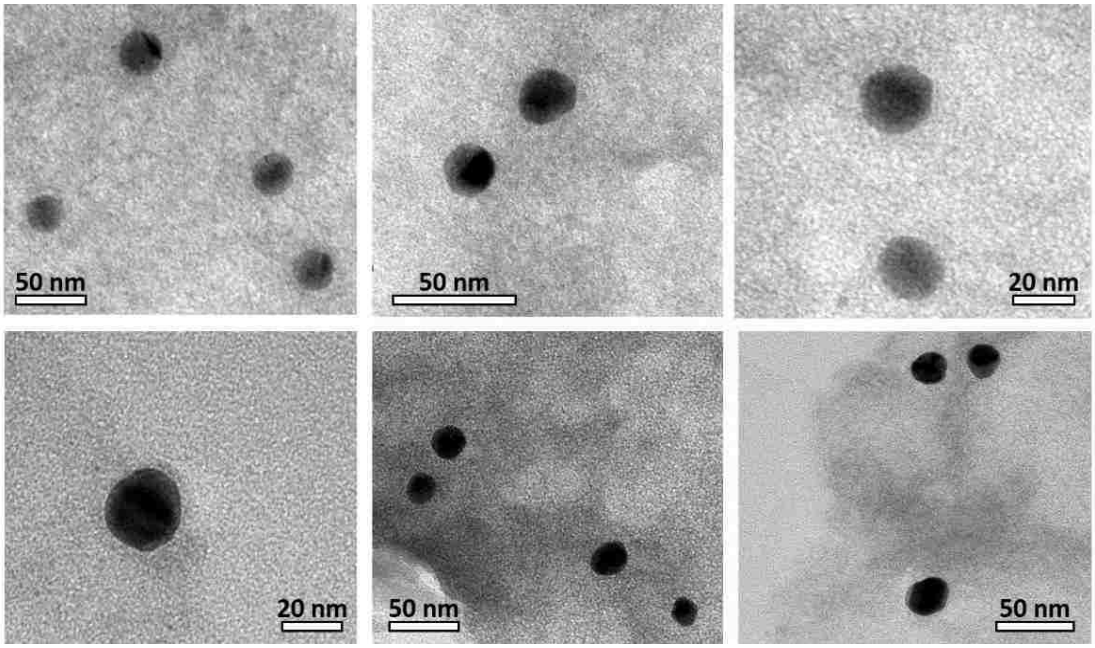

Figure A5.4. Transmission electron microscopy images of the 1:2 TiO_2-Au nanocomposites sample.

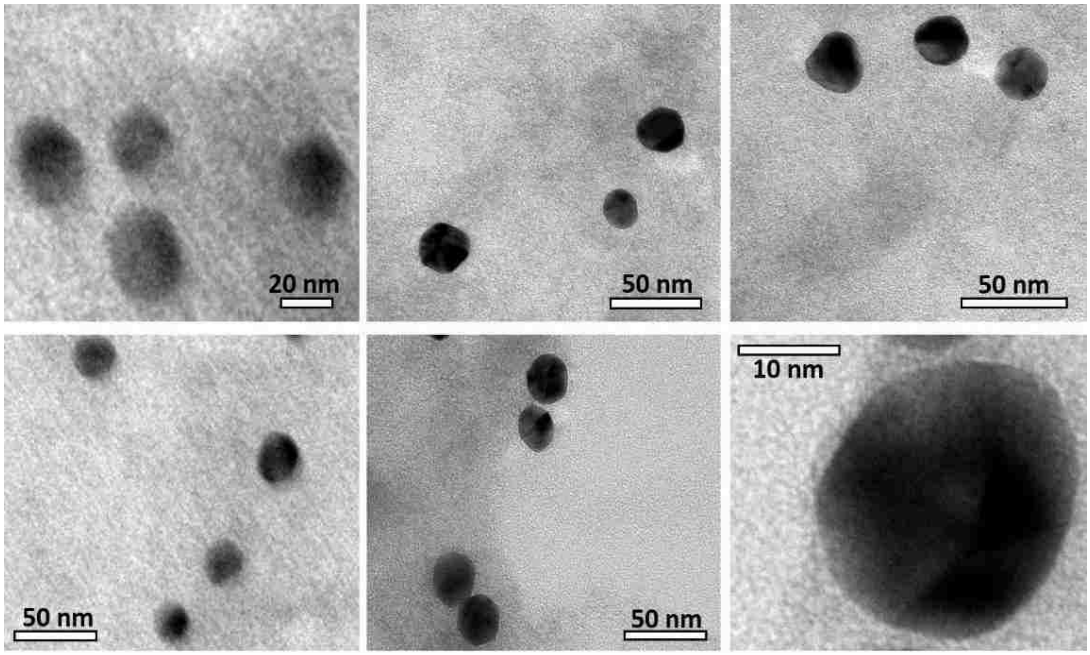

Figure A5.5. Transmission electron microscopy images of the 1:3 TiO_2-Au nanocomposites sample.

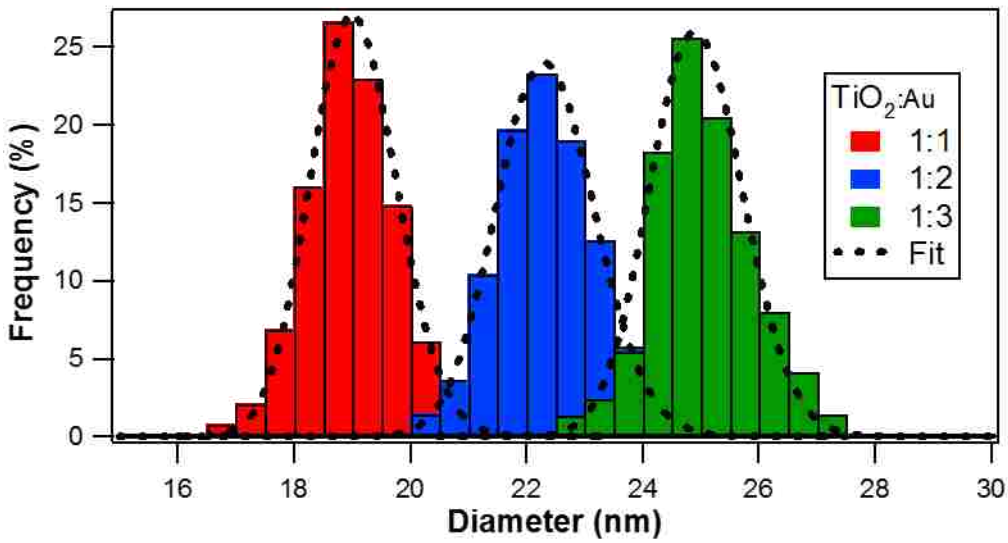

Figure A5.6. Histogram representing the size distribution of the 1:1, 1:2, and 1:3 TiO_2:Au nanocomposite samples. The experimental results are fit to a lognormal function.

The errors in the measured nanoparticle sizes are determined from the standard deviations after surveying more than 400 nanoparticles. The sizes of the gold nanoclusters at the surface of TiO_2 nanoparticles are estimated from the increases of the overall TiO_2 nanoparticle sizes. Table A5.1 lists the nanocluster sizes s determined by the TEM measurements given by the radius increase with $s = r_{TiO_2-Au} - r_{TiO_2}$ where r_{TiO_2-Au} is the average nanocomposite radius and r_{TiO_2} is the average radius of the TiO_2 nanoparticles. The errors in the sizes of the gold nanoclusters adsorbed to the TiO_2 nanoparticle surface are determined by error propagation from the standard deviations of the sizes of the TiO_2 nanoparticles and the TiO_2-Au nanocomposites.

A5.2 Phonon Analysis

The acoustic phonon oscillation frequencies from the different TiO_2-Au nanocomposites are compared to three different size-dependent models that are based on free gold nanospheres, core-shell nanoparticles, and free gold nanorods in order to assess the most likely description of the nancluster morphology. In the first model, the gold nanoclusters are assumed to form perfect spheres tangentially adsorbed at the TiO_2 nanoparticle surface. In this case, the theoretical sizes of the gold nanospheres can be calculated from the experimental values of the phonon oscillation frequenices using the solution of the Navier equation given by $\omega_0 = Re\xi_0 v_L^s / r$, where v_L^s is the longitudinal sound velocity of the nanosphere,

r is the radius of nanosphere, and ξ_0 is the normalized frequency of the radial mode.[1] This model has been successfully applied to free metallic nanospheres in water and embedded in glass.[1, 2] The theoretically predicted gold nanocluster radii calculated from the experimental values of the oscillation frequencies using this model are shown in Table A5.1 for v_L^S = 3240 m/s and ξ_0 = 2.944 for the values for free gold nanospheres.[1] However, the radii of the nanoclusters calculated from this model are larger by almost a factor of two compared to the sizes obatined from the TEM measurements, assuming this architecture. This suggests that the gold nanoclusters on the TiO_2 surface are not perfect spheres tangentially attached to the surface, but may be described by hemispherical nanoclusters adsorbed to the surface, especially at lower gold concentrations.

In the second model of the acoustic phonon analysis, gold nanoclusters at the TiO_2 nanoparticle surface are assumed to have rod-like shapes. In this case, the lengths of the rods are calculated using an equation given by[2, 3] $T = 2L/\sqrt{E/\rho}$, where E is the Young's modulus and ρ is the density. The calculated values of the gold rod lengths L determined from the experimental values of the oscillation periods T are shown in Table A5.1 for $E = 42$ GPa and $\rho = 19.7$ g/cm^3. These values deviate from the sizes determined by the TEM measurements for the three TiO_2-Au samples, so the nanoclusters are not well described using the nanorod model.

In the final model of analysis, the TiO_2-Au nanocomposites are assumed to have a core-shell architecture. In this case, the theoretical sizes of the gold nanoshells are calculated from the experimental values of the phonon oscillation frequenices using a model derived from the Helmholtz equation.[4] Here, the equation of the size-dependent oscillation frequency is given by $\omega_0 = \frac{2v_L^S\beta_S}{R_2}(3 - 4\beta_S^2)^{1/2}$, where R_2 is the sum of the core radius and the shell width, and β_S is given by v_T^S/v_L^S, where v_L^S and v_T^S are the longitudinal and transverse sound velocities in the gold shell, respectively, according to the heavy shell approximation. The calculated values of the shell widths w are shown in Table A5.1 using the experimentally measured phonon frequencies with v_L^S and v_T^S equal to 3240 m/s and 1200 m/s, respectively. The shell width w equals $R_2 - R_1$, where R_1 is the core radius. The calculated values of w are larger than the experimental results

obtained by TEM, which indicates that the nanocomposites are not accurately described by a core-shell architecture with a fully formed shell. However, previous studies suggest that very thin shells lead to larger oscillation periods than expected due to an imhomogeneous and porous shell structure, which may be consistent with the results reported here.

Table A5.1. The nanocluster sizes $s\ (expt)$ measured by TEM for the three TiO_2-Au nanocomposite samples compared to theoretical size predictions from the experimentally measured acoustic phonon oscillations based on free gold nanospheres of radius $r\ (sphere)$, free gold nanorods of length $L\ (rod)$, and TiO_2-gold core-shell nanoparticles of shell width $w\ (shell)$.

Sample	s (expt)	r (sphere)	L (rod)	w (shell)
1:1 TiO_2:Au	4.6 ± 0.3 nm	4.3 nm	2.1 nm	5.8 nm
1:2 TiO_2:Au	6.0 ± 0.3 nm	5.8 nm	2.8 nm	9.5 nm
1:3 TiO_2:Au	7.2 ± 0.3 nm	6.9 nm	3.3 nm	12.1 nm

The TEM measurements and the corresponding acoustic phonon frequencies from the transient absorption results from the TiO_2-Au nanocomposites are compared to sizes calculated from analytical models based on different nanocomposite architectures. Gold nanoclusters adsorbed to the TiO_2 nanoparticle surface can be described as hemispherical in shape. Alternatively, the gold nanoclusters can aggregate on the surface to form a porous, imhomogeous shell. Individual hemispherical nanoclusters may form at lower gold concentrations, and then the nanoclusters may interconnect with neighboring nanoclusters to form extended porous shells at higher gold concentrations. More work is still needed to accurately determine the morphologies, size distributions, and separation distances of the gold nanoclusters adsorbed to the TiO_2 nanoparticle surface.

A5.3 References

(1) C. Voisin, D. Christofilos, N. Del Fatti, F. Vallée, Physica B: Condensed Matter **316**, 89 (2002).

(2) L. Wang, S. Takeda, C. Liu, N. Tamai, J. Phys. Chem. C **118**, 1674 (2014).

(3) M. Hu, X. Wang, G. V. Hartland, P. Mulvaney, J. P. Juste, J. E. Sader, J. Am. Chem. Soc. **125**, 14925 (2003).

(4) C. Guillon, P langot, N. Del Fatti, F. Vallée, A. S. Kirakosyan, T. V. Shahbazyan, T. Cardinal, M. Treguer, Nano Lett. **7**, 138 (2007).

APPENDIX 6 – CHARACTERIZATION OF $[Ru(bipy)_3][BETI]_2$ NANOGUMBOS

A6.1 Characterization of GUMBOS and NanoGUMBOS

The $[Ru(bipy)_3][BETI]_2$ GUMBOS are characterized using nuclear magnetic resonance (both ^{1}H-NMR and ^{19}F-NMR), mass spectrometry, X-ray diffraction (XRD), X-ray crystallography, thermogravimetric analysis (TGA), and differential scanning calorimetry (DSC). The $[Ru(bipy)_3][BETI]_2$ nanoGUMBOS are additionally characterized using transmission electron microscopy (TEM), ultraviolet-visible absorption spectroscopy, and fluorescence spectroscopy. The chemical structures of ruthenium(II)-tris-(2,2'-bipyridine) and bis(pentafluoroethylsulfonyl)imide that make up the $[Ru(bipy)_3][BETI]_2$ nanoGUMBOS are shown in Figure A6.1. The ^{1}H-NMR spectra of the $[Ru(bipy)_3][BETI]_2$ GUMBOS in dimethyl sulfoxide are performed using a Bruker Avance 400 MHz NMR spectrometer and show peaks at δ 8.83 (d, J= 7.96Hz, 6H), 8.17 (t, J=7.32, 6H), 7.72 (d, J=5.68 Hz, 6H), and 7.53 (t, J=6.18, 6H). Similarly, the ^{19}F-NMR spectra show peaks at δ −117.64 and −79.33. Mass spectrometry is performed using a Bruker Ultraflextreme MALDI TOF mass spectrometer to measure the mass to charge ratios of 570 amu for the cation and 380 amu for the anion, as expected for these molecular ions. The X-ray diffraction pattern of the GUMBOS, shown in Figure A6.2, displays many sharp lines illustrating the high crystallinity of the sample. Additionally, X-ray crystallography is performed to determine that the crystal structure has monoclinic symmetry with a C2/c space group. The *a*, *b*, and *c* cell lengths are determined to be 24.4334 Å, 15.4669 Å, and 17.4480 Å, respectively, with a total cell volume of 4734.7 Å^3. The alpha, beta, and gamma cell angles are 90 degrees, 134.105 degrees, and 90 degrees, respectively.

Thermogravimetric analysis using a Hi Res Modulated TGA 2950 shows that the $[Ru(bipy)_3][BETI]_2$ GUMBOS have high purity and thermal stability. The sample is heated from room temperature to 600 ^{o}C at the rate of 10 ^{o}C min^{-1}, with the TGA plot shown in Figure A6.3 revealing a very high decomposition temperature of around 385 ^{o}C, compared to several decomposition temperatures near 100 ^{o}C, 140 ^{o}C, 330 ^{o}C, and 380 ^{o}C for $[Ru(bipy)_3]Cl_2 \cdot 6H_2O$.[1] The thermal phase transition characteristic

of the $[Ru(bipy)_3][BETI]_2$ GUMBOS is studied with a Q100 differential scanning calorimeter (DSC, TA instruments, New Castle, DE). A few milligrams of the GUMBOS is weighed in an aluminum crucible and sealed with an aluminum lid. The sample is scanned from −40 °C to 250 °C with a rate of 5 °C min^{-1} under a nitrogen flow of 50 mL min^{-1}. Figure A6.4 shows that the GUMBOS display a very sharp melting point peak at 230 °C with no evidence of a glass transition peak, demonstrating that the compound is highly crystalline and free of impurities. This contrasts with previous differential scanning calorimetry measurements on $[Ru(bipy)_3]Cl_2 \cdot 6H_2O$ which show several broad peaks between 100 °C and 400 °C. The melting point of the GUMBOS measured using MPA 160 and MPA 161 DigiMelt SRS systems is consistent with the melting point determined from differential scanning calorimetry.

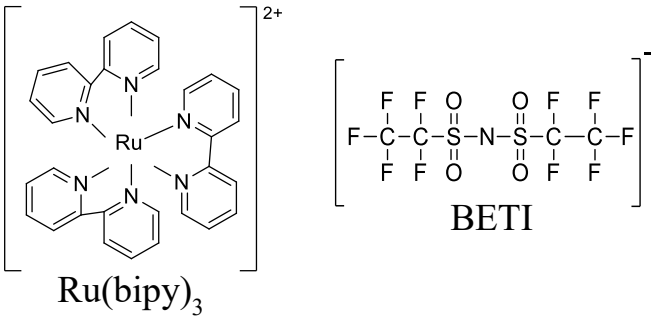

Figure A6.1. Chemical structures of the $Ru(bipy)_3^{2+}$ and $BETI^-$ molecular ions.

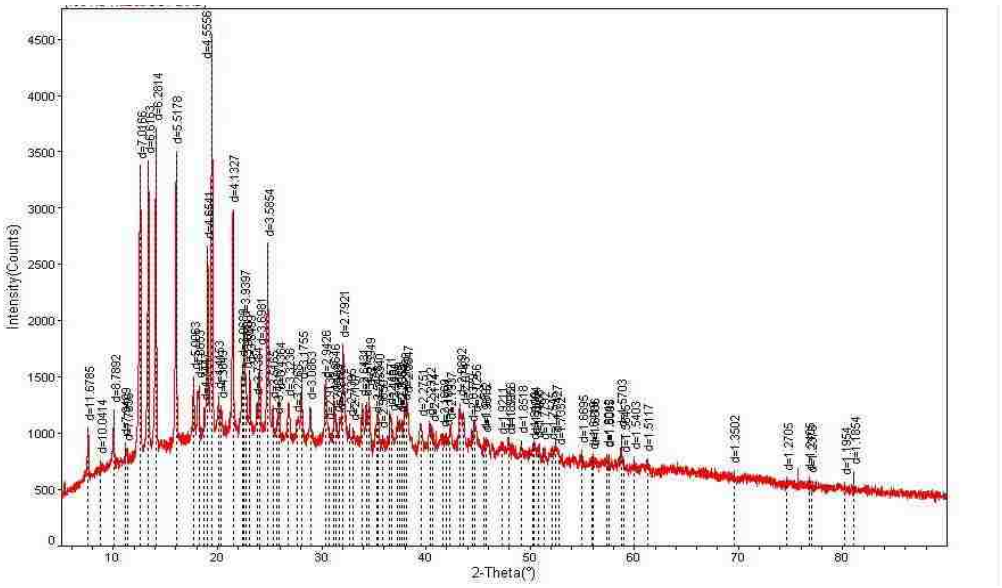

Figure. A6.2. Powder X-ray diffraction pattern of $[Ru(bipy)_3][BETI]_2$ GUMBOS.

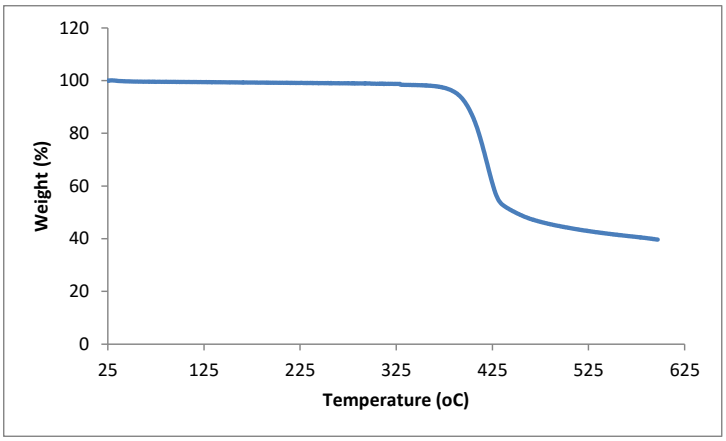

Figure A6.3. TGA plot for $[Ru(bipy)_3][BETI]_2$ GUMBOS.

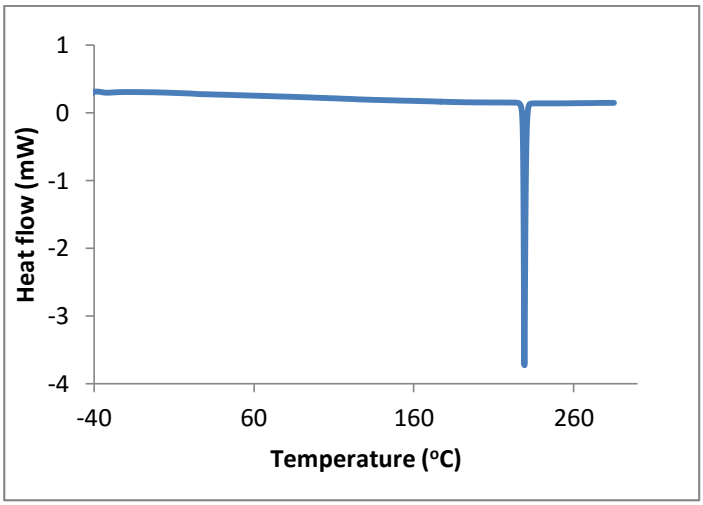

Figure A6.4. DSC plot for GUMBOS showing a sharp melting peak.

Transmission electron microscopy of nanoGUMBOS is obtained using a Dulong America's LVEMS Benchtop TEM to measure the size distribution and morphology of the nanoparticles. Aliquots of 4 µL from the nanoGUMBOS aqueous solutions, prepared under different ultrasonication conditions as described in the chapter 6, are placed on separate carbon-coated copper grid and air-dried at room temperature overnight. TEM images, shown in Figure A6.5 (a), (b), and (c), determine the nanoparticles to be spherical in shape with size distributions of 97 nm ± 19 nm, (b) 56 nm ± 13 nm, and (c) 23 nm ± 5 nm, respectively.

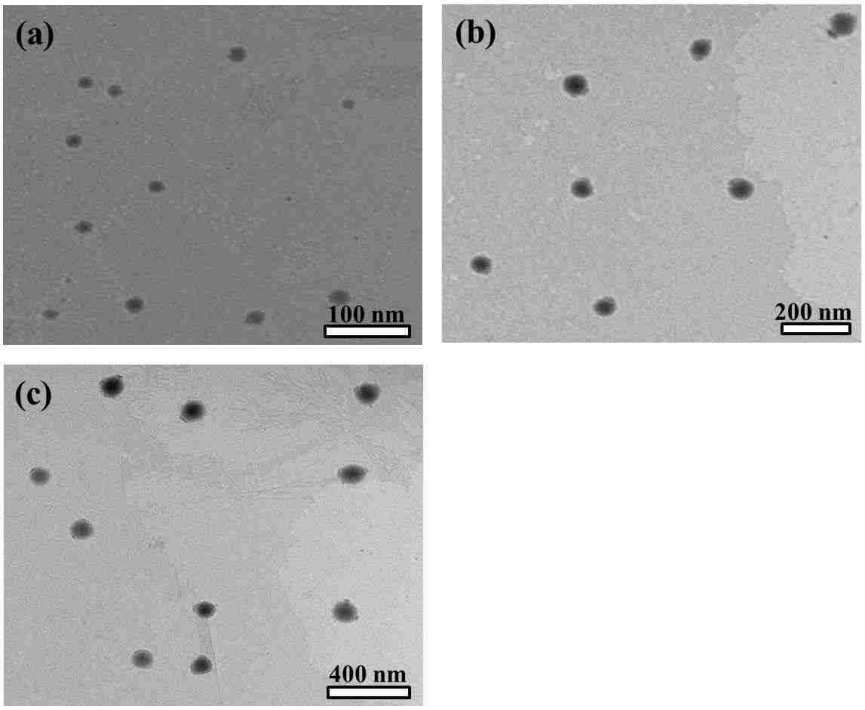

Figure A6.5. Transmission electron microscopy (TEM) images of the $[Ru(bipy)_3][BETI]_2$ nanoGUMBOS prepared under varying ultrasonication conditions showing size distributions of (a) 23 nm ± 5 nm, (b) 56 nm ± 13 nm, and (c) 97 nm ± 19 nm, respectively.

Ultraviolet-visible absorption spectra of 70 μM aqueous $Ru(bipy)_3Cl_2$ and the $[Ru(bipy)_3][BETI]_2$ nanoGUMBOS in water are displayed in Figure A6.6. The $[Ru(bipy)_3][BETI]_2$ nanoGUMBOS are prepared to have the same overall ruthenium bipyridine concentrations of 70 μM for direct comparisons with the aqueous $Ru(bipy)_3Cl_2$ measurements. The nanoGUMBOS and dye solutions show similar peaks, with the high energy peak at 290 nm assigned to the ligand to ligand (LL) π-π* transition while the second peak near 455 nm is ascribed to the singlet metal to ligand charge transfer (MLCT) (d-π*) transition. The molar extinction coefficients decrease significantly in nanoGUMBOS, possibly due to molecular confinement and optical shielding of internal molecules in the central volume of the nanoGUMBOS by molecules closer to the surface.

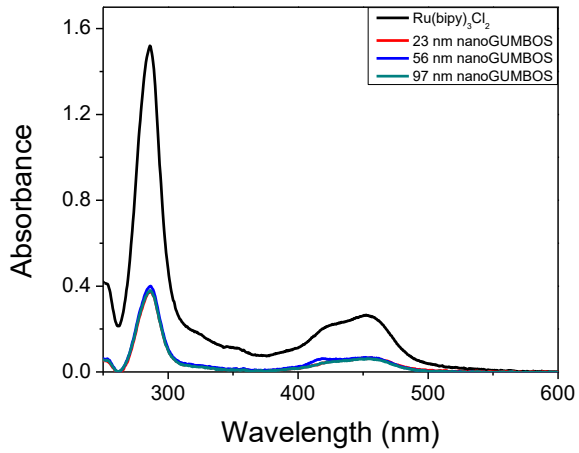

Figure A6.6. Absorption spectra of aqueous $Ru(bipy)_3Cl_2$ (black line) and $[Ru(bipy)_3][BETI]_2$ nanoGUMBOS with average sizes of 23 nm (red line), 56 nm (blue line), and 97 nm (green line).

A6.2 Transient Absorption Time Profiles and Fits

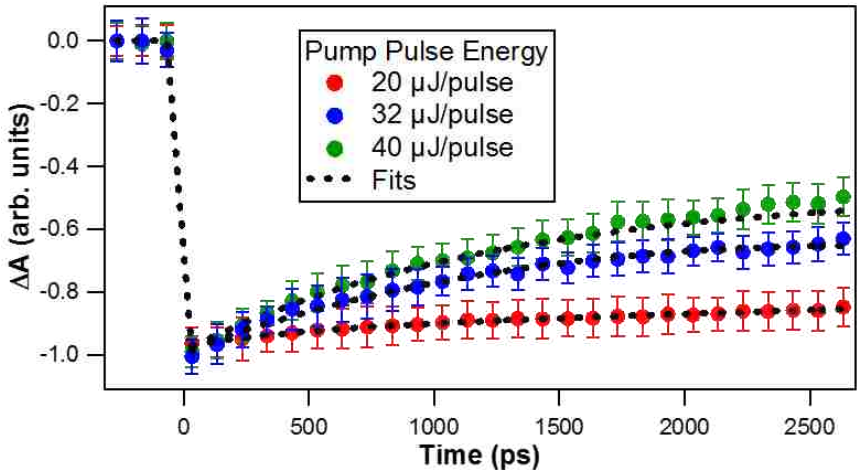

Figure A6.7. Time-dependent transient absorption spectra of 0.4 mM aqueous $Ru(bipy)_3Cl_2$ measured at 450 nm at various pump pulse energies. The data are fit using bi-exponential functions.

Figure A6.7 shows the transient absorption ground-state depletion time profiles of aqueous $Ru(bipy)_3Cl_2$ using excitation with 400 nm pump pulse energies of 20, 32, and 40 µJ. The spectra are normalized for clarity. The relaxation decays are fit using bi-exponential functions of the form $y_0 + A_1 \exp\left(-\frac{t}{\tau_1}\right) + A_2 \exp\left(-\frac{t}{\tau_2}\right)$ to obtain the lifetimes and amplitudes of the fits, which are given are Table A5.1. These relaxation decays are attributed to excited states of $Ru(bipy)_3^{2+}$ that are accessible through multi-photon processes that are only observed at higher pump pulse energies. The values of the lifetimes and the ratio of A_1/A_2 at different pump pulse energies remain fairly constant to within

experimental uncertainty. These lifetimes are similar to the ones obtained from transient absorption on the size-dependent $[Ru(bipy)_3][BETI]_2$ nanoGUMBOS, signifying that these are the same states involved in the relaxation dynamics.

Table A6.1. Time constants and amplitudes obtained from fitting the ground-state depletion decays using bi-exponential functions at various excitation energies.

Pump Pulse Energy (μJ)	τ_1 (ps)	τ_2 (ps)	A_1	A_2	y_0
20	8196 ± 523	3639 ± 280	1.1 ± 0.2	-0.8 ± 0.1	1.3 ± 0.1
32	8020 ± 408	3590 ± 182	4.4 ± 0.5	-3.0 ± 0.3	1.7 ± 0.1
40	7905 ± 370	3475 ± 128	3.5 ± 0.5	-2.8 ± 0.3	2.4 ± 0.1

Figures A6.8, A6.9, and A6.10 display representative transient absorption time profiles of the 23 nm, 56 nm, and 97 nm $[Ru(bipy)_3][BETI]_2$ nanoGUMBOS, respectively, at probe wavelengths of 420 nm, 430 nm, and 455 nm, after the baseline shifts are subtracted. All transient absorption time profiles are fit to the functions $A_1 \exp\left(-\frac{t}{T_1}\right) + A_2 \exp\left(-\frac{t}{\tau_2}\right) + A_3 \exp\left(-\frac{t}{\tau_3}\right)$ where A_i and τ_i are the amplitudes and lifetimes of the i^{th} dynamical process, respectively,[3] for each wavelength for each nanoGUMBOS sample, as described in the manuscript. The relative contributions for each fit for the time profiles for the different nanoGUMBOS samples are shown in Figures A6.8, A6.9, and A6.10, along with the total fits. The lifetimes τ_1, τ_2, and τ_3 are attributed to the non-standard triplet metal centered complex, the non-standard triplet metal to ligand charge transfer complex, and intermolecular energy transfer, respectively. The amplitudes vary with wavelength to determine the decay spectra for each lifetime, shown in Figure A6.6 of the manuscript. The time constants obtained from fits of transient absorption of the nanoGUMBOS are listed in Table A6.2.

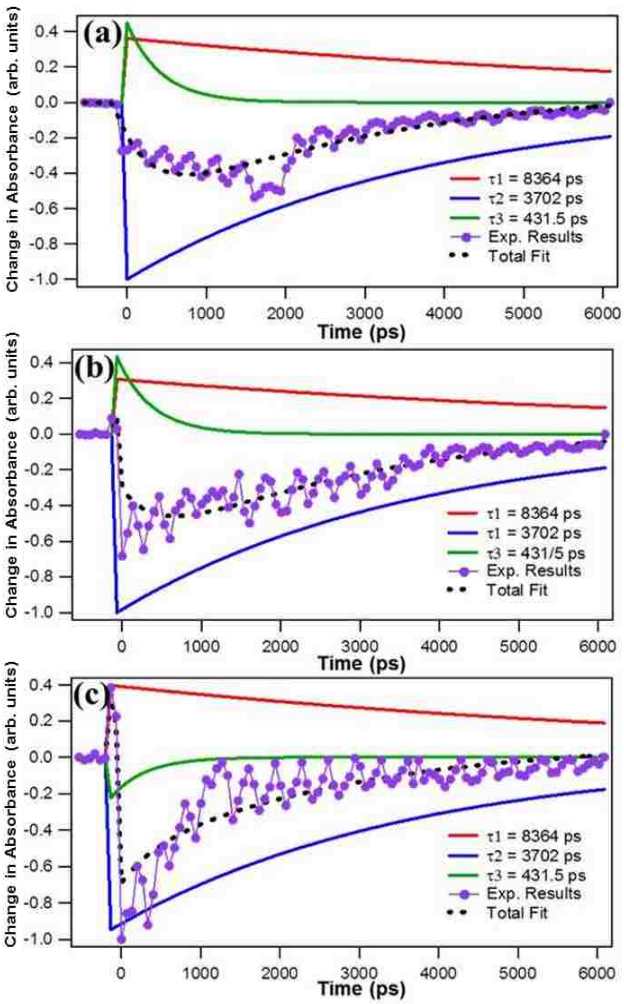

Figure A6.8. Representative time profiles of 23 nm $[Ru(bipy)_3][BETI]_2$ nanoGUMBOS measured at probe wavelengths of (a) 420 nm, (b) 430 nm, and (c) 455 nm. The experimental data are fit using a sum of multiple exponential functions and individual plots are generated as a function of pump-probe time delay.

A6.3 Phonon Analysis of $[Ru(bipy)_3][BETI]_2$ NanoGUMBOS

The time-dependent differences between the experimental measurements and the multiexponential best fits for the nanoGUMBOS contain the phonon oscillations for additional analysis. Figure A6.11 shows the residual oscillations of the phonons that are fit using a sinusoidal function given by $I(t) = y_0 + Aexp\left(-\frac{t}{\tau_4}\right)\sin(2\pi ft + \varphi)$, where f, φ, and τ_4 are the frequency, the phase shift, and phonon lifetime, respectively. The curves are offset for clarity. These oscillations are measured at 445 nm for the best signal to noise, although the same phonon lifetimes and frequencies are observed at all wavelengths, to within experimental uncertainty. Figure A6.12 shows the residual transient absorption

signal oscillations from the three nanoGUMBOS samples between the pump-probe time delay of 900 ps and 2000 ps at higher temporal resolutions with the corresponding sinusoidal fits. The oscillation periods, phase shifts, and phonon lifetimes for the different nanoGUMBOS sizes are shown in Table A6.3. These values are consistent between the lower temporal resolution scans, shown in Figure A6.11, and the higher temporal resolution scans, shown in Figure A6.12, to within experimental uncertainty.

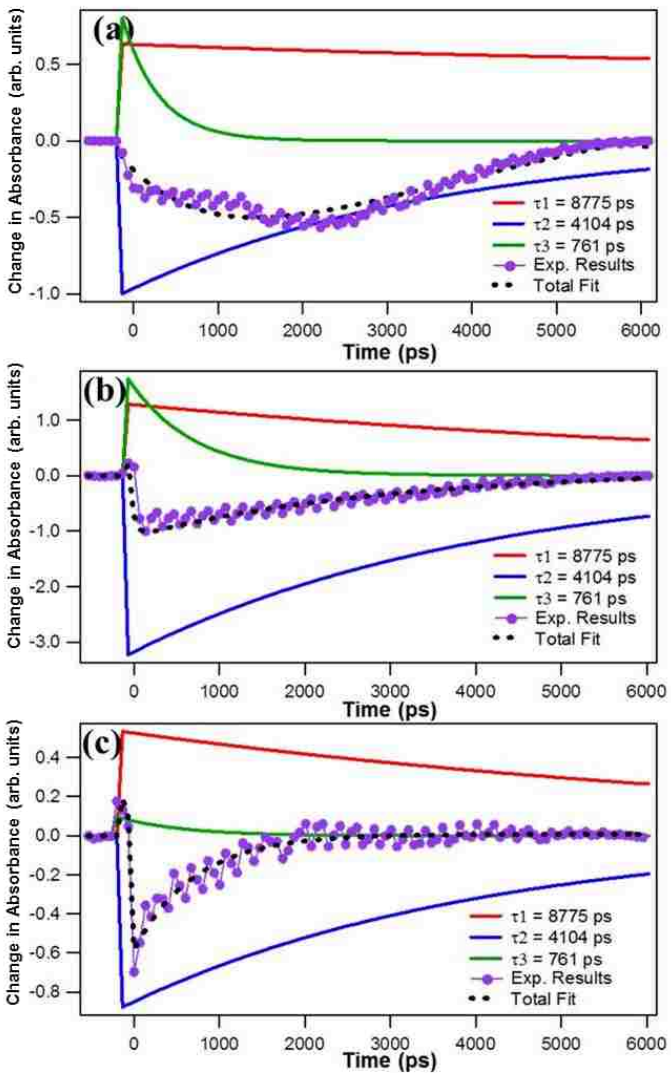

Figure A6.9. Representative time profiles of 56 nm $[Ru(bipy)_3][BETI]_2$ nanoGUMBOS measured at probe wavelengths of (a) 420 nm, (b) 430 nm, and (c) 455 nm. The experimental data are fit using a sum of multiple exponential functions and individual plots are generated as a function of pump-probe time delay.

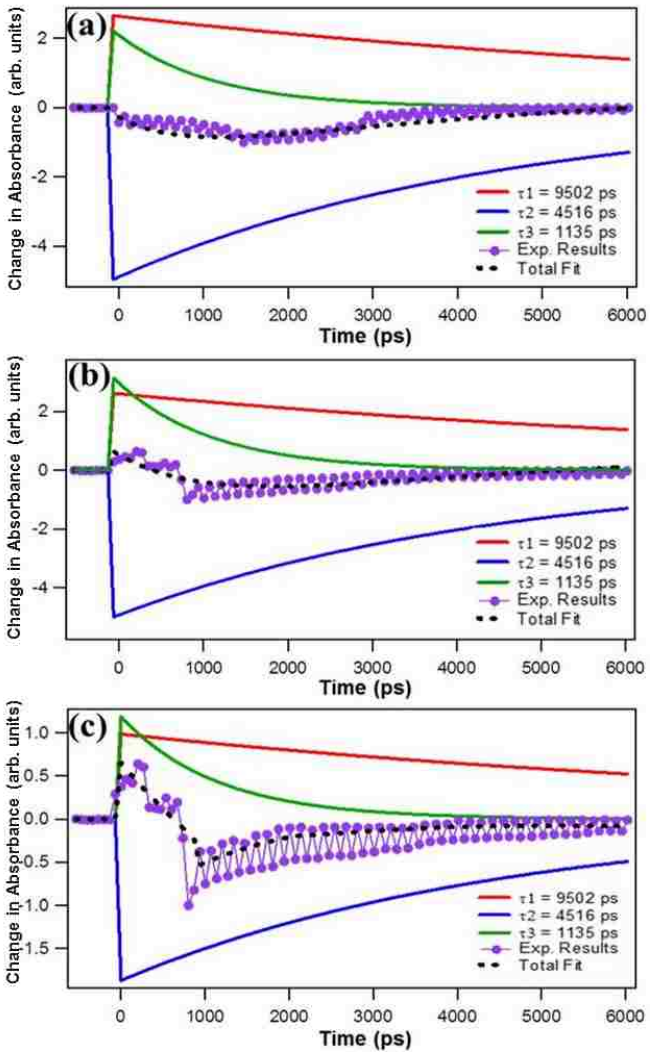

Figure A6.10. Representative time profiles of 97 nm $[Ru(bipy)_3][BETI]_2$ nanoGUMBOS measured at probe wavelengths of (a) 420 nm, (b) 430 nm, and (c) 455 nm. The experimental data are fit using a sum of multiple exponential functions and individual plots are generated as a function of pump-probe time delay.

Table A6.2. Time constants obtained from fits of spectrally-resolved transient absorption time profiles from $[Ru(bipy)_3][BETI]_2$ nanoGUMBOS using a sum of exponential functions.

diameter (nm)	τ_1 (ps)	τ_2 (ps)	τ_3 (ps)
23	8364 ± 65	3702 ± 41	432 ±76
56	8775 ± 136	4104 ± 55	761 ± 22
97	9502 ± 74	4516 ± 72	1135 ± 122

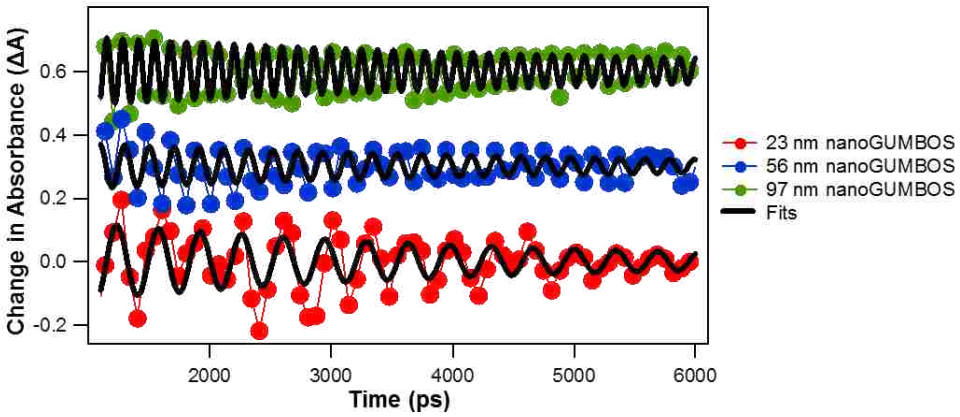

Figure A6.11. Residual signals from the transient absorption time profiles after subtracting the multiexponential best fits, showing the phonon oscillations for the different nanoGUMBOS sizes, along with the corresponding fits.

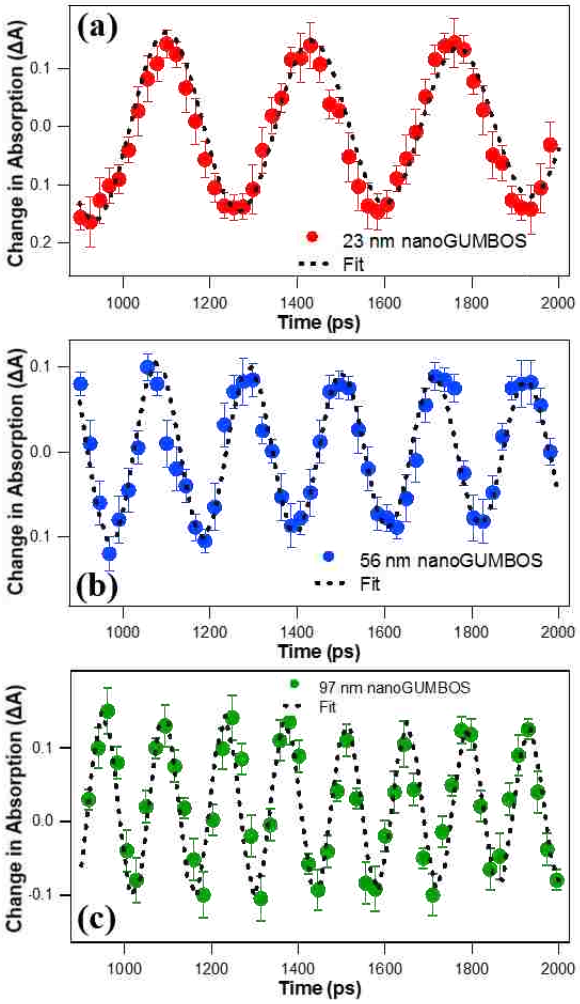

Figure A6.12. Residual signals from the transient absorption time profiles of the (a) 23 nm, (b) 56 nm, and (c) 97 nm nanoGUMBOS after subtracting the corresponding multiexponential best fits, showing the phonon oscillations under higher temporal resolution along with the corresponding fits.

Table A6.3. Size-dependent acoustic phonon oscillation periods, phase shifts, and phonon lifetimes of the $[Ru(bipy)_3][BETI]_2$ nanoGUMBOS.

diameter (nm)	T_{ac} (ps)	φ (rad)	τ_4 (ps)
23	334 ± 6	5.9 ± 0.1	3426 ± 354
56	209 ± 5	3.5 ± 0.2	4119 ± 521
97	140 ± 4	2.9 ± 0.1	5163 ± 594

The frequencies of the phonon oscillations can be fit using a model based on the size-dependent force constant of the nanocrystals.[4] The size-dependent frequencies can be written as a function of the size-dependent bond energy and bond length, where structural properties and thermodynamic parameters play an important role on the size-dependent phonons. The vibration frequency of bulk crystals ω_b can be written as

$$\omega_b = c_2 \times (\frac{\varepsilon}{h^2})^{\frac{1}{2}}$$

where ε is the bond energy, h is the bond length, and c_2 is a constant. The size-dependent frequency $\omega(d)$ can be written as

$$\omega(d) = c_2[\frac{\varepsilon(d)}{h(d)^2}]^{\frac{1}{2}}$$

where d the diameter of the nanoparticles, $\varepsilon(d)$ is the size-dependent bond energy, and $h(d)$ is the size-dependent bond length. The ratio of the size-dependent frequency to the vibration frequency of bulk crystals is given by

$$\frac{\omega(d)}{\omega_b} = \frac{h}{h(d)}\sqrt{\frac{\varepsilon(d)}{\varepsilon}}$$

with,

$$\frac{h}{h(d)} = \frac{1}{1 \pm \frac{3}{2d}\sqrt{\frac{\kappa d_0 h S_{vib} H_m T^2}{R V_c T_m^2}}}$$

where κ is the compressibility of the crystal, d_0 is the critical size, S_{vib} is the vibrational entropy, H_m is the enthalpy at the melting point T_m, V_c is molar volume of the crystal, and R is the ideal gas constant. The $\pm$ sign is carried during the derivation from the expression of the surface stress of the nanocrystals with $\frac{8\kappa f^2}{3\gamma_0} = d_0$, where γ_0 is the bulk value of the excess free energy.[5] γ_0 is approximated using the Gibbs-Thomson equation.[6] Both positive and negative values of the stress are possible depending on the interface structure of the nanocrystals, which can result in either lattice expansion or lattice contraction, respectively. The ratio of $\varepsilon(d)$ to ε can be written as

$$\frac{\varepsilon(d)}{\varepsilon} = \frac{1 - \frac{6\gamma_s V_c}{Ed}}{1 - \frac{n_s}{n}\frac{d_0}{d}}$$

where γ_s is the excess surface free energy of the crystal, E is the cohesion energy of one molar crystal, n is the coordination number of an atom or molecule in the bulk crystal, and n_s is the decrease of surface coordination number compared to n.

Figure A6.13 shows the fitting of the experimental results of $\omega(d)/\omega_b$ as a function of the nanoparticle diameter d using this model, showing good agreement. The value of h estimated from the crystal structure is 0.52 nm. The melting point T_m of the nanoGUMBOS used in the fit is 503 K. V_c is determined from the ratio of the molar mass of $[Ru(bipy)_3][BETI]_2$ to the density of the unit cell to be 2845 $cm^3.mol^{-1}$. n_s/n is determined for a monoclinic crystal structure to be 0.5. The other values used in the phonon fit are estimated to be approximately equal to the values provided in reference 3 while providing the best fit for the experimental data with $\kappa = 0.5 \times 10^{-10}\ \mathrm{Pa^{-1}}, \mathrm{d_0} = 3.12\ \mathrm{nm}, \mathrm{S_{vib}} = 10\ \mathrm{J.g-atom^{-1}K^{-1}}, \mathrm{H_m} = 100 \times 10^3\ \mathrm{J.mol^{-1}}, \gamma_s = 0.5\ \mathrm{J.m^{-2}}, \mathrm{E} = 400 \times 10^3\ \mathrm{J.mol^{-1}}$, and $\omega_b = 0.0074\ \mathrm{ps^{-1}}$.

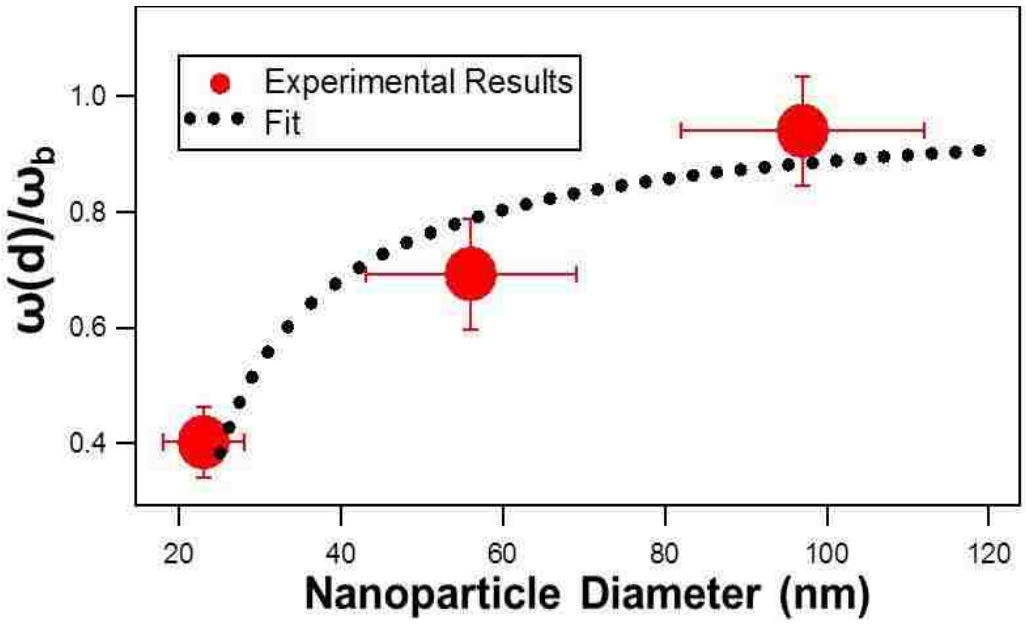

Figure A6.13. Ratio of the size-dependent frequency to the bulk frequency of $[Ru(bipy)_3][BETI]_2$ nanoGUMBOS as a function of nanoparticle size. The experimental data are fit using a model based on the size-dependent force constant of the nanocrystals.

The crystalline nanoGUMBOS are held together by relatively weak electrostatic and van der Waals forces, so it is very likely that the effects of the bulk and shear viscosity on the surface are more significant compared to closely-packed metallic or semiconductor nanoparticles, such as gold, silver, and titanium dioxide, which have much stronger bonding throughout the crystalline material. Additionally, the strong interaction of the nonpolar molecules at the nanoGUMBOS surface with the polar water solvent is expected to lead to lattice contraction, which is described using the negative sign in the equation for the size-dependence bond lengths. This model is shown to be an accurate description of the observed size-dependent phonon frequencies of these crystalline nanoGUMBOS, suggesting that significant surface stress due to the interaction with the aqueous solvent results in a size-dependent lattice contraction and the anomalous trend where phonon frequencies increase with increasing nanoparticle size. We have also analyzed these nanoGUMBOS in D_2O and have preliminary data which are consistent with our hypothesis of this phenomenon. Further studies are underway in D_2O and changing pH conditions and these observations will be reported in a subsequent manuscript.

A6.4 References

(1) Amman, A.; Easton, E. B. Novel Organic–Inorganic Hybrid Material Based on Tris(2,2'-bipyridyl)dichlororuthenium(II) Hexahydrate and Dawson-Type Tungstophosphate $K_7[H_4PW_{18}O_{62}]\cdot 18H_2O$ as a Bifuctional Hydrogen Peroxide Electrocatalyst for Biosensors. *Sensors and Actuators B* **2012**, *161*, 520–527.

(2) McClanahan, S. F.; Kincaid, J. R. ^{3}MLCT Lifetimes of Tris(2-2'-bipyridine) Ruthenium (II). Position-Dependent Deuterium Effect. *J. Am. Chem. Soc.* **1986**, *108*, 3840–3841.

(3) Punzi, A.; Martin-Gassin, G.; Grilj, J.; Vauthey, E. Effect of Salt on the Excited-State Dynamics of Malachite Green in Bulk Aqueous Solutions and at Air/Water Interfaces: a Femtosecond Transient Absorption and Surface Second Harmonic Generation Study. *J. Phys. Chem. C* **2009**, *113*, 11822–11829.

(4) Liang, L. H.; Shen, C. M.; Chen, X. P.; Lui, W. M.; Gao, H. J. The Size-Dependent Phonon Frequency of Semiconductor Nanocrystals. *J Phys: Condens Matter* **2004**, *16*, 267–272.

(5) Jiang, Q.; Liang, L. –H.; Zhao, D. –S. Lattice Contraction and Surface Stress of fcc Nanocrystals. *J. Phys. Chem. B* **2001**, *105*, 6275–6277.

(6) Jiang, Q.; Shi, H. –X.; Zhao, M. Free Energy of Crystal–Liquid Interface. *Acta Mater.* **1999**, *47*, 2109–2112.

APPENDIX 7 – SYNTHESIS AND CHARACTERIZATION OF PORPHYRIN-BASED NANOGUMBOS

A7.1 Materials

Zinc (II) meso-tetra(4-carboxyphenyl)porphyrin (acid form) was purchased from Frontier Scientific, Inc. (Logan, UT, USA). Trihexyl(tetradecyl)phosphonium chloride ([P66614][Cl]) was purchased from Sigma-Aldrich (St. Louis, MO, USA). The reaction scheme of the [M-TCPP][P66614] GUMBOS is shown in Figure A7.1.

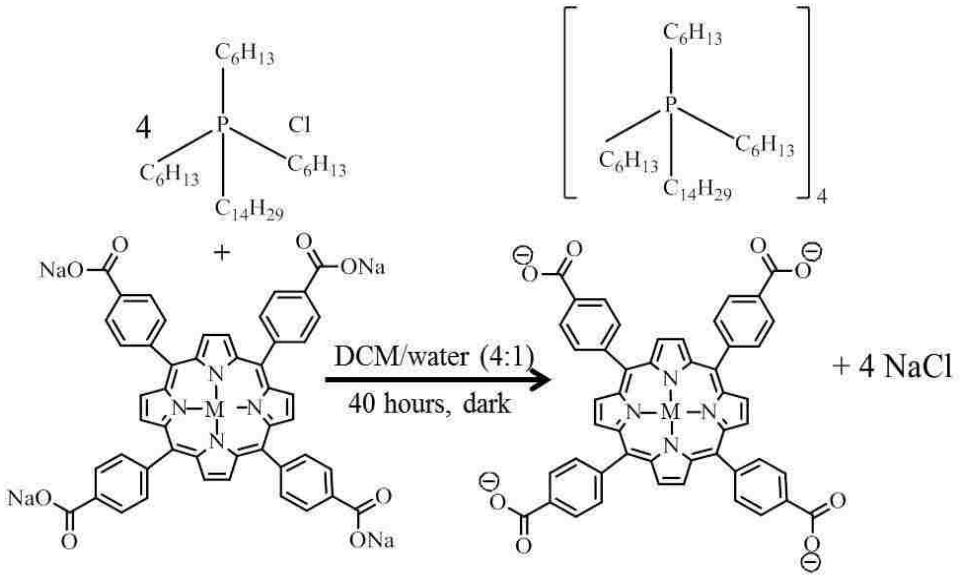

Scheme A7.1 Reaction scheme of the synthesis of [M-TCPP][P66614] GUMBOS.

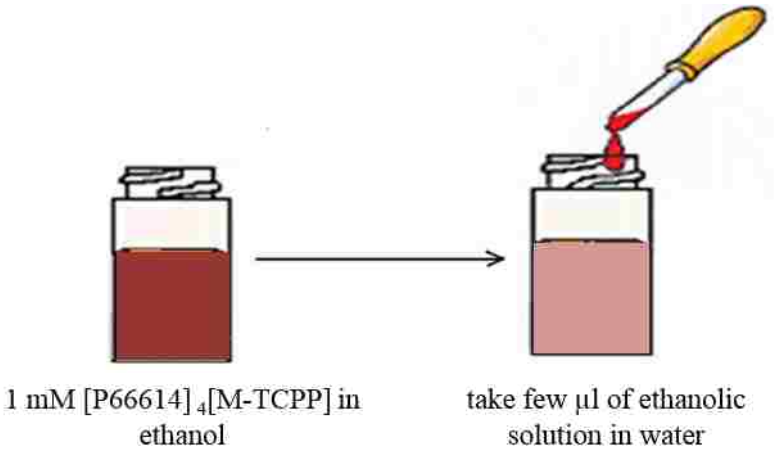

Scheme A7.2 Scheme shown the synthesis of colloidal nanoGUMBOS in water from the GUMBOS in ethanol.

A7.2 Absorbance and Fluorescence Spectra

The absorbance spectra of TCPP molecular dye and [TCPP][P66614]$_4$ nanoGUMBOS are shown in Figure A7.1. The Soret band is centered at 413 nm and 421 nm for TCPP dye and [TCPP][P66614]$_4$ nanoGUMBOS respectively. The absorbance spectra of Zn-TCPP molecular dye and [Zn-TCPP][P66614]$_4$ nanoGUMBOS are shown in Figure A7.2. The Soret band is centered at 420 nm and 435 nm for Zn-TCPP dye and [Zn-TCPP][P66614]$_4$ nanoGUMBOS respectively. The Q bands are centered after 500 nm for all the dyes and the nanoGUMBOS.

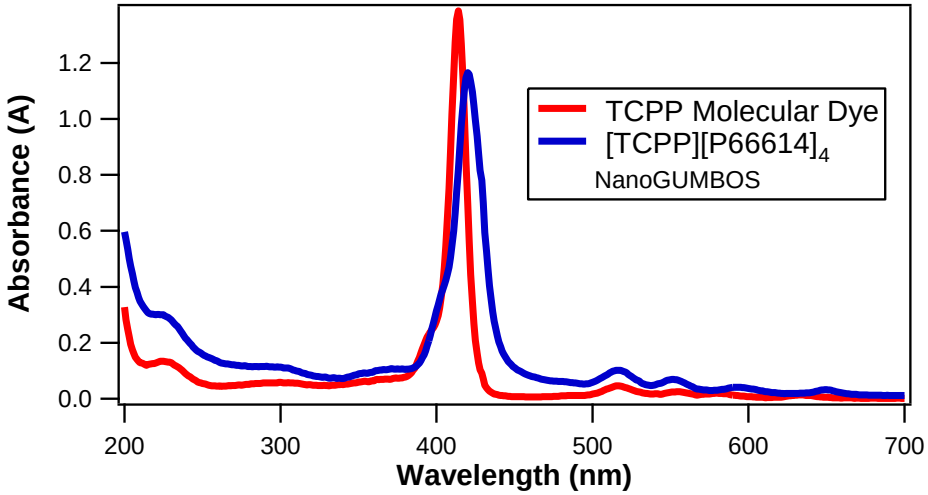

Figure A7.1. Absorbance spectra of (red line) 10 μM TCPP molecular dye and (blue line) 10 μM [TCPP][P66614]$_2$ nanoGUMBOS.

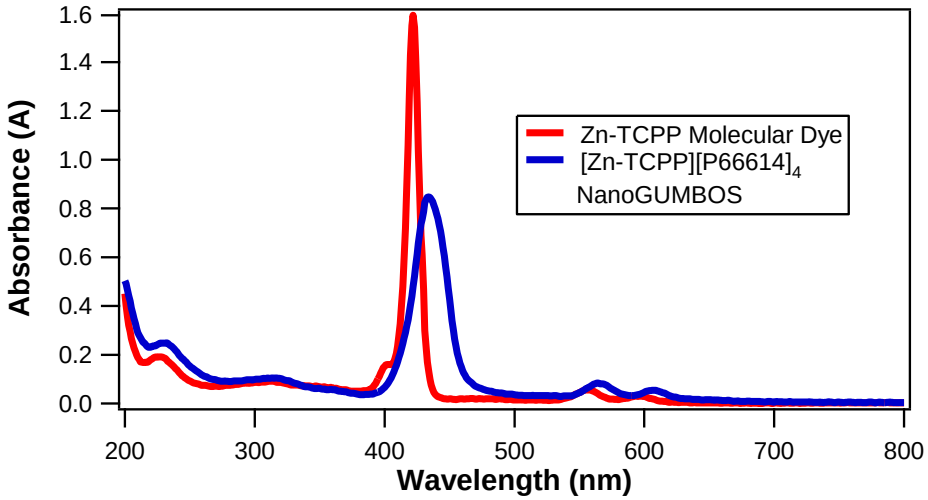

Figure A7.2. Absorbance spectra of (red line) 10 μM Zn-CPP molecular dye and (blue line) 10 μM [Zn-TCPP][P66614]$_2$ nanoGUMBOS.

The fluorescence spectra of TCPP molecular dye in water and $[TCPP][P66614]_4$ nanoGUMBOS in water are shown in Figure A7.3. TCPP dye possesses a high intensity fluorescence band centered at 640 nm and a lower intensity band centered at 720 nm. In the case of $[TCPP][P66614]_4$ nanoGUMBOS, the first low wavelength band is enhanced and red-shifted to 660 nm. The second higher wavelength band is red-shifted to 725 nm. The fluorescence spectra of Zn-TCPP molecular dye in water and $[Zn\text{-}TCPP][P66614]_4$ nanoGUMBOS in water are shown in Figure A7.4. Zn-TCPP dye possesses a high intensity fluorescence band centered at 610 nm and a lower intensity band centered at 660 nm. In the case of $[TCPP][P66614]_4$ nanoGUMBOS, the first low wavelength band is quenched and red-shifted to 625 nm. The higher wavelength band is enhanced and red-shifted to 680 nm.

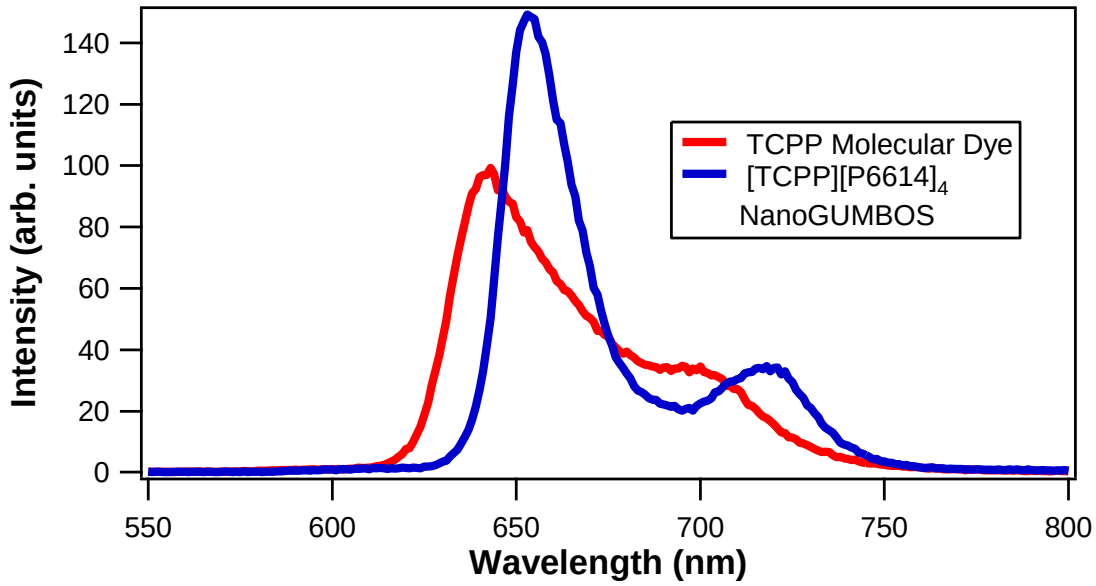

Figure A7.3. Fluorescence spectra of (red line) 10 μM TCPP molecular dye in water and (blue line) 10 μM [P66614][Zn-TCPP] colloidal nanoGUMBOS after excitation at 420 nm.

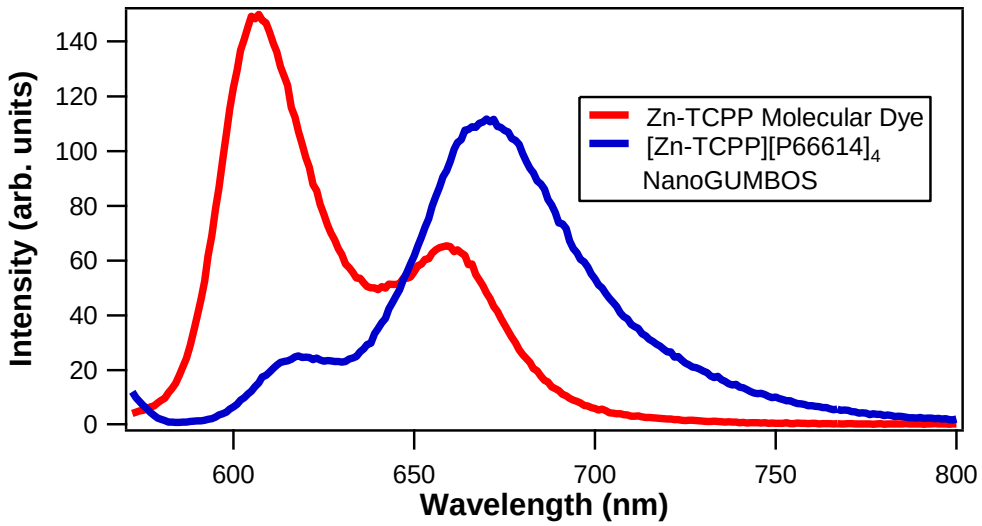

Figure A7.4. Fluorescence spectra of (red line) 10 μM Zn-TCPP molecular dye in water and (blue line) 10 μM [P66614][Zn-TCPP] colloidal nanoGUMBOS after excitation at 420 nm.

A7.3 TEM Images

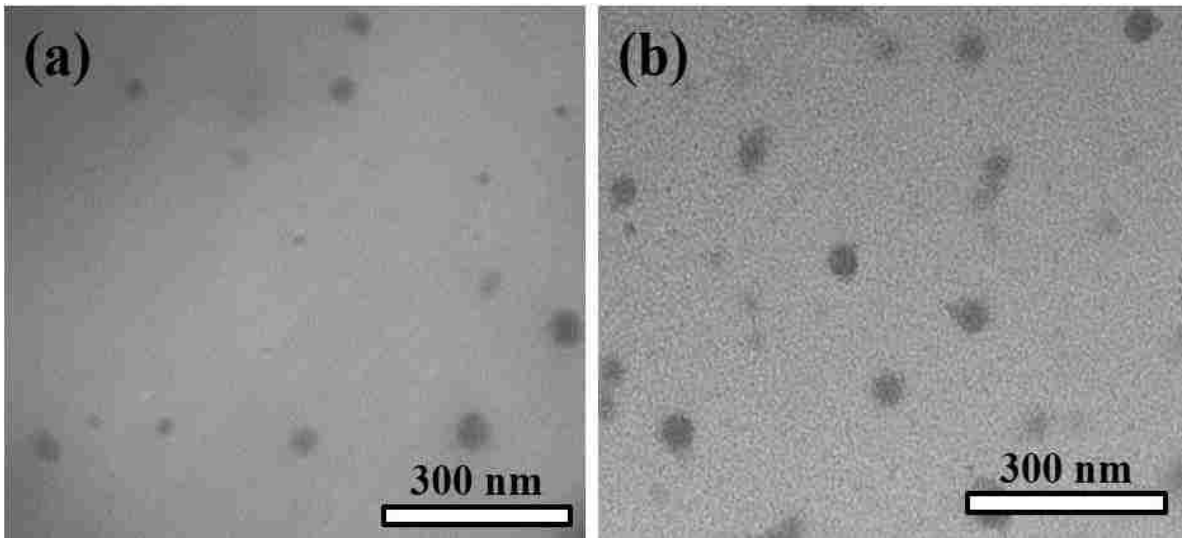

Figure A7.5. TEM images of (a) 49 nm $[TCPP][P66614]_4$ nanoGUMBOS , (b) 52 nm $[Zn\text{-}TCPP][P66614]_4$ nanoGUMBOS.

VITAE

Tony E. Karam studied chemistry at Saint-Joseph University in Lebanon, where he received his B.S. in chemistry in 2008. In 2011, he received a M.S. degree in chemistry from the American University of Beirut, where he studied nonlinear dynamics and periodic precipitation focusing on chemical reactions coupled to transport properties. He is currently a Ph.D. candidate in the Haber group at Louisiana State University. His research interests focus on the use of ultrafast and nonlinear spectroscopy for the study of processes such as molecular adsorption, molecular structure and orientation, and energy and electron transfer at nanoparticle surfaces.